


Summer 6-8-2017

Mechanical Characterization of Polymer Concrete with Nanomaterials

AlaEddin Douba
University of New Mexico

Follow this and additional works at: https://digitalrepository.unm.edu/ce_etds

 Part of the [Civil Engineering Commons](#), and the [Nanoscience and Nanotechnology Commons](#)

Recommended Citation

Douba, AlaEddin. "Mechanical Characterization of Polymer Concrete with Nanomaterials." (2017).
https://digitalrepository.unm.edu/ce_etds/173

This Thesis is brought to you for free and open access by the Engineering ETDs at UNM Digital Repository. It has been accepted for inclusion in Civil Engineering ETDs by an authorized administrator of UNM Digital Repository. For more information, please contact disc@unm.edu.

AlaEddin Douba

Candidate

Civil Eingeering

Department

This dissertation is approved, and it is acceptable in quality and form for publication:

Approved by the Dissertation Committee:

Dr. Mahmoud Reda Taha , Chairperson

Dr. Yu-Lin Shen

Dr. John Stormont

**Mechanical Characterization of Polymer Concrete with
Nanomaterials**

By

Ala Eddin Douba

B.S. in Civil Engineering and Mathematics, American University of Sharjah, UAE, 2014

THESIS

Submitted in Partial Fulfillment of the
Requirements for the Degree of

**Master of Science
Civil Engineering**

The University of New Mexico
Albuquerque, New Mexico

July, 2017

DEDICATION

To my family, the good and the bad in my journey, to not giving up on my dreams and especially to the memory of my grandfathers.

Also, to all the Syrian refugees and Syrian young adults with big dreams and no means.

ACKNOWLEDGEMENT

Praise to be God

I would like to express my gratitude and appreciation to my advisor Dr. Mahmoud Reda Taha for his continuous support and monitoring during my Master's degree and research. His guidance helped me to seek more knowledge and acquire more patience.

I also want to extend my thankfulness to my committee members Dr. Yu-Lin Shen and Dr. John Stormont for their time and fair evaluation of my thesis. Sincere thanks also go to Dr. Usama Kandil for his contributions to all papers and help decoding FTIR observations.

Special gratitude goes to Mr. Kenny Martinez for always having my back, helping me through all experiments, for every cup of morning coffee and for sharing his cookies.

Many thanks also go to all the research team: Elisa Borowski, Amy Garner/Noah, Moneeb Genedy, Sherif AbouBakr, Mojgan Maadandar, Rahul ChennaReddy, Eslam Soliman, Mehmet Emiroglu, and Nicole Trujillo.

Finally, my profound gratitude is for my roommate Adrian Faustine, girlfriend Sarah Brown and her family for being my second family and for their love and support.

This research was supported by Southern Plains Transportation Center (SPTC), Sandia National Laboratories, Department of Energy (DOE) and University of New Mexico (UNM). This support is gratefully acknowledged. Gratitude to Transpo Inc. and Epoxy Chemicals Inc. for donating all epoxy and aggregate materials.

Mechanical Characterization of Polymer Concrete with Nanomaterials

By

Ala Eddin Douba

B.S. in Civil Engineering and Mathematics, American University of Sharjah, UAE, 2014

ABSTRACT

Nanomaterials are defined by those whose characteristic length scale lies within the nanometer scale. Their extreme dimension achieves extraordinary mechanical properties superior to other micro and macro additives. The introduction of nanotechnology to Civil Engineering utilizes low volume inclusions of nanomaterials to alter the properties of conventionally used bulk materials. Polymer Concrete (PC) where epoxy polymer binders replace cement binders, has become a common repair material among many other application and often can be considered an alternative to Portland cement concrete (PCC). PC is often used in bridge deck overlays, manholes, machine foundations and repairs. Its diverse chemical composition and high flowability makes it a supreme candidate to take advantage of nanomaterials induced chemical and mechanical effects.

This research effort is designated to examine the impact of various loadings of different nanomaterials on PC's mechanical and microstructural properties. Nanomaterials used are alumina nanoparticles (ANPs), silica nanoparticles (SNPs), pristine and carboxyl multi-walled carbon nanotubes (P-MWCNTs and COOH-MWCNTs). The polymer epoxy matrix chosen are Siloxane and Novolac epoxies used by the industry for bridge deck overlays and repairs respectively. Mechanical tests included flowability, tension, compression, flexure, fracture toughness, slant shear, and fatigue tests alongside electrical conductivity monitoring. Microstructural investigation

included scanning electron microscope (SEM), dynamic modulus analyzer (DMA), and Fourier transform infrared spectrograph (FTIR). Analytical study of rule of mixture, stiffness mismatch and true shear stresses using finite element modeling (FEM) were also utilized.

Dispersion was performed using magnetic stirring and ultrasonication which were verified in all PCNC mixes using SEM. Mechanical and microstructural tests show that the investigated nanomaterials at different contents generate varying mechanical and chemical effects in PC. Significant difference between 1D and 0D nanomaterials and between functionalized and non-functionalized are observed. Nevertheless, PC nanocomposites (PCNC) showed significant improvements in mechanical performance. All PCNC samples exhibited appreciable tensile strength between 9 – 15 MPa and large ductility up to 5.5% strain at failure representing an order of magnitude improvement from PCC. Hybrid MWCNTs mixes showed the best tensile properties of all suggested mixes. Further investigation using DMA and FTIR tests showed increased crosslinking with increasing COOH content due to carbonyl group formations. Improvements in fracture toughness were also recorded for all PCNC up to 80% from neat. PC and PCNC showed distinctive non-linear behavior that is best quantified using QBFM. Fatigue life due to ductility and fracture toughness improvements increased by 55%. The compressive strength of all PCNC ranged between 23 MPa and 60 MPa and in general nanomaterials resulted in a decrease in compressive strength. The bond strength of PC also increased by maximum of 51%. FTIR analysis showed that the bond strength of PCNC is highly dependent on chemical interaction with the interface. The bond strength is also severely affected by the stiffness mismatch and Poisson's ratio as shown by FEM and analytical mechanics causing up to 130% increase in bond strength. The proposed PCNC can serve as smart material enabling structural health monitoring (SHM) and is highly suitable as a structural material specifically for earthquakes.

PUBLICATIONS LIST

Published Journal Papers:

- **Douba, A.**, Emiroglu, M. Tarefder, R., Kandil, U., Reda Taha, M. M. “Improving fracture toughness of polymer concrete using carbon nanotubes”, *Journal of the Transportation Research Board*. Accepted February, 2017.
- Emiroglu, M. **Douba A.**, Tarefder, R., Kandil, U., Reda Taha, M. M. “New polymer concrete with superior ductility and fracture toughness using alumina nanoparticles”, *Journal of Materials in Civil Engineering (ASCE)*. 84 (8–9). doi:10.1061/(ASCE)MT.1943-5533.0001894.
- **Douba, A.**, Genedy, M., Matteo, E., Stormont, J. and Reda Taha, M. M. “The significance of nanomaterials on apparent slant shear strength of epoxy polymer concrete and steel”. *International Journal of Adhesion and Adhesive*, 74: 77–85. doi:10.1016/j.ijadhadh.2017.01.001.

In-Progress Journal Papers:

- **Douba, A.** Emiroglu, M. Kandil, U., Reda Taha, M. M. “A very ductile polymer concrete using a mixture of pristine and carboxylic functionalized carbon nanotubes”, *Cement and Concrete Research*. Submitted May, 2017.
- **Douba, A.** Emiroglu, M. Kandil, U., Reda Taha, M. M. “Polymer concrete by design using carbon nanotubes”, *American Concrete Institute (ACI): Materials*.
- **Douba, A.** and Reda Taha, M. M. “Analytical evaluation of stiffness mismatch in slant shear test”. *ASCE Journal of Experimental Mechanics*.
- **Douba, A.**, Tarefder, R. and Reda Taha, M. M. “Health monitoring of smart PC with prolonged fatigue life”. *ASCE Journal of Engineering Mechanics*

Conferences:

- **Douba, A.**, Genedy, M., and Reda Taha M. M. “PC with superior ductility Using Mixture of Pristine and Fictionalized Carbon Nanotubes”. *16th international Congress on Polymers in Concrete (ICPIC 2018)*, Washington, April, 2018.
- **Douba, A.**, Genedy, M., Tarefder, R. and Reda Taha M. M. “Improving fracture toughness of polymer concrete using MWCNTs”. *Proceedings of 9th International Conference on Fracture Mechanics of Concrete and Concrete Structures (FraMCoS 9)*. May 29, 2016
- **Douba, A.**, Genedy, M., Matteo, M., Stormont, J. and Reda Taha, M. M. “Apparent vs. true bond strength of steel and pc with nanoalumina”. *Proceedings of 15th international Congress on Polymers in Concrete (ICPIC 2015)*, Singapore, October, 2015.

Presentations

- **Douba, A.**, Genedy, M., Tarefder, R. and Reda Taha, M. M. “Improving fracture toughness of polymer concrete using MWCNTs”. American Concrete Institute (ACI) Spring Convention 2016, Milwaukee, WI.
- **Douba, A.**, Garner, A., Genedy, M. and Reda Taha, M. M. “smart monitoring of fatigue damage in polymer concrete using carbon nanotubes”. American Concrete Institute (ACI) Spring Convention 2016, Milwaukee, WI.

Patents

- Reda Taha, M. M., **Douba, A.**, Emiruglo, M., and Kandil, U. F. “Methods for making polymer concretes with extreme ductility for resilient infrastructure under extreme events”. *US Provisional Patent Filed*, April 2016.
- Reda Taha, M. M., Kandil, U. F., **Douba, A.**, and Emiruglo, M. “Electrically and thermally conductive polymer concrete”. *Published application* STC Ref. No. 2015-124-02, IPN WO 2017/008048.

TABLE OF CONTENTS

Dedication.....	ii
Acknowledgement	iv
Abstract.....	v
Publications list.....	vii
Table of Contents.....	ix
List of Figures.....	xiv
List of Tables	xxi
Chapter one: Introduction	1
1.1 Background	1
1.2 Motivation and Objectives	2
1.3 Scope of Work.....	5
1.4 Thesis outline	6
Chapter Two: Literature Review	8
2.1 Introduction to Polymer Concrete Nanocomposites.....	8
2.1.1 Polymers	8
2.1.2 Polymer concrete	9
2.1.3 Nanotechnology.....	13
2.2 Polymer Concrete In-Situ	15
2.2.1 Bridge deck overlays.....	18

2.2.2 Repairs of wellbores	20
2.3 Effects of Nanomaterials on Epoxy Polymer Systems	22
2.3.1 Dispersion and flowability.....	22
2.3.2 Compressive strength.....	25
2.3.3 Tensile strength.....	30
2.3.4 Bond strength.....	32
2.3.5 Modulus of elasticity and Poisson’s ratio	33
2.3.6 Fatigue life	34
2.3.7 Fracture Toughness	36
2.3.8 Structural Health Monitoring Using Nanomaterials	40
Chapter 3: Experimental Methods	43
3.1 Materials	44
3.1.1 Epoxy polymer matrix	44
3.1.3 Aggregate filler	45
3.1.3 Nanomaterials	45
3.2 Nanocomposite Preparation	47
3.3 Flowability Test	53
3.4 Tension Test.....	54
3.5 Fracture Toughness Test.....	56
3.5.1 Linear elastic fracture mechanics (LEFM) analysis	61

3.5.2 Quasi-brittle fracture mechanics (QBFM) analysis: Effective crack modulus method.....	66
3.5.3 Quasi-static fracture mechanics: Work-of-fracture (Factionous crack model)....	71
3.6 Fatigue test	73
3.7 Structural Health Monitoring in Flexure.....	76
3.8 Slant Shear Test	78
3.9 Static Elastic Properties	81
3.10 Scanning Electron Microscope (SEM)	82
3.11 Fourier Transform Infrared Spectrogram (FTIR)	83
3.12 Dynamic Modulus Analyzer (DMA)	84
3.13 Finite Element Analysis in ABAQUS	86
Chapter 4: Results and discussion.....	94
4.1 Flowability Test.....	97
4.2 Tension test	99
4.2.1 Direct tensile test.....	100
4.2.2 Modulus of rupture.....	114
4.3 Fracture toughness test	118
4.3.1 Linear elastic fracture mechanics (LEFM) analysis.....	121
4.3.2 Quasi-brittle fracture mechanics analysis: Effective crack modulus method	

4.3.3	Quasi-brittle fracture mechanics: Work of fracture	129
4.4	Fatigue test	134
4.5	Structural health monitoring (SHM)	136
4.5.1	Percolation test	137
4.5.2	SHM in flexure.....	138
4.6	Functional group analysis.....	143
4.7	Slant shear test.....	147
4.8	Compression test	149
4.9	Elastic properties	151
4.9.1	Experimental results	152
4.9.2	Rule of mixture.....	154
4.10	Finite element analysis using ABAQUS	160
4.11	Stiffness mismatch analytical solution	164
4.12	Scanning Electron Microscope	169
4.13	Fourier transform infrared spectroscopy (FTIR)	174
4.14	Dynamic modulus analyzer (DMA)	181
Chapter 5: Conclusion.....		183
References		188
Appendix A: Matlab codes		201
1.	Linear elastic fracture mechanics codes:.....	201

A.1.1 Reading text files	201
A.1.2 Curve fitting for evaluating “A” according to ACI 446 report	201
A.1.3 Bi-linear approximation code.....	202
A.1.4 Evaluating fracture toughness	204
2. Work of fracture codes:.....	207
3. Quasi brittle fracture mechanics codes:	207
A.3.1 Evaluating the critical crack depth and elastic fracture parameters (G & K)	207
A.3.2 Evaluating the J-integral	210
Appendix B: Fracutre test setup shop-drawings	211

LIST OF FIGURES

Figure 1.1: Events flow expressing the scope of work. -----	7
Figure 2.1: Linear and chained polymer chains graphical representation. -----	9
Figure 2.2: The structure of polymers as chains of monomers -----	9
Figure 2.3: The different types of nanomaterials classified based on their characteristic dimension. -----	14
Figure 2.4: Carbon fiber textured polymer concrete facade panels by ULMA architectural solutions. -----	17
Figure 2.5: Bridge deck system schematics as part of the superstructure. -----	19
Figure 2.6: PC overlays in-situ courtesy of Transpo Inc. -----	20
Figure 2.7: Leakage pathways of abandoned oil-wells with b. between cement and steel casing and d. through the casing (Gasda et al. 2004). -----	21
Figure 2.8: Schematics of particle separation during dispersion due to shear energy. -----	23
Figure 2.9: Paris law prescribing the secondary fatigue life behavior. -----	35
Figure 3.1: Transmission electron microscope (TEM) images of (a) ANPs and (b) MWCNTs --	47
Figure 3.2: Preparation of epoxy nanocomposite showing dispersion steps for magnetic stirring and ultrasonication. -----	47
Figure 3.3: Production of polymer concrete slurry -----	49
Figure 3.4: Flowability measurement of PC showing flow caliber, cone and table and test procedure. -----	54
Figure 3.5: Tension samples molds and respective dimensions. -----	55
Figure 3.6: Tension test and its schematics -----	55
Figure 3.7: Dimensions and schematics of fracture specimen per ACI 446 and as used. -----	57
Figure 3.8: Fracture test setup in experiment and schematics. -----	58
Figure 3.9: Reference frame as used and its schematics. -----	58
Figure 3.10: Self adjustment of the reference frame; as the PC prisms bend due to fracture, the reference frame remains in its location collecting accurate displacement. -----	59

Figure 3.11: Basic principles used for analysis of notched beam set-up data to extract the bilinear fracture curve of PC.-----	61
Figure 3.12: Schematics of the methods prescribed to translate the test data from three-point bending to direct tension test.-----	62
Figure 3.13: Model of Quasi-Brittle Fracture materials showing the increase in stress due to the fracture process zone (Shah et al. 1995).-----	67
Figure 3.14: The secant compliance approach describing the effective elastic modulus fracture mechanics method (Shah 1983).-----	68
Figure 3.15: QBFM analysis for-loop using the effective crack modulus (Reda Taha et al. 2002)-----	68
Figure 3.16: Fatigue test setup schematics and actual.-----	73
Figure 3.17: PC samples in four-point bending setup showing electrical conductivity measurement points.-----	78
Figure 3.18: In-situ fatigue test showing the loading frame and the source meter connected to measure change in electrical resistance to monitor fatigue damage evolution in PC.-----	78
Figure 3.19: Slant shear sample and its schematics.-----	80
Figure 3.20: Vertical alignment using high resolution camera of PC and steel prior to testing.--	80
Figure 3.21: Compression sample with its schematics showing locations of all strain gauges---	82
Figure 3.22: Hitachi S-5200 Nano scanning electron microscope (SEM).-----	83
Figure 3.23: PerkinElmer FTIR machine used in microstructural analysis.-----	84
Figure 3.24: The DMA machine showing (a) the instrument and (b) Epoxy sample with P-MWCNTs placed in three-point bending clamp.-----	85
Figure 3.25: Back-solving procedure in ABAQUS to estimate the interface properties-----	86
Figure 3.26: 6-node tetrahedral and 8-node hexagonal elements used in ABAQUS simulations	87
Figure 3.27: Mesh sensitivity analysis performed on NPC-Neat model-----	87
Figure 3.28: FE model using ABAQUS simulation environment: (a) Boundary conditions (b) Bilinear shear stress-slip relation (c) Meshed model using 74,524 elements.-----	88
Figure 3.29: Load-displacement curves of maximum shear sensitivity analysis in ABAQUS---	89
Figure 3.30: Load-displacement curves of critical energy sensitivity analysis in ABAQUS.-----	90

Figure 3.31: Load-displacement curves of interfacial stiffness sensitivity analysis in ABAQUS	91
Figure 3.32: Load-displacement curves of viscosity coefficient sensitivity analysis in ABAQUS.	93
Figure 4.1: Variation of nanomaterials and their content at different stages of testing for Siloxane PC (SPC)	95
Figure 4.2: Variation of nanomaterials and their content at different stages of testing for Novolac PC (NPC)	96
Figure 4.3: Flowability test result for Siloxane PC (SPC) mixes with nanomaterials.	97
Figure 4.4: Flowability test results of Siloxane PC (SPC) using hybrid mixes of P-MWCNTs and COOH-MWCNTs.	97
Figure 4.5: Flowability test results for Novolac PC (NPC).	98
Figure 4.6: Direct tension test showing different dog-boned samples loaded with MTS Bionix and utilizing an extensometer to measure strain.	100
Figure 4.7: Tensile test stress-strain curves for Siloxane PC (SPC) mixes containing P-MWCNTs at different contents.	100
Figure 4.8: Tensile test stress-strain curves for Siloxane PC (SPC) mixes containing COOH-MWCNTs at different contents.	101
Figure 4.9: Tensile test stress-strain curves for Siloxane PC (SPC) mixes containing ANPS at different contents.	101
Figure 4.10: Stretching of the PC surface during tension test.	102
Figure 4.11: Tensile strength of Siloxane PC (SPC) mixes.	103
Figure 4.12: Tensile strength of Siloxane PC (SPC) mixes containing different contents of P-MWCNTs.	104
Figure 4.13: Tensile strength of Siloxane PC (SPC) mixes containing different contents of COOH-MWCNTs.	104
Figure 4.14: Tensile strength of Siloxane PC (SPC) mixes containing different contents of ANPS	105
Figure 4.15: Tensile strain at failure of different Siloxane PC (SPC).	107
Figure 4.16: Tensile strain at failure of Siloxane PC (SPC) mixes containing different contents of P-MWCNTs.	107

Figure 4.17: Tensile strain at failure of Siloxane PC (SPC) mixes containing different contents of COOH-MWCNTs. -----	108
Figure 4.18: Tensile strain at failure of Siloxane PC (SPC) mixes containing different contents of ANPS. -----	108
Figure 4.19: Toughness of Siloxane PC (SPC) mixes in tension test. -----	110
Figure 4.20: Toughness of Siloxane PC (SPC) mixes in tension test containing P-MWCNTs. -----	111
Figure 4.21: Toughness of Siloxane PC (SPC) mixes in tension test containing COOH-MWCNTs. -----	111
Figure 4.22: Toughness of Siloxane PC (SPC) mixes in tension test containing ANPS. -----	112
Figure 4.23: Elastic modulus of Siloxane PC (SPC) mixes. -----	113
Figure 4.24: Flexural test of PC prisms using three-point bending showing stretched vs unstretched surface areas. -----	115
Figure 4.25: Flexural test of PC prisms using four-point bending showing excessive deformation (large ductility) and stretched vs unstretched surfaces. -----	116
Figure 4.26: Modulus of rupture results of Siloxane PC (SPC). -----	116
Figure 4.27: Fracture toughness test showing excessive crack mouth opening displacement (CMOD) and non-linear crack patterns. -----	118
Figure 4.28: Crack mouth opening displacement (CMOD) – load curves for Siloxane PC (SPC) mixes containing P-MWCNTs. -----	120
Figure 4.29: Crack mouth opening displacement (CMOD) – load curves for Siloxane PC (SPC) mixes containing COOH-MWCNTs. -----	120
Figure 4.30: Crack mouth opening displacement (CMOD) – load curves for Siloxane PC (SPC) mixes containing ANPs. -----	121
Figure 4.31: Bi-linear approximation of fracture toughness of Siloxane PC (SPC) containing P-MWCNTs. -----	122
Figure 4.32: Total critical energy release rate (fracture toughness) results of quasi-brittle fracture mechanics analysis using effective crack modulus method of Siloxane PC (SPC). -----	125
Figure 4.33: Total critical energy release rate (fracture toughness) results of quasi-brittle fracture mechanics analysis using effective crack modulus method of Siloxane PC (SPC) containing P-MWCNTs. -----	126

Figure 4.34: Total critical energy release rate (fracture toughness) results of quasi-brittle fracture mechanics analysis using effective crack modulus method of Siloxane PC (SPC) containing COOH-MWCNTs-----	126
Figure 4.35: Total critical energy release rate (fracture toughness) results of quasi-brittle fracture mechanics analysis using effective crack modulus method of Siloxane PC (SPC) containing ANPS.-----	127
Figure 4.36: Energy release rate (fracture toughness) results of quasi-brittle fracture mechanics analysis using work of fracture method of Siloxane PC (SPC).-----	131
Figure 4.37: Comparison of quasi-brittle fracture mechanics models results of fracture toughness (measured with energy release rates) between effective crack modulus and work of fracture for Siloxane PC (SPC) containing P-MWCNTs.-----	132
Figure 4.38: Comparison of quasi-brittle fracture mechanics models results of fracture toughness (measured with energy release rates) between effective crack modulus and work of fracture for Siloxane PC (SPC) containing COOH-MWCNTs.-----	132
Figure 4.39: Comparison of quasi-brittle fracture mechanics models results of fracture toughness (measured with energy release rates) between effective crack modulus and work of fracture for Siloxane PC (SPC) containing ANPs.-----	133
Figure 4.40: Fatigue test results of selected SPC mixes.-----	135
Figure 4.41: Percolation test for Siloxane epoxy containing P-MWCNTs and COOH-MWCNTs.-----	137
Figure 4.42: SHM of SPC-CNT-P2.0 in flexure-----	138
Figure 4.43: Electrical damage feature and strain in flexure test of SPC-Neat vs flexural stress.-----	139
Figure 4.44: Mechanical damage feature and strain in flexure test of SPC-Neat vs flexural stress.-----	139
Figure 4.45: Electrical damage feature and strain in flexure test of SPC-CNT-P2.0 vs flexural stress.-----	140
Figure 4.46: Mechanical damage feature and strain in flexure test of SPC-CNT-P2.0 vs flexural stress.-----	141
Figure 4.47: Electrical and Mechanical damage feature in flexure test of SPC-CNT-P2.0 vs flexural stress.-----	141
Figure 4.48: Calibrated electrical damage feature to the mechanical damage feature for SPC-CNT-P2.0-----	142

Figure 4.49: Tensile stress-strain curves of SPC mixes of hybrid P-MWCNTs and COOH-MWCNTs at 2.0 wt.% total content. -----	143
Figure 4.50: Tensile strength of SPC mixes at 2.0 wt.% MWCNTs content including P-MWCNTs, COOH-MWCNTs or mix of both.-----	144
Figure 4.51: Tensile strain at failure of SPC mixes at 2.0 wt.% MWCNTs content including P-MWCNTs, COOH-MWCNTs or mix of both.-----	144
Figure 4.52: Toughness of SPC mixes at 2.0 wt.% MWCNTs content including P-MWCNTs, COOH-MWCNTs or mix of both. -----	145
Figure 4.53: Mechanical performance of SPC mixes normalized by SPC-Neat (11.8 MPa, 1.85%, 176.3 kJ/m ³) with respect to COOH weight content of epoxy resin at 2.0 wt.% total MWCNTs content.-----	145
Figure 4.54: Apparent shear stress of Novolac PC (NPC) mixes using slant shear test.-----	147
Figure 4.55: Slant shear fracture surface post-failure for Novolac PC (NPC) samples at 2.0 wt.% content of their respective nanomaterials content.-----	148
Figure 4.56: Compressive strength of selected Novolac PC (NPC) mixes based on best performance in slant shear test.-----	149
Figure 4.57: Before and after compression test showing extreme ductility of NPC-Neat -----	150
Figure 4.58: Stress-strain of Novolac PC (NPC) extracted from compression tests with strain gauges. -----	151
Figure 4.59: Elastic modulus measurements of Novolac PC (NPC) extracted from compression test with strain gauges.-----	152
Figure 4.60: Poisson's ratio measurements of Novolac PC (NPC) extracted from compression test with strain gauges.-----	153
Figure 4.61: Load-displacement of Novolac PC (NPC) prepared with COOH-MWCNTs, ANPs and SNPs comparing experimental and FEA.-----	160
Figure 4.62: True shear strength compared to apparent shear strength of NPC mixes. -----	162
Figure 4.63: Load-displacement extract from finite element analysis of neat PC showing magnified slippage at 0.720mm, 0.802mm, and 0.837mm. -----	163
Figure 4.64: Shear contours showing locations of maximum local shear stress during slippage of SPC-CNT-0.5 of (a) 0.720 mm (b) 0.802 mm and (c) 0.837 mm. -----	163
Figure 4.65: Schematics of slant shear stiffness mismatch variables -----	164

Figure 4.66: Relative stiffness mismatch calculated using Eq. (4.13) for two steel parts with respect to the distance across slant shear sample (y). -----	166
Figure 4.67: the variability of the average stiffness mismatch with the change of elastic modulus of the top part normalized by the bottom part (λ) described in Eq. (4.15). -----	166
Figure 4.68: SEM scans of S-Neat used as reference for the topological feature. -----	169
Figure 4.69: SEM scans for hardened epoxy containing (a) and (b) 0.5 wt.% ANP and (c) and (d) 3.0 wt.% ANP. -----	170
Figure 4.70: SEM images of epoxy samples containing P-MWCNTs showing no agglomeration at 2.0 wt.%. -----	171
Figure 4.71: SEM images of epoxy samples containing COOH-MWCNTs showing uniform dispersion at 2.0 wt.%. -----	171
Figure 4.72: 1.9 wt.% P-MWCNTs with 0.1 wt.% COOH-MWCNTs -----	172
Figure 4.73: 0.1 wt.% P-MWCNTs with 1.9 wt.% COOH-MWCNTs -----	172
Figure 4.74: FTIR spectrograph for Siloxane epoxy with P-MWCNTs at 0.5 and 2.0 wt.% contents -----	174
Figure 4.75: FTIR spectrograph of Siloxane epoxy with COOH-MWCNTs at 0.5 and 2.0 wt.% contents. -----	174
Figure 4.76: FTIR spectrograph of Siloxane epoxy for functional group analysis at 2.0 wt.% total content of both pristine and functionalized MWCNTs. -----	175
Figure 4.77: Schematic representing the chemical interaction of both types of MWCNTs with epoxy (a) COOH-MWCNTS reaction with epoxy (b) P-MWCNTs reaction with epoxy. -----	177
Figure 4.78: FTIR spectrograph of Siloxane epoxy with 0.5, 2.0 and 3.0 wt.% ANPs. -----	177
Figure 4.79: FTIR spectrograph for Novolac epoxy at 1.0 wt.% content for COOH-MWCNTs, ANPs and SNPs. -----	179
Figure 4.80: FTIR spectrograph of Novolac epoxy with SNPs at 0.5, 1.0 and 2.0 wt.% contents -----	179
Figure 4.81: Crosslinking density of selected Siloxane epoxy samples using DMA. -----	181

LIST OF TABLES

Table 3-1: Nanomaterials properties and information	45
Table 3-2: Neat PC mixes	50
Table 3-3: Siloxane PC mixes with MWCNTs where epoxy resin is 287 kg/m ³ , hardener is 125 kg/m ³ and aggregates are 1557 kg/m ³	51
Table 3-4: PC mixes with siloxane epoxy and ANPs designation where epoxy resin is 287 kg/m ³ , hardener is 125 kg/m ³ and aggregates are 1557 kg/m ³	52
Table 3-5: PC mixes with Novolac epoxy at different nanomaterials where epoxy resin is 287 kg/m ³ , hardener is 125 kg/m ³ and aggregates are 1557 kg/m ³	52
Table 3-6: PC mixes with Siloxane epoxy containing hybrid mix of MWCNTs where epoxy resin is 287 kg/m ³ , hardener is 125 kg/m ³ and aggregates are 1557 kg/m ³	53
Table 3-7: Loading rates details used in fracture tests of PC mixes.	59
Table 3-8: Fracture mechanics models based on material’s behavior.	60
Table 3-9: ABAQUS example problem guide for viscosity coefficient.	92
Table 3-10: Peak shear stress variability at different viscosity coefficients.	93
Table 4-1: Linear elastic fracture mechanics (LEFM) analysis parameters and output.	122
Table 4-2: QBFM analysis results using effective crack modulus	124
Table 4-3: QBFM analysis results using work of fracture.....	130
Table 4-4: Mechanical properties of selected SPC mixes for fatigue test.	134
Table 4-5: Elastic modulus and density values as used in rule of mixture analysis.	155
Table 4-6: Volume of nanomaterials and epoxy for model 1 of rule of mixture.....	156
Table 4-7: Elastic modulus predictions based on model 1.	156
Table 4-8: Elastic modulus predictions based on model 2.	157
Table 4-9: Elastic modulus predictions based on model 3 at different α values.	158
Table 4-10: Interface properties in slant shear test for damage and cohesive behavior definitions.	161

CHAPTER ONE: INTRODUCTION

1.1 Background

Nanotechnology according to the National Nanotechnology Initiative (NNI) is defined as the engineering of functional systems in the molecular scale. In general, nanomaterials and systems can be classified as passive or active nanosystems. Passive nanosystems are those that disperse nanomaterials and nanostructures within a host matrix designed to perform a single task. Active nanosystems include sensors, actuators and other nanostructures that perform multiple tasks. Nanomaterials can be classified into 0D, 1D and 2D nanomaterials in which either three, two or one of their dimension is at the nanoscale respectively. Nanotechnology therefore can be fused into civil engineering materials through passive nanosystems while active nanosystems are better suited to provide self-healing capabilities, aid in non-destructive testing, and structural health monitoring (SHM) activities.

Polymer concrete (PC) is type of concrete that replaces cementitious materials with epoxy polymer systems. PC can serve in severe environmental conditions and within a large range of pH (1~13) according to U.S. Composite Pipe, Inc. offering protection to reinforcement and high chemical resistance. PC can adapt to many applications and its physical, chemical and mechanical properties depend on the selection of polymer binder and aggregate filler. No interfacial transition zone (ITZ) like that found in Portland cement concrete (PCC) exist in PC. Hence, PC provide improved fracture toughness and tensile strength. Polymer binders are often selected based on chemical exposure conditions as well as critical mechanical properties of the specific application such as fatigue life, compressive strength, bond strength and tensile strength. On the other hand,

PC allows the use of different aggregate particle sizes ranging from 0.5mm to 20 mm giving it a broad spectrum for use in structural elements as well as finishing and repair jobs. For example, PC was first used in façade panels in 1950s (*Prusinski, 1987*) and its use continued to grow over time to be commonly used for bridge deck overlays, machine foundations, drainage systems, channels, and reinforced manholes.

The use of PC as well as latex modified concrete (LMC) have been increasing as many civil engineering industries are becoming more comfortable and confident selecting polymer based concrete (PMC) over PCC. In 1971 the American Concrete Institute (ACI) formed the ACI- 548 Committee for Polymers and Adhesives for Concrete. This was later carried to establish the first conference considering PC as a construction material held in England in 1975 carrying the name: International Congress on Polymers in Concrete (ICPIC). Ever since, PC has been established by both the industry and researchers as a construction and a structural material.

1.2 Motivation and Objectives

Concrete is one of the one of the most common civil engineering materials due to its high efficiency in construction, low cost and most importantly growing industrial confidence. However, PCC has many known limitations such as excessive shrinkage cracking, low tensile strength, low strength to weight ratio, low ductility, short fatigue life, low toughness, and its prone to chemical and weather degradation. Therefore, improving concrete's performance, by incorporating nanotechnology, is an inevitable step not only to counter its limitations but also to establish smart structures. Research efforts to incorporate nanotechnology however face many impairments such as establishing uniform dispersion, the large range of nanomaterials available, determining the optimum content of nanomaterials, and the interaction of the various commonly used cementitious

fillers. Furthermore, as hydration is a continuous process that result in changing concrete's mechanical and chemical characteristics with time, extensive long-term testing such as fatigue, creep and shrinkage are necessary evaluations. Such time-dependent behavior however along-side the large range of associated admixtures prove isolating nanomaterials effects pathways difficult. On the other hand, PC exhibits much more controlled and rapid curing with no shrinkage phenomenon. Furthermore, the various range of chemical based polymers used in PC enables isolating the various chemically induced effects of nanomaterials. PC also counters some of PCC known weaknesses such as tensile strength, fatigue life and chemical resistance enabling direct mechanical properties investigations such as direct tension tests. Hence, PC provides a promising vial to embrace nanotechnology into structural applications as well as pave a much clearer path into incorporating nanomaterials into PCC.

Another key feature of incorporating nanotechnology in PC lays within many of its applications such as its use in bridge deck overlays, machine foundations, and repairs of wellbores. In those applications, PC advantages over other construction materials are fully engaged. Bridge deck overlays and machine foundations are often subjected to high cyclic loadings, high tensile stresses, and/or harsh environmental conditions. On the other hand, repairs require high flowability in combination with high bond strength and chemical resistance. Specific polymer binders have been selected for those applications namely Siloxane polymer system for bridge deck overlays and Novolac polymer system for repairs of wellbores. Although such systems outperform PCC, further improvements can prolong the service life extensively increasing the sustainability of such structures as well as reducing maintenance costs.

This research aims at investigating the use of different nanomaterials to produce PC nanocomposites (PCNC) that outperform PC as well as PCC. Further, identifying the effect of

different contents of the nanomaterials used on the mechanics and microstructure of PC. Two epoxy systems have been used namely Novolac and Siloxane. For Novolac, alumina nanoparticles (ANPs), carboxyl functionalized multi-walled carbon nanotubes (COOH-MWCNTs), and silica nanoparticles (SNPs) were selected. Mechanical characterization included slant shear tests for bond strength as well as flowability, compressive strength and modulus of elasticity. On the other hand, tensile strength, toughness, fracture toughness, flowability and modulus of elasticity were the critical parameters investigated for bridge deck overlays as well as machine foundations utilizing Siloxane. Those parameters were selected as the key considerations influencing fatigue life which is generally the common source of degradation. Nanomaterials selected for this application are ANPs, COOH-MWCNTs and Pristine MWCNTs (P-MWCNTs). ANPs and SNPs are examples of 0D nanomaterials while MWCNTs are 1D nanomaterials. The nanomaterials investigated provide good comparison of the different mechanical and chemical abilities of 0D against 1D as well as functionalized against non-functionalized.

This investigation aims to highlight how low content inclusions of nanomaterials in PC can induce significant changes in specific mechanical properties. Such properties that are key in PC applications would significantly reduce maintenance requirements, prolong service life and improve sustainability. Thus, applications of such innovative PC with nanomaterials can be practiced. Further, this research effort aims to introduce how altering nanomaterials inclusion loadings alongside the wide selection of polymer binders can be used in producing PC by design. Desired mechanical, chemical and physical properties can be achieved by proper choice of polymer binder, nanomaterials and their content. Furthermore, this work aim to disclose mechanical and chemical induced features of nanomaterials in PC. Combined with the overall

effects of nanomaterials on PC and microstructural analysis on the host matrixes, this work aims to provide a strong foundation to introducing nanotechnology in PC and potentially smart PC.

1.3 Scope of Work

This work examines how different nanomaterials at different contents influence the mechanical properties of PC with different polymer binders. Two epoxy types were selected namely Siloxane and Novolac as they are commonly used for bridge deck overlays and repairs. Mechanical tests carried for each type of PC were designed to examine key mechanical features that are critical to their applications. Further microstructural analysis was carried to examine chemical effects and the efficiency of the used dispersion technique. Fourier transform infrared spectroscopy (FTIR), scanning electron microscope (SEM) and dynamic modulus analyzer (DMA) tests were selected to evaluate the formation of chemical bonds, examine dispersion, and determine the changes in crosslinking density.

The service life of PC is most critical for bridge deck overlays as well as machine foundations. Although fatigue testing can provide conclusive results on the effectiveness of nanomaterials in prolonging overlays life, the key characteristic and mechanisms in which fatigue life is affected cannot be solely identified by fatigue tests. To determine the key aspects on how different nanomaterials aid to prolong service life, a three-stage testing program was conducted. In stage one, flowability, microstructural and tension tests were carried for all nanomaterials at varying contents. In stage two, fracture toughness was evaluated using linear elastic fracture mechanics (LEFM) and quasi-brittle fracture mechanics (QBFM). Finally, the best performing nanocomposite PC mixes were tested for their fatigue life. Structural health monitoring (SHM) analysis was also performed for PC mixes incorporating P-MWCNTs in flexure. The electrical

damage feature was investigated alongside the mechanical damage feature. Additional investigation into the functional group content was performed through hybrid PC mixes of P-MWCNTs and COOH-MWCNTs in tension. In repairs of wellbores, the bond strength and ease of application of PC is most critical. Slant shear and flowability tests were then adapted along with compressive strength testing with strain gauges. However, due to the significant stiffness mismatch between PC and steel, conventional mechanics approach of obtaining stress by dividing load over area was in question. Finite element modeling (FEM) was then carried by using the material properties extracted from compressive strength testing to determine the true shear stresses exerted. A bi-linear shear stress – slip model was adopted in developing the bond between PC and steel. Further analytical mechanics exact approach was utilized to measure the relative stiffness mismatch. For both types of epoxies, the number of contents investigated was minimized by selecting the best performing and most critical mixes.

1.4 Thesis outline

This thesis contains a total of five chapters. The first chapter convey a brief introduction, motivation and scope of work. Chapter two provides literature review related to PC, wellbores and bridge deck overlays, effects of nanomaterials on mechanical properties, fracture toughness, bond tests and stiffness mismatch, and structural health monitoring. Chapter three presents the information about the materials, experimental methods, test procedures, and analysis methods. Chapter four is designated to the findings of mechanical characterization of PC and PCNC with their respective microstructural and analytical investigations and discussions. The conclusions of previous chapters with some recommendations for future work are summarized in chapter five. Figure 1.1 shows the flow of the related testing events described.

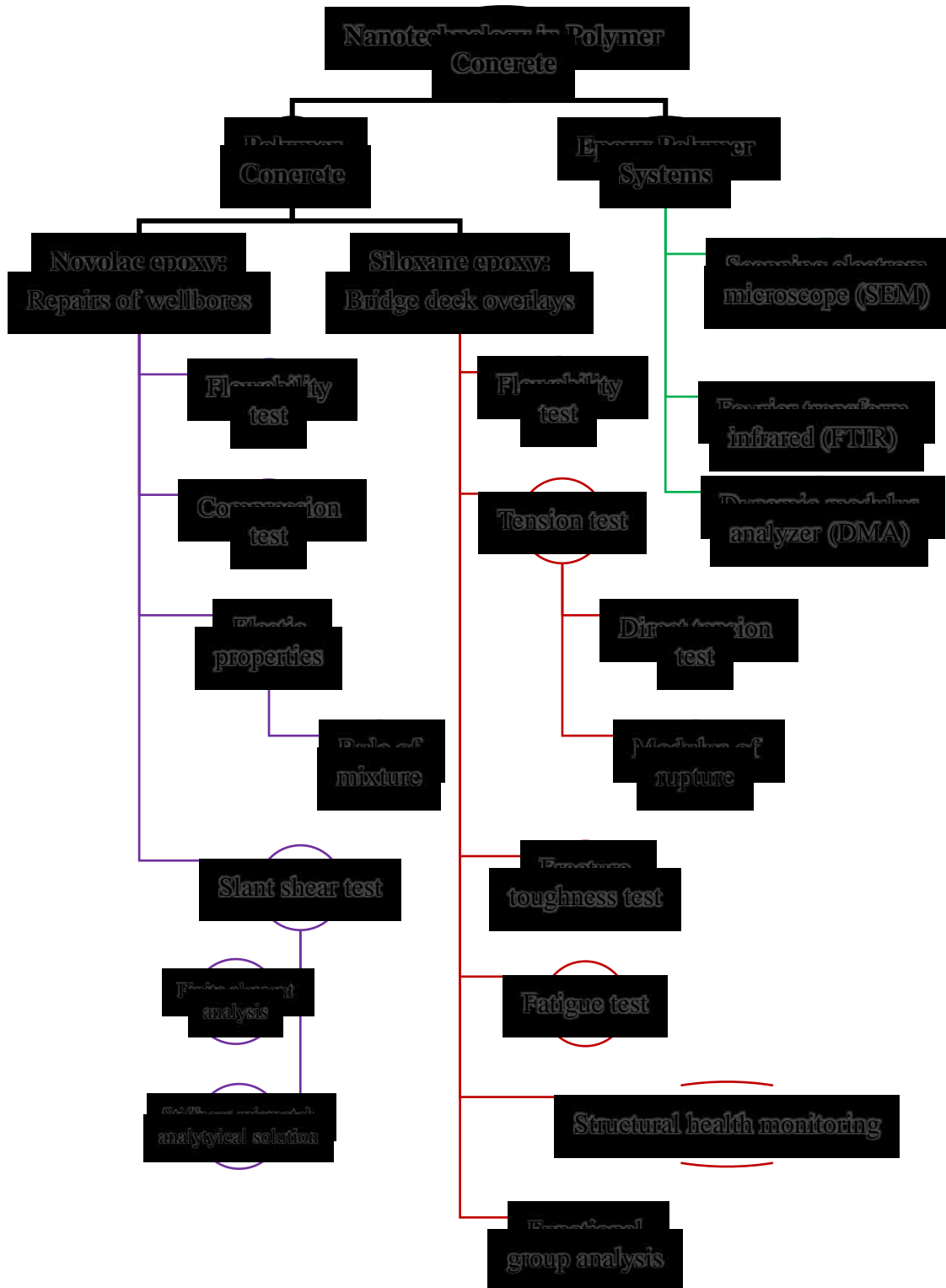


Figure 1.1: Events flow expressing the scope of work.

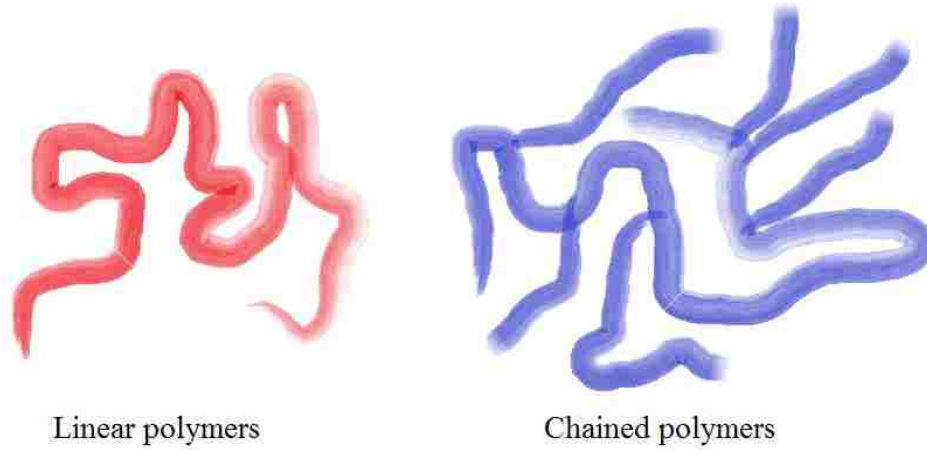
CHAPTER TWO: LITERATURE REVIEW

2.1 Introduction to Polymer Concrete Nanocomposites

2.1.1 Polymers

In recent years, many industries have been relying on polymers and polymer impregnated products. In fact, polymers have become the backbone of many engineering disciplines such as petrochemical, aerospace, automobile, and chemical engineering. Some of the most commonly used polymer based materials are carbon fiber reinforced polymer composite (CFRP), glass fiber reinforced polymer composite (GFRP), Teflon, Nylon, and Silicone which can be found in airplanes, jet fighters, spaceships, satellites, vehicles, water treatment plants, and household tools. Polymers can be explained by partitioning the word polymer to: “Poly” which means many and “mer” which means part or segment. Polymers are the formations of multiple molecules, called monomers, in the form of chains or other complicated structures. Those structures can either be linear or branched as shown in Figure 2.1. Monomers, the basic component of a polymer, are molecules that can bond or link together forming lengthy chains or complex hierarchal structures in the process of polymerization. Figure 2.2 illustrates the previous and how repeated sets of monomers act together forming polymers. Polymers have gained more preference in engineering applications as they can easily be manipulated with different monomers to produce certain mechanical performances and chemical protection. The length of polymer chains can also be manipulated to alter their physical properties changing their viscosity, temperature ranges and stiffness. Polymers produced using one type of monomer are referred to as homopolymers while those made of multiple types of monomers are referred to as copolymers. In addition, polymers can be classified as elastomers, thermosets and thermoplastics in accordance to their level of

crosslinking. Elastomers typically provide the lowest crosslinking density, thermoset polymers have the highest and strongest crosslinking and thermoplastics are in between (Kardon *et al.* 1997).

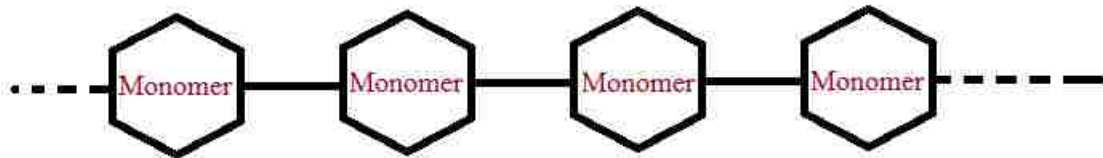


Linear polymers

Chained polymers

Figure 2.1: Linear and chained polymer chains graphical representation.

Polymer:



Monomer
Examples:

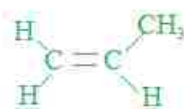


Figure 2.2: The structure of polymers as chains of monomers

2.1.2 Polymer concrete

Concrete is one of the most fundamental materials civil engineers rely on. In fact, Chemistry World, the magazine of the Royal Society of Chemistry, estimates that concrete has become the most widely used material in the world. Portland cement concrete (PCC) is most commonly used type of concrete and relies on cement hydration to develop its desired mechanical properties. As a result, PCC is subject to shrinkage, cracking and time-dependent degradation in its mechanical properties. Therefore, PCC structures are often weak in resisting environmental

conditions, chemical exposure and time-dependent mechanical degradations. This requires extensive maintenance efforts and protective measures. Furthermore, it's estimated that cement production is responsible of five percent of the annual anthropogenic global CO₂ production (*Kline and Kline 2015*). Thus, civil engineers and structural industries have been in continuous search for new more sustainable construction materials. One of these materials are polymer based concrete (PBC) in which polymers are integrated into concrete. There are three different types of PBC:

1. *Polymer impregnated concrete (PIC)*: polymers or monomers are used to impregnate or infiltrate hardened and cured concrete which is subsequently hardened using radiation, heat or chemically (*Partap, 2002*).
2. *Polymer modified concrete (PMC)*: polymers are added during mixing of ordinary concrete in the range of 10 – 20% of the cement binder. Hardening of PMC is dependent on cement hydration and small range of polymers can be used such as acrylic, styrene-butadiene latex (SBR), polyvinyl acetate, or ethylene vinyl acetate (*Fowler, 1999*).
3. *Polymer concrete (PC)*: cementitious binders of PCC are replaced with polymer binders such as epoxy, unsaturated polyester (UP) or poly methyl methacrylate (PMMA). Hence, Cement hydration processes are replaced by polymerization which can be controlled using radiation, heat or with chemicals.

Those types of concrete rely on polymer composites which are commonly available materials that offer a reduced CO₂ footprint with better environmental impact. Polymers also provide improved adhesion and durability properties than PCC as they depend on polymerization rather than cement hydration. Polymerization is described by the reaction of free chains of monomer molecules that creates lengthy polymeric chains. Such reaction often requires chemical, radial, heat or any of their combination to initiate hardening. In epoxy based polymer systems, two

components are often present where each part provide one free end of the monomer chain. Thus, mixing both components initiate polymerization reactions that are often heat dependent. Those components are referred to as the resin and the hardener.

PIC generally provide compressive strength three to four times higher than that of the ordinary concrete it's made of (*Fowler, 1999*). Tensile and flexural properties of PIC are also improved greatly (*Fowler, 1999*). More importantly, since polymer chains are formed after hardening of PCC, the permeability of PIC is greatly improved along with its modulus of elasticity. This is attributed to the interpenetration of cement hydrate, polymer and aggregate phases (*Nair et al. 2010*). While polymers in PIC are added to PCC after hardening, they are introduced during mixing of PCC in PMC. Therefore, the selection of polymers is restricted by its reactivity to water and cement hydration byproducts such as calcium carbonate (CaCO_3) or calcium silicate hydrates (C-S-H) (*ACI 548.6R 1996*). Styrene-butadiene (SBR) latex and Acrylic PMC provide excellent bond strength and are colorfast. Therefore, they become popular materials in architectural panels and finishing jobs (*Fowler, 1999*). On the other hand, PC eliminates the use of cements and water relying solely on polymers and polymerization processes. PC therefore can be considered as a replacement for PCC where PIC and PMC are extensions of PCC. All PBC use similar range of aggregates and fillers from 0.5mm to 25mm. Furthermore, their properties and performance are dependent on the choice of polymer and curing environment.

PC provide a wide range of mechanical, physical and chemical properties that can be tailored to its application. The broad range of polymers available in many industries provide a wide spectrum of different PC types with specific properties. In fact, its compressive strength ranges between 20 – 130 MPa while its tensile strength can reach up to 12 MPa (*ACI 548.6R 1996*). It can also exhibit high shear strength up to 20 MPa and flexural strength reaching 40 MPa (*ACI*

548.6R 1996). For example, Rebeiz et al. and Gorninski et al. achieved a 95 MPa compressive strength using Isophthalic polyester PC at 15-20% content of fly ash (*Rebeiz et al. 2004, and Gorninski et al. 2007*). Yeon et al. achieved compressive strength of 80 MPa after 168 hours of low temperature curing of acrylic PC (*Yeon et al. 2014*). The highest compressive strength of 128 MPa was achieved using vinyl ester mortar with silane coupling agent (*Chmielewska et al. 2006*). PC strength is not only influenced by the choice of polymer system but the aggregate filler as well. By substituting graded mixture of coarse and fine sand with fly ash and silica fume the flexural capacity of PC drops from 28 MPa to 15 MPa (*Haidar et al. 2011, and Barbuta et al. 2010*). The flexural capacity of PC without reinforcement can reach up to 40 MPa due to its high ductility and ability to withstand large strains (*Chmielewska et al. 2006*). PC also provides high bond strength and long fatigue service life along with all its notable mechanical properties. Czarnecki and Chmielewska showed that PC produced using low viscosity vinyl ester mortar modified with silane coupling agent has a bond strength of 2.8 MPa in pull-off tests (*Czarnecki and Chmielewska 1999*). Wheat et al. showed that fatigue loading of PC overlays on PCC beams does not lead to any delamination of bond strength between both substrates up to 2 million cycles (*Wheat et al. 1993*).

Nonetheless, PC like all materials have many limitations. Specifically, PC has a creep compliance two to three times of that of PCC (*ACI 548.6R 1996*). Some additives were suggested to reduce such phenomenon but those investigations are limited. For example, Rebeiz et al. increased the content of fly ash in the aggregate filler which resulted in a 5% reduction in creep compliance (*Rebeiz et al. 2004*). The bond strength of PC also declines rapidly up to 45% when subjected to cyclic thermal loadings that are often associated with bridge deck overlays (*Rebeiz et al. 2004*). The importance of research in regards to those PC properties is then crucial. PC provides a promising alternative to PCC with its remarkable mechanical, physical and chemical properties.

Nevertheless, research efforts are needed to counter its limitations and further emphasize the industrial trust in it as a structural material.

2.1.3 Nanotechnology

Nanomaterials provide significantly large surface area that is several orders of magnitude higher than micro fibers at equivalent weight content due to their extreme dimensions (*Ganguli et al. 2006*). Further, nanomaterials have significantly high number of particles providing large prospect for particle-matrix interaction. Since most often nanomaterials are of significantly smaller dimension than polymer molecules, nanomaterials can alter the mechanical properties of polymer systems through various chemical processes. This is attributed to their ability to interrupt polymerization of the polymer system parts, cause microfilm rotations or hinder its formation. Nanomaterials are also able to interact with the free chains of each polymerization monomer consuming, interrupt polymerization reaction or strengthen it. Therefore, different contents and various nanomaterials result in different mechanisms that influence the properties of their host matrix. Nanomaterials can also have no chemical reaction or effect on the host matrix and rather improve the packing density of the host matrix.

In many cases, single or multiple molecules can be attached to nanomaterials through functionalization. Those molecules or functional groups can be attached at selective locations such as ends or across the surface. Such process can be utilized to manipulate the chemical effect of nanomaterials on polymerization of the host matrix. This is often performed by controlled selection of the host matrix chemistry and carefully matching nanoparticle or their functional groups. Thus, creating a wide spectrum on the chemical effects induced on the host system that can be tailored to produce specific effects. Nanomaterials are classified as 0D, 1D or 2D nanomaterials in which either three, two or one dimension is in the nanoscale respectively. Figure 2.3 shows schematically

different types of nanomaterials. Since all 0D nanomaterials dimensions are of the nanoscale, its often hard to attach multiple functional groups or select location of functionalization. 1D and 2D nanomaterials on the other hand are excellent candidates for selective functionalization as they have one or two dimensions in the microscale. However, 1D nanomaterials are often considered superior to those of 2D nanomaterials as they provide significantly high aspect ratio dramatically increasing their stiffness while maintaining high nano-induced effects. Also, 1D nanomaterials provide similar benefits to those of 0D nanomaterials as they offer significantly large surface area.

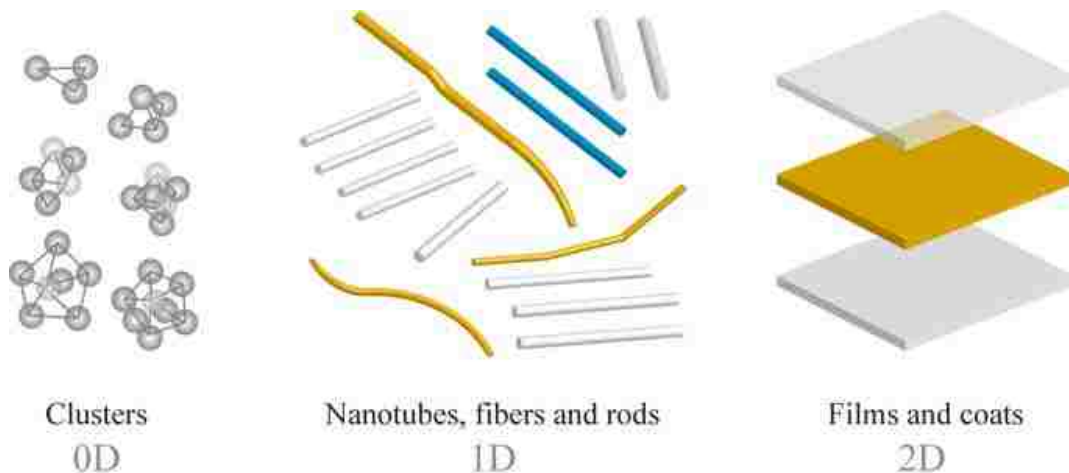


Figure 2.3: The different types of nanomaterials classified based on their characteristic dimension.

Despite the rise in use of nanotechnology in many industries, many civil engineering diligences are still hesitant to adopt the previous (and somewhat outdated) technologies such as micro and macro fiber additives. Many newly constructed structures around the world therefore are left outdated and designed with similar concepts and materials to those in the mid 1900's. Many industries relate abandoning new technologies to the limited added benefits or inconsistent literature findings. Suggested improved performance associated with micro and macro fiber additives to PCC remain minimal and -in many cases- not quite compensating to the increase in cost and labor. On the other hand, nanotechnology offers significant improvements in structural

health monitoring (SHM), self-healing capabilities and improvements in mechanical properties with very limited drawbacks. Nanotechnology therefore is a promising tool to induce significant improvements that can outweigh their associated initial cost. Hence, it's an attractive gate which would help civil engineering industries be more keen to adopt newer technologies and bring structures up to date.

PC with its high flowability and polymerization based reaction offer an attractive vail to incorporate nanotechnology into structural materials. Furthermore, perhaps by joining both technologies that civil engineering industries would begin to adopt newer materials into structures rather than steel and concrete. PC nanocomposites (PCNC) offer superior mechanical properties that can be specifically tailored for their application. Furthermore, nanotechnology help reduces or eliminates many of the limitations associated with PC that drove structural use away. Lastly, the various types of polymers and nanomaterials offers a wide range of materials properties modification and present a promising window into materials by design.

2.2 Polymer Concrete In-Situ

PC was first used as anterior architectural panels and in production of synthetic marble in the 1950s. The precast panels were composed of polyester resin and pure silica (*Prusinski 1978*). PC was suitable for such application because of its high strength, wind load resistance, resistance to harsh weather conditions, and high load bearing capacity (*Kaeding and Prusinki 2003, & Wahby and Prusikni 2005*). Till date, PC façade architectural panels are used as shown in Figure 2.4 by ULMA architectural solutions. Up to 1972, PC have only been used for architectural purposes. At that year, however, glass fiber reinforcement was introduced to PC marking the first point that PC started to gain more structural use. Later in the 1970's and 1980's PC was used structurally in thin

bridge deck overlays, machine foundations, pipes and pipes liners, and hazardous waste containment while maintaining its previous use in panels and synthetic marble. In the 1990's, researchers started to acknowledge that since PC has high compressive strength, strong chemical exposure resistance, and more ductility than PCC it would be suitable for structural members. Its mechanical and chemical properties provide excellent protection for steel requiring less cover to be used with reinforced PC (*Rebeiz and Fowler 1996*). Rebeiz and Fowler in fact recognized that because of PC's high ductility, conventional stress calculations of the equivalent stress block method would underestimate reinforced PC beams strength (*Rebeiz and Fowler 1996*). Thus, marking critical differences in experimental analysis of PC and reinforced PC behavior. Only till 2010 however that an effective moment of inertia method was developed for reinforced PC beams to analyze their flexural structural capacity (*Park et al. 2010*). Because of their high ductility and high strains, PC provide a superior candidate for structural reinforced columns specially in high seismic activity regions. Oyawa casted and tested reinforced PC columns under axial loads and showed enhanced ductility along with sufficient load bearing capacity (*Oyawa et al. 2001 and Oyawa 2007*). Nonetheless, structural applications of PC to this day have been restricted due to limited research and industrial appeal.



Figure 2.4: Carbon fiber textured polymer concrete facade panels by ULMA architectural solutions.

Since its start in 1950's, PC has been used in many projects involving coverings of highway surfaces, bridge decking, pavement overlays, sewer pipes, manholes, structural and decorative panels, repairs of concrete cracks, drinking water filtration slabs, industrial flooring, underground piping, parking structures, airport runways, tunnel linear segments, U-shape gutters, footpath panels, machine basis and foundations, swimming pools, electrolytic cells, transmission towers, insulators, and as part of hydraulic precast systems in dams, dikes, reservoirs and piers (*Reis et al. 2003, Shokrieh et al. 2015, Vipulanandan and Paul 1993, Agavrioloie et al. 2012, Yeon et al. 2014, Toufigh et al. 2017, Reis 2005, Toufigh et al. 2013, Wheat et al 1993, Partap, 2002*). However, PC up-to date have not been fully utilized for structural members due to specific limitations. Firstly, PC imposes an initial increase in cost up of 10 to 100 times of that of PCC per unit volume due to the high cost of polymers (*Fowler, 1999*). Secondly, as polymers in general behave poorly at elevated temperature, PC may not provide optimum performance when exposed to fire. Lastly, polymers require increased labor efforts due to unfamiliarity of construction industry with it. Also,

an increase in safety regulations is required due to some polymers toxic, corrosive or hazardous properties prior to hardening. However, the cost of polymers is in continuous decrease as manufactures find new techniques for production. Furthermore, despite the increase in initial cost, the reduction in maintenance requirements of PC can largely compensate. Further investigation of PC is required to examine the effect of elevated temperature exposure as well as thermal cycles. It is also evident that PC requires improvements in its physical, mechanical and thermal properties to facilitate its use structurally. Thus, the use of nanomaterials in PC can improve its thermal resistance, improve its mechanical properties resulting in reduced structural cross-sections and prolong its service life further decreasing its service and overall cost.

2.2.1 Bridge deck overlays

Bridge decks are part of the bridge superstructure that represents the roadway, pedestrian walkway or the combination of both as shown in Figure 2.5. Bridge decks are often constructed using wood, aluminum, fiberglass, steel or reinforced concrete. Most commonly, reinforced concrete and steel gratings are used for construction. Bridge deck overlays are typically made of PCC or PC and are used to preserve bridge decks and function as the pavement system. They serve as multi-purpose element in which firstly, they are responsible to provide protection to the substructure from chemical, weather and abrasive exposure. Secondly, bridge decks are required to provide sufficient skid resistance and good friction to traffic in different weather conditions. Lastly, maintenance requirements are often emphasized to be minimal as to minimize service disruptions. Therefore, bridge deck overlays require to have high bond strength to substructure (steel or reinforced concrete), high chemical, abrasion and weather resistance, high friction, along with substantial mechanical performance including prolonged fatigue life, and high fracture toughness, tensile strength, compressive strength and ductility. Often, PBC are preferred to PCC

as they require significantly less thickness (19 - 75 mm compared to +75mm), provide rapid curing (traffic is allowed after 4 hours), require minimal surface preparation (typically 6mm of the top PCC surface need to be removed), and provide significantly lower permeability and thus chemical and weather resistance (*Shannon and Richard 1996*). PC also has been estimated to offer up to six times the vibration elevating properties of PCC (*Wang et al. 2013*). In fact, Departments of Transportation (DOT) across the country have adopted PC and PBC overlays (*Bridge deck overlay system Brochure 2016*). In Kansas state, PC were used to resurface 2.4 miles of the interstate 135 (I-135). Similarly, 18,778 linear feet of PC were used in overlays of multiple highways in Louisiana. New Mexico state hosted the largest bridge deck overlay system of 14,000 yd³ on the interstate 40 (I-40) where PC was used for all five lanes along with both emergency lanes. Example of PC application in bridge decks and highways are shown in Figure 2.6. PC overlays are also often used at parking structures and areas, rural roadways, industrial sites, on-ramps, school zones, toll authority entrances, hospital entrances, bike lanes and pedestrian walkways (*Bridge deck overlay system Brochure 2016*).

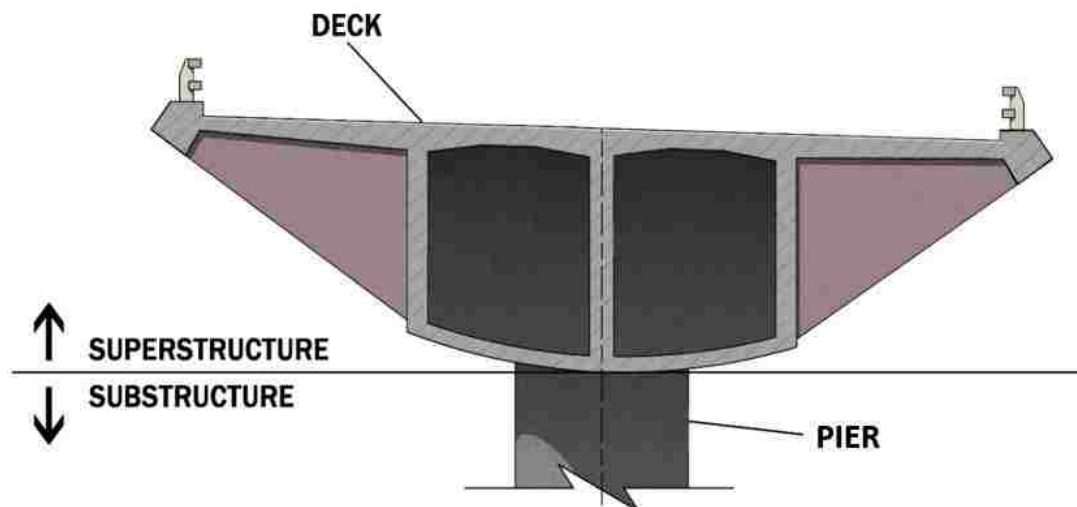


Figure 2.5: Bridge deck system schematics as part of the superstructure.



Figure 2.6: PC overlays in-situ courtesy of Transpo Inc.

2.2.2 Repairs of wellbores

In recent years, global warming and climate change have become a demanding concern for many research agencies and entities around the world. It presents one of the most complex issues researchers are facing. In short, toxic emissions and gases specifically carbon dioxide (CO₂) has created a greenhouse effect causing an increase in the earth's temperature. Researchers agree that action is required to reduce the carbon footprint as well as adapt to the climate change. One of the suggested mitigation tools is CO₂ geological sequestration in abandoned wellbores. That is, the collection, entrapment and storage of the toxic chemical in the liquid form within abandoned geological formations through abandoned oil wells. Oil wells provide an existing and available mean to reach empty aquifers and porous rock formations several miles below the ground level. However, a key challenge remains in preventing leakage of the entrapped gasses by ensuring seal integrity of the wellbore. In general, oil wells are encased wellbores with steel casings where cement sheaths are pumped between the casing and rock formations. When abandoned, those wells are plugged with grout, concrete or bentonite. Several leakage pathways can be identified in CO₂

sequestration such as between casing and cement, cement plug and casing, through cement plug, through steel casing, or between cement and rock as shown in Figure 2.7. Thus, repair of the seal integrity is crucial to prevent geological and environmental contamination.

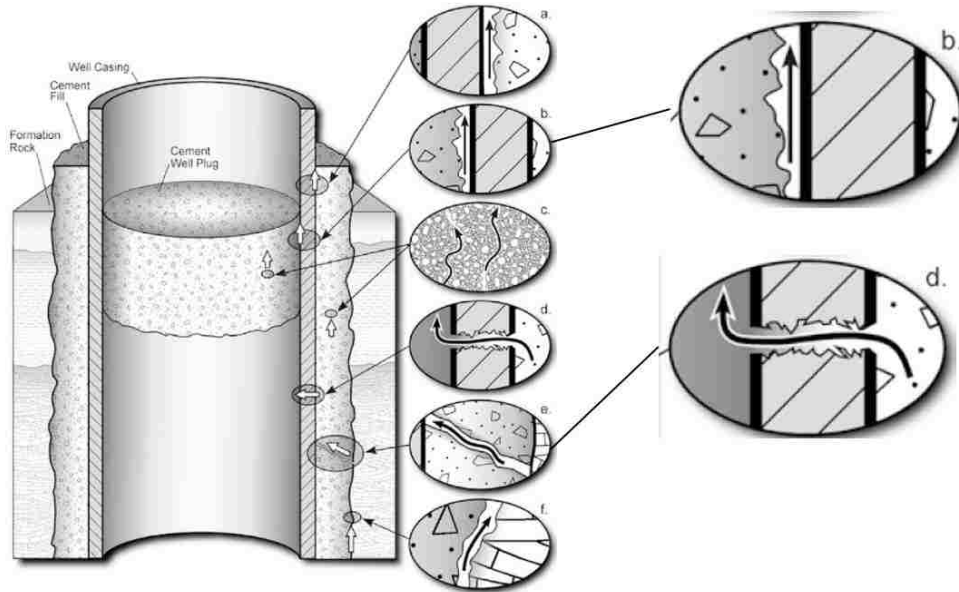


Figure 2.7: Leakage pathways of abandoned oil-wells with b. between cement and steel casing and d. through the casing (Gasda et al. 2004).

Wellbores seal integrity is dependent on its constituent materials' durability. However, steel is susceptible to corrosion, concrete is subject to cracking and their interface is subject to cracking, degradation and debonding. Polymers and PBC therefore provide an attractive and viable repair material to ensure seal integrity. PC specifically offers high chemical, pH, and abrasion resistances and impermeability while also providing high bond strength, compressive strength, and flowability (ACI 548.5R 1998, Douba et al. 2017). However, the service life of wellbores and their repair material need to be maximized to allow improved protection against contamination as well as minimize all future maintenance requirements (Genedy et al. 2017). Thus, the use of PC as repair material in wellbores necessitates improved bond strength to steel casing. Full investigation on the shear stresses exerted on the PC-steel interface is also required to ensure PC's optimal performance as the repair material.

2.3 Effects of Nanomaterials on Epoxy Polymer Systems

This work suggests incorporating nanomaterials to improve the properties of PC. Prior research efforts to improve the properties of PC relied solely on microfiber additives, manipulating aggregate and filler contents, or varying hardening temperature or agents. Very limited work investigated the effects of nanomaterials on PC. In fact, Shokrieh et al. and Daghash et al. are the only prior investigation into incorporating nanoclay and examine the tensile and fracture properties of its PC (*Shokrieh et al. 2012*). Daghash et al. also investigated the effects of MWCNTs on the impact strength of PC (*Daghash et al. 2016*). Nonetheless, many research work have been performed on epoxy, UP and PMMA composites utilizing nanomaterials such as nanoclay, alumina nanoparticles (ANPs), silica nanoparticles (SNPs), nanodiamond, nanosilver, gold nanomaterials, titanium oxide nanomaterials, graphene nanoplatelets and single, double and multi walled carbon nanotubes (MWCNTs). Those findings are the focus of the following sections. Furthermore, as several mechanical tests are used within this work, findings of previous research work on the critical aspects of these tests are discussed as well.

2.3.1 Dispersion and flowability

As mentioned previously, passive nanosystems can alter different properties of the host matrix utilizing different interactive pathways over their large surface area. In general, the smaller the particle dimension is, the larger is its interface with the host matrix. As a result, more significant nano-induced improvements can be achieved. On the other hand, higher surface area of nanosystems results in increased shear friction making it difficult to obtain uniform systems. In fact, the level of influence of nanosystems on the host matrix is dependent on the level of dispersion (*He et al. 2013, Williams et al. 2013, Theodore et al. 2011, Zhu et al. 2004, David et al. 2014*). Dispersion of nanomaterials can be defined as the separation or de-agglomeration of those particles

into individual particles within the host matrix as shown schematically in Figure 2.8. Entangled, agglomerated and concentrated arrangement of nanomaterials result in worsened mechanical performance as well as significantly increased viscosity (*He et al. 2013, Maggi 2014, Shimpi et al. 2011, Haitao and Jianhua 2010, Hamidi et al. 2008, Maity et al. 2010, Tyson et al. 2011*). Dispersion requires providing sufficient energy to separate or de-agglomerate the nanomaterials, distribute those particles within the host matrix and create sufficient particle suspension to maintain uniformity. As most of these properties relay on the particles' individual surface area, 1D nanomaterials (like MWCNTs) are then more challenging to disperse than 0D nanomaterials (like ANPs) (*Chuah et al. 2014*). In addition, agglomeration and entangling of MWCNTs are increased at relatively high weight contents due to the decrease of distance between particles (*Balakrishnan and Saha 2011, Hsieh et al. 2011, Grossiord et al. 2006, Liao et al. 2004*). Balakrishnan and Saha used transmission electron microscope (TEM) to show that the size of agglomerates increases from 0.42 μm to 1.8 μm when changing the content of pristine MWCNTs from 0.2 to 0.6 wt.% of the polymer resin (*Balakrishnan and Saha 2011*).

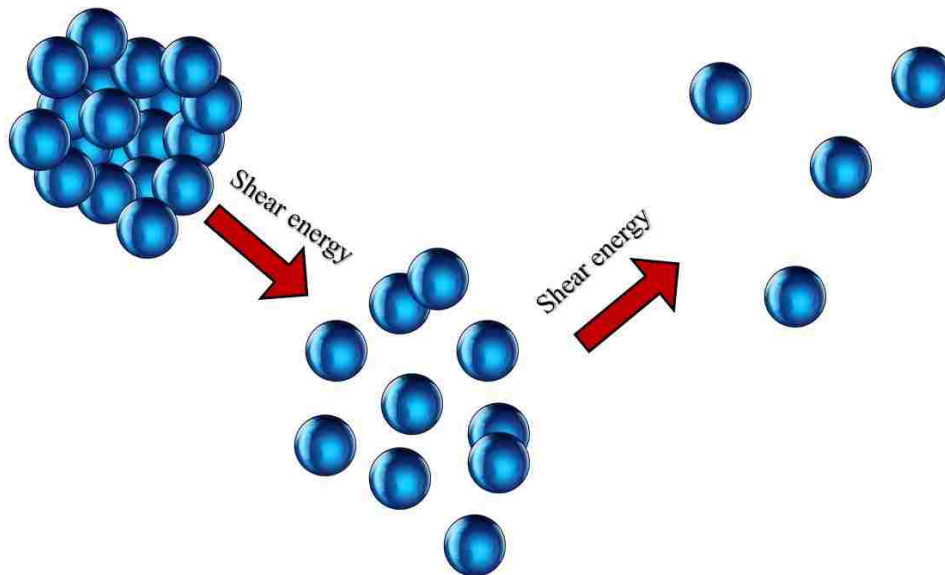


Figure 2.8: Schematics of particle separation during dispersion due to shear energy.

In general, dispersion techniques followed in literature are summarized by: ultrasonication via bath or probe, milling via ball, stirred media, centrifugal, jetting, stirring, shear mixing, homogenization, chemical functionalization, extrusion or by combining several techniques (*Chuah et al. 2014, He et al. 2013, Shimpi et al. 2011, Haitao and Jianhua 2010, Haleem et al. 2015, Williams et al. 2013, PROSPECT Report 2009*). Each of these methods provide different level of shear energy in order to deagglomerate nanomaterials and suspend them within the host matrix. Nanomaterials' agglomeration hinders the mechanical performance or create localized stress concentration zones. Milling provides an advantage for large scale batching but is slow and can result in nanomaterials architecture breakdown or damage (*PROSPECT Report 2009*). However, it provides the only technique that de-agglomerates nanomaterials prior to incorporating them into the host matrix. Probe sonication, shear mixing and high pressure homogenization are highly efficient dispersion methods with high shear energy (*PROSPECT Report 2009*). Yet, these methods are often expensive and require careful application to avoid damaging the nanomaterials as well as the host matrix. Stirring on the other hand provide cheaper dispersion method but provides significantly less shear energy that often result in reagglomeration of nanomaterials. Stirring alone therefore is not considered as an effective dispersion technique unless its coupled with functionalization or sonication to maintain particle suspension. In fact, Haleem et al. showed that functionalization of nanodiamonds can completely prohibit reagglomeration when dispersing using stirring alone (*Haleem et al. 2015*). Another relatively less expensive dispersion technique is sonication bath. While it provides less shear energy than sonication probe, this technique when coupled with stirring or milling often result in uniform dispersion (*Shimpi et al. 2011, Haitao and Jianhua 2010, Hamidi et al. 2008, Maity et al. 2010, Williams et al. 2013, PROSPECT Report 2009*). Obtaining uniform dispersion of nanomaterials within the host matrix is considered crucial

to effectively improve the mechanical properties of the host matrix. However, this can impose increased cost or can prevent large scale batching of nanocomposites. Uniform dispersion also leads to minimizing adverse effects of viscosity and therefore flowability. In fact, Hamidi et al. showed that excessive loading of nanoclay result in losing uniform dispersion and thus increased viscosity and void content (*Hamidi et al. 2008*). Similarly, loadings of chopped glass and carbon fibers have been reported to produce lower workability (*Toufigh et al. 2013*). While increasing the temperature of the polymer matrix can result in temporary improvements in viscosity, it's use must be kept to minimum to minimize segregation (*Ahn et al. 2009*).

As this work focuses on improving the properties of PC nanocomposites to encourage its structural use, obtaining uniform dispersion with inexpensive techniques is crucial. This work therefore utilizes several inexpensive dispersion techniques such as functionalization, stirring and sonication bath. Furthermore, the content of nanomaterials is limited to avoid severe reduction of PC flowability that might not only worsen its mechanical performance but impose difficulties and limitation with in-situ applications.

2.3.2 Compressive strength

The compressive strength of PC is critical in estimating its ability to be utilized in structural applications. In PCC, the compressive strength is limited by the strength of its aggregate or the strength of cement paste (*Aitcin and Mehta 1990, Aitcin and Neville 1993*). Similarly, the compressive strength of PC depends on its constituent's strength and can be engineered to provide compressive strengths in the range of 20 MPa up to 130 MPa (2,900 to 19,000 psi). The compressive strength and in general the mechanical performance of PC is dependent on the type and content of polymer matrix, type and content of aggregate, added fillers, curing temperature,

strain rate and crosslinking. The sections below detail the effect of these properties on the compressive strength of PC.

2.3.2.1 Polymer type and content:

In the mix design of PC, the content of polymer matrix is often minimized to reduce its cost. The contents used in literature varied in the range of 11% to 30% of the total mix weight (Agavriiloaie *et al.* 2012, Martinez-Barrera *et al.* 2013, Elalaoui *et al.* 2012, Reis 2005, Son and Yeon 2012, Tawfik and Eskander 2006, Ahn *et al.* 2009). Extremely restricted polymer content result in insufficient adhesion while extreme dosages can lead to bleeding and leaching of the resin (Shokrieh *et al.* 2015). The type of polymer, its content and crosslinking density can be directly linked to the compressive strength of PC. In general, increasing the content of polymer corresponds to an increased compressive strength (Elalaoui *et al.* 2012). However, such relationship does not hold linearly as (Toufigh *et al.* 2017) showed that the increase of polymer content from 10% to 14% does not result in increased compressive strength (Toufigh *et al.* 2017). Also, similar loadings of different polymers result in different compressive strength as controlled by the chemical structure of the polymer matrix. Reis, Son & Yeon and Toufigh *et al.* utilized polymer content of 11% and 12% of methyl methacrylate (MMA), methyl ethyl ketone peroxide, and bisphenol A-based epoxy producing PC with a compressive strength of 113 MPa, 130 MPa, and 68 MPa respectively (Reis 2005, Son and Yeon 2012, Toufigh *et al.* 2017). On the other hand, Toufigh *et al.* and Martinez-Barrera *et al.* reported 25% and 30% polymer content with a compressive strength of 78 MPa and 27 MPa respectively (Toufigh *et al.* 2013, Martinez-Barrera *et al.* 2013). Agavriiloaie *et al.* also reported the use of 30% similarly to Martinez-Barrera *et al.* and reached twice the compressive strength at 52 MPa (Agavriiloaie *et al.* 2012, Martinez-Barrera *et al.* 2013). Therefore, while the selection of high polymer content is often required to ensure high workability

and homogeneity of the PC, the chemical structure of the polymer is far greater factor of the compressive strength than its content.

2.3.2.2 Added fillers:

The use of added fillers such as fly ash and chopped fibers have been widely reported in literature to improve the mechanical performance of PCC. Recently, researchers began to abandon micro and macro fillers in pursuit of greater improvements via nanomaterials. In PC, similar trends have been carried while the literature available on the effect of nanomaterials is still limited. In fact, only one prior investigation has been published utilizing nanoclay while examining the mechanical performance of PC (*Shokrieh et al. 2012*). Nonetheless, many researchers investigated epoxy and polymer nanocomposites. Such findings are expected to translate to PC as they influence PC's host matrix.

Previous findings of micro added fillers in PC show improvements in the range of 2% to 20% (*Shokrieh et al. 2011, Martinez-barrera et al. 2013, Reis 2005, Toufigh et al. 2013*). Increasing the content of fly ash (used as a fine aggregate filler) result in increasing the strength of PC from 101 to 120 MPa by decreasing the number and size of voids (*Gorninski et al. 2004*). Chopped glass and carbon fibers at contents ranging from 0.5% to 7.5% showed less effective improvements ranging from 2% to 9% and 7% to 16% respectively (*Reis 2005, Toufigh et al. 2013*). Other fibers included irradiated and non-irradiated luffa fibers, coconut, sugar cane and banana fibers with similar improvements to that of chopped synthetic fibers (*Reis 2006, Martinez-barrera et al. 2013*). It can be concluded therefore that incorporating micro and macro fillers and fibers result in compressive strength improvements. However, such improvements can also be achieved by manipulating the content and type of polymer matrix as discussed previously.

2.3.2.3 Nanomaterials:

While incorporating nanoclay into epoxy systems showed no effect on the compressive strength (*Liu et al. 2005*), small improvements have been recorded with PC incorporating nanoclay (*Shokrieh et al. 2012*). On the other hand, considerably more significant improvements have been reported in the range of 18% to 36% of the compressive strength of epoxy composites prepared with 0.5% to 3.0% of MWCNTs (*Chakraborty and Terrasi 2011*). As nanomaterials provide improved packing density properties similar to fly ash as well as the ability to alter the crosslinking density, it's expected that incorporating nanomaterials will result in improved stress transfer, strengthened polymer matrix and overall improved compressive strength. Furthermore, nanomaterials can mitigate some of the negative effects associated with fiber additives such as reduced workability and homogeneity, increased friction, rough finishing and altered damping and vibration properties (*Wang et al. 2013, Toufigh et al. 2013*).

2.3.2.4 Curing and testing temperature:

PC curing is often controlled by its polymer matrix and it directly impact its mechanical performance and compressive strength. In most cases, accelerated curing is performed to achieve high early mechanical properties. Accelerated curing is established through elevated temperatures increasing polymeric chains mobility and hence the rate of polymerization. For example, Vipulanandan and Paul showed that introducing heat curing result in 50% increase of PC's compressive strength (*Vipulanandan and Paul 1993*). In general PC has rapid strength development as it achieves 86.8% of its seven days' average mechanical strength at only three days (*Hyun and Yeon 2012*). Such property is specifically advantageous in maintenance applications such as highway pavements where service outage time needs to be minimized. PC can also develop its full compressive strength at low temperatures as Son and Yeon showed that PC

utilizing MMA reaches compressive strengths of 90 MPa to 113 MPa at -20°C (*Son and Yeon 2012*).

The mechanical performance of PC is dependent upon its environment temperature and its glass transition temperature. Extreme elevated temperatures result in transforming the polymer matrix from a hard state into soft and rubbery state in which its strength decay rapidly. Since PC incorporate high percentage of filler and aggregates, however, its glass transition temperature and flammability are greatly enhanced (*Elalaoui et al. 2012*). This is evident as Shokrieh et al. showed that freeze and thaw cycles lasting seven days of -30°C to $+70^{\circ}\text{C}$ have no impact on PC's compressive strength (*Shokrieh et al. 2011*). While Elaloui et al. showed that prolonged exposure to elevated temperatures result in degradation of polymer properties and weakening of PC, PC proves more efficient than PCC up to 225°C in maintaining its compressive strength and mitigating weight loss (*Elalaoui et al. 2012*). Flexural and tensile performance of PC however are more prone to temperature than its compressive strength. This is directly attributed to increased deformability of PC at elevated temperatures significantly increasing its tensile stresses. Nevertheless, Blaga and Beaudoin showed that continuous exposure of PC to 60°C does not affect its strength while short-term exposure of 100°C to 120°C can significantly alter such properties (*Blaga and Beaudoin 1985*).

2.3.2.5 Aggregate fillers and other parameters:

The strength of all composites is dependent upon the constituents' strength and their strain rate. When high polymeric matrix strength is maintained, the mechanical performance of PC is dependent upon its aggregate and fillers strength. In general, larger size aggregates tend to have lower compressive strength than smaller aggregates. This is attributed to fracture mechanics size effect theory in which larger specimens have higher probability to propagate a crack in tension.

Such effect has been showed by Shokrieh et al. as they showed increasing the aggregate size from 1 mm to 6 mm decreases the compressive strength of PC (*Shokrieh et al. 2011*). On the other hand, other parameters influencing the crosslinking ability of the polymer matrix such as radiation, the polymer-aggregate bond and the strain rate greatly contribute to the mechanical performance of PC (*Martinez-barrera et al. 2013, Vipulanandan and Paul 1993*). Such parameters are however generally hard to quantify in field applications and therefore have not been studied significantly.

2.3.3 Tensile strength

The tensile strength of PCC and PC has often been estimated using indirect tensile tests namely flexural and split tension tests. Direct tension tests are rarely utilized to avoid rapid cracking of PCC due to its low tensile strength and ductility. Therefore, to be able to compare PCC and PC tensile behavior, similar mechanical tests must be conducted. However, PC provide a flexural strength in the range of 11.5 MPa to 42 MPa and split tensile strength in the range of 11 MPa to 14 MPa while the flexural capacity and split tensile strength of PCC are often limited to 6 MPa and 3 MPa respectively (*Reis and Ferrira 2004, Son and Yeon 2012, Agavrioloie et al. 2012, Ahn et al. 2009*). Furthermore, PC shows significantly higher ductility reaching displacements at failure in the range of 2 mm to 4 mm (*Shokrieh et al. 2015, Reis and Ferrira 2004, Agavrioloie et al. 2012, Ahn et al. 2009*). Direct tension test therefore appears more suitable to describe the tensile behavior of PC.

In order to characterize PC deformation behavior, it can be separated into: hardening shrinkage during initial chemical reaction, thermal deflection due to temperature fluctuation, elastic due to elastic loading, and creep due to long-term loading (*Yeon et al. 2014*). Each of these behaviors are affected differently by various parameters such as the choice of polymer matrix, aggregate size, added fillers, and curing temperature. For example, incorporating chopped fibers

into PC improves its flexural performance and displacement at failure due to the fibers crack arresting mechanisms (*Reis et al. 2004*). Such results have been reported for coconut, glass, and carbon fibers with contents ranging from 2 wt.% to 7.5 wt.% and improvements up to 30% in both flexural strength and displacement at failure (*Reis 2004, Reis et al. 2005, Reis 2006, Toufigh et al. 2013*). Hyun and Yeon also showed that increasing the curing temperature from -20°C to +20°C increases the flexural strength and split tensile strength (*Hyun and Yeon 2012*).

Nanomaterials are expected to provide similar and enhanced reinforcing mechanisms to that of chopped fibers. For example, improvements in tensile strength due to MWCNTs inclusions were reported in varying effectiveness within 9% to 51% (*Theodore et al. 2011, Balakrishman and Saha 2011, Hameed et al. 2015, Patankar et al. 2011, Yeh et al. 2008, Lu-Qi and Wagner 2007, Xiao et al. 2015, Ghosh et al. 2015, Chen et al. 2008, Sha et al. 2016*). Increasing the content often resulted in increasing the strength but in a decaying fashion. More significant improvements have been reported up to 168% in tensile strength through parallel alignments of single walled CNTs (*Wang et al. 2008*). Alignment in the perpendicular direction however showed less improvements and rather a decrease in strength beyond 2.0 wt.% content (*Wang et al. 2008*). It's therefore suggested that the random orientation of CNTs contribute to the variation in the reported tensile properties. Furthermore, the chemical effect induced by incorporating nanomaterials can result in different behavior based on the polymer matrix. For example, Qi et al. reported reduced tensile strength due to incorporating nanoclay while Shokrieh et al. reported no significant changes (*Qi et al. 2006, Shokrieh et al. 2012*). Those effects highlight the varying effectiveness of CNTs on the tensile strength of polymer composites reported earlier.

2.3.4 Bond strength

Bond strength of polymers to substrates is developed due to physical and chemical bonds (Pocius 2011). Chemical bonds are induced by chemical reaction of the polymer to the adhering substrate. Physical bonds are developed through Van Der Waal forces (Zhai et al. 2006). Inclusion of nanomaterials can enable a chemical interaction and/or generate new chemical bonds that would not be activated with the neat polymer. Bond strength tests include pull-off, twist-off (Pocius 2011), flexural (Julio et al. 2004) and slant shear tests (Zhai et al. 2006, Julio et al. 2004). Pull-off test reports the most conservative bond strength among all tests as it provides the lowest bond strength values (Zhai et al. 2006, Julio et al. 2004, Momayez et al. 2005, Saldanha et al. 2013). Momayez et al. showed that in comparison with slant shear, splitting prism and Bi-surface shear tests, pull-off is the most suitable for bond strength tests where tension is the dominant state of stress (Momayez et al. 2005). Tests like slant shear and Bi-surface shear impose a state of indirect tension by applying compression forces that result in shear stress over the bonded surface in question. The slant shear test is more suitable for examining vertical or inclined rather than horizontal bond surface. Two types of failure are associated with slant shear test; cohesive and adhesive failures. Cohesive failure occurs within one of the substrates materials resulting in failure outside the interface. Thus, this failure type correlates to a state of stress where the shear stress in the polymer exceeds its ultimate shear strength. Adhesive failure on the other hand takes place at the bond interface between the two materials. Most standards suggest an angle of 60 degrees with the horizontal surface favors adhesive failures (Julio et al. 2004, Saldanha et al. 2013). Materials that possess significantly high compressive strength tend to experience adhesive failure when surface roughness and interface angle are carefully chosen (Julio et al. 2004). In fact, Wheat et al.

concluded that proper sandblasting of PCC interface with PC overlay is sufficient to prevent delamination of the bond between the two substrates (*Wheat et al. 1993*).

2.3.5 Modulus of elasticity and Poisson's ratio

Materials in the elastic region are often described by their modulus of elasticity and Poisson's ratio. The modulus of elasticity can be defined by the proportion of material's stress and strain within elastic limits while Poisson's ratio represents the ratio of proportional decrease of lateral strain to the proportional increase in longitudinal strain. Such parameters are key in describing the elastic behavior of materials and are often used in stress analysis and finite element modeling. In general, polymer materials have considerably low modulus of elasticity values ranging from 0.1 GPa to 7 GPa. Most common construction materials such as concrete, aluminum and steel often have higher values of 20 GPa, 70 GPa and 200 GPa respectively. Polymers also have significantly higher Poisson's ratio up to 0.40 compared with concrete, aluminum and steel values of 0.20, 0.33 and 0.3. Since PC without nanomaterials follows the rule of mixture, PC modulus of elasticity values' fall in between that of concrete and polymer ranging between 8 GPa and 30 GPa (*Reis and Ferrira 2004 , Gorninski et al. 2004, Reis 2005*) and its Poisson's ratio has been reported up to 0.25 (*Ahn et al. 2009, Wheat et al 1993*). However, it's important to emphasize that limited literature have examined the Poisson's ratio of PC. This is attributed to its high ductility that result in common measurement methods (such as strain gauges and calipers) to predict inaccurate measurements. This is further discussed in the result of compression tests with strain gauges.

Nevertheless, similar characteristics that affect the compressive and tensile strengths of PC persist in modulus of elasticity and Poisson's ratio. For example, Vipulanandan and Paul showed that by improving the compressive strength of PC without affecting its ductility, the elastic

modulus improves (*Vipulanandan and Paul 1993*). Martinez-Barrera et al. on the other hand showed that by subjecting PC to high levels of radiation resulting in increased flexural strain, the elastic modulus drops (*Martinez-Barrera et al. 2013*). Martinez-Barrera et al. additionally showed that reduced ductility due to incorporating synthetic fibers in PC result in lower elastic modulus as the tensile strength was not affected (*Martinez-Barrera et al. 2013*). Such findings however are not consistent among literature findings. *Reis (2005)* reported no effects of glass or carbon fibers in the elastic modulus of PC despite improvements in compressive strength (*Reis 2005*). This is attributed to improvements in ductility that offset the difference caused by compressive strength improvements. Engineers have often utilized the elastic modulus to be key mechanical property in structural design to predict the ductility of materials. However, PC exhibit large variance in its mechanical properties that can result in high strength brittle PC, high strength ductile PC, low strength brittle PC and low strength ductile PC. Such variance depends largely on the polymer type as well as its content, type of aggregate filler and method of curing as discussed in earlier sections. Nevertheless, the elastic modulus and Poisson's ratio remain as elastic properties that are sensitive to strain rate, test machine and strain measurement device.

2.3.6 Fatigue life

Fatigue is the weakening of materials caused by repetitive loading that is often well below the materials strength. Fatigue loads can be classified with respect to the stress amplitude, maximum stress, stress range, and frequency. Fatigue can be considered a fracture dominant mechanical process in which a crack must first initiate, its length need to extend and lastly reach the critical crack dimension resulting in failure. When examining the rate of crack growth in respect to loading cycles, Anderson, Gomez and Paris noticed that three stages exist: initially, secondary and tertiary. Prior to initially, a threshold region exists in which fatigue cracks do not

propagate. Initially and territory stages are often hard to measure experimentally due to rapid crack growth, the extreme geometric of crack tip opening, accessibility, resolution limitations and the random distribution of cracks. The material's behavior in fatigue depends on its microstructure, grain size, flow properties and fracture process zone properties. In the secondary stage; however, the linear behavior can be described using Paris' law stated in Eq. (2.1) according to the fatigue behavior shown in Figure 2.9 where a is the crack length, N is the number of cycles, C and m are material constants, and ΔK is the range of the stress intensity factor ($K_{max} - K_{min}$). Paris law has been modified by several researchers and developed the Goodman relationship, Forman models, Wheeler model, Elber's model and many more (Dowling 2007). Those models have been developed as Paris law does not include the effects of loading history and mean history and depends on uniaxial loading, long cracks and linear elastic fracture mechanics conditions. Although some models modify Paris' law with Miner's rule, reduced crack growth factors, or stress ratio, many researchers do not depend on it to describe the fatigue behavior of their material.

$$\frac{da}{dN} = C \Delta K^m \quad (2.1)$$

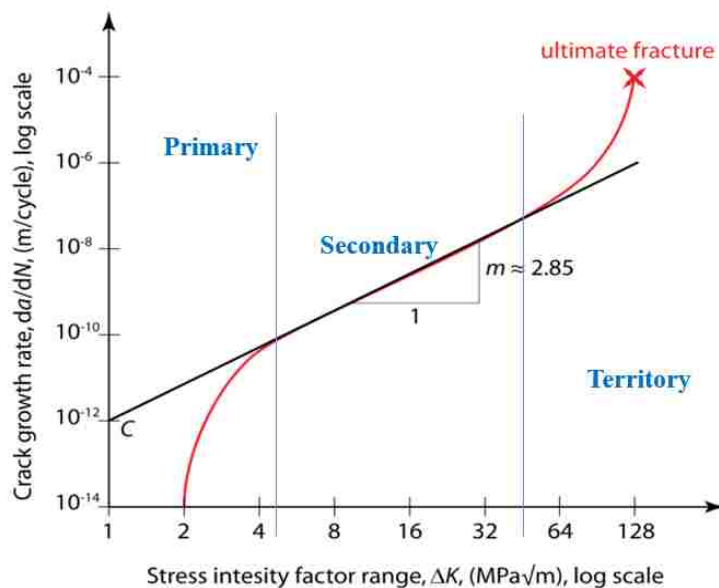


Figure 2.9: Paris law prescribing the secondary fatigue life behavior.

The high complexity of fatigue fracture based models result in many researchers depending on stress-number of cycles (S-N) curves to describe the fatigue life of their material. The simplified theory allows for similar simplified experimental methods. Such method has proven more helpful when comparing the effect of different additives as they often result in curve shifts. Fatigue life of PC remain key mechanical performance criteria in many of its applications such as overlays, machine foundations and repairs. In fact, vertical cracks have been reported for PC overlays caused by thermal stresses, traffic cyclic loads, degradation of the interface and loss of flexibility in the binder (*Wheat et al. 1993*). Nevertheless, the high ductility of PC, its polymer matrix viscoelastic properties, and slow elastic strain recovery prove fatigue evaluation to be more complicated. Those findings are discussed in details for fatigue test in chapter 3. Nevertheless, literature reported PC with sufficiently high fatigue life as Wheat et al. reported no delamination after 2,000,000 loading cycles of 1 in. and 2 in. PC overlays on PCC beams loaded to 55% of their shear capacity (*Wheat et al. 1993*). As the work prescribed in this work relies on simplistic S-N curves to describe fatigue life, further investigations of the tensile strength and fracture toughness have been utilized.

2.3.7 Fracture Toughness

Fracture toughness can be described by the material's resistance to crack propagation. This topic has been under extensive research since Inglis's paper in 1913 titled "Stress in a plate due to the presence of cracks and sharp corners". In that paper, Inglis noted that the stress at an elliptical hole approaches infinity towards its boundary. In 1920, Griffith examined the energy required to create new surfaces due to crack propagation in his paper titled "The Phenomena of Rupture and Flow in Solids". Thus, uncovering the role of energy in fracture mechanics. In 1939, Westergaard in his paper titled "Bearing Pressures and Cracks" proved that the stress state near crack tips approaches infinity irrespective of crack geometry. While many researchers produced significant

work to design various fracture toughness parameters, in essence, all fracture toughness models trace back to these original works that resulted in the stress intensity factor and critical energy release rate parameters.

Several fracture toughness test standards are present and have been used in literature such as ACI 446 report (2009), ASTM E1820 (2011), ASTM D5045 (2014), ASTM C1421 (2016), ASTM E2818 (2016) and RILEM (1985) (the international union of laboratories and experts in construction materials, systems and structures, from the name in French) . ASTM standards and RILEM classify fracture toughness using the stress intensity factor which is used to measure the critical energy release rate or J-integral (when applicable). ACI 446 (2009) report on the other hand evaluates the critical energy release rate and obtain an equivalent stress intensity factor. ACI 446 and ASTM standards rely heavily on either linear elastic fracture mechanics (LEFM), small fracture process zones, dominant linear stress-strain or on elastic values such as modulus of elasticity and bulk's modulus. However, Concrete, PC and many polymer composites can exhibit significant non-linearity, quasi-brittle fracture and large fracture process zones. Thus, such methods can result in inaccurate evaluation of the fracture toughness. While ASTM provide specific test standards for welds, plastic materials, ceramics, and general guidelines, ACI 446 and RILEM are directed towards either concrete or polymer composites respectively. The RILEM method utilizes a two parameter fracture mechanics approach. Thus, researchers examining the fracture toughness of PC have relied heavily on RILEM (*Reis et al. 2004, Reis and Ferrira 2004, Reis 2006*). However, RILEM suggests ignoring the energy dissipated at the end of the test due to sample's rotation which result in underestimating the fracture toughness of small samples by 20% when compared with exact calculations (*Elices et al. 1997*). Thus, comparison of literature findings

on the fracture toughness must be correlated to the test and analysis methods. Furthermore, different methods will yield different effects of nanomaterials or additives on the host material.

Using RILEM standards, several researchers examined the fracture toughness of PC and the effects of incorporating carbon, glass, coconut, sugar cane and banana fibers and nanoclays (*Reis et al. 2004, Reis and Ferrira 2004, Reis 2006, Shokrieh et al. 2012*). It's important to note that a major limitation of those investigation is the difficulty of rapid unloading of PC samples to 5% post peak as suggested by RILEM standards which often result in overestimating the fracture toughness (*Reis and Ferrira 2004*). Nonetheless, at 2.0 wt.% content of carbon fiber, Reis et al. reported 340% and 140% increase in fracture toughness using carbon and glass fibers (*Reis et al. 2004*). Reis and Ferrira however reported 29% and 13% increase in fracture toughness using similar contents of both fibers (*Reis and Ferrira 2004*). Such discrepancy is a result of evaluating the fracture toughness using the critical energy release rate for Reis et al. and the stress intensity factor for Reis and Ferrira. Reis on the other hand reported coconut, banana and sugar cane fibers effects on the fracture toughness of PC using both the stress intensity factor and critical energy release rate (*Reis 2006*). Their results show improvements in the stress intensity factor by 15%, 18% and 22% for coconut, sugar cane and banana fibers and 100%, 16% and 41% in the critical energy release rate respectively (*Reis 2006*). The significant discrepancy on the effects of fibers on the fracture toughness using stress intensity factor and energy release rate highlight previous discussions. Nevertheless, it's evident that incorporating fibers improved the fracture toughness of PC due to their mechanical crack arresting mechanisms.

The effects of nanomaterials on the fracture toughness of PC have not been investigated except by Shokrieh et al. examining nanoclays and Emiruglo et al. with ANPs. Their results show improvements in the fracture toughness by 12.5% and 132% (*Shokrieh et al. 2012, Emiruglo et al.*

2017). To further inspect the effects of nanomaterials on PC, examining the effects of nanomaterials on polymer and epoxy composite can provide significant insight as they observe PC's host matrix. It's important however to emphasize that most literature on the effect of nanomaterials on fracture toughness of epoxy and polymer composite rely heavily on the stress intensity factor as well as using ASTM and RIELM methods (*Shokrieh et al. 2012, Sumfleth et al. 2010, Gojny et al. 2004, Zhou et al. 2008, Gomez-del Rio et al. 2016, Yu et al. 2008, Park et al. 2015, Qi et al. 2006, Liu et al. 2005*). Investigations of nanoclays on epoxy composites show similar improvements in fracture toughness to those reported of PC (*Qi et al. 2006, Liu et al. 2005*). In general, researchers have focused on CNTs since 1D nanomaterials provide similar fiber like mechanisms whereas effects of 0D nanomaterials are heavily chemically induced. In general, literature suggests improved fracture toughness of epoxy and polymer composites due to CNTs inclusion (*Seyhan et al. 2009, Tang et al. 2013, Kabir et al. 2007, Sumfleth et al. 2010, Gojny et al. 2004, Zhou et al. 2008, Gomez-del Rio et al. 2016, Yu et al. 2008, Park et al. 2015, White and Sue 2011, Ma et al. 2015, Zhang et al. 2015, Opelt et al. 2015*) with further improvement taking place as the CNTs content increases (*Ganguli et al. 2006, Sumfleth et al. 2010, Yu et al. 2008, Ma et al. 2015, Zhang et al. 2015*). However, Ma et al. and Opelt et al. showed a decrease of stress intensity factor with the increase in content of pristine MWCNTs (*Ma et al. 2007, Opelt et al. 2015*). Nevertheless, most of the investigations neglected the fact that inclusion of significantly stiffer material in a polymer matrix (1 TPa compared to ~100s MPa) along with possible chemical bonds and change in crosslinking density might alter the polymer nanocomposite stiffness. For example, the elastic modulus of epoxy incorporating MWCNTs, was reported to increase by 3% to 26% (*Seyhan et al. 2009, Tang et al. 2013, Balakrishnan and Saha 2011, Hsieh et al. 2011, Gojny et al. 2004, Zhou et al. 2008, Zhang et al. 2015, Opelt et al. 2015*). Therefore, the critical

elastic energy release rate or critical plastic energy release rate J-integral would provide a more robust fracture toughness measure. In fact, researchers found greater increase in fracture toughness in the range of 56% to 138% measured by energy release rate compared with 27% to 51% measured by stress intensity factor (*Seyhan et al. 2009, Tang et al. 2013, Hsieh et al. 2011, White and Sue 2011, Ma et al. 2015*). The content of MWCNTs reported to induce such improvements in fracture toughness often ranged between 0.05 and 1.5 wt.% content (*Ganguli et al. 2006, Seyhan et al. 2009, Ma et al. 2007, Sumfleth et al. 2010, Gojny et al. 2004, Zhou et al. 2008, Gomez-del Rio et al. 2016, White and Sue 2011, Ma et al. 2015, Zhang et al. 2015, Opelt et al. 2015 and Borowski et al. 2015*).

2.3.8 Structural Health Monitoring Using Nanomaterials

Structural health monitoring (SHM) is the material or structural deterioration and damage detection in which the overall performance and structural state are quantified. Several techniques have been utilized for SHM including impedance based techniques, vibration signature, strain measurement, acoustic emissions and many more (*Sukwon et al. 2012*). Most SHM methods rely on the source and sensor method in which materials cracking, damage or deterioration act as the source that are collected by specific sensor. In impedance techniques, the material's electrical resistivity changes are measured by impedance sensors that are then used to quantify deteriorations. The change of electrical resistivity under mechanical strains is referred to as piezoresistive effect. In general, increased pressure result in increased resistance. Similarly, cracks or damage can result in decreased electrical conductivity (increased resistance) aiding in structural health monitoring. To enable SHM utilizing piezoresistivity, the material must have low resistivity (high conductivity) with minimal fluctuations enabling stable currents and the measuring device must have resolution high enough to measure such conductivity. Polymers and epoxy systems

typically have higher resistivity resulting in low current stability. Thus, changes in resistivity due to damage or cracking result in insignificant resistance changes. Incorporating specific nanomaterials however aid in increasing conductivity (lowering resistivity) resulting in more stable current flow. Of those materials, researchers have investigated iron oxide nanomaterials (Fe_2O_3), carbon fibers, carbon black, carbon nanotubes (CNTs) and graphene nanoplatelets (Vipulanandan and Mohammed 2015, Liew et al. 2016, Garlof et al. 2017, Thostenson and Chou 2008, Azhari and Banthia 2012, Arboleda et al. 2013, Yamamoto et al. 2012, Yan and Jeong 2017). Specific focus has been carried on CNTs as multifunctional additives able to improve mechanical performance and improve electrical and thermal conductivity (Liew et al. 2016, Thostenson and Chou 2008, Yamamoto et al. 2012). CNTs also offer low percolation threshold enabling high conductivity at low contents (Thostenson and Chou 2008). Its nanocomposites have been used in literature in strain, damage, cracking and failure measurements, vapor sensing, and classifying shear out failure of joints (Liew et al. 2016, Thostenson and Chou 2008, Azhari and Banthia 2012). In general, CNTs provide two sources of electrical resistance: intrinsic resistance of CNTs and contact resistance at CNTs junctions. Of these two, contact resistance plays a major role in the formation of conductive networks within insulator matrix at threshold levels (Sarkar and Das 2014, Coppola et al. 2013, Sun et al. 2014). Furthermore, achieving uniform dispersion of CNTs play a major role in reaching percolation threshold at low contents (Liew et al. 2016, Arboleda et al. 2013). When achieved, electrical conductivity has been reported to increase from 700% up to 8 orders of magnitude (Vipulanandan and Mohammed 2015, Liew et al. 2016, Azhari and Banthia 2012, Yamamoto et al. 2012). Threshold levels also depend on the content of added fillers as well as curing effects for polymer composites as well as concrete (Vipulanandan and Mohammed 2015, Arboleda et al. 2013). Enabled electrical conductivity result in self-sensing smart materials

(SSSM) that can be utilized to monitor structural health using wireless sensors. Furthermore, some researchers have been investigating coupling piezoresistive nanocomposite generators (PNG) with CNTs to improve their voltage output (*Yan and Jeong 2017*). While PNG and electrically conductive PC have not been researched, previously mentioned literature on polymer and cementitious composites provide promising background on such techniques. Furthermore, by utilizing PNG along CNTs in PC overlays, highways, bridges, and machine foundations can be monitored wireless as well as provide sufficient electric voltage to power necessary lightings.

CHAPTER 3: EXPERIMENTAL METHODS

This chapter details the material properties, experimental methods used for testing, as well as analysis methods. Two polymer epoxy systems were selected where each is used in the industry for their specific project namely Novolac for repairs and Siloxane for bridge deck overlays. For Siloxane PC (SPC), three types of nanomaterials were investigated namely alumina nanoparticles (ANPs), pristine multi-walled carbon nanotubes (P-MWCNTs) and carboxyl functionalized multi-walled carbon nanotubes (COOH-MWCNTs). Magnetic stirring and ultrasonication were used for nanomaterials dispersion. Scanning electron microscope (SEM) was used to investigate dispersion of all nanomaterials at different contents. Flowability and direct tension tests were then carried for PC at varying nanomaterials content and the results were analyzed for flowability, tensile strength, tensile strain at failure, toughness and modulus of elasticity. Then, the best performing contents were selected and fracture toughness tests were carried along with modulus of rupture. Analysis of test results were performed using linear elastic fracture mechanics (LEFM) in correspondence to ACI 446 report. Later, two approaches of quasi-brittle fracture mechanics (QBFM) were utilized using the effective crack modulus as well as the work of fracture. The best performing mixes were then selected again and fatigue tests were conducted to evaluate PC nanocomposite (PCNC) service life. Structural health monitoring (SHM) was also carried on flexure tests with SPC mixes incorporating P-MWCNTs. The final mechanical test was tension test carried on hybrid mixes of P-MWCNTs and COOH-MWCNTs to further investigate the effect of functionalization on the mechanical performance of PC. Finally, to investigate the effect of different nanomaterials on PC, microstructural analysis composed of Fourier infrared transformation spectroscopy (FTIR) and dynamic modulus analyzer (DMA) were carried. Those tests investigated the changes in the epoxy polymer matrix examining the formation of specific chemical groups and crosslinking density.

In Novolac PC (NPC), ANPs, COOH-MWCNTs and Silica nanoparticles (SNPs) were selected for repairs applications. Mechanical tests were carried using slant shear and compressive strength with strain gauge tests to determine the materials' properties including compressive strength, modulus of elasticity and Poisson's ratio. As both parts of slant shear test provide significantly different stiffness, further investigation on the true shear stresses were carried using finite element analysis (FEA) in ABAQUS and using analytical mechanics. Finally, the rule of mixture design was performed to examine whether nanocomposites can utilize elastic models based on micro or macro inclusions. The sections below provide all materials, test schematics, procedures, setups and analysis methods used to carry this investigation.

3.1 Materials

3.1.1 Epoxy polymer matrix

Novolac epoxy which is a low viscosity cycloaliphatic polyamine was selected for wellbore repairs and supplied by Epoxy Chemicals, Inc. This type of epoxy has a high chemical resistance against inorganic acid solvents and aggressive chemicals that are often present in wellbores. The hardener component allows for a long working life and has a low viscosity as well. Such properties are key as repairs are often performed by injections at deep levels.

Siloxane epoxy is a polysulfide epoxy containing silane which is commonly used in thin bridge deck overlays and thing slurry repairs. The polymer epoxy system was provided by Transpo Inc. as part of their Thing Slurry Overlay T-48 system. This system has a rapid curing time with good bond strength to both steel and concrete surfaces. It also provides a high early strength, high elasticity, and UV light, moisture and chemical resistivity. The resin is mixture of Bisphenol

A/Epichlorohydrin Epoxy Resin including silane. The hardener is Diethylenetriamine (DETA), Phenol, 4,4'-(1-methylethylidene) bis-, and Tetraethylenepentamine.

3.1.3 Aggregate filler

In all mixes, crystalline silica (quartz) and ceramic microspheres powder was used as mixing filler to produce the slurry to be cast and harden.

3.1.3 Nanomaterials

Table 3-1: Nanomaterials properties and information

<i>Name</i>	<i>Chemical composition</i>	<i>Type of nanoparticle</i>	<i>Dimension</i>	<i>Supplier</i>	<i>Density (g/cm³)</i>	<i>Surface area (m²/g)</i>
<i>ANPs</i>	Al ₂ O ₃	0D nanomaterials	<50 nm	Sigma-Aldrich	3.89	>40
<i>SNPs</i>	SiO ₂	0D nanomaterials	< 7nm	AEREOSIL	2.20	>380
<i>P-MWCNTs</i>	C > 95 wt.% Ash <1.5 wt.%	1D nanomaterials	5-10 nm inner Ø 10-20 nm outer Ø 10-30 µm length	Cheaptubes	2.10	>110
<i>COOH-MWCNTs</i>	C > 95 wt.% Ash <1.5 wt.% COOH=1.23 wt.%.	1D nanomaterials	5-10 nm inner Ø 10-20 nm outer Ø 10-30 µm length	Cheaptubes	2.10	>110

This investigation utilized four different types of nanomaterials in which two are 0D nanomaterials and two are 1D nanomaterials. The 0D nanomaterials are alumina nanoparticles (ANPs) and silica nanoparticles (SNPs). 1D nanomaterials included pristine multi-walled carbon nanotubes (P-MWCNTs) and carboxyl functionalized multi-walled carbon nanotubes (COOH-MWCNTs). The selected nanomaterials allow examining the effect of different nanomaterials of

different dimensionality 0D vs 1D. Further, examine the effect of different chemical interactions generated by the different chemical nature of those particles. Finally, examine the effect of functionalization in 1D nanomaterials with specific group that can react with the polymer epoxy system selected. The information for all nanomaterials are listed below and their properties are summarized in Table 3-1: Nanomaterials properties and information

3.1.3.1 Alumina nanoparticles

The ANPs used are aluminium oxide nanopowder manufactured by Sigma Aldrich, Inc. Those particles are often present as odourless powder with a maximum particle size of 50 nm, a melting point of 2040°C, and a relative density of 3.89 g/cm³. A transmission electron microscope (TEM) image of the used ANPs is shown in Figure 3.1 (a).

3.1.3.2 Silica nanoparticles

The SNPs used are AEREOSIL® 380 from Evonik Degussa, which is hydrophilic fumed silica with an average BET surface area of 380 m²/g and an average particle diameter of 7 nm. AEROSIL® 380 is a chemically prepared silicon dioxide powder that is white in color and odorless, and has a melting point of 1700 °C and a density of 2.2 g/cm³.

3.1.3.3 Multi-walled carbon nanotubes

Two types of MWCNTs were used including pristine (P-MWCNTs) and carboxyl functionalized (COOH-MWCTs). Both types of nanotubes have an outer diameter of 20-30 nm, inner diameter of 5-10 nm and 10-30 µm length. The MWCNTs were produced using Catalyzed Chemical Vapor Deposition Technique (CCVD) by Cheap-Tubes and are shown in Figure 3.1 (b). Functionalization was performed by manufacturer by means of acid treatment chemistry of H₂SO₄/HNO₃. Carboxyl groups were attached at the ends and side walls of the nanotubes. This

process is often performed by adding H₂O₂ to the chemical treatment as reported by Zhu et al. and Osorio et al (Zhu et al. 2003, Osorio et al. 2008). The nanotubes are of purity greater than 95%, a relative density of 2.1 g/cm³ and surface area of 110 m²/g. P-MWCNTs are electrically conductive with value greater than 100 S/cm.

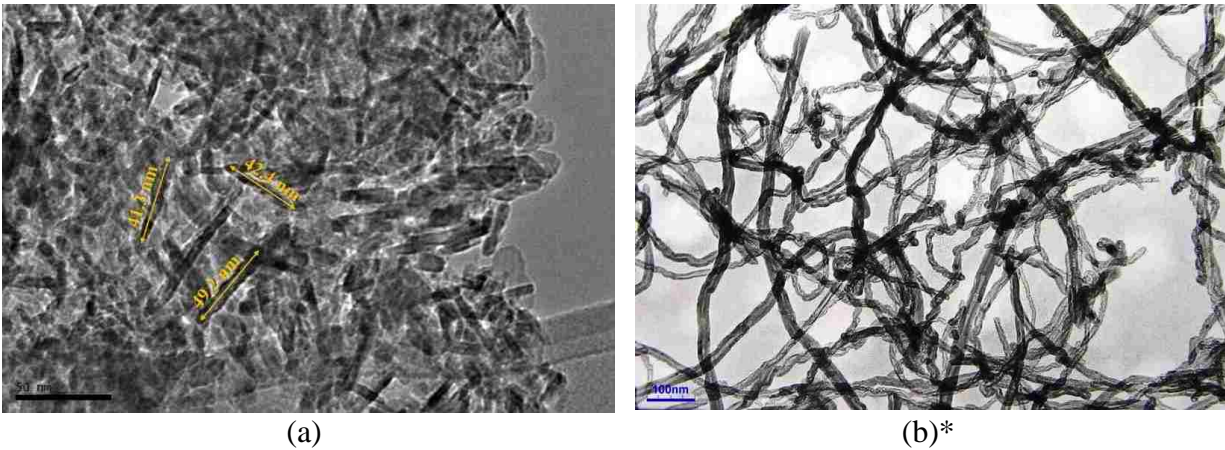


Figure 3.1: Transmission electron microscope (TEM) images of (a) ANPs and (b) MWCNTs

*Courtesy of CheapTubes

3.2 Nanocomposite Preparation

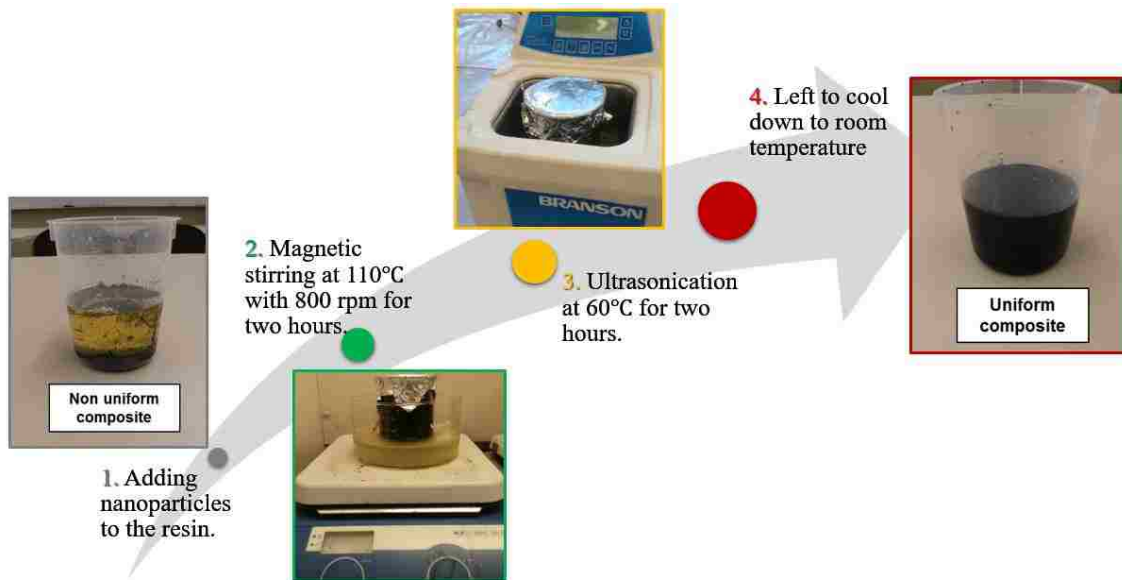


Figure 3.2: Preparation of epoxy nanocomposite showing dispersion steps for magnetic stirring and ultrasonication.

Dispersion of nanomaterials was performed using two stages: magnetic stirring followed by ultrasonication as shown in Figure 3.2. This technique was kept constant for all mixes regardless of content or type of nanoparticles used to avoid any processing effects on the polymer particles. First, the specific content of nanomaterials was weighed with an accuracy of 0.01 grams and added to the epoxy resin. The resin was then placed in oil bath and heated to 110°C and magnetic stirring was applied at 800 rpm. The resin container was closed with aluminum foil to entrap the heat and seal the resin at the high stirring value. After two hours, the magnetic stirrer is removed and the resin nanocomposite is placed in ultrasonication bath. The bath contains a degassed distilled water at 60°C. Ultrasonic waves are then applied for another two hours. The resin nanocomposite was then removed from the bath and left to cool down to room temperature over 2 hours before it was used. Neat mixes are not subjected to the previous cycle. The temperatures, stirring speed and duration and ultrasonication duration selected are to ensure reduced viscosity of the epoxy resins during dispersion without any molecular polymer damage. Those parameters have been examined by our research team and those parameters have proved to yield uniform dispersion (*Aboubakr et al. 2014, Soliman et al. 2012, Soliman et al. 2015*). Ultrasonication improves dispersion by generating microscopic bubbles within the resin that release energy and prevents particle agglomeration, thus leading to a uniform dispersion. Both the oil and water baths ensure uniform temperature along the resin container. Distilled water was used in ultrasonication bath to reduce the number of particles present such as minerals and salts in which they decrease the efficiency of such technique. Degassing eliminates then unnecessary air bubbles in the distilled water solution to ensure full utilization of ultrasonic waves.

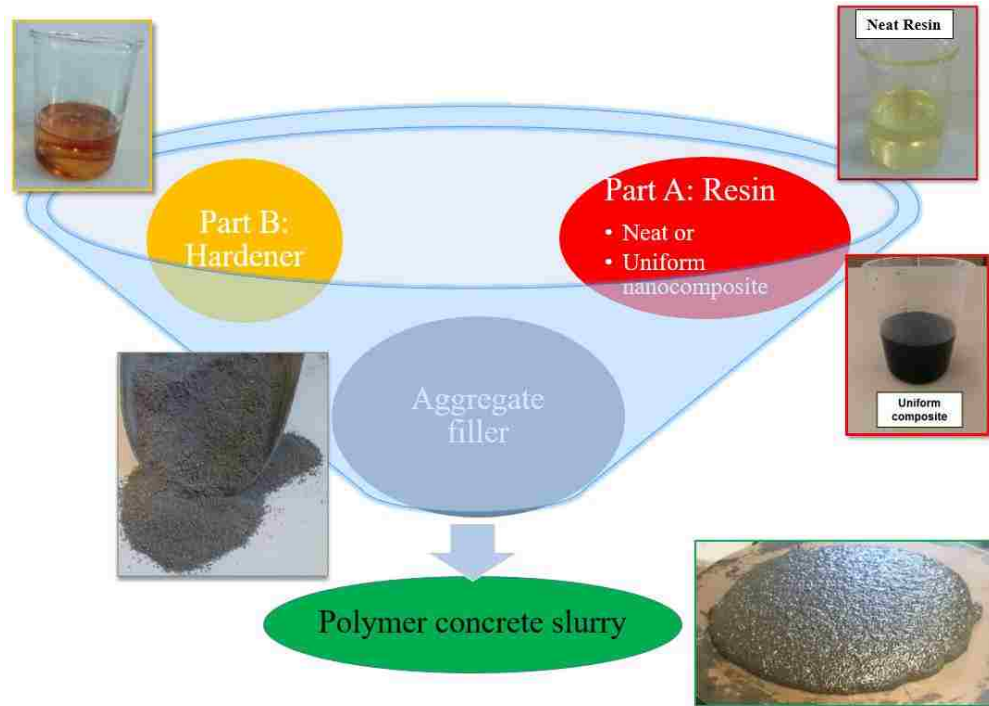


Figure 3.3: Production of polymer concrete slurry

To produce PC slurry, the neat epoxy or epoxy nanocomposite was mixed with the hardener (often referred to as parts A and B) for two minutes to produce a uniform polymer epoxy matrix. The specific aggregate was then added to the mix gradually and mixed for another two minutes. The slurry was then used to measure the flowability and prepare all samples. Figure 3.3 shows schematics of producing PC slurry. Novolac PC (NPC) samples were kept at room temperature for 7 days while heat curing was performed on Siloxane PC (SPC) samples. For heat cured samples, the samples were demolded after 16 hours of cast and placed in heated oven at 60°C for 24 hours. Heat treatment was used for SPC due to lengthy testing time for such samples compared to NPC. By heat curing the samples, accelerated polymerization takes place eliminating variations in the material properties when testing over several days. NPC samples were tested for compression and slant shear in which those tests can be completed within one day. SPC samples were tested in tension, modulus of rupture and fracture. The latest requires lengthy testing time and hence testing

several specimens require testing procedures over several days. The number of samples tested per mix along with the standardized method for casting are detailed in their respective sections.

Microstructural analysis samples were produced with no aggregate filler. Neat and nanocomposite epoxy resins were prepared in similar fashion to as mentioned previously. The resin or nanocomposite resin were added to the hardener and hand mixed using thin metal rod at medium speed for 2 minutes. This mixing technique was selected to prevent air bubbles from forming which can significantly influence microstructural analysis. The mix was then cast into sheets of different thickness of 0.5 mm, 1 mm and 4 mm. The sheets followed similar curing to their respective PC mix. Novolac epoxy sheets were therefore cured at room temperature for 7 days while Siloxane epoxy samples were heat cured at the oven after 16 hours from casting for 24 hours at 60°C. The hardened epoxy polymer sheets were then machined with electric blade saw with specific dimensions for the respective microstructural test. Table 3-2 -

summarize all PC mixes along with epoxy mixes containing no aggregate filler. Mixes are designated NPC for Novolac PC, SPC for Siloxane PC, N for Novolac epoxy coupons, S for Siloxane epoxy coupons, ANP for alumina nanoparticles, SNP for siloxane nanomaterials, CNT for carbon nanotubes, P for pristine, C for carboxyl and the integer specifies the nanomaterials content as weight of the resin.

Table 3-2: Neat PC mixes.

<i>Designation</i>	<i>Epoxy type</i>	<i>Nanomaterial type</i>	<i>Nanomaterials content</i>	<i>Content (Kg/m³)</i>		
				Resin	Hardener	Filler
<i>SPC-Neat</i>	Siloxane	None	0.00%	287	125	1557
<i>NPC-Neat</i>	Novolac	None	0.00%	287	125	1557

Table 3-3: Siloxane PC mixes with MWCNTs where epoxy resin is 287 kg/m³, hardener is 125 kg/m³ and aggregates are 1557 kg/m³.

<i>Designation</i>	<i>Nanomaterial type</i>	<i>Nanomaterials content</i>
<i>SPC-CNT-C0.1</i>	COOH-MWCNTs	0.10%
<i>SPC-CNT-C0.25</i>		0.25%
<i>SPC-CNT-C0.5</i>		0.50%
<i>SPC-CNT-C0.75</i>		0.75%
<i>SPC-CNT-C1.0</i>		1.00%
<i>SPC-CNT-C1.5</i>		1.50%
<i>SPC-CNT-C2.0</i>		2.00%
<i>S-CNT-C0.5</i>		0.50%
<i>S-CNT-C2.0</i>		2.00%
<i>SPC-CNT-P0.1</i>		P-MWCNTs
<i>SPC-CNT-P0.25</i>	0.25%	
<i>SPC-CNT-P0.5</i>	0.50%	
<i>SPC-CNT-P0.75</i>	0.75%	
<i>SPC-CNT-P1.0</i>	1.00%	
<i>SPC-CNT-P1.5</i>	1.50%	
<i>SPC-CNT-P2.0</i>	2.00%	
<i>S-CNT-P0.5</i>	0.50%	
<i>S-CNT-P2.0</i>	2.00%	

Table 3-4: PC mixes with siloxane epoxy and ANPs designation where epoxy resin is 287 kg/m³, hardener is 125 kg/m³ and aggregates are 1557 kg/m³.

<i>Designation</i>	<i>Nanomaterial type</i>	<i>Nanomaterials content</i>
<i>SPC-ANP-0.5</i>	ANPs	0.50%
<i>SPC-ANP-1.0</i>		1.00%
<i>SPC-ANP-2.0</i>		2.00%
<i>SPC-ANP-3.0</i>		3.00%
<i>S-ANP-0.5</i>		0.50%
<i>S-ANP-2.0</i>		2.00%
<i>S-ANP-3.0</i>		3.00%

Table 3-5: PC mixes with Novolac epoxy at different nanomaterials where epoxy resin is 287 kg/m³, hardener is 125 kg/m³ and aggregates are 1557 kg/m³.

<i>Designation</i>	<i>Nanomaterial type</i>	<i>Nanomaterials content</i>
<i>NPC-ANP-0.5</i>	ANPs	0.50%
<i>NPC-ANP-1.0</i>		1.00%
<i>NPC-ANP-2.0</i>		2.00%
<i>NPC-ANP-3.0</i>		3.00%
<i>NPC-ANP-4.0</i>		4.00%
<i>NPC-SNP-0.5</i>	SNPs	0.50%
<i>NPC-SNP-1.0</i>		1.00%
<i>NPC-SNP-2.0</i>		2.00%
<i>NPC-CNT-C0.5</i>	COOH-MWCNTs	0.50%
<i>NPC-CNT-C1.0</i>		1.00%
<i>NPC-CNT-C2.0</i>		2.00%
<i>N-ANP-1.0</i>	ANPs	1.00%
<i>N-SNP-1.0</i>	SNPs	1.00%
<i>N-CNT-C1.0</i>	COOH-MWCNTs	1.00%

Table 3-6: PC mixes with Siloxane epoxy containing hybrid mix of MWCNTs where epoxy resin is 287 kg/m³, hardener is 125 kg/m³ and aggregates are 1557 kg/m³.

<i>Designation</i>	<i>Nanomaterial #1</i>	<i>Nanomaterial #1 content</i>	<i>Nanomaterial #2</i>	<i>Nanomaterial #2 content</i>
<i>SPC-CNT-P0.1/C1.9</i>	P-MWCNTs	0.10%	COOH-MWCNTs	1.90%
<i>SPC-CNT-P0.5/C1.5</i>		0.50%		1.50%
<i>SPC-CNT-P1.5/C0.5</i>		1.50%		.50%
<i>SPC-CNT-P1.9/C0.1</i>		1.90%		0.10%

3.3 Flowability Test

Immediately after preparing the PC slurry, the flowability test was conducted. This test was carried in accordance to ASTM C1437 (2013). This test is typically used for hydraulic cements or mortars containing cementitious materials. Since no ASTM standards are present, PC slurry is treated as a hydraulic cement since it serves in the same function. To perform the test, a cone with 70mm upper diameter, 100mm lower diameter and 50mm height was selected. The cone is centered on top of a standard flow table confirming with ASTM C230/230M (2014). The PC slurry is then filled over two layers each compacted 20 times. Tamping and compaction of each layer were uniform inclining the tamper towards the sides of the cone. This was performed using a tamper that corresponds with ASTM C39/C39M (2016). The compacted slurry was then left to sit for one minute while the table was swiped clean and dry. The cone is then lifted over 5 seconds to allow PC slurry to debond from the cone sides. The flow table is then dropped 25 times over 15 seconds. All four slurry diameters scribed on the flow table were then measured using the specific caliber listed in ASTM C230/230M (2014). The sum of those diameters was reported as percentage of the original cone base. Figure 3.4 shows the schematics of the flowability test process and tools.



Figure 3.4: Flowability measurement of PC showing flow caliber, cone and table and test procedure.

3.4 Tension Test

Direct tension test of PC samples was performed to obtain the tensile properties of different SPC mixes. Unlike ordinary concrete where the tensile properties are measured through indirect tension tests, direct tension test is possible with PC due to its high ductility. The test was carried per ASTM D638 (2014) for plastics as PC exhibit similar ductility behavior. Of the standard, type III sample was selected and the loading rate was kept at the minimum permissible of 3.75mm/min. PC was casted into dog-bone shaped molds with a thickness of 10 mm in one layer compacted 25 times. Figure 3.5 shows the fabricated molds as well as the sample geometry. MTS Bionix Servohydraulic machine with 1N resolution and ± 25 kN range was used. The test utilized an MTS extensometer with 0.0001 microstrain resolution and 1 in. gauge length. PC surface was roughened using 50 grit sanding belt and the MTS specific grips of 6.35-12.7 mm wide grips were utilized to prevent slippage. Figure 3.6 displays the fixture of the test as well as its schematics. Five samples were tested from each mix to ensure statistical significance of the acquired results. The elastic

modulus was measured from the resulting stress-strain curves obtained. Due to the non-linear behavior of PC, the elastic modulus was estimated based on the most linear portion of the curve.

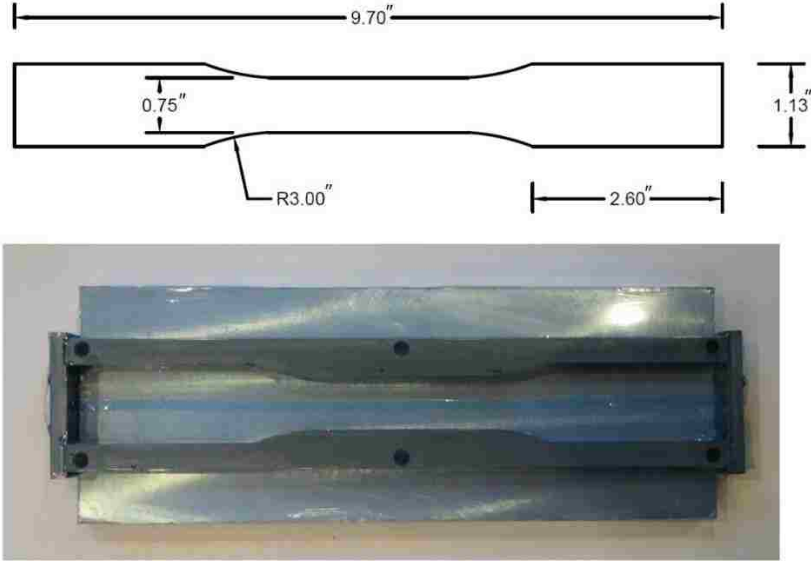


Figure 3.5: Tension samples molds and respective dimensions.

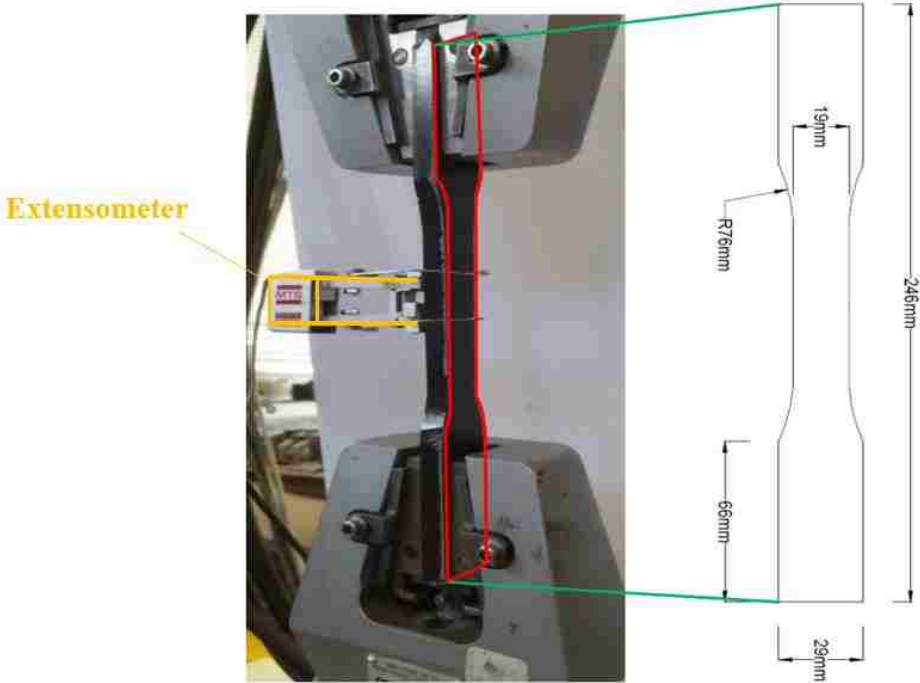


Figure 3.6: Tension test and its schematics

3.5 Fracture Toughness Test

Fracture toughness of SPC mixes was evaluated through three-point bending of notched PC prisms. ACI 446 (2009) report on fracture testing of concrete was used to establish the loading fixture, setup, mechanisms and sample geometries. The report suggests limiting the prisms' dimensions per the sample's depth. For a specimen with depth "D", the length must be greater than $3D + 50\text{mm}$ (2in) loaded with span of $3D \pm 5\%$, the notch depth should be limited in the range of $D/3 \pm 10\%$, and the notch's depth should be smaller than $0.02D$. Abiding by those regulations, the length of PC prisms was selected to be 300 mm with $25 \times 25 \text{ mm}^2$ cross section. All fracture test prisms were notched using a machine saw to obtain a notch of 0.75 mm width and 8.4 ± 0.25 mm depth. Prisms dimensions along with ACI guidelines are shown in Figure 3.7. A three-point bending frame was also manufactured per the guidelines listed in ACI446 report. The frame provided rollers at both supports where one of the supports as well as the loading head can rotate for $\pm 10^\circ$. The loading span was 150 mm allowing 75 mm double over hang eliminating the self-weight moment at the crack tip. Figure 3.8 shows the loading frame as well as its schematics. Two knife blades were glued around the notch in which a crack mouth opening displacement (CMOD) gauge was attached. A special CMOD gauge was used with a wider range of $-2/+12\text{mm}$ rather than the 8 mm conventionally used with ordinary concrete. ACI 446 suggests the use of reference frame to accurately collect the displacement at the crack tip. Such frame was constructed to allow two linear variable differentiable transformers (LVDT) to be attached to the frame and induce no loads on the prism. The frame was designed to capture the displacement at both sides of the prism near the crack tip and to adjust to the sample's rotation caused by bending. Figure 3.9 shows the schematics of the reference frame and the actual frame. Since the frame is simply supported over the sample with similar span of 150 mm, the reference frame can self-adjust to the prisms rotation

as the crack is propagating as shown in Figure 3.10. Due to machine limitations, a crack mouth opening displacement (CMOD) feedback loop was not possible to control the loading rate as recommended by ACI report. Therefore, several samples were used to estimate displacement control load rates with displacement limits. Those rates were selected to ensure that peak load was reached within 3-5 minutes and the test completed within 20-30 minutes. This also ensures that the full softening effect of load-CMOD curves can be obtained for analysis. Table 3-7 summarizes the selected load rates for all SPC mixes. Twelve samples were prepared for each mix: three samples were used to evaluate the modulus of rupture, three were used to validate the loading rate, and six prisms were used to conduct fracture test. The data acquisition system collected data for both LVDTs, displacement, CMOD and force at the frequency of 10 Hz. Appendix B contains the shop drawings for both the reference and loading frames.

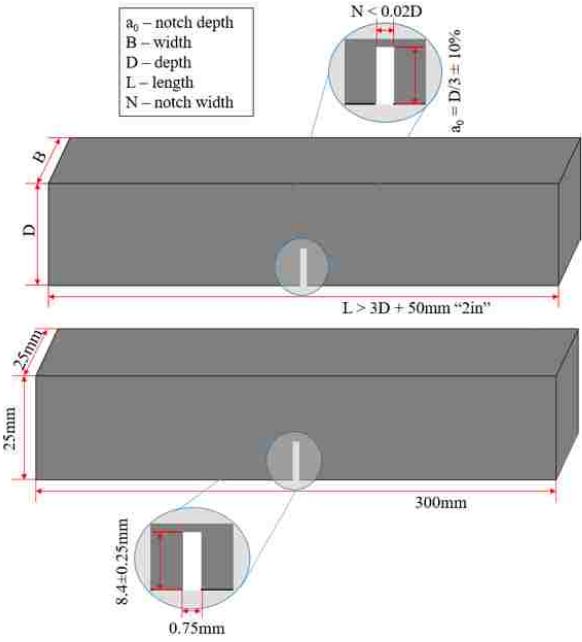


Figure 3.7: Dimensions and schematics of fracture specimen per ACI 446 and as used.

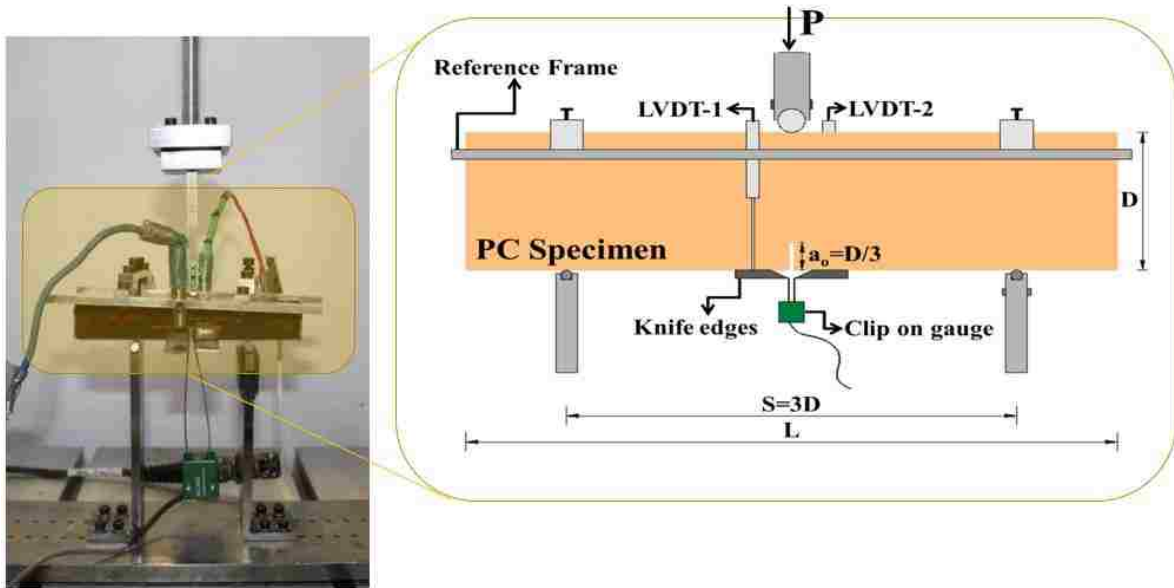


Figure 3.8: Fracture test setup in experiment and schematics.

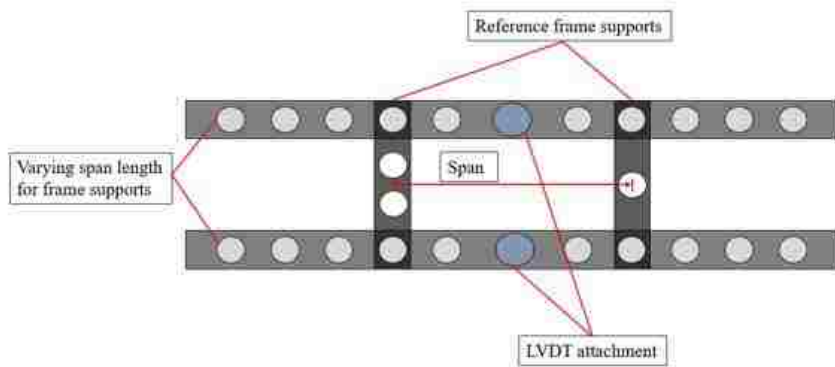
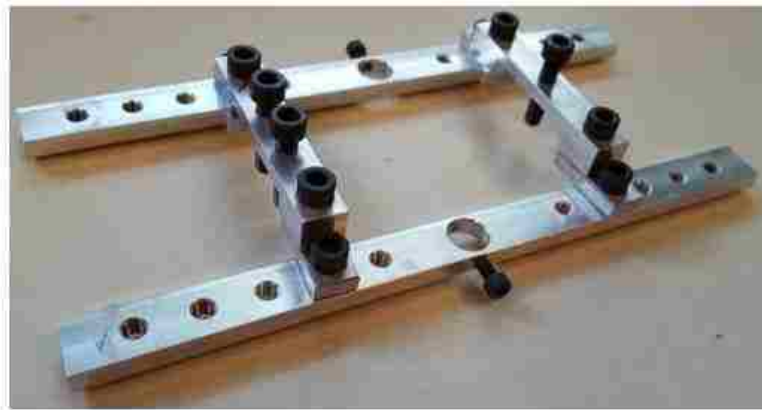


Figure 3.9: Reference frame as used and its schematics.

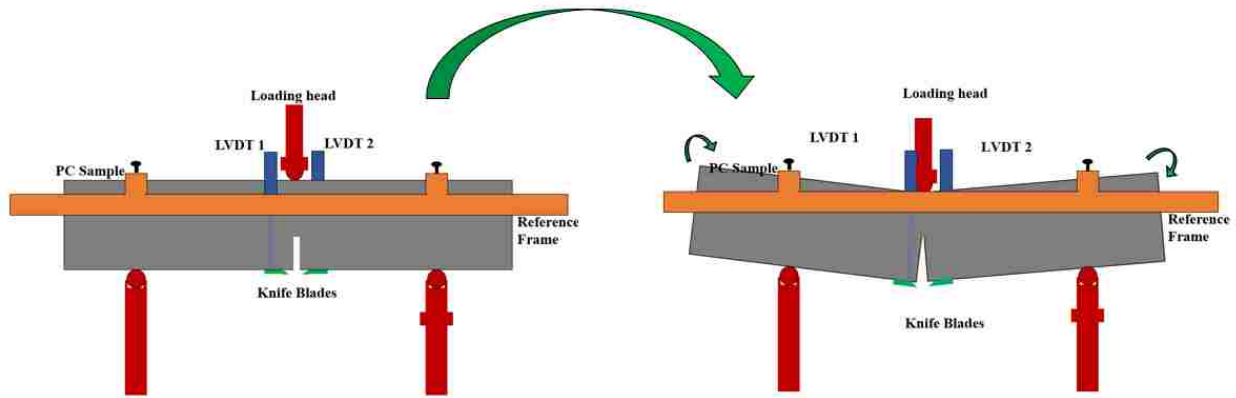


Figure 3.10: Self adjustment of the reference frame; as the PC prisms bend due to fracture, the reference frame remains in its location collecting accurate displacement.

Table 3-7: Loading rates details used in fracture tests of PC mixes.

<i>SPC mix</i>	<i>Nanomaterial</i>	<i>Load rate 1 (mm/min)</i>	<i>Load rate 1 limit (mm)</i>	<i>Load rate 2 (mm/min)</i>
<i>SPC-Neat</i>	None	0.25	1.25	0.20
<i>SPC-CNT-C0.5</i>	COOH-MWCNTs	0.30	1.50	0.25
<i>SPC-CNT-C1.0</i>		0.35	1.75	0.30
<i>SPC-CNT-C1.5</i>		0.40	2.00	0.35
<i>SPC-CNT-C2.0</i>		0.45	2.25	0.40
<i>SPC-CNT-P0.5</i>		P-MWCNTs	0.30	1.50
<i>SPC-CNT-P1.0</i>	0.35		1.75	0.30
<i>SPC-CNT-P1.5</i>	0.40		2.00	0.35
<i>SPC-CNT-P2.0</i>	0.35		1.75	0.30
<i>SPC-ANP-0.5</i>	ANPs	0.25	1.25	0.20
<i>SPC-ANP-1.0</i>		0.30	1.50	0.25
<i>SPC-ANP-2.0</i>		0.35	1.75	0.30
<i>SPC-ANP-3.0</i>		0.40	2.00	0.35

Analysis of fracture testing of PC has not been established ins standards yet. In fact, there is no one standard method for analysis of fracture testing of concrete or many materials. In general,

three different fracture mechanics principles are generally applied in fracture mechanics analysis namely linear elastic fracture mechanics (LEFM), quasi-brittle fracture mechanics (QBFM) and elastic plastic fracture mechanics (EPFM). Each of these models reflect different energy release rate mechanisms. This affect the total energy consumed (U_{total}) to completely fracture the specimen which can be classified to elastic energy ($U_{elastic}$), energy consumed in the fracture process zone (U_{FPZ}) or a combination of both. Accordingly, a unique fracture energy release rate parameter can be used to describe the fracture toughness. For LEFM, a critical energy release parameter G_{Ic} is sufficient as the energy consumed in the fracture process zone (FPZ) is negligible. Materials that abide by EPFM on the other hand consumes most of their energy in the FPZ in which the elastic energy becomes negligible and the critical J-integral release rate (J_{Ic}) becomes sufficient to described the fracture toughness. Quasi-brittle materials are classified by consuming considerably comparable energies both elastically and through the FPZ. Hence, a new total energy release rate (T_{Ic}) parameter is introduced in this paper that sums J-integral and G_{Ic} . Those models and their parameters are summarized in Table 3-8.

Table 3-8: Fracture mechanics models based on material's behavior.

<i>Model</i>	<i>Energy components</i>	<i>Resulting fracture toughness unique energy parameter</i>
<i>Linear Elastic Fracture Mechanics (LEFM)</i>	$U_{total} = U_{elastic} + U_{FPZ}$	$U_{total} = G_{Ic}$
<i>Quasi-Brittle Fracture Mechanics (QBFM)</i>	$U_{total} = U_{elastic} + U_{FPZ}$	$U_{total} = G_{Ic} + J_{Ic} = T_{Ic}$
<i>Elastic Plastic Fracture Mechanics (EPFM)</i>	$U_{total} = U_{elastic} + U_{FPZ}$	$U_{total} = J_{Ic}$

3.5.1 Linear elastic fracture mechanics (LEFM) analysis

The ACI 446 report suggests modified linear elastic fracture mechanics (LEFM) approach based on fictitious crack model proposed by Hillerborg and co-workers (*Hillerborg et al. 1976*). In this model, the crack is realized as constitutive consequence across the crack. As cracks form and propagate, the stress is redistributed generating shear stresses in the fracture process zone (FPZ) as shown in Figure 3.11. Thus, cracks are treated as constitutive consequences along the crack rather than discontinuities. One of the common applications of this model is to assume a bi-linear cohesive stress versus crack tip opening displacement (CTOD) curve. Such curve depends on concrete's tensile strength and on establishing full softening effect of concrete's fracture. The ACI report lists a procedure on how to approximate experimental data using a bi-linear curve as shown in Figure 3.12. The fracture toughness then can be estimated by the energy consumed in the work of fracture governed by the critical CTOD ($CTOD_c$) and the tensile strength of concrete. The ACI report suggests using the fracture energy (G_F) as a measure of the fracture toughness avoiding direct measurement of the stress intensity factor (K_I) or the characteristic critical K_I (K_{Ic}).

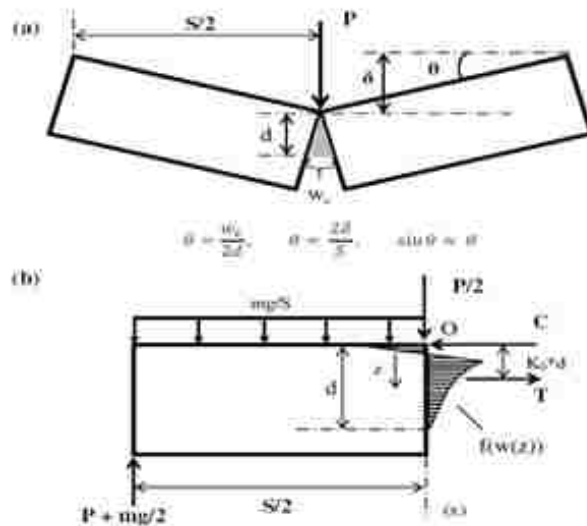


Figure 3.11: Basic principles used for analysis of notched beam set-up data to extract the bilinear fracture curve of PC.

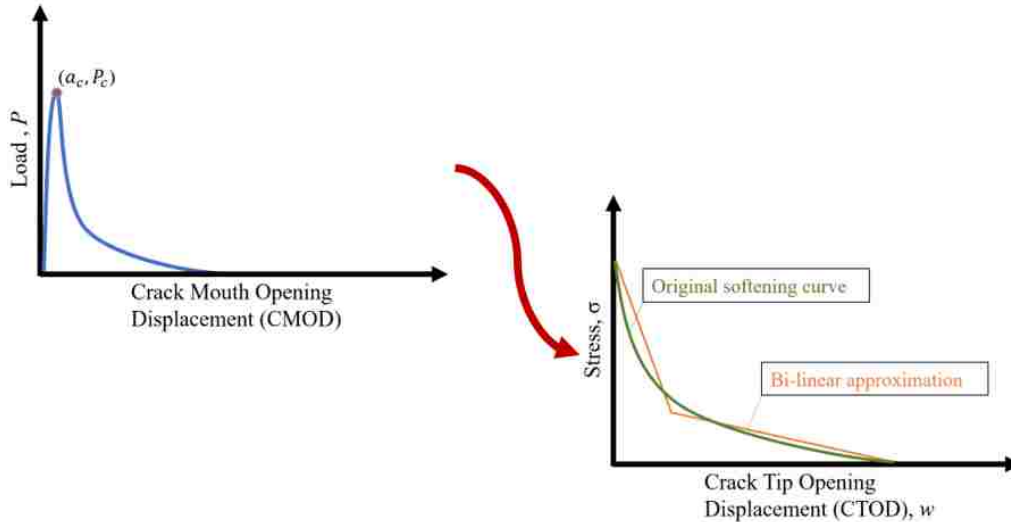


Figure 3.12: Schematics of the methods prescribed to translate the test data from three-point bending to direct tension test.

Such procedures are detailed in chapter 4 of the ACI report and are listed in Eq. (3.1) through Eq. (3.12). To perform such analysis for all samples, a Matlab code was developed to analyze the data, develop the bi-linear curves and calculate the critical fracture energy. Those codes are attached in Appendix A. Equations 3 through 6 aim to determine an equivalent load due to self-weight and estimate the net plastic flexural strength. Using these values, the load-CMOD curves are corrected using least squares fitting prescribed in Eq. (3.5), (3.6) and (3.7). The results of the corrected curves are then used to resolve the plastic flexural strength and calculate the brittleness length shown in Eq. (3.8) and (3.9). Then the area under the curve (representing the work of fracture WF) is calculated in Eq. (3.10) using the CMOD axis intercept with slope of the initial softening curve calculated in Eq. (3.11), the tensile strength, the brittleness length and the corresponding displacement range. Then, the fracture energy (G_F) and the critical stress intensity factor (K_{Ic}) for the specific sample dimension is measured using Eq. (3.12) and (3.13). The ACI report estimates the tensile strength of concrete using an indirect tension test of split tension test. For this work, those values were obtained rather by a different indirect tension test namely flexural bending rather than using direct tension test results. Later once the fracture toughness parameters

are determined, Eq. (3.14) was used to ensure the validity of such analysis on PC. In that equation, the yield stress was assumed to be at 90% of the ultimate tensile strength. The yield stress and modulus of elasticity were determined from direct tension test.

$$P_0 = mg \left(1 - \frac{L}{2S} \right) \quad (3.1)$$

$$f_p = \frac{P_{\max} S}{2Bb^2} \quad (3.2)$$

$$C_i = \frac{\Delta(\text{CMOD})}{\Delta P'} \quad (3.3)$$

$$E = \frac{6Sa_0}{C_i BD^2} V_1(\alpha'_0) \quad (3.4)$$

where, $\alpha_0 = \frac{a_0+h}{D+h}$ and

$$V_1(\alpha) = 0.8 - 1.7\alpha + 2.4\alpha^2 + \frac{0.66}{(1-\alpha)^2} + \frac{4D}{S} (-0.04 - 0.58\alpha + 1.47\alpha^2 - 2.04\alpha^3)$$

$$X = \left(\frac{4D}{S} \right)^2 \left(\frac{1}{(w_M - w_{MA})^2} - \frac{1}{(w_{MR} - w_{MA})^2} \right) \quad (3.5)$$

$$P_1 = X(A + KX) \quad (3.6)$$

$$P_{1\max} = P'_{\max} + P_0 \quad (3.7)$$

$$f_{p1} = \frac{P_{1\max} S}{2Bb^2} \quad (3.8)$$

$$l_1 = \kappa D \left[\frac{11.2}{(x^2 - 1)^2} + \frac{2.365}{x^2} \right] \quad (3.9)$$

$$W_F = W_{Fm} + \frac{2A}{\delta_R + \delta_A} \quad (3.10)$$

$$w_1 = 1000 \frac{2f_t}{E} l_1 \quad (3.11)$$

$$G_F = 1000 \frac{W_F}{Bb} \quad (3.12)$$

$$K_{IC} = \sqrt{G_f E} \quad (3.13)$$

$$l \geq 2.5 \left(\frac{K_{IC}}{\sigma_y} \right)^2 \quad (3.14)$$

-Notation-

a_0 - Notch length (initial crack length)

A – Far-tail constant

b - Ligament length = D - a_0

B - Thickness of specimen

C_i - Initial compliance of beam specimen

CMOD - crack mouth opening displacement

D - Depth of specimen

E - Elastic modulus

f_t - Tensile strength

f_p - Net plastic flexural strength

g - Specific gravity = 9.81 m/s²

G_F - mean fracture energy.

h - Distance from the CMOD measuring line to the specimen surface
 K - Tail fitting parameter
 l_1 - Brittleness length
 L - Length of specimen
 m - Mass of the specimen
 N - Notch width
 P - Total load on specimen
 P_0 - Self-weight equivalent load
 P' - Measured load on specimen
 P_1 - Corrected load on specimen
 P'_{\max} - Effective peak load on a specimen
 r - Distance from the measuring line of the displacement extensometers to the center plane of the specimen
 S - Span of the test specimen
 w_1 - Horizontal intercept of the linear initial portion of the softening curve
 w_{MA} - CMOD at zero P_1
 w_{MR} - CMOD at the end of the test
 W_F - total work of fracture
 X - Auxiliary variable for far tail fitting
 α_0 - Relative notch length = a_0/D
 δ_A - Load point displacement at zero P_1
 δ_R - Load point displacement at the end of test
 $\kappa = 1 - \alpha_0^{1.7}$

3.5.2 Quasi-brittle fracture mechanics (QBFM) analysis: Effective crack modulus method

Results of LEFM analysis showed that the limits described in Eq. (3.14) were not met as will be discussed later. Also, both load-CMOD and stress-strain curves obtained for all PC mixes demonstrated significant nonlinearity. PC is highly ductile type of concrete with high deformations in tension, bending and fracture. Therefore, a quasi-brittle approach was selected to better reflect the energy consumption mechanisms. Quasi-brittle materials are described as those materials capable of exhibiting moderate strain hardening prior to attaining ultimate stress or with materials exhibiting significant softening post peak stress. As discussed earlier, quasi-brittle materials fracture energy is distributed between energy consumed elastically and energy consumed in the fracture process zone (FPZ). The elastic energy is often characterized then by energy required to create new surfaces as the crack propagate through the material. For the crack to extend, however, the cohesive energy of the material must be overcome. The area ahead of the crack tip designated as the FPZ often exhibit elevated stress condition as have been proven first by Westergaard 1939 and later by many scholars and shown in Figure 3.13. Thus, an extended amount of energy is consumed in the FPZ which in quasi-brittle material can be very comparable to elastic energies. Specifically, Shah et al. showed that concrete materials often consume fracture energy through crack branching, micro cracking and crack deflection (*Shah et al. 1995*). Hence, QBFM is more suitable to capture PC fracture toughness and the effect of incorporating nanomaterials into PC.

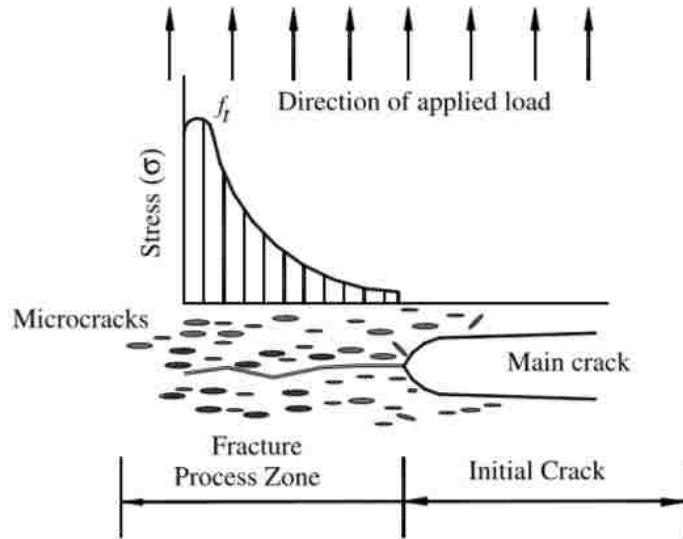


Figure 3.13: Model of Quasi-Brittle Fracture materials showing the increase in stress due to the fracture process zone (Shah et al. 1995).

The first QBFM approach is based on the effective elastic crack model. This model is based on the two-parameter fracture model suggested by Jenq and Shah (*Jeng and Shah 1985*). In their model, the fracture toughness is characterized by two critical parameters, critical stress intensity factor (K_{Ic}) and critical crack tip opening displacement ($CTOD_c$). An effective elastic crack length is estimated through the secant compliance of the elastic part of the unloading load-CTOD curve. Using the effective crack, similar analysis of that of LEFM can be performed to measure the fracture release energy (G_I) or the stress intensity factor (K_I). Karihaloo and Nallathambi proposed using this model to determine the fracture toughness of concrete using three-point bending (*Karihaloo and Nallathambi 1990*). However, their approach depended on obtaining the secant compliance at the maximum load to obtain the effective elastic crack length. The secant compliance in this approach is obtained by connecting the maximum load to the origin of the load-deflection curve as shown in Figure 3.14. The maximum load corresponds then to the critical effective crack length in which K_{Ic} is calculated using LEFM. Reda Taha et al. proposed a closed-loop approach analyzing four-point bending of notched concrete beams to obtain the critical

effective crack length as show in Figure 3.15 (*Reda Taha et al. 2002*). In their model, the secant modulus is obtained by setting the elastic modulus at the elastic limit to be equal to that at the peak stress. The elastic modulus in both cases is estimated using the deflection of the beam caused by cracking, shear along with the elastic deflection.

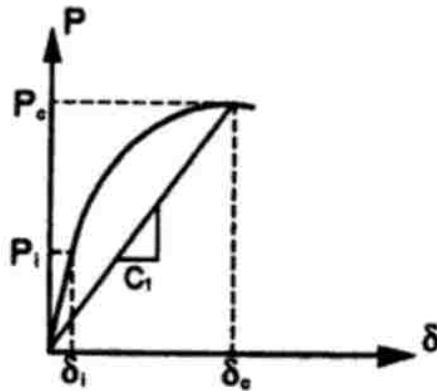


Figure 3.14: The secant compliance approach describing the effective elastic modulus fracture mechanics method (*Shah 1983*).

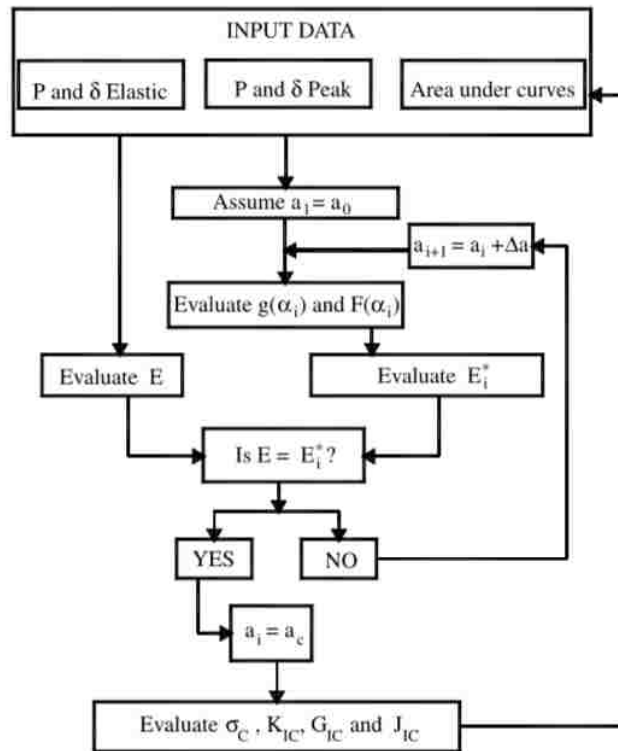


Figure 3.15: QBFM analysis for-loop using the effective crack modulus (*Reda Taha et al. 2002*)

The approach used by Reda Taha et al. was modified to account for fracture toughness testing using three-point bending (*Reda Taha et al. 2002*). Furthermore, a Matlab code was developed to carry the closed loop approach showed in Figure 3.15. Eq. (3.15) to Eq. (3.26) are used in this analysis and the Matlab code is attached in appendix A. Finally, since different nanomaterials will impact different fracture toughness parameters differently a total fracture toughness energy parameter (T_{Ic}) was used in which it combined the elastic energy as well as the energy consumed in the fracture process zone.

$$K_{Ic} = g_1(\alpha)\sigma_c\sqrt{\pi a_c} \quad (3.15)$$

$$G_{Ic} = \frac{K_{Ic}^2 (1 - \nu^2)}{E_{UN}} \quad (3.16)$$

$$J_{Ic} = \frac{2}{H_c b} (A_N - A_{UN}) \quad (3.17)$$

$$E_{elastic} = \frac{1}{bd\delta_e} \left(\frac{13wl^4}{32d^2} + \frac{3P_e l^3}{4d^2} + \frac{3(1+\nu)P_e l}{4} + \frac{9P_e l^2}{2d} F(\alpha_i) \right) \quad (3.18)$$

$$E_{critical} = \frac{1}{bd\delta_c} \left(\frac{13wl^4}{32d^2} + \frac{3P_c l^3}{4d^2} + \frac{3(1+\nu)P_c l}{4} + \frac{9P_c l^2}{2d} F(\alpha_c) \right) \quad (3.19)$$

$$g_1(\alpha) = 1.122 - 1.4\alpha + 7.33\alpha^2 - 13.08\alpha^3 + 14\alpha^4 \quad (3.20)$$

$$g(\alpha) = g_1(\alpha)\sqrt{\pi} \quad (3.21)$$

$$F(\alpha_x) = \int_0^{\alpha_x} \alpha g(\alpha)^2 d\alpha \quad (3.22)$$

$$H_c = d - a_c \quad (3.23)$$

$$A_N = \sum_{i=0}^{n_p} \frac{(\Delta_{i+1} - \Delta_i)(P_{i+1} + P_i)}{2}; n_p = \frac{P_c}{N_c} \quad (3.24)$$

$$A_{UN} = \sum_{i=0}^{n_p} \frac{(\Delta_{i+1} - \Delta_i)(P_{i+1} + P_i)}{2} ; n_p = \frac{P_c}{N_c} \quad (3.25)$$

$$T_{Ic} = G_{Ic} + J_{Ic} \quad (3.26)$$

-Notation-

a - crack depth.

a_c - critical crack depth.

A_N - area under the load-displacement of notched specimen up to the peak load of that specimen.

A_{UN} - area under the load-displacement of unnotched specimen up to the peak load of similar notched specimen.

b - specimen's width.

d - specimen's depth.

$E_{elastic}$ - plane strain elastic modulus of notched specimen.

$E_{critical}$ - plane strain elastic modulus of an imaginary beam including effective elastic crack.

E_{UN} - elastic modulus of uncracked sample.

$g1(\alpha)$ - geometric correction factor.

G_{Ic} - critical energy release rate.

H_c - critical ligament length.

J_{Ic} - critical J-integral.

K_{Ic} - critical stress intensity factor.

l - span length between supports.

N_c - number of steps up to peak load of notched specimen.

P_e - load at the elastic limit of notched specimen.

P_c - peak load of notched specimen.

P_i - load at given time step.

T_{Ic} - total critical energy release rate.

w - self-weight of the specimen.

α - notch to depth ratio.

α_i - initial notch to depth ratio.

α_c - critical notch to depth ratio.

δ_e - displacement at the elastic limit of notched specimen.

δ_c - displacement at peak load of notched specimen.

Δ_i - displacement at given time step.

σ_c - critical stress of notched prism.

ν - Poisson's ratio = 0.35.

3.5.3 Quasi-static fracture mechanics: Work-of-fracture (Factionous crack model)

This method of analysis utilizes the cohesive crack model (also called factionous crack model) similarly to that mentioned in 3.6.2. This model was first proposed by Hillerborg (1976) in which cracking is assumed to be characterized by two regions: true (physical) crack and factionous crack (fracture process zone). The true crack is assigned to that part of cracking where complete surface separation is established, CMOD is relatively constant, and both stress and displacement are discontinuous. The factionous crack represents the region inside the true crack where crack initiation occurs and the peak stress reaches the tensile strength. This method of analysis measures the absorbed energy when breaking the specimen in half by measuring the area under the load-CMOD curves normalized by the fracture area as shown in Eq. (3.27). The area is measured by

Riemann sum method and is later presented as an equivalent stress intensity factor using Eq. (3.28). While this method seems attractive to many scholars due to its simplicity and ease of application. It has been shown to have limited applicability specifically when plastic-frictional processes occur. Also, this method is based on time-independent fracture mechanics and ignores the loading and unloading compliances (*Bazant 1996, Bazant 2002, Wecharatana and Shah 1983*). In this work, this method of analysis is depicted to emphasize using total energy release rate parameter (T_{Ic}) proposed in 3.6.2. As this method of analysis exclude the specimen's compliance, the variation in nanomaterials effects on crack arrest, matrix stiffness, tensile strength, bond, and crosslinking are hard to isolate.

$$G_f = \frac{A}{b(d-a)} \quad (3.27)$$

$$K_{Ic} = \sqrt{\frac{G_f E}{1 - \nu^2}} \quad (3.28)$$

-Notation-

A - area under load-CMOD curve.

a - crack depth.

b - specimen's width.

d - specimen's depth.

G_f - fracture energy

E - elastic modulus of specimen

K_{Ic} - critical stress intensity factor

ν - Poisson's ratio = 0.35.

3.6 Fatigue test

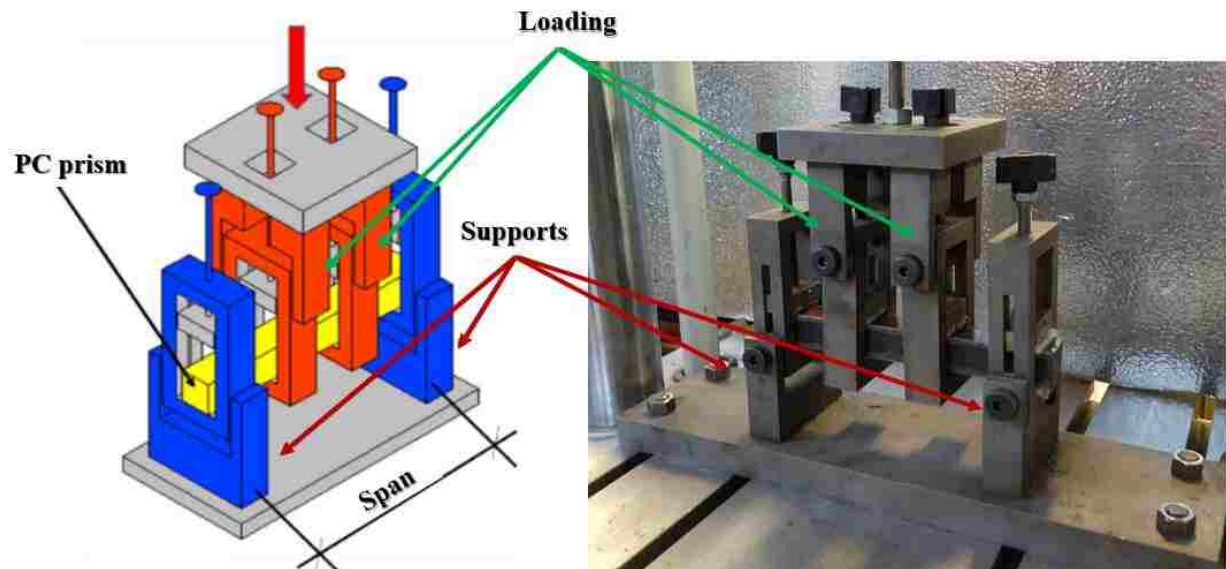


Figure 3.16: Fatigue test setup schematics and actual.

Fatigue life of PC samples with and without nanomaterials have been examined using four-point bending setup. There is no standard fatigue test for concrete because of the difficulty in conducting fatigue tests on concrete with repeatable results. Therefore, a modified four-point bending setup borrowed from AASHTO T321-07 used for fatigue testing of asphalt overlays was used as shown in Figure 3.16. Fatigue tests incorporate several parameters such as stress range, amplitude, mean, ratio and frequency. The stress range (σ_{range}) describes the difference between the maximum and minimum applied stresses ($\sigma_{\text{range}} = \sigma_{\text{max}} - \sigma_{\text{min}}$). The stress amplitude (σ_a) is the amount of stress deviation from the mean stress (σ_{mean}) which is the average of the maximum and minimum stress. The stress ratio (R) is defined by the ratio of the maximum to the minimum stress ($R = \sigma_{\text{max}} / \sigma_{\text{min}}$) and the frequency is the number of load cycles per second). Furthermore, the load can be controlled through displacement or force to generate the test parameters. PC's due to its high ductility and deformability result in substantial challenges in conducting the fatigue/service life test. Those challenges are discussed below.

Typically, samples in fatigue test are loaded to 40% - 80% of their flexural capacity. Materials described in the design codes and other peer reviewed work often have displacements at failure of 1 – 3 mm. PC on the other hand can reach displacement at failure up to 20 mm as will be discussed. Therefore, loading PC by 40% – 80% of its capacity result in large and significantly high deformation ranges. For example, a concrete sample loaded to 60% of its capacity is loaded between 0.2 and 0.4 mm. To maintain similar load parameters, PC prisms will be loaded between 10 and 16 mm. The large range of deformation (6 mm compared to 0.2 mm) along with high frequency can shift loading from quasi-static to dynamic. This result in shifting the test parameters from quasi-static fatigue life to dynamic impact strength. The predicted life of PC and PCNC will be severely minimized and the effect of nanomaterials cannot be established accurately.

While previously discussed limitations are associated only with displacement control tests, switching to force/load control test result in other limitations. When PC samples are loaded using specified force range, the sample will foresee pure tension at the same side. However, the sample viscoelastic effect start to relax the sample to its current deformed shape. For example, a neat SPC specimen that is loaded between 400 and 600 N will report a displacement of 6 and 10 mm respectively. However, the viscoelastic effect relaxing the PC prism will result in decreasing the stress achieved at the specified displacements of 6 and 10 mm. Therefore, the displacement of the PC must increase to induce maintain the applied load. PC prism will then foresee increased deformation that can shift the range of 6 – 10 mm to 10 – 15 mm. The increase in curvature result in an increase in stress. Hence, the use of force control result in inconsistent stress loads of PC prisms that depend on PC's stiffness and crosslinking density. Both parameters are affected differently by different nanomaterials at different contents. Thus, such effect is not kept constant when comparing all samples.

It's also important to consider the elastic strain recovery of PC when examining the loading frequency. Concrete and plastics often exhibit most of their deformations elastically with rapid elastic strain recovery. That is, when a concrete/plastic beam is loaded within their elastic limit and the load is suddenly removed, the sample return to its original undeformed shape immediately. PC on the other hand exhibit significant viscoelastic effects, high deformability and slow elastic strain recovery. When PC specimen is loaded in flexure and the load is removed, the sample will return slowly to its original undeformed shape. Because PC sustain high deformations, this process can take significantly longer than the fatigue loading frequency. ASTM and AASHTO codes generally describe 5 – 10 Hz to be ideal to simulate bridge live loadings. For a concrete beam loaded between 40% - 60% of its capacity, the sample will maintain tensile stresses on the top side of the prism. On the other hand, since a PC prism under similar stress conditions cannot return to its undeformed shape immediately, compressive stress is needed to bend the prism from its deformed shape at 60% to that at 40% of flexural capacity. This result in increasing the overall tension state within PC prism as tension will be generated at the top of the specimen loading from 40% to 60% and at the bottom when loading shifts from 60% to 40%. Thus, introducing significant errors within fatigue life testing that can significantly shorten the expected life due to testing errors.

Several challenges persist in fatigue testing of PC as discussed earlier such as loading frequency and limitation on force and displacement control loading. Many of the previously discussed limitations can be minimized by decreasing the loading frequency. However, low frequency loading can result in significantly prolonging the test duration. For example, using 0.01 Hz for a sample that withstand 10,000 loading cycle requires 278 hours (~ 12 days) for each sample and total of 60 days to test five samples (enough for statistical significance). Extended testing schemes require considering the change in mechanical properties induced by improved curing age.

Furthermore, the service life of PC is expected to increase with nanomaterials which significantly increase the testing time requirements.

Due to previously discussed limitations, the number of mixes examining fatigue life of PC have been minimized to the best performing MWCNTs and ANPs content. Loading frequency was selected at 0.25 Hz with sampling rate of 2.5 Hz with displacement control loading of 1 mm and 2 mm. SPC-Neat samples were tested in four-point flexure at an equivalent load rate to determine the stress level induced based on flexural capacity. The displacement limits were selected to minimize the effect of the loading frame, viscoelastic properties and elastic strain recovery of PC. The fatigue life was determined by measuring the number of cycles required for samples to reach 50% of the 50th cycle flexural stiffness calculated in Eq. (3.29) where k_n is the stiffness at cycle n , P_{max_n} and P_{min_n} are the maximum and minimum load at cycle n .

$$k_n = P_{max_n} - P_{min_n} \quad (3.29)$$

3.7 Structural Health Monitoring in Flexure

Structural health monitoring (SHM) was performed through continuous recording of electrical conductivity of a PC prism subject to loading. This method of SHM depends on continuous collection of electrical resistivity of the material over time. Applied stresses induce damage and cracking creating deficiencies in the material's conductivity. The decrease in conductivity is then classified by an increase in resistivity which is collected using a 2-channel Keithley 2636B source meter SMU instrument. PC in general have a very low conductivity of 8.0×10^{-9} S/m and can be classified as an insulator material. Its electrical conductivity in fact is low enough to be comparable to that of glass at 1×10^{-11} S/m. Changes in resistivity induced by damage

and cracking therefore are too small to be captured and classified. MWCNTs on the other hand are relatively good conductors as their conductivity is often greater than 1×10^2 S/m. Incorporating MWCNTs to PC therefore improve the electrical conductivity of PC prisms enabling SHM through electrical resistivity monitoring. The functionalization of MWCNTs result in embedment of the nanotubes within the host matrix isolating them. Thus, COOH-MWCNTs are unable to improve the electrical conductivity of PC. On the other hand, SNPs and ANPs are isolating materials that when dispersed in PC and polymers reduce their electrical conductivity. Therefore, SHM of PC prisms are only valid using P-MWCNTs.

SHM of PC prims is specifically critical to bridge deck overlays which are subjected to cyclic loading. Therefore, this investigation was limited to Siloxane PC (SPC) mixes. As an initial investigation, PC prims were loaded in flexure and monitored using the source meter. Prisms were loaded in four-point bending frame like that used in fatigue test. This method of loading eases SHM over three-point bending as damage and cracking are controlled over longer portion of the prim. The electrical resistivity collection points are then placed to sandwich that area as shown in Figure 3.17. The frame supports were isolated using double edge tape and $\frac{1}{4}$ in thick plastic caps to prevent any interference with monitoring. The collection points were created by wrapping a highly conductive copper wiring and then coating it with silver paint. The location of the collection points was selected to capture resistivity changes over the complete cross-section of the prims enabling accurate SHM of PC prisms. Photo of the actual PC prim along with the source meter is shown in Figure 3.18.

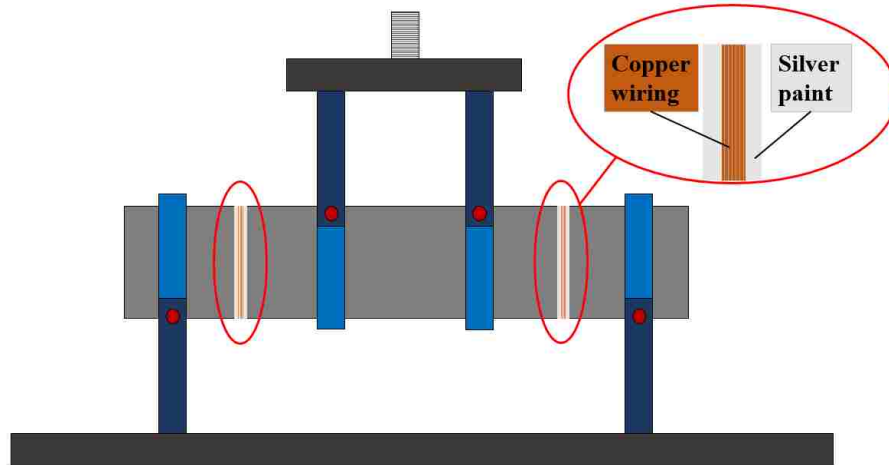


Figure 3.17: PC samples in four-point bending setup showing electrical conductivity measurement points.



Figure 3.18: In-situ fatigue test showing the loading frame and the source meter connected to measure change in electrical resistance to monitor fatigue damage evolution in PC.

3.8 Slant Shear Test

The use of oil wells as reservoirs for toxic fluids such as methane, carbon dioxide and many others have been the recent focus of many industries and researchers. Such efforts focus on constructing new oil wells or repair abandoned ones with novel materials able to withstand high chemical exposure, geotechnical stresses, and fluid and gas stresses while maintaining seal integrity. In general, oil wells are built by drilling a specific size hole (borehole) into the earth and

then inserting sections of steel pipe (casing) with a smaller diameter. The space between the borehole and the casing is then filled with concrete materials (annulus). Type-G cement which contains clinker is often used for such applications as it provides high sulfate resistance, pumpability and impermeability. However, cracking of the annulus originated by shrinkage and increased by geomechanical stresses is inevitable. Thus, repairs of wellbores cracks between the annulus and steel casing are critical to ensure the seal integrity. PC and PCNC not only offer high potential for repairs but also serve as a promising alternative to Type-G cement concreting of the annulus. Repair material and the annulus are often subjected to shear stresses deteriorating the bond with the casing. Bond strength of repair materials is often examined through pull-off, twist off, flexure and slant shear tests. Of those tests, slant shear test is the best suitable to examine the bond strength of inclined or vertical surfaces rather than horizontal.

Novolac PC (NPC) mixes incorporating nanomaterials were suggested as such novel material as Novolac polymers provides high chemical resistance, permeability and pumpability. Slant shear tests were performed in accordance to ASTM C882/C882M (2013). PC/PCNC slurry was cast on top of a steel part inclined at 60° with the horizontal and sandblasted to a minimum of 5.0 mil (0.1016mm) clean. Each sample was casted in two layers each compacted 25 times. Five samples were tested per mix to ensure statistical significance as required by the ASTM standard. All samples were cured at room temperature for 7 days then loaded in compression at 0.1 in/min using Instron universal testing machine (UTM). Figure 3.19 shows the schematic of slant shear sample as well as a PC/steel sample. The vertical alignment of PC with the steel part was inspected with microscope prior to testing to ensure no initial slippage, displacement or dislocations are present on the interface as shown in Figure 3.20.

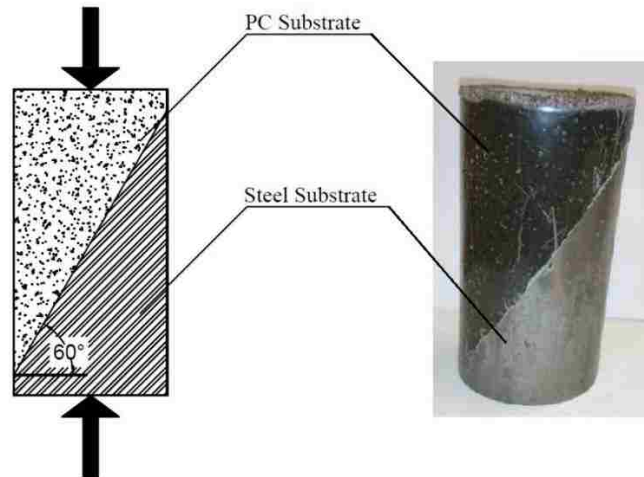


Figure 3.19: Slant shear sample and its schematics.

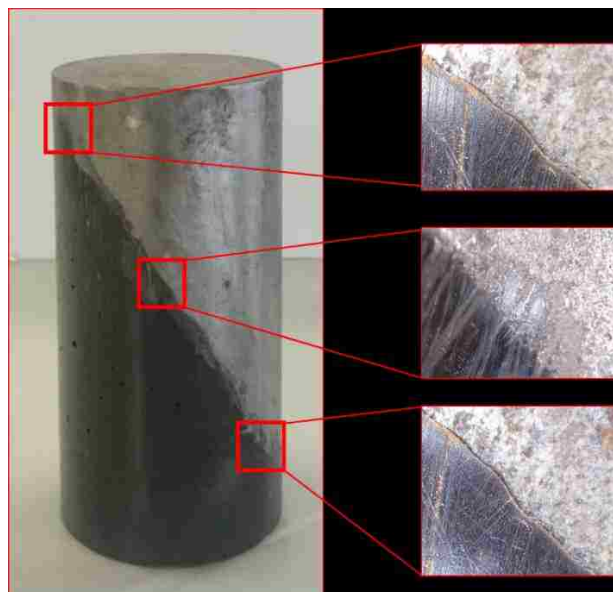


Figure 3.20: Vertical alignment using high resolution camera of PC and steel prior to testing.

The stress calculation to evaluate material's bond strength often follows the ASTM standards. That is, the bond strength is obtained by dividing the maximum vertical load over the slanted area of contact leading to what is denoted here as the apparent bond strength as shown in Eq. (3.30). However, as two different materials can be tested as the different parts of the slant shear, stiffness mismatch at the interface exist. This often leads to elevated stress states that are not accounted for by the ASTM. This is further discussed with the results in section 4.10 and 4.11 of this thesis.

$$\text{Apparent shear} = \tau_a = \frac{P \sin(60)}{A / \cos(60)} = \frac{P}{A} \sin(60) \cos(60) \quad (3.30)$$

where P is the applied force acting in the interface and A is the interface area

3.9 Static Elastic Properties

Compressive strength of all NPC materials was done in accordance to ASTM C39/C39M (2016) using 2 in. diameter and 4 in. high cylinders. Five samples at 7 days were tested for each mix to ensure statistical significance. When preparing specimen, each was filled in two layers each compacted 25 times. Furthermore, strain gauges were used to record both vertical and horizontal strains of selected NPC mixes namely NPC-CNT-C0.5, NPC-ANPS-0.5, NPC-ANPS-2.0, NPC-SNP-0.5, NPC-SNP-2.0 and NPC-Neat. The strain values were used to measure the modulus of elasticity and Poisson's ratio per ASTM C469/C469M (2014). Two vertical and two horizontal strain gauges were utilized on opposite surfaces to provide those readings. Figure 3.21 shows a compression sample with schematics of the strain gauges. The strain gauges used are 0.5 in. gauge length, and 0.18 wide with strain range of $\pm 5\%$ with linear pattern. Young's modulus and Poisson's ratio were extracted from the measured stress-strain curves using Eq. (3.31) and (3.32).

$$\text{Modulus of Elasticity} = E = \frac{\text{Stress}}{\text{Strain}} = \frac{\sigma_{40} - \sigma_{0.0005}}{\varepsilon_{40} - 0.0005} \quad (3.31)$$

$$\text{Poisson's ratio} = \rho = \frac{\text{Vertical strain}}{\text{Horizontal strain}} = \frac{(\varepsilon_{y_{40}} - \varepsilon_{y_{0.0005}})}{(\varepsilon_{40} - 0.0005)} \quad (3.32)$$

Where, σ_{40} : Stress corresponding to 40% of ultimate stress

ε_{40} : Longitudinal strain corresponding to σ_{40}

$\sigma_{0.0005}$: Stress corresponding to longitudinal strain of 0.0005

$\varepsilon_{y_{40}}$: Transverse strain corresponding to σ_{40}

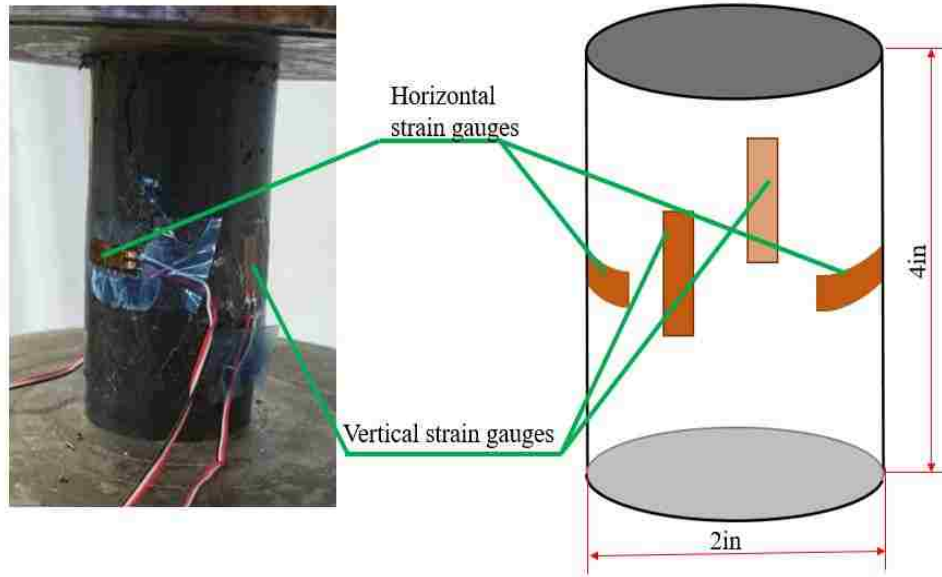


Figure 3.21: Compression sample with its schematics showing locations of all strain gauges

3.10 Scanning Electron Microscope (SEM)

As mentioned previously, one of the major challenges associated with nanomaterials inclusion is the difficulty in obtaining uniform dispersion. The method of magnetic steering and ultrasonication were utilized at elevated resin temperature to disperse all nanomaterials. Increased content of nanomaterials results in increased difficulties in dispersion and can jeopardize particle suspension. To investigate the effectiveness of the applied dispersion method, samples containing the highest content (2.0 wt.%) of each of the nanomaterials investigated were scanned using SEM. This investigation was limited to Siloxane polymer system samples as Siloxane has increased viscosity over Novolac which is more challenging in dispersion. Thus, by confirming proper dispersion of Siloxane samples at the highest content, samples containing lower nanomaterials content or Novolac polymer system are guaranteed to provide uniform dispersion and good particle suspension since the shear dispersion energy is kept constant.

Scans of neat epoxy (S-Neat) samples were also collected to provide a reference for this investigation. All samples were of hardened epoxy with no filler since the aggregates are only added after dispersion is complete. The microscope used is Hitachi S-5200 Nano SEM capable of magnification in the range of 100 – 2 million times which is shown in Figure 3.22. Scanning resolution is 1.7 nm at 1kV and 0.5 nm at 30kV. The samples were cut using steel blade to expose the inner layer of the epoxy rather than examine the surface. Samples were coated with gold prior to scanning in order to eliminate associated polymer discharging effects. Scans were collected at 5.0 kV and 10.0 kV as appropriate at various locations.



Figure 3.22: Hitachi S-5200 Nano scanning electron microscope (SEM).

3.11 Fourier Transform Infrared Spectrogram (FTIR)

To better understand the chemical effects induced by incorporating nanomaterials at different contents, Fourier transform infrared spectrogram (FTIR) was performed. This test is aimed to identify the presence of functional groups in a molecule by measuring collected absorbed bands. In general, a radiation source generates light across all spectrum that passes through the sample. Because of the sample's specific spectrum, specific wavelengths are decreased. All spectrum wavelengths are then collected and recorded as intensity vs time information. Fourier

transform is then applied to convert raw data including time to intensity vs frequency spectrum. A reference spectrum is then applied using a superimposed laser beam in order to correct for the baseline and correct for the sample's limitation. To perform this test, a horizontal Attenuated Total Reflectance (ATR) and a DiComp Crystal made of a diamond ATR with Zinc Selenide focusing element were used to collect 4000 scans at a resolution of 1 cm^{-1} . The samples had an area of 25.4 mm^2 and were 1 mm thick with no aggregate filler. Scans of the FTIR were analyzed using PerkinElmer FTIR with Universal ATR accessory as shown in Figure 3.23. All scans were then converted to absorbance using Kramers-Kronig equations (*Griffiths 2007*).



Figure 3.23: PerkinElmer FTIR machine used in microstructural analysis.

3.12 Dynamic Modulus Analyzer (DMA)

To study the viscoelastic behavior of the polymer resins, dynamic modulus analysis (DMA) was performed using DMA Q800 from TA Instruments shown in Figure 3.24a. This test applies sinusoidal stresses to the material being measured to determine the complex modulus. Three-point bending and direct tension tests were conducted to assert different mixes' glass transition

temperature, epoxy's elastic modulus, storage modulus and to later evaluate the crosslinking density. The crosslinking density is the number of moles of network chains per unit volume that can be estimated using the theory of rubbery modulus (*Thirukumaran 2015, Hill 1996*). All tests were conducted at 1 Hz and all temperature ramps were given at 3°C/min up with 0.15 microstrain. The glass transition temperature (T_g) was determined using tan-delta peak approach while the rubbery modulus of the samples was determined at 50°C above T_g from the flexural loss modulus. Direct tension of epoxy samples was conducted at controlled room temperature of 24°C. Eq. (3.33) was used to determine the crosslinking density where ν_e is crosslink density, E' is the tensile storage modulus in the rubbery plateau, T is the temperature in Kelvins, R is the gas constant taken as 8.3145 J/(K mol). The samples' dimension for three-point bending was 20 mm x 12 mm x 3 mm while the sample for tension was 25 mm x 4 mm x 1 mm which are shown in Figure 3.24b.

$$\nu_e = \frac{E'}{3RT} \quad (3.33)$$

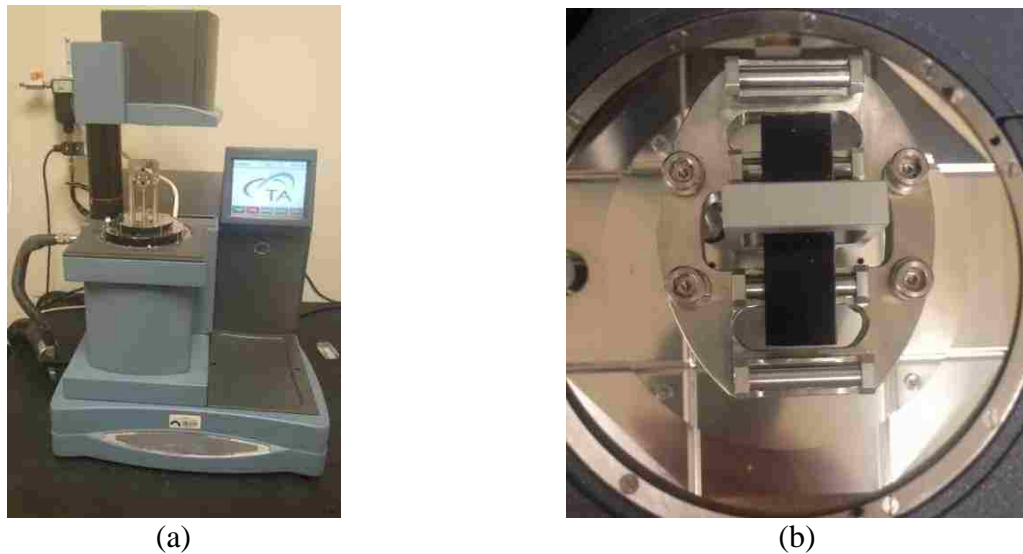


Figure 3.24: The DMA machine showing (a) the instrument and (b) Epoxy sample with P-MWCNTs placed in three-point bending clamp.

3.13 Finite Element Analysis in ABAQUS

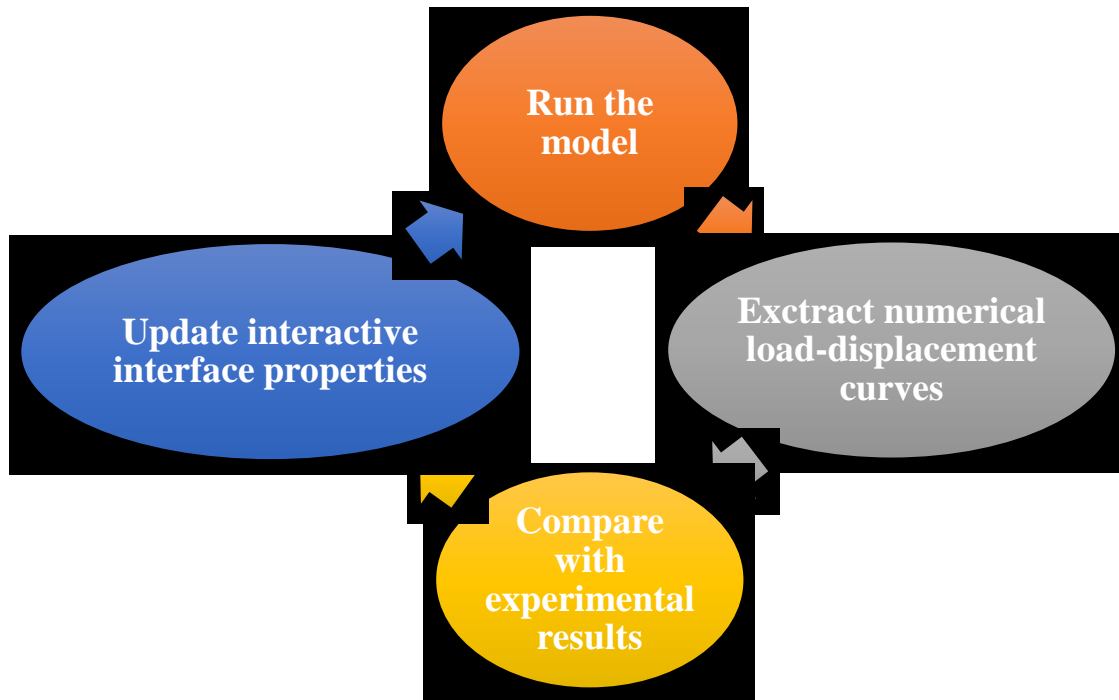


Figure 3.25: Back-solving procedure in ABAQUS to estimate the interface properties

The applications investigated in this work depend greatly upon the bond strength of PC to its substrate. As discussed previously, the slant shear test does not consider the stiffness mismatch between both tested substrates. This effect was further investigated using FEA utilizing ABAQUS 6.14. In this analysis, the interface interaction parameters were defined with respect to pure in-plane shear contact interface defined by damage and cohesive behavior interactions (ABAQUS, 2015). Load-displacement curves were extracted from the simulations and the interface interaction properties were back-solved by matching the experimental results to the extracted curves. This procedure is explained in Figure 3.25

To perform such simulations, PC was defined as a nonlinear elastic-plastic material using the constitutive stress-strain response measured in the uniaxial compression tests. The steel was assumed to be elastic perfectly plastic material. The model was meshed using two types of

elements: 8-node linear hexagonal and 6-node linear tetrahedral as shown in Figure 3.26. These element types can produce computationally inexpensive solutions for stress calculations without generating stress singularities. Mesh sensitivity analysis was performed on NPC-Neat for both element types varying the mesh size from 9,480 elements to 74,524 elements. Results of the mesh sensitivity analysis are shown in Figure 3.27.

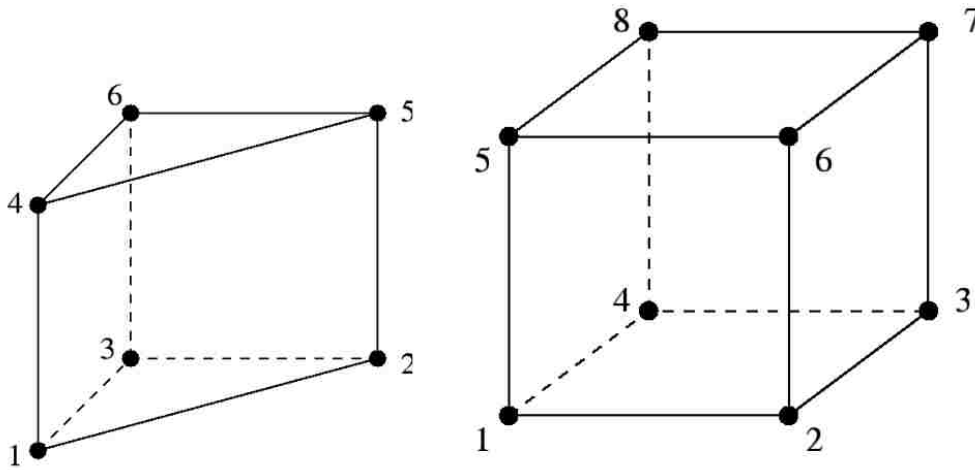


Figure 3.26: 6-node tetrahedral and 8-node hexagonal elements used in ABAQUS simulations

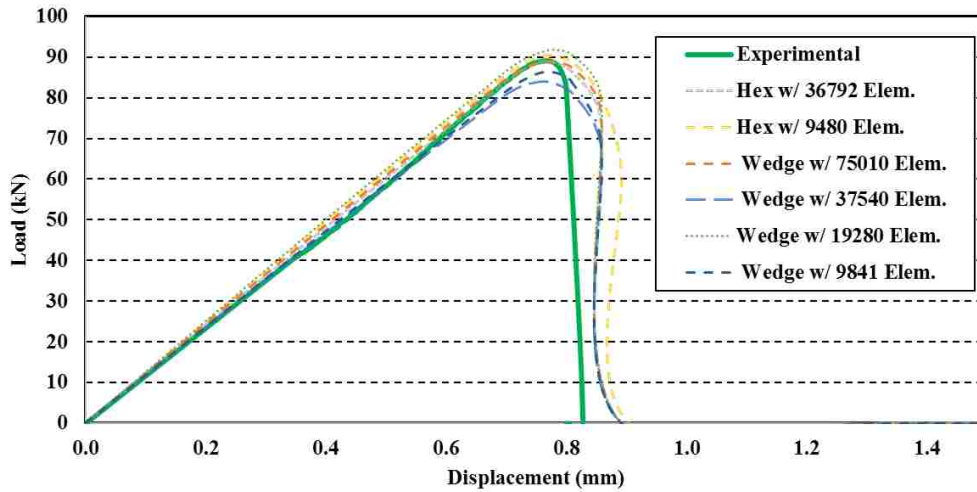


Figure 3.27: Mesh sensitivity analysis performed on NPC-Neat model

The interface between PC and steel was defined using a zero-thickness cohesive contact element based on the bilinear shear-slip relationship shown in Figure 3.28 (b). Boundary

conditions fixed the steel part from the bottom and prevented lateral deformation of the assembly. Displacement was applied to the top of PC to simulate slant shear test loading mechanism. Applied boundary conditions are shown in Figure 3.28 (a) while the final model meshed using 6-node linear tetrahedral elements are shown in Figure 3.28 (c).

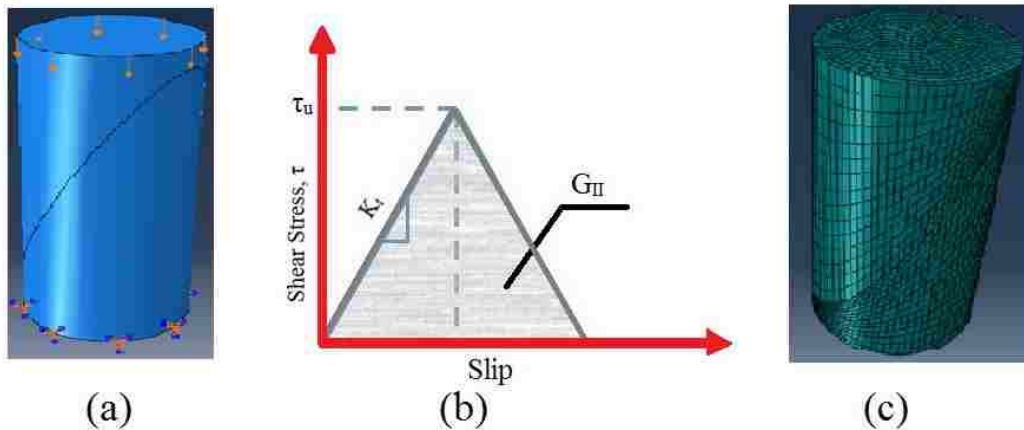


Figure 3.28: FE model using ABAQUS simulation environment: (a) Boundary conditions (b) Bilinear shear stress-slip relation (c) Meshed model using 74,524 elements.

The cohesive behavior element characterizes the initial slope of the stress-slip curve (K_I) which is governed by the interfacial stiffness between the two test parts. The damage element on the other hand is prescribed using three components; initiation, evolution and stabilization. Firstly, damage initiation represents that maximum nominal stress (τ_{II}) characterized by the peak of the stress-slip curve. Secondly, damage evolution in this model was used based on the critical energy release rate in mode II (G_{II}) which denotes the area under the stress-slip curve. Finally, damage stabilization represents the energy dissipation module and is governed by the viscosity coefficient (V). In general, lower values of V signify rapid energy release and since failure in slant shear test is sudden, a constant low value of 0.001 was selected for all models. Since the bond strength of PC to steel substrates is solely defined by those parameters, a sensitivity analysis of damage and cohesive behavior variables were examined on NPC-Neat model. The results achieved and discussed later in Chapter 5 are used here in this analysis in which it was found that the best

matching interfacial properties are defined by $\tau = 43$ MPa, $G_{II} = 19$ N/mm and $K_t = 56$ MPa/mm. The sensitivity analysis is performed to ensure that the selected values would fall within numerical solution boundaries (noise) as described for similar back-solving methods (Abdel Wahab 2014).

3.12.1 Shear stress (τ_u) sensitivity analysis

Load-displacement curves of this analysis are shown in Figure 3.29 where it's determined that $\tau = 43$ MPa provide the best fitting behavior. Given all other parameters fixed, increasing the shear values is viable up to a maximum $\tau = 45$ MPa. Higher shear values result in divergent model whereas either the stiffness need to be minimized or the shear energy need to be maximized to maintain convergence. On the other hand, decreasing the peak shear stress results in slower release of energy and gradual slip. Hence, lower values of peak shear stress are not valid as they do not simulate the experimental behavior as depicted in Figure 3.29. Therefore, it can be concluded that the present peak shear value ($\tau = 43$ MPa) is within numerical boundaries of the unique solution and be used to simulate experimental data.

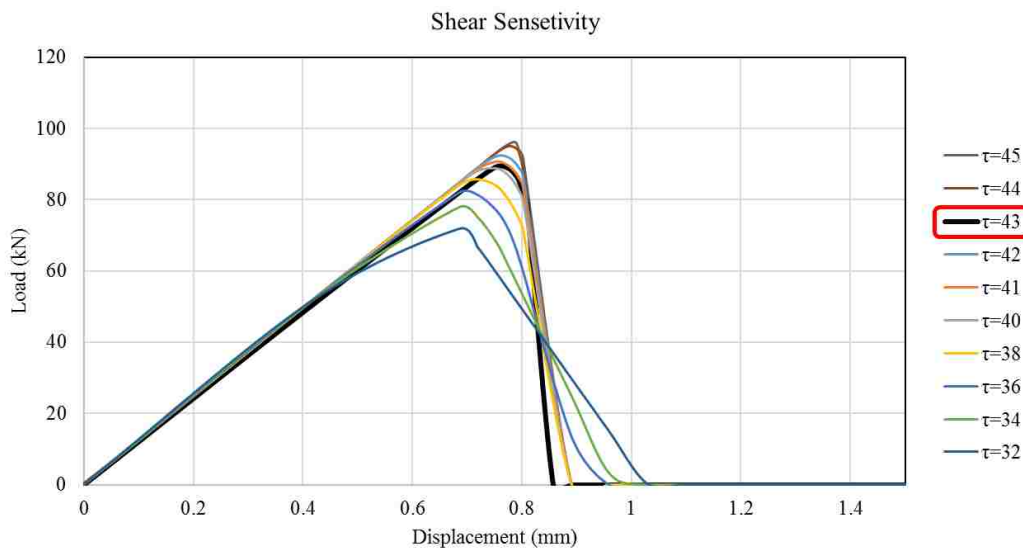


Figure 3.29: Load-displacement curves of maximum shear sensitivity analysis in ABAQUS

3.12.2 Critical Energy (G_{II}) sensitivity analysis

Similar analysis to that presented above was carried over the critical energy release rate in shear mode fracture (G_{II}). The resulting load-displacement curves are presented in Figure 3.30. It's evident that changing G_{II} values result in change in the peak shear stress as well as post peak energy release rate. Given the interfacial stiffness and peak shear stress, high values of G_{II} result in gradual slip and gradual release of energy which does not comply with experimental findings. Hence, a value of $G_{II} < 24$ N/mm was required to achieve sudden slippage and rapid release of energy for this specific model. Of the values investigated, $G_{II}=19$ N/mm was selected as it falls within numerical noise of simulations and matches well with the experimental data. Nonetheless, it's clear that a unique G_{II} value exist that allows ABAQUS simulations to comply with experimental findings.

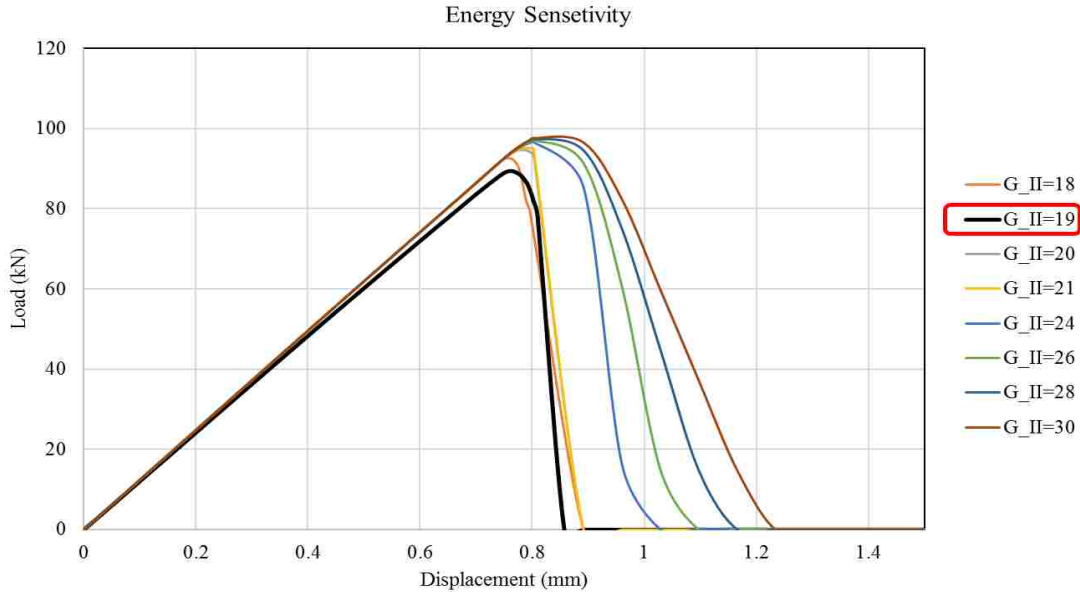


Figure 3.30: Load-displacement curves of critical energy sensitivity analysis in ABAQUS.

3.12.3 Interfacial stiffness (K_t) sensitivity analysis

The sensitivity of ABAQUS modeling to interfacial stiffness K_t was carried as well and is shown in Figure 3.31. Interfacial stiffness impacts the energy release rate of the model for given peak shear stress (τ) and critical energy release rate (G_{II}). Hence, higher values of K_t results in gradual slippage and slower release of energy post peak stress. While in shear-slip behavior both G_{II} and τ are dependent upon all parameters in this relationship, the interfacial stiffness is not affected by the change of those parameters given a converging solution. Therefore, matching this parameter to the experimental data was done first. It's also important to note that decreasing K_t to very low values result in singularities at peak load as the one observed for $K_t=50$ MPa/mm. Hence, such simulations are invalid representation of the experimental and ca not be used in data validation.

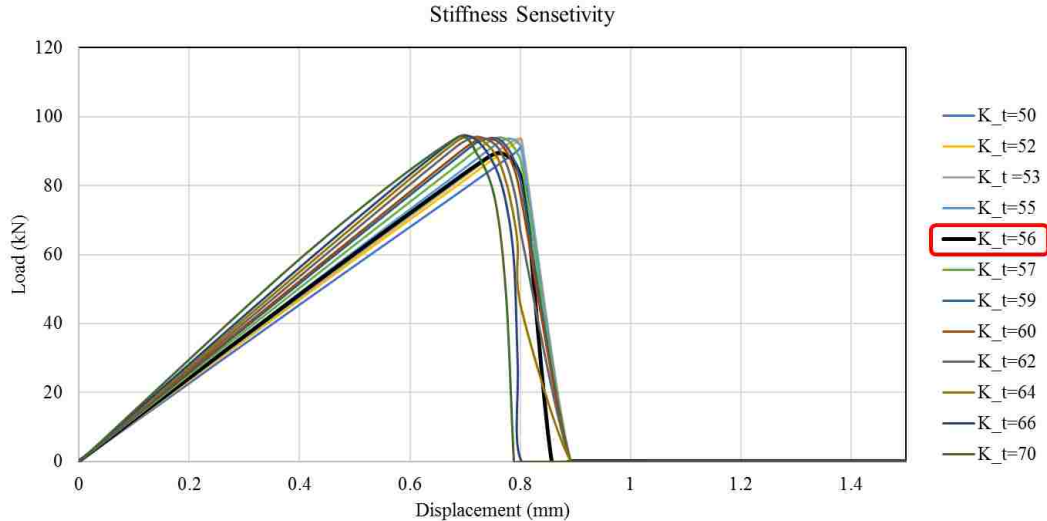


Figure 3.31: Load-displacement curves of interfacial stiffness sensitivity analysis in ABAQUS

3.12.4 Viscosity coefficient (V) sensitivity analysis

While all variables discussed here are used to define the interface interaction properties, the previous variables combined creates the shear-slip relationship. On the other hand, the viscosity

coefficient was used to improve convergence by suppressing numerical instabilities and ensuring that stiffness matrix remains positive. The ABAQUS Example Problem Guide for version 6.13 lists a sensitivity study in which a selection of $V=0.001$ had an overestimate by few percent of the failure strength but nonetheless resulted in better convergence rate. The results of such analysis are described in Table 3-9 (η is the viscosity coefficient referred to as V in this text):

Table 3-9: ABAQUS example problem guide for viscosity coefficient.

	<i>Experimental result</i>	<i>Numerical result</i>			
		V=0.001	V=0.0004	V=0.00016	V=0.000064
<i>Strength</i>	446	463.7	453.8	449.2	448.2

Since the back-solving technique depends on trial and error, improving the convergence rate for all models proves critical in producing inexpensive solutions. A sensitivity study was also performed on several models to ensure that the selection of $V=0.001$ does not alter the simulation outcomes or differs the results significantly when shear-slip variables are selected. The load-displacement curves of the PC-Neat simulation at different stabilization value V are presented in Figure 3.32. Furthermore, Table 3-10 also describe the peak shear stress of these simulations. This sensitivity analysis confirms that the use of the selected V value does not significantly change the desired outcome of simulations but rather facilitate convergence.

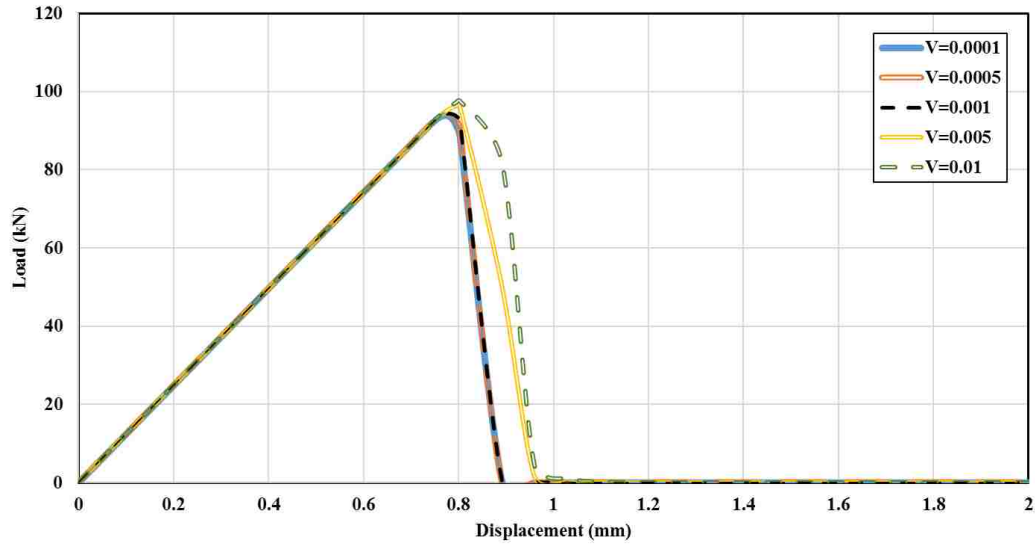


Figure 3.32: Load-displacement curves of viscosity coefficient sensitivity analysis in ABAQUS.

Table 3-10: Peak shear stress variability at different viscosity coefficients.

	<i>Viscosity coefficient (V)</i>				
	V=0.0001	V=0.005	V=0.001	V=0.005	V=0.01
<i>Peak load (kN)</i>	93.80	94.10	94.36	96.54	97.65
<i>Percentage change from V=0.0001</i>	0.0%	0.3%	0.6%	2.9%	4.1%

CHAPTER 4: RESULTS AND DISCUSSION

In this chapter, Siloxane PC (SPC) and Novolac PC (NPC) mechanical and microstructural characterization are discussed. For each type of epoxy, several stages of testing were carried to identify the critical aspects on how each of the selected nanomaterials alters PC's mechanical properties. The different stages of testing are described in Figure 4.1 for SPC mixes and Figure 4.2 for NPC mixes. In each stage, specific contents of each nanomaterial are selected based on the best performing PC nanocomposite (PCNC). Selection was aimed to minimize the number of mixes examined while providing sufficient number of mixes to discretize the different mechanisms altering PC's behavior. The sections in this chapter describe specific mechanical properties per PCNC type. Sections 4.1 describes the flowability results of all SPC and NPC mixes and was the first stage for each type of PC. Sections 4.2 – 4.9 describe the results of all mechanical tests such as tension, fracture toughness, fatigue, structural monitoring, slant shear, and compression. Sections 4.9 through 4.11 expands on the effect of stiffness mismatch in relation to the results of slant shear test and the role of nanomaterials in altering the elastic properties of PC. Sections 4.12, 4.13 and 4.14 describe the microstructural analysis of the critical PC mixes with their respective epoxy nanocomposites. Analysis of the apparent and mechanical characteristic properties that different nanomaterials alter the behavior of PC are depicted in mechanical test sections (4.2 – 4.9). The chemical induced PCNC behavior are discussed in 4.13 and 4.14 and tied to the results of mechanical tests.

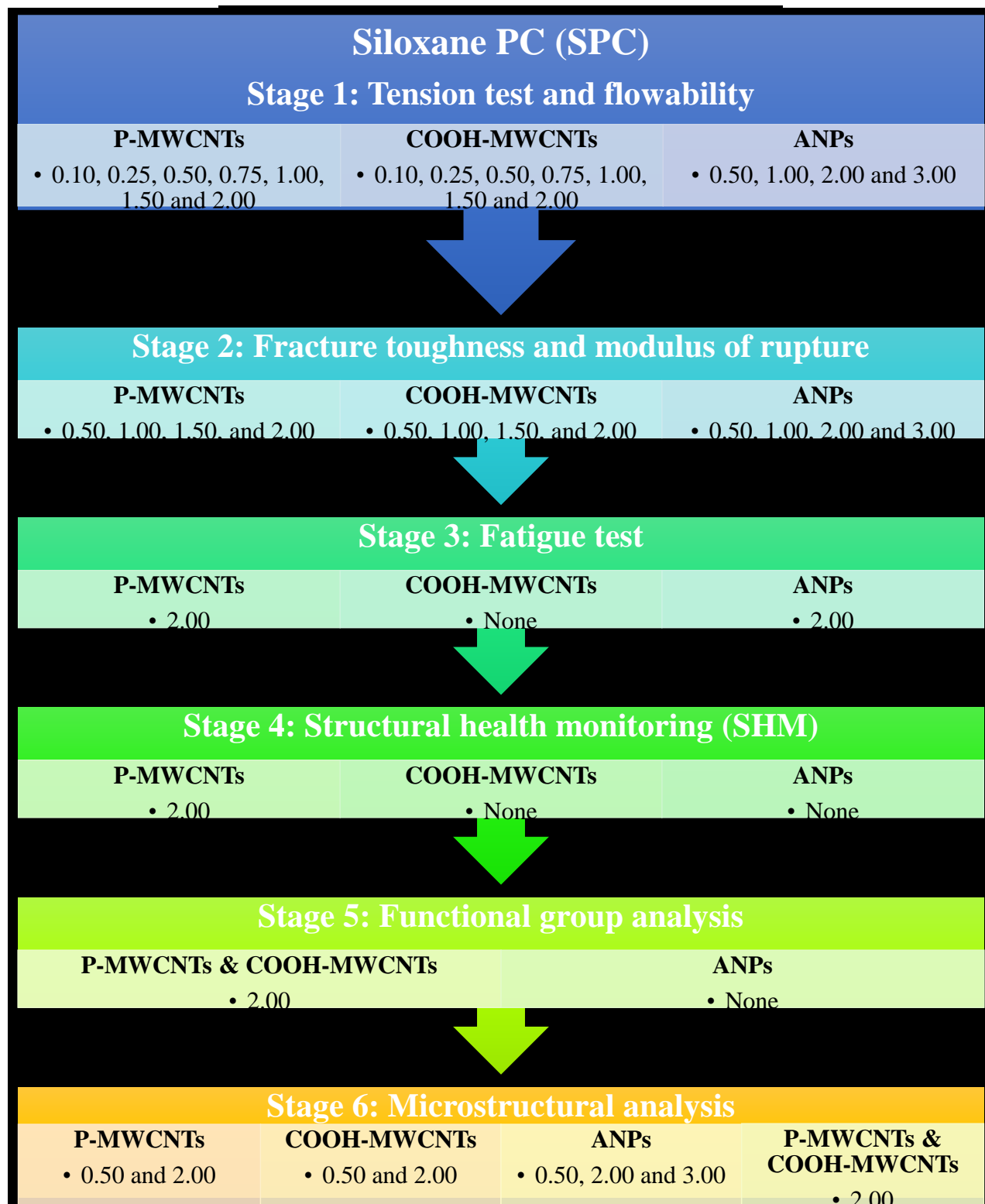


Figure 4.1: Variation of nanomaterials and their content at different stages of testing for Siloxane PC (SPC)

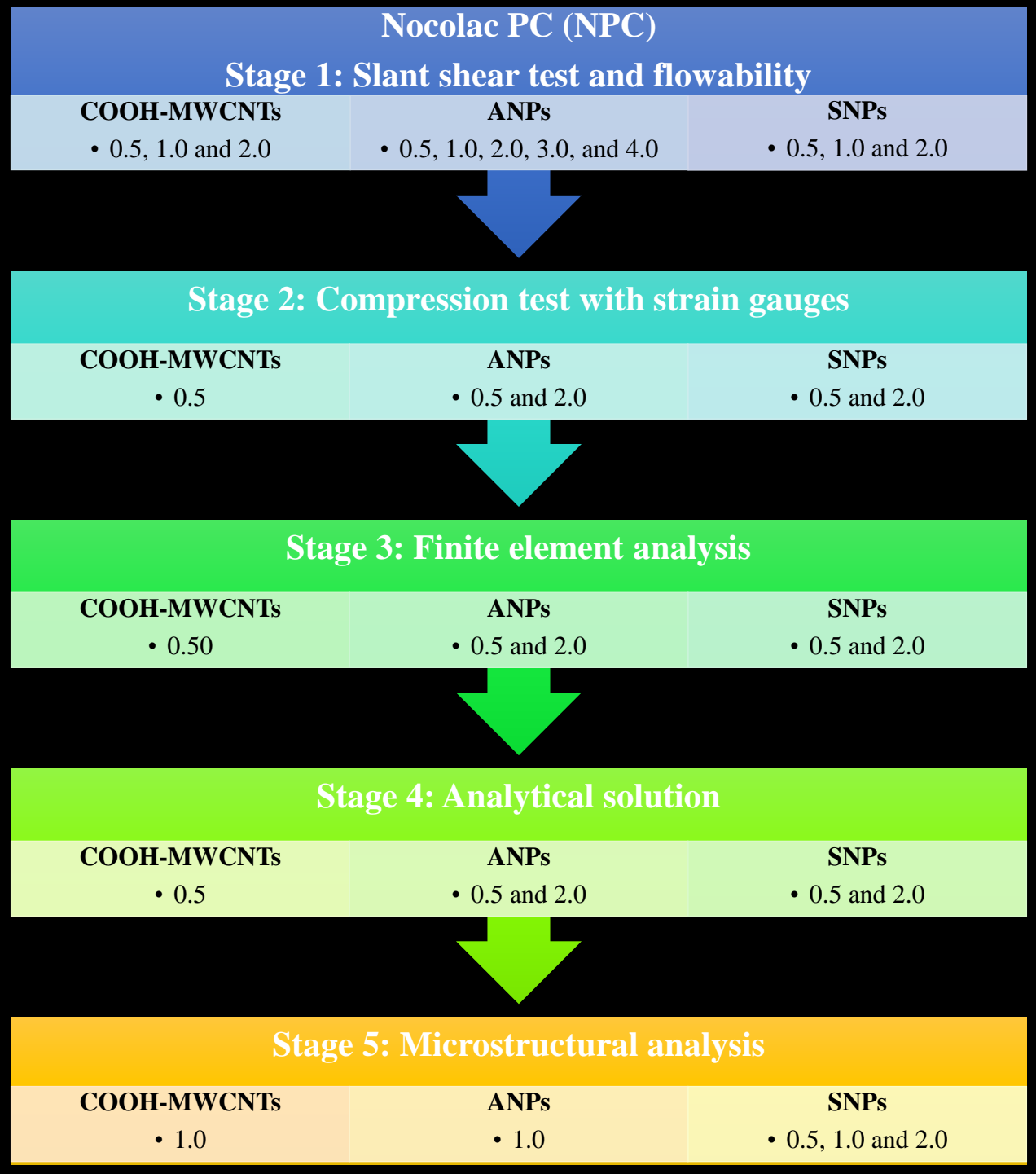


Figure 4.2: Variation of nanomaterials and their content at different stages of testing for Novolac PC (NPC)

4.1 Flowability Test

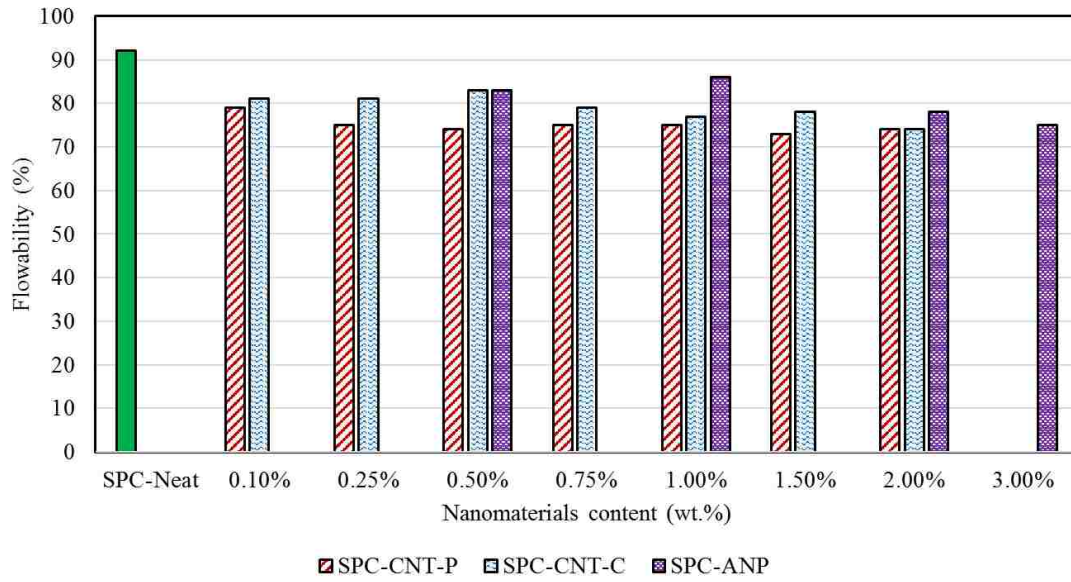


Figure 4.3: Flowability test result for Siloxane PC (SPC) mixes with nanomaterials.

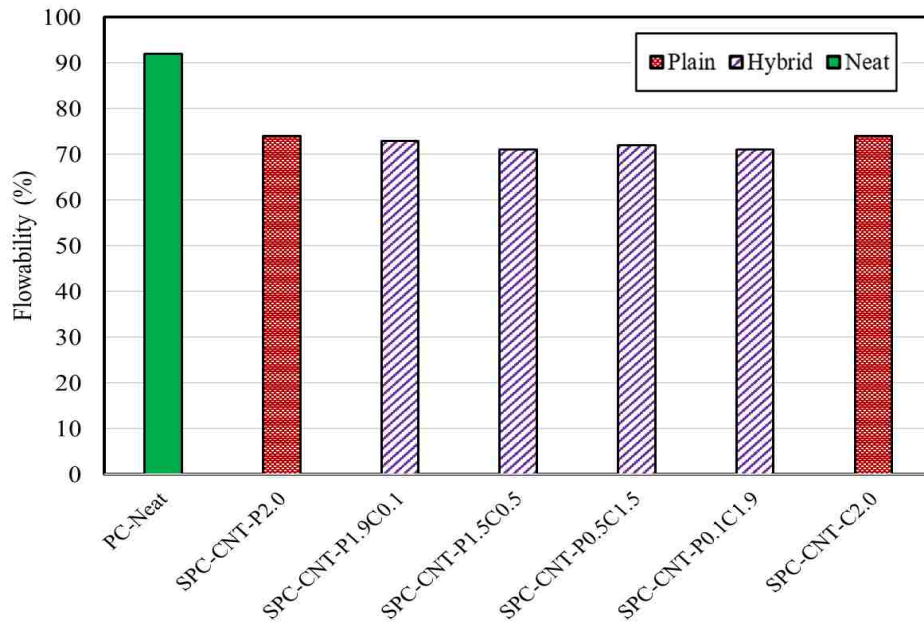


Figure 4.4: Flowability test results of Siloxane PC (SPC) using hybrid mixes of P-MWCNTs and COOH-MWCNTs.

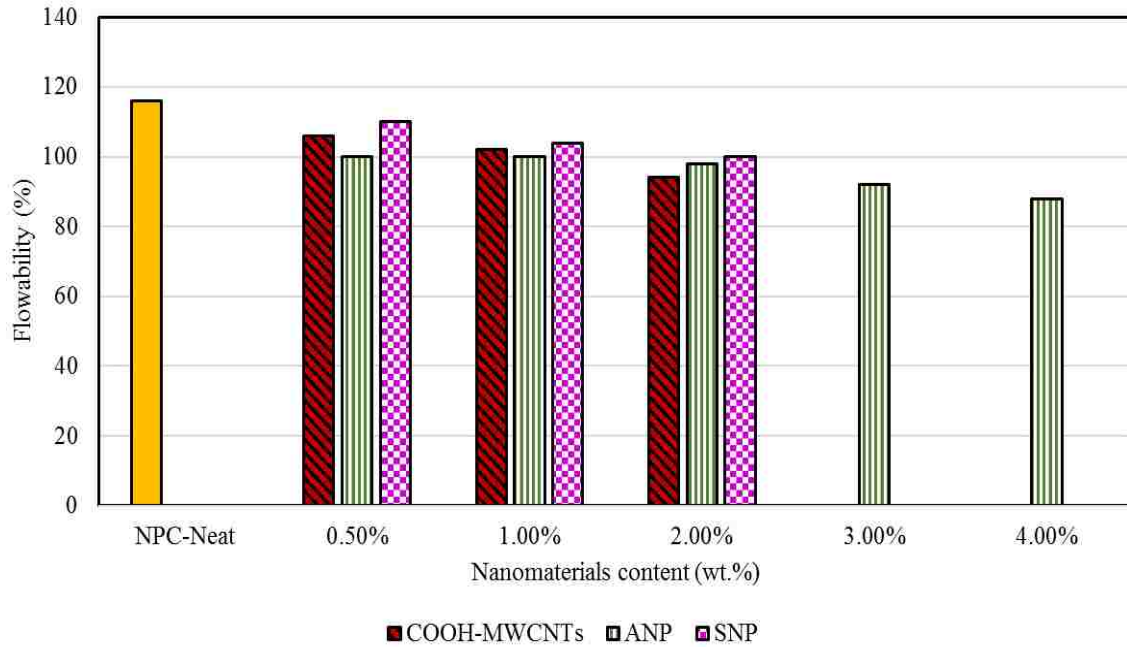


Figure 4.5: Flowability test results for Novolac PC (NPC).

Incorporating nanomaterials into polymer systems and PC result in increased viscosity reducing flowability (workability). The high flowability of PC is one of the main characteristics that makes it an attractive material for bridge deck overlays and substrates. Immediately after mixing all components of PC, the flowability of all mixes was measured per section 3.3. The results are shown in Figure 4.3 for Siloxane PC (SPC) mixes with only one type of nanomaterial, Figure 4.4 for hybrid SPC mixes and Figure 4.5 for all Novolac PC (NPC) mixes. The results show that incorporating nanomaterials at any of the examined contents 0.10 wt.% up to 4.0 wt.% result in decreased flowability. Mixes prepared with Siloxane epoxy showed lower flowability than that of Novolac epoxy which is attributed to the higher viscosity of Siloxane epoxy. Therefore, dispersion of nanomaterials in Siloxane epoxy requires more energy than in Novolac. Mixes prepared with Siloxane epoxy showed a decrease in flowability in the range of 10% to 23% Mixes prepared with Novolac epoxy showed similar decrease in the range of 5% to 24%. In both epoxies, when COOH-MWCNTs and ANPs have been utilized at 0.5 and 2.0 wt.% contents, the flowability decrease

from the respective neat PC mix was consistent. The decrease recorded is 10% at 0.5 wt.% content of ANPs or COOH-MWCNTs and 18% and 20% for ANPs and COOH-MWCNTs at 2.0 wt.% content respectively. In general, higher nanomaterials content result in lower flowability due to the increased viscosity and friction of the resin. In the order of the lowest flowability to the highest, the nanomaterials used are ordered from P-MWCNTs, COOH-MWCNTs, ANPs then SNPs. The previous pattern discloses that nanomaterials with larger dimensions generate large decrease in flowability. Also, as mixes prepared with COOH-MWCNTs had higher flowability than those prepared with P-MWCNTs, it's evident that functionalization aid in establishing higher flowability. Therefore, it is important to consider the level of dispersion of nanomaterials when examining the flowability of PC. Improper dispersion results in agglomerated particles increasing friction and viscosity and thus hindering flowability.

4.2 Tension test

Two types of tension tests were conducted for SPC mixes; flexural and direct tension. In the flexural test, the tensile strength (modulus of rupture) was evaluated whereas in direct tension test, the tensile strength, strain at failure and toughness were evaluated. Direct tension test is considered as the first stage of mechanical characterization of SPC mixes. The results of direct tension test were used to minimize the number of investigated PCNC mixes. Based on the depicted patterns, specific mixes were removed in which only critical mixes affecting PC behavior were maintained for the following stage.

4.2.1 Direct tensile test

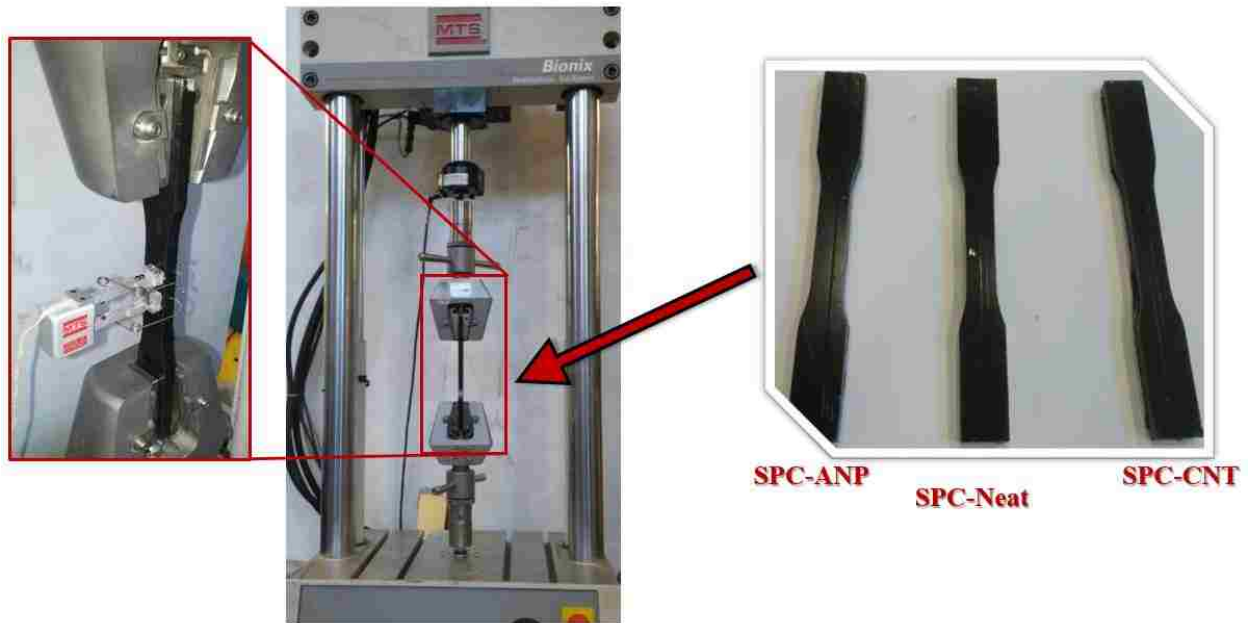


Figure 4.6: Direct tension test showing different dog-boned samples loaded with MTS Bionix and utilizing an extensometer to measure strain.

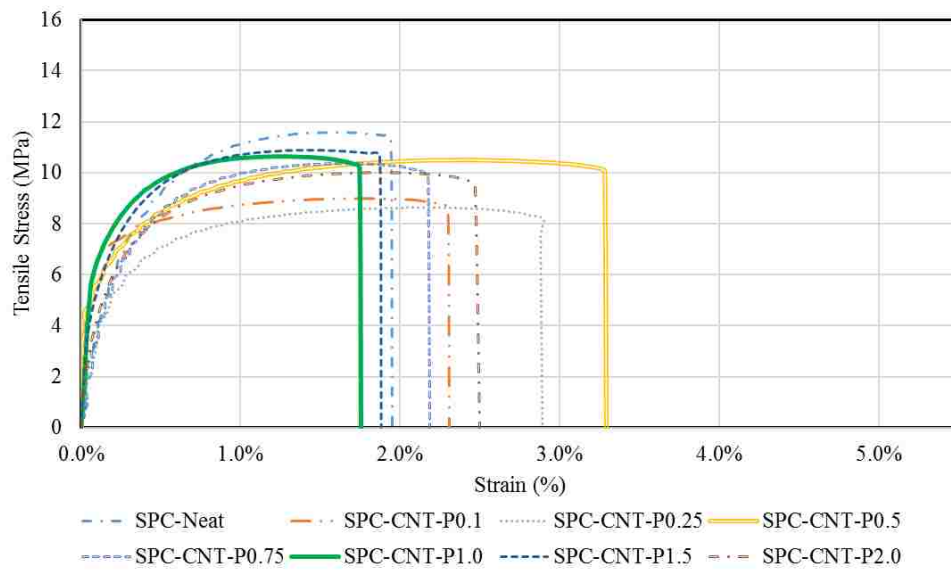


Figure 4.7: Tensile test stress-strain curves for Siloxane PC (SPC) mixes containing P-MWCNTs at different contents.

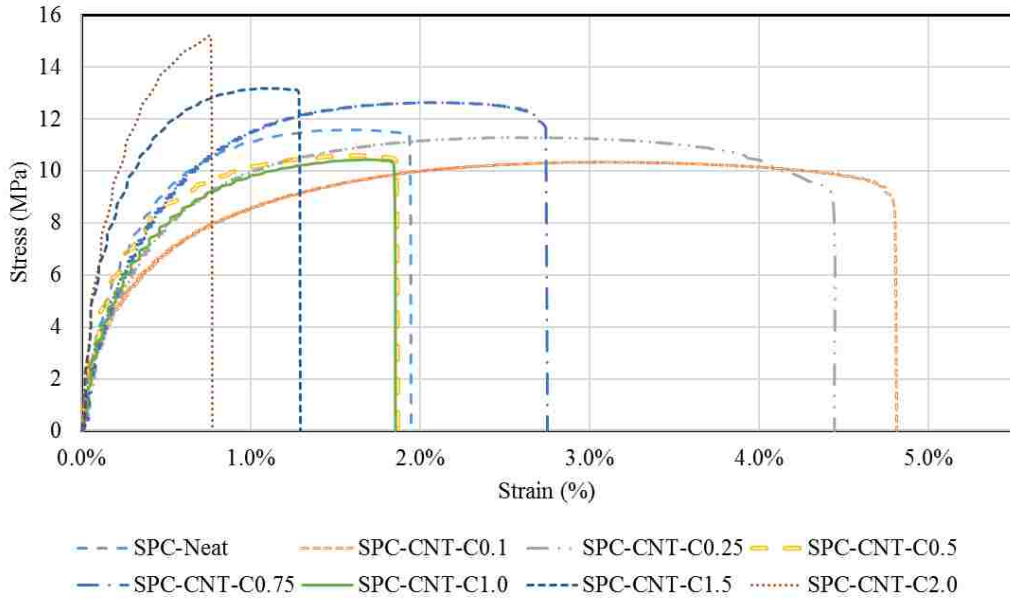


Figure 4.8: Tensile test stress-strain curves for Siloxane PC (SPC) mixes containing COOH-MWCNTs at different contents.

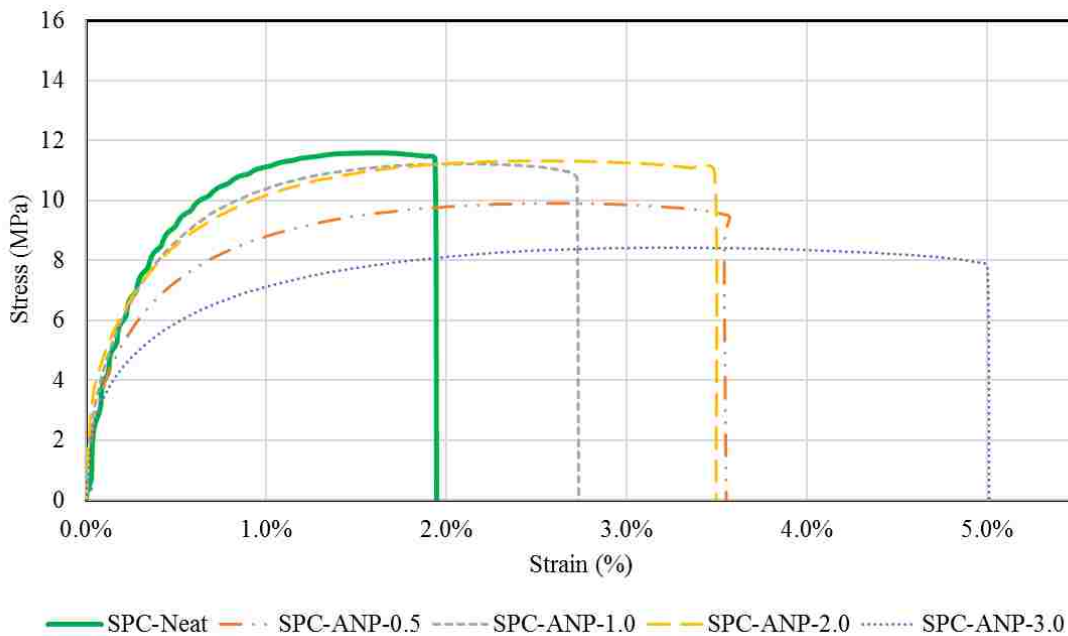


Figure 4.9: Tensile test stress-strain curves for Siloxane PC (SPC) mixes containing ANPS at different contents.

Direct tension test was performed per section 3.4. Selected samples are shown in Figure 4.6 as well as the testing setup. For each mix, five samples were tested and the mean sample's stress-strain diagram is reported in Figure 4.7 - Figure 4.9. The curves show significant non-linear

behavior of all PC mixes where the initial linear loading is diminished. Furthermore, it's evident that all PC mixes with high failure strain show significant strain and deformation within 10% of their peak loads. In fact, mixes such as SPC-CNT-C0.1, SPC-CNT-P0.5, and SPC-ANPS-2.0 maintain 90% of their tensile strength between 20% and 100% of their failure strain values. Nonetheless, it's important to note that many samples show significant non-linearity as well as slippage appearing as crisscross (zigzag) at their initial load. Thus, establishing the elastic modulus requires linear approximations of the initial loading slopes. Analysis of the effects of the different nanomaterials on the mechanical performance of PC is discussed in the following sections.

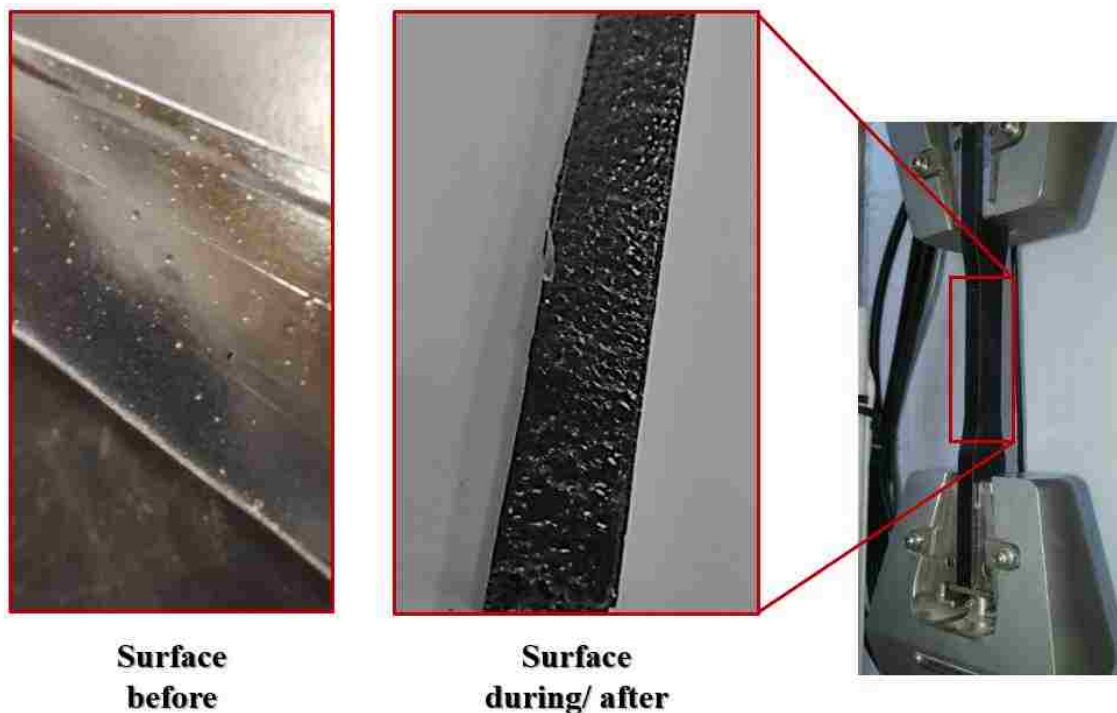


Figure 4.10: Stretching of the PC surface during tension test.

In all tests, the samples failed with one crack propagating within the mid-third length of the sample. Samples whose failure occurred at the grips were discarded. While testing, stretching of the PC prisms was evident over the sample's surface as shown in Figure 4.10. The surface wrinkling (stretching) was observed to increase as samples were loaded. Upon failure, the samples

maintained the wrinkled surface for 20 minutes before returning to their previous smooth surface. Such behavior indicates the time-dependent behavior of all PC mixes. While PCC immediately restores elastic deformations, PC reverts elastic deformation slowly. While this phenomenon explains the significant non-linearity in stress-strain diagram, fracture toughness, modulus of rupture and fatigue tests procedures require careful selection of their parameters to accommodate the slow elastic recovery. The load rate in this test was nevertheless kept the same for all mixes to allow direct comparison with PCC by maintaining ASTM requirements.

4.2.1.1 Tensile strength

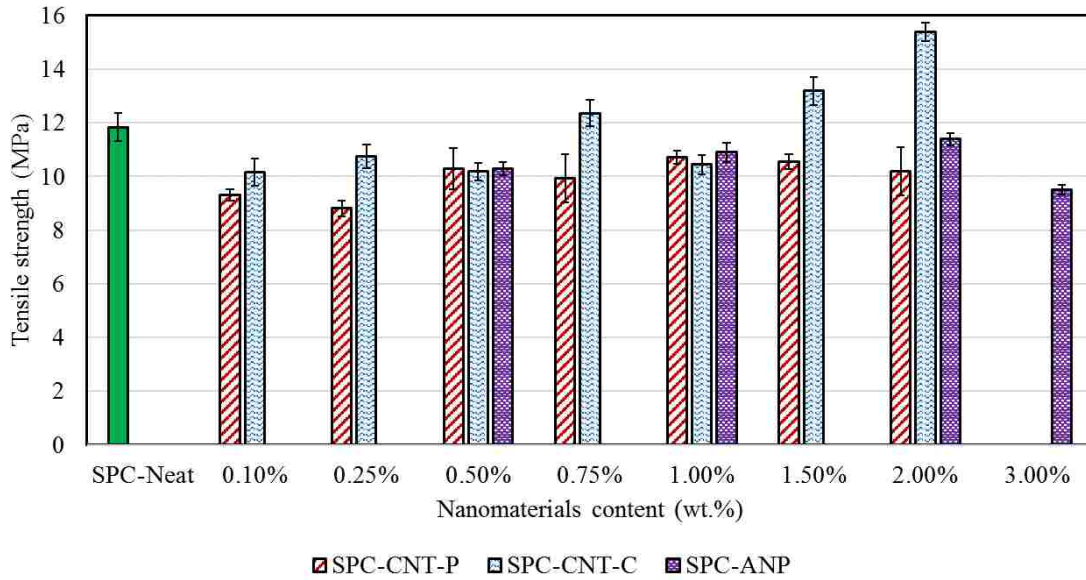


Figure 4.11: Tensile strength of Siloxane PC (SPC) mixes.

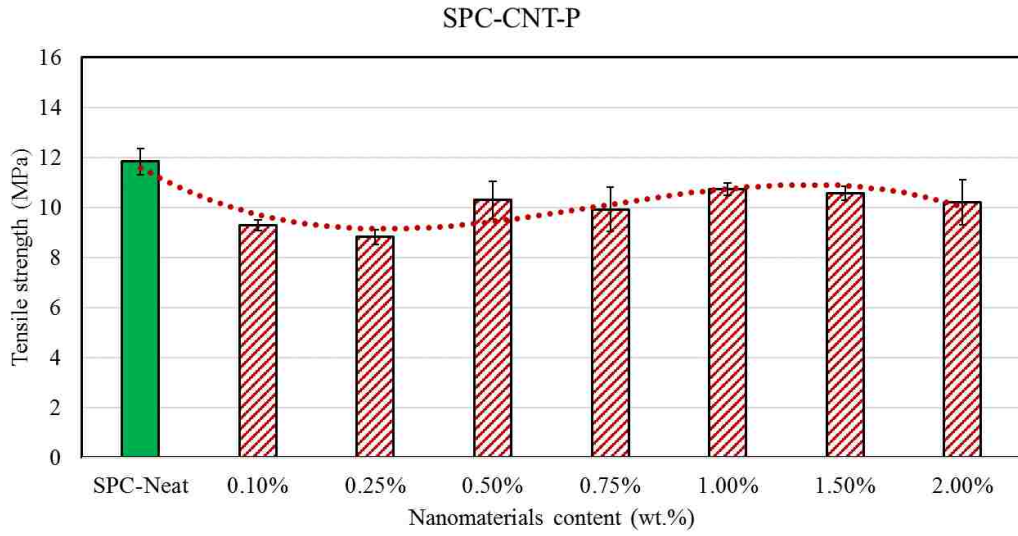


Figure 4.12: Tensile strength of Siloxane PC (SPC) mixes containing different contents of P-MWCNTs.

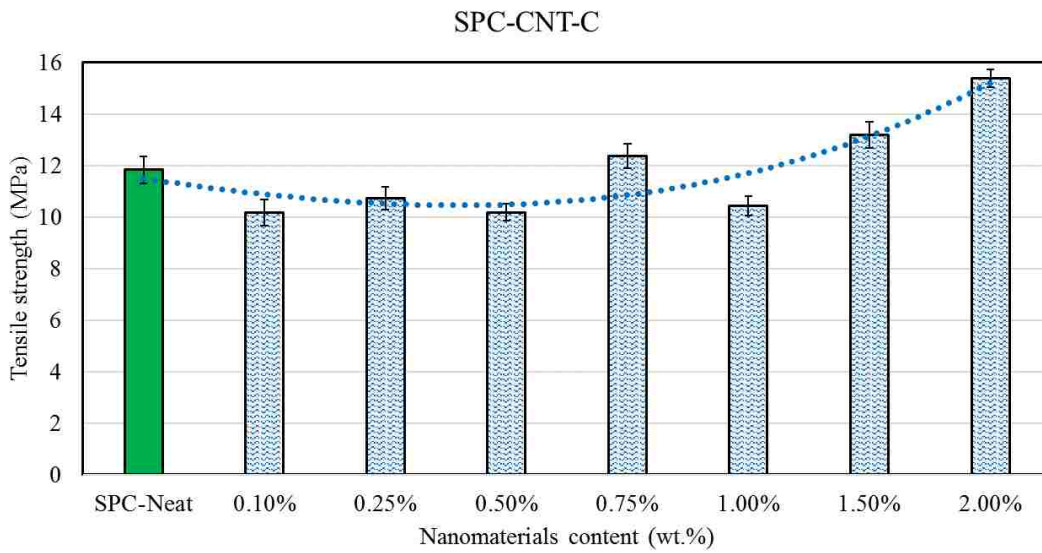


Figure 4.13: Tensile strength of Siloxane PC (SPC) mixes containing different contents of COOH-MWCNTs.

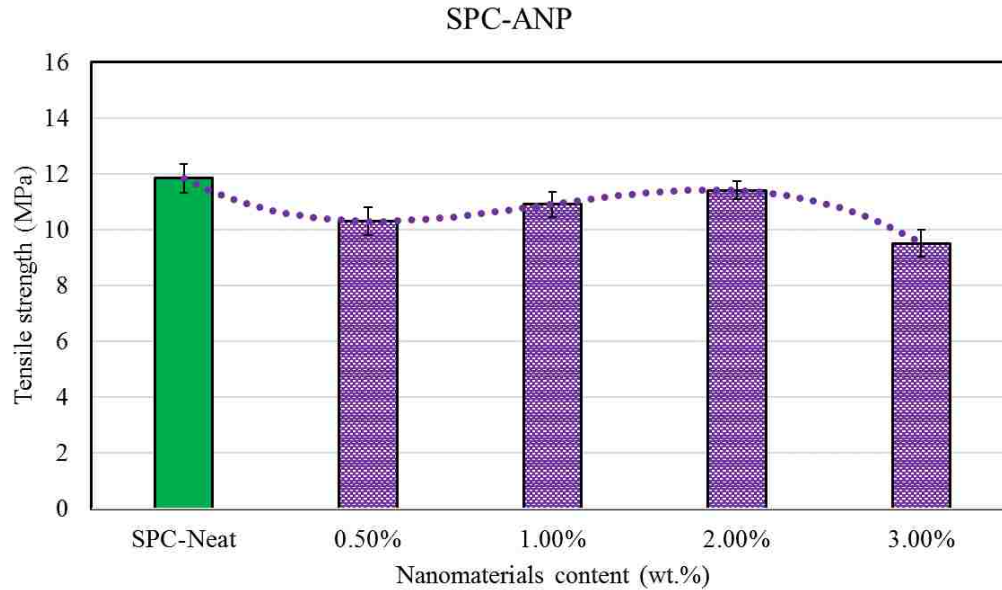


Figure 4.14: Tensile strength of Siloxane PC (SPC) mixes containing different contents of ANPS

Analysis results for the tensile strength of all PC mixes are shown in Figure 4.11 for all PC mixes. In general, PC with or without nanomaterial shows significantly high tensile strength in the range of 9 – 15 MPa; 3 – 5 times higher than that of the highest reported direct tensile strength of PCC (Swaddiwudhipong et al. 2003). To describe the effect of different contents of P-MWCNTs, COOH-MWCNTs and ANPS, their results and pattern have been depicted separately in Figure 4.12 - Figure 4.14. PC mixes incorporating P-MWCNTs show a decrease of tensile strength in the range of 9% to 26%. The lowest tensile strength was that of mixes incorporating low contents of P-MWCNTs such as 0.10 and 0.25 wt.%. Increasing the content up to 1.0 wt.% show less reduction in tensile strength with increasing P-MWCNTs content. Further increase in content up to 2.0 wt.% however diminishes those improvements (between 0.5 and 1.0 wt.% content) with increasing the content. Of all SPC nanocomposite mixes, those incorporating P-MWCNTs showed the lowest tensile strength while maintaining an appreciable minimum tensile strength of 9 MPa. On the other hand, results show that functionalization of MWCNTs can result in increased tensile strength however only at higher contents. The highest tensile strength of all examined PC mixes is that of

SPC-CNT-C2.0 at 15.4 MPa representing 30% increase from SPC-Neat. The pattern depicted in Figure 4.13 show that incorporating COOH-MWCNTs at contents less than 1.5 wt.% content result in limited decrease in tensile strength up to 14% at 0.1 wt.% content. Increasing the content of COOH-MWCNTs result in increasing the tensile strength. Finally, mixes incorporating ANPS show two different patterns similarly to P-MWCNTs. Incorporating low contents of ANPS result in reduced tensile strength by 13%. Increasing the content result in less reduction of tensile strength up to insignificant changes from that of PC-Neat at 2.0 wt.% content. However, increasing the content beyond 2.0 wt.% result in diminished improvements in tensile strength with a decrease in tensile strength of 20% at 3.0 wt.% content.

The overall tensile strength of PC nanocomposite mixes can be characterized by a general decrease of tensile strength at low contents. When non-functionalized nanomaterials are used such as P-MWCNTs and ANPS, a decrease of tensile strength is expected. While this decrease can be minimized at contents between 1.0 wt.% and 2.0 wt.%, it's predicted that contents great than 2.0 wt.% will only result in worsened tensile strength. On the other hand, the use of functionalized nanomaterials suggests improvements in tensile strength at high levels of functional group content. In this work, mixes incorporating 1.5 wt.% COOH-MWCNTs and greater showed improvements in tensile strength compared to neat.

4.2.1.2 Tensile strain at failure

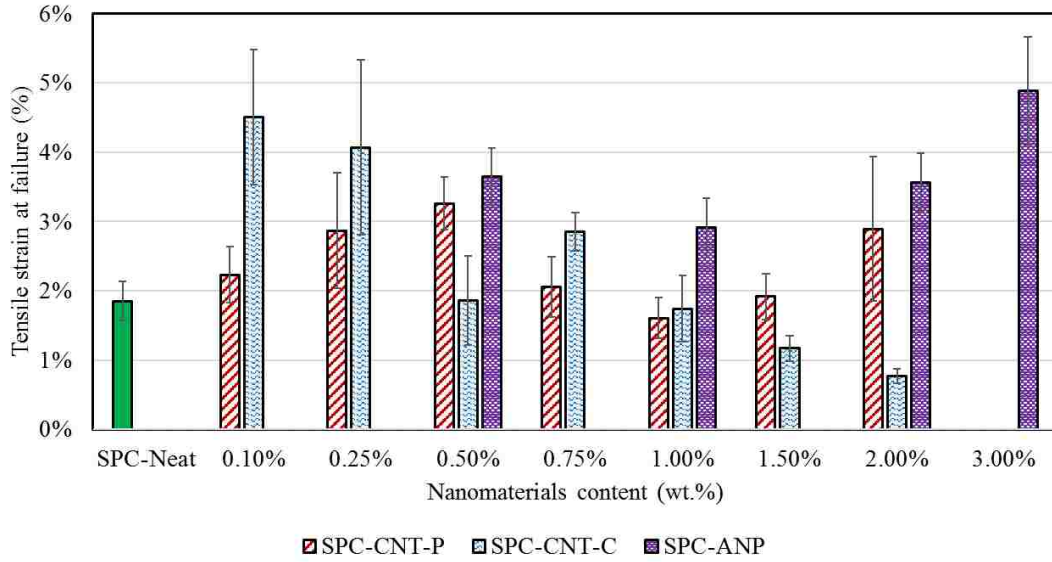


Figure 4.15: Tensile strain at failure of different Siloxane PC (SPC).

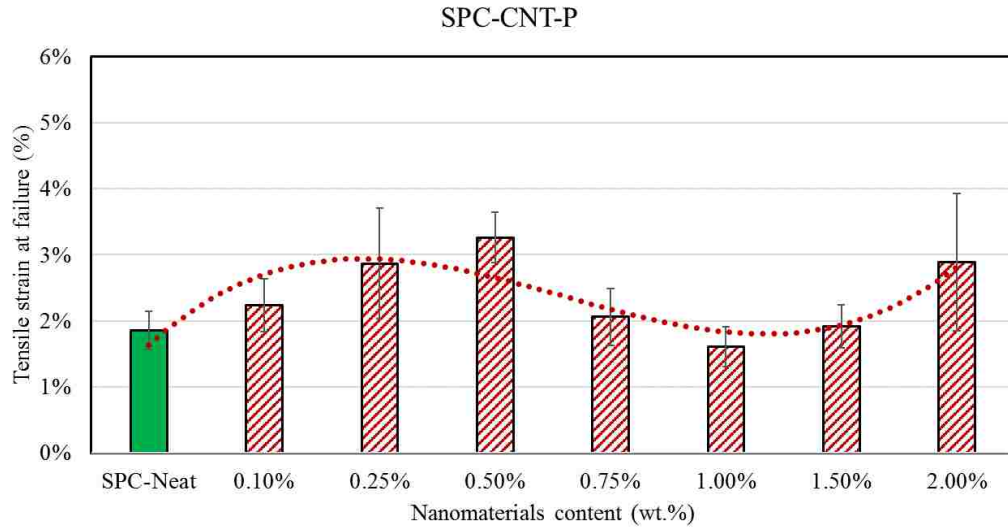


Figure 4.16: Tensile strain at failure of Siloxane PC (SPC) mixes containing different contents of P-MWCNTs.

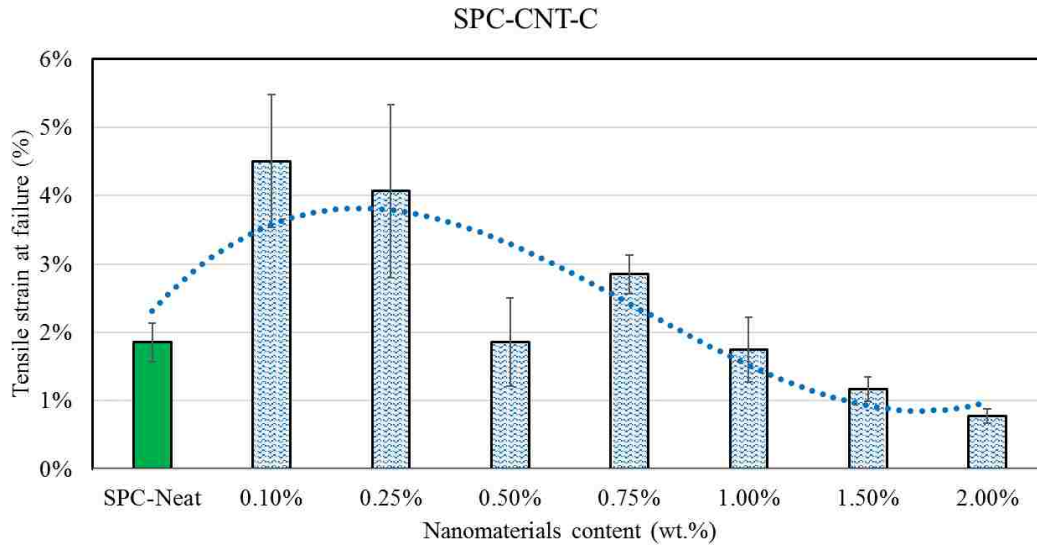


Figure 4.17: Tensile strain at failure of Siloxane PC (SPC) mixes containing different contents of COOH-MWCNTs.

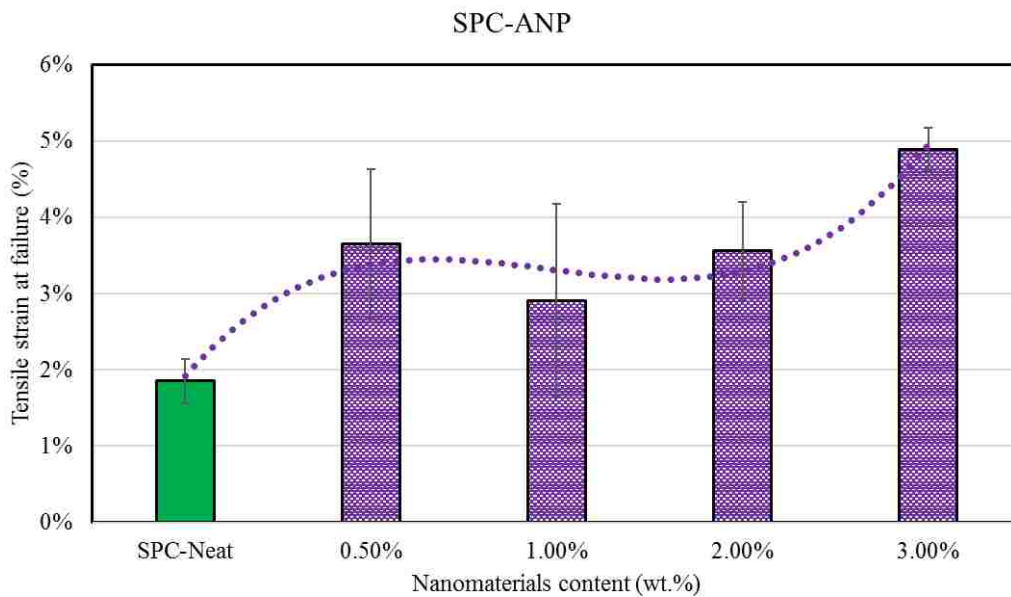


Figure 4.18: Tensile strain at failure of Siloxane PC (SPC) mixes containing different contents of ANPS.

Contrary to the results of tensile strength, all PC nanocomposite mixes showed improved failure strains apart from SPC-CNT-C2.0 as shown in Figure 4.15. In fact, the proposed SPC mixes show superior and unprecedented ductility (failure strain) reaching 4.9%. The highest strain achieved of all mixes was that of SPC-ANPS-3.0 of 4.9% while PC mixes with P-MWCNTs and

COOH-MWCNTs showed maximum tensile strain at failure of 4.5% and 3.3% at 0.1 and 0.5 wt.% content respectively. The increase in ductility represent an order of magnitude improvement over that of PCC which is often characterized by 0.05% failure strain (Swaddiwudhipong et al. 2003). Mixes incorporating P-MWCNTs show reverse trend to that of tensile strength as depicted in Figure 4.16. An increase of ductility is observed at low contents up to 0.5 wt.% content whereas tensile strength was decreasing. Increasing the content result in diminished increase of ductility up to 1.0 wt.% content. Further increase beyond 1.0 wt.% result in improved ductility reaching similar values of those at lower contents. Functionalization of MWCNTs result in significant improvements in ductility at very low contents reaching 4.5% at 0.1 wt.% content as shown in Figure 4.17. Higher COOH-MWCNTs content result in worsened ductility that underperform SPC-Neat at 1.0 wt.% content. The lowest ductility measured of all mixes was that of SPC-CNT-C2.0 which reported the highest tensile strength. PC mixes incorporating ANPS followed similar pattern to that of P-MWCNTs (similarly to tensile strength patterns as well). Low contents of ANPS result in improved ductility reaching 3.7%. Increasing the content of ANPS up to 2.0 wt.% result in diminished improvements as depicted in Figure 4.18. However, increasing the content beyond 2.0 wt.% result in achieving higher levels of ductility than at lower content reaching 4.9%.

An inverse to the pattern depicted for tensile strength is depicted for failure strains. In all mixes, high levels of ductility are attained at lower contents of 0.1 wt.% to 0.5 wt.% while tensile strength is decreased. Higher contents of the non-functionalized nanomaterials show a decrease of ductility up to 1.5 – 2.0 wt.% contents where significant improvements are achieved thereafter. It's important to indicate that all PC mixes prepared with non-functionalized nanomaterials show higher improvements in ductility compared to their weakened tensile strength compared to SPC-Neat. On the other hand, introducing functional groups seems to provide significant improvements

over non-functionalized nanomaterials in ductility with lessened reduced tensile strength at very low contents (less than 0.5 wt.%). Higher contents however show that functionalization results in reduced ductility with the improved tensile strength. While non-functionalized nanomaterials seem to provide a varying effect at different contents, functionalization of nanomaterials proves to be unidirectional. That is, the mechanical performance of PC prepared with functionalized nanomaterials will either decrease or increase with the increase in content.

4.2.1.3 Toughness

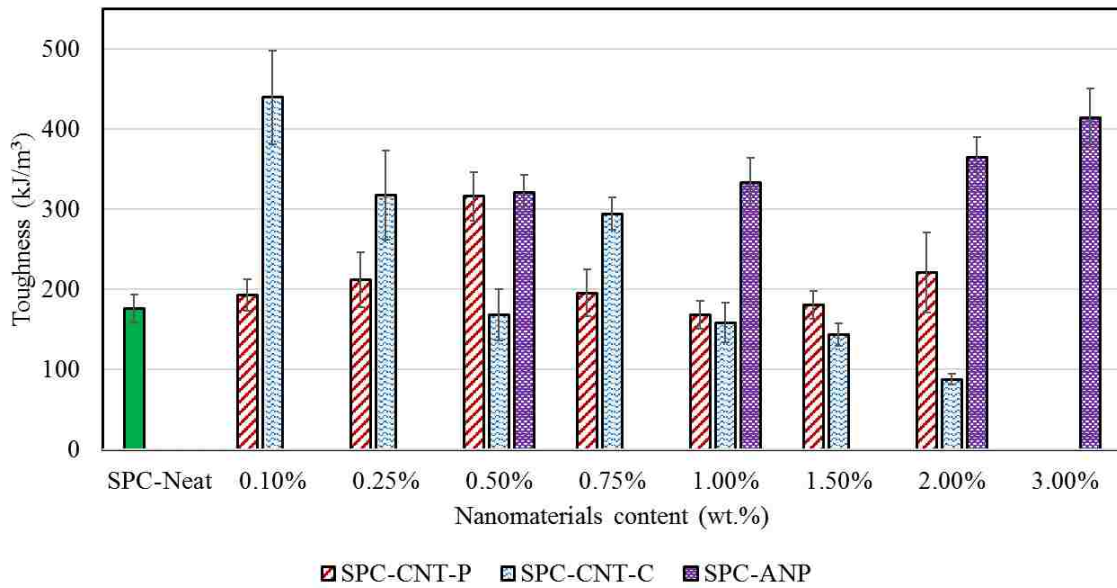


Figure 4.19: Toughness of Siloxane PC (SPC) mixes in tension test.

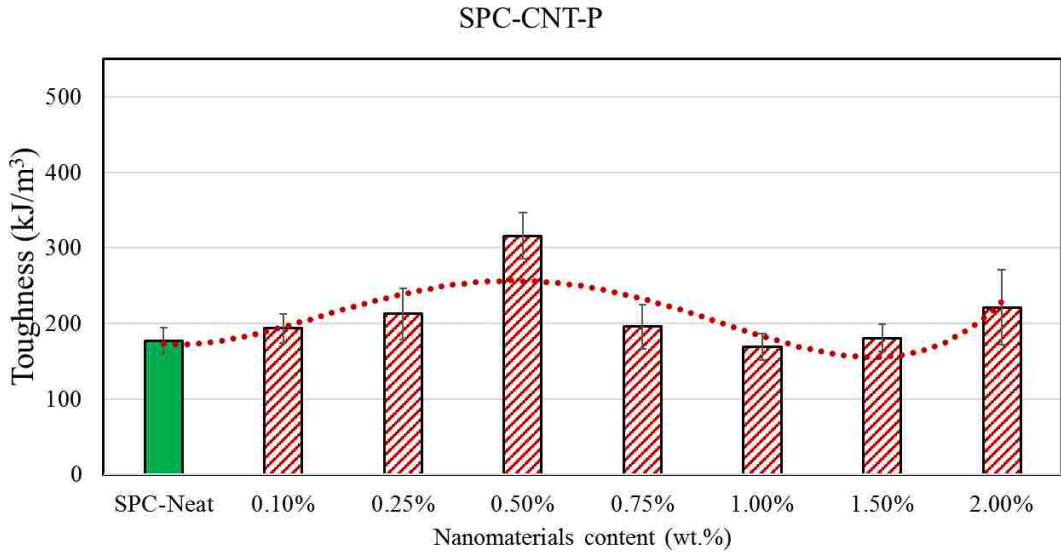


Figure 4.20: Toughness of Siloxane PC (SPC) mixes in tension test containing P-MWCNTs.

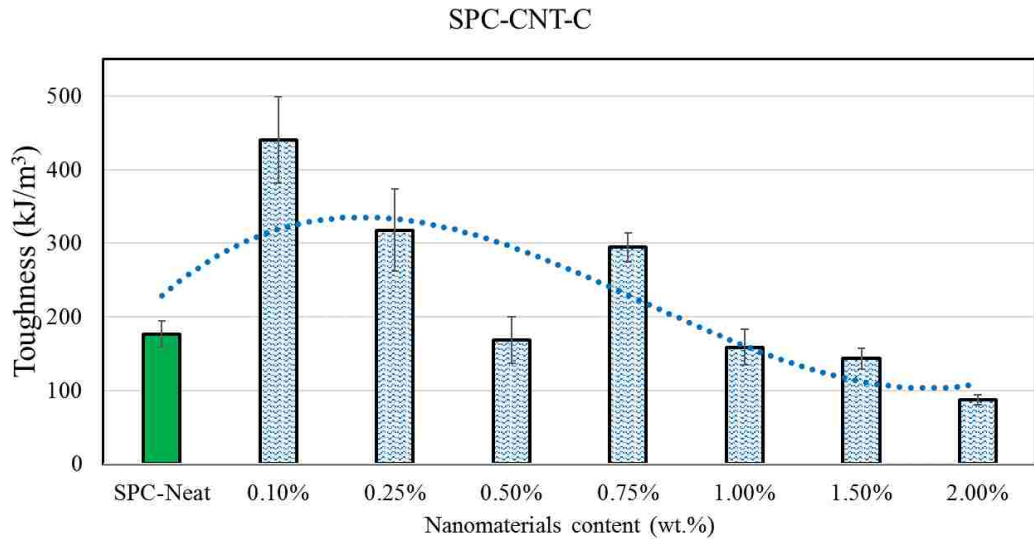


Figure 4.21: Toughness of Siloxane PC (SPC) mixes in tension test containing COOH-MWCNTs.

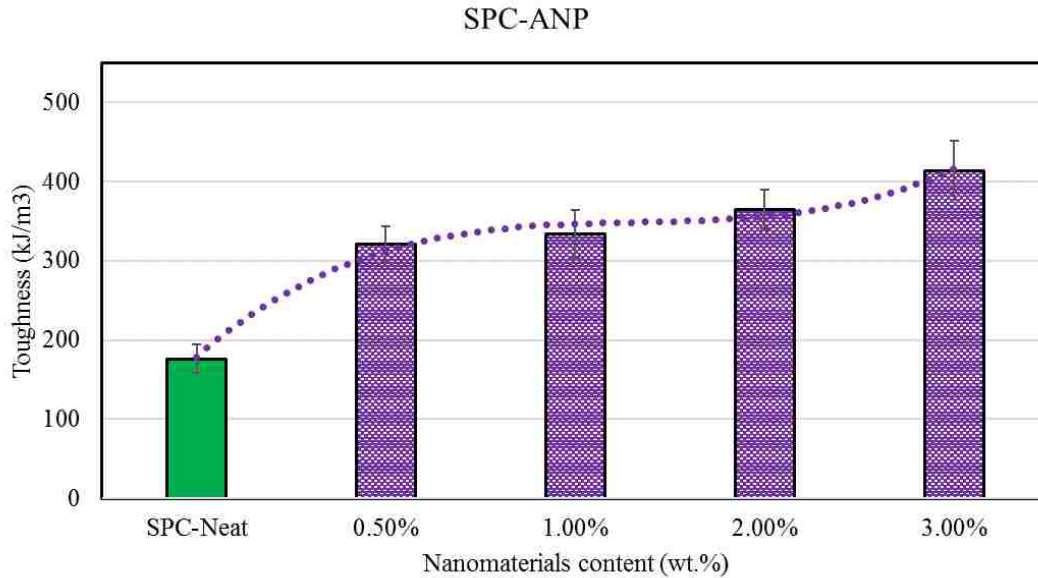


Figure 4.22: Toughness of Siloxane PC (SPC) mixes in tension test containing ANPS.

The results of toughness show similar patterns to that depicted for failure strains for all nanocomposite SPC mixes as shown in Figure 4.19. SPC mixes incorporating P-MWCNTs show less improvements in toughness than that of ductility as shown in Figure 4.20. This is caused by the decrease in tensile strength depicted earlier. The improvement in toughness therefore is in the range of 10% to 80% for all mixes except for SPC-CNT-P1.0 and SPC-CNT-P1.5 showing no significant changes from that of SPC-Neat. SPC mixes prepared with ANPS show higher toughness improvements than that of P-MWCNTs at all contents ranging from 82% to 135%. The improved performance is due to the higher ductility and the less worsened tensile strength. It's important to note that the best improvement in SPC mixes prepared with P-MWCNTs are at 0.5 wt.% content compared to 3.0 wt.% content of ANPS. Nevertheless, SPC mixes prepared with nonfunctionalized nanomaterial prove to provide significant improvements in energy absorption. Mixes prepared with functionalized nanomaterials on the other hand show similar improvements in toughness at 0.1 and 0.25 wt.% content at 150% and 80% from SPC-Neat respectively. As increasing the content of COOH-MWCNTs result in increased tensile strength and worsened

failure strain, higher contents show a decrease of toughness. This is caused by more rapid worsening of failure strains than the increase in tensile strength. It's noteworthy however to emphasize that functionalization of MWCNTs produce SPC mix of the same toughness at half the content of P-MWCNTs (0.25 wt.% compared to 0.50 wt.%).

4.2.1.4 Modulus of elasticity

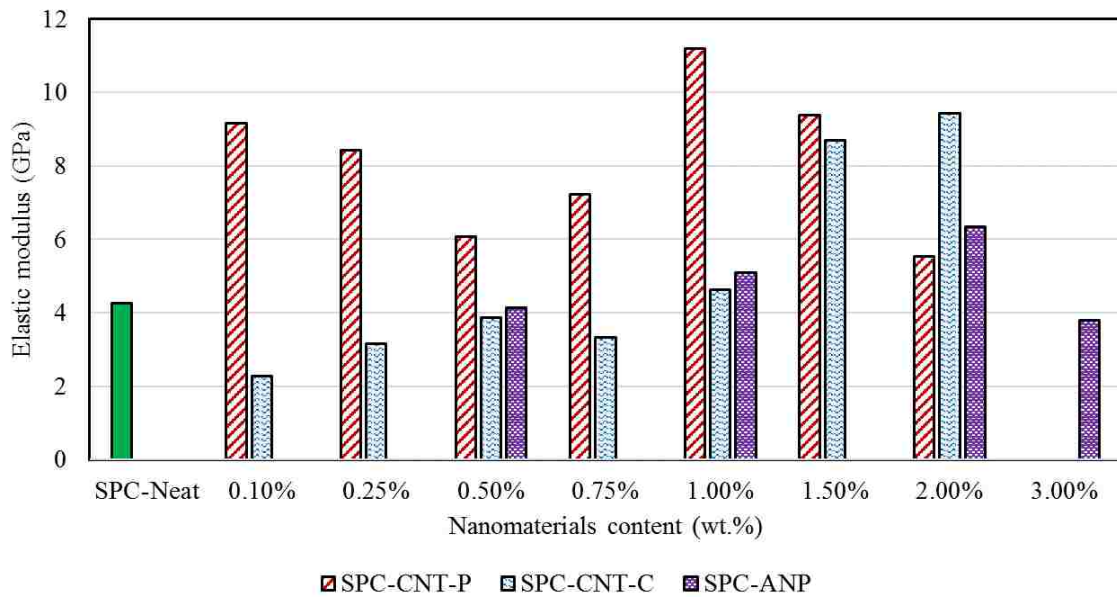


Figure 4.23: Elastic modulus of Siloxane PC (SPC) mixes.

Analysis of the initial slope of stress-strain diagrams shown in Figure 4.7 - Figure 4.9 result in establishing the elastic modulus of all mixes. As mentioned earlier, the examined mixes show significant non-linearity as well as minimal slippage appearing as crisscross (zigzag) at their initial load. Nevertheless, the elastic modulus was measured by linear approximation of the initial load slopes and the results are shown in Figure 4.23. All PC mixes show significantly lower elastic modulus than that associated with PCC (10-30 GPa) while providing higher values than that of pure epoxy polymer systems (0.1-3 GPa). The recorded measurements show similar patterns to those depicted in failure strains and toughness. However, while mixes prepared with ANPS showed higher failure strains and toughness than P-MWCNTs, those mixes showed lower elastic

modulus. This result however is expected as both mixes provide similar tensile strength. Nevertheless, all nanocomposite mixes show improved elastic modulus compared to neat except for those prepared with COOH-MWCNTs between 0.1 and 1.0 wt.%.

4.2.2 *Modulus of rupture*

For PC's tensile performance investigation, the tensile strength of the different SPC mixes were also evaluated using three and four-point bending. At this stage, mixes incorporating 0.1, 0.25 and 0.75 wt.% contents were discarded. For mixes prepared with P-MWCNTs, those mixes showed no significant contribution to the content vs tensile performance patterns. Mixes incorporating COOH-MWCNTs were aimed to examine the effect of functionalization of MWCNTs. While SPC-CNT-C0.1 showed the highest ductility, the effect on crosslinking at the significantly low content raises significant microstructural analysis inquires. Characterization of chemical effects of COOH content at the suggested extremely low content exceeds the scope of this work. Finally, mixes incorporating 0.1 and 0.25 wt.% content showed the highest variation in their results. The results of fracture toughness that have higher variation therefore require significant statistical evaluation that exceeds the scope of this work.

Flexural test served as a multi-purpose test in which not only the mechanical performance of the designated mixes was investigated but also to validate the test setups of fracture and fatigue tests. In Fracture toughness tests, the test procedures and analysis require three-point bending setup and result of modulus of rupture. Linear elastic fracture mechanics analysis (LEFM) requires an indirect tension test measurement to conduct the analysis. Indirect tension tests in general predict higher tensile strength than direct one. This is attributed to the compressive stresses persisting within the sample that decrease the sample's tension stressed volume affecting less cracks and

defects. Furthermore, the compressive stresses generated aid in creating confinement increasing crack propagation energy requirements resulting in higher tensile strength. In fatigue test, AASHTO specifications require four-point bending setup to avoid any shear failure as well as to ensure uniform loading and unloading of the specimen. The four-point bending setup was also used to establish the speed in which the initial load is ramped with by determining the stiffness of PC prisms under four-point bending. The modulus of rupture values discussed below however are those of three-point bending as their values are required to comply to ACI 446 requirements. Figure 4.24 and Figure 4.25 show the three and four-point bending setups as PC samples are loaded.

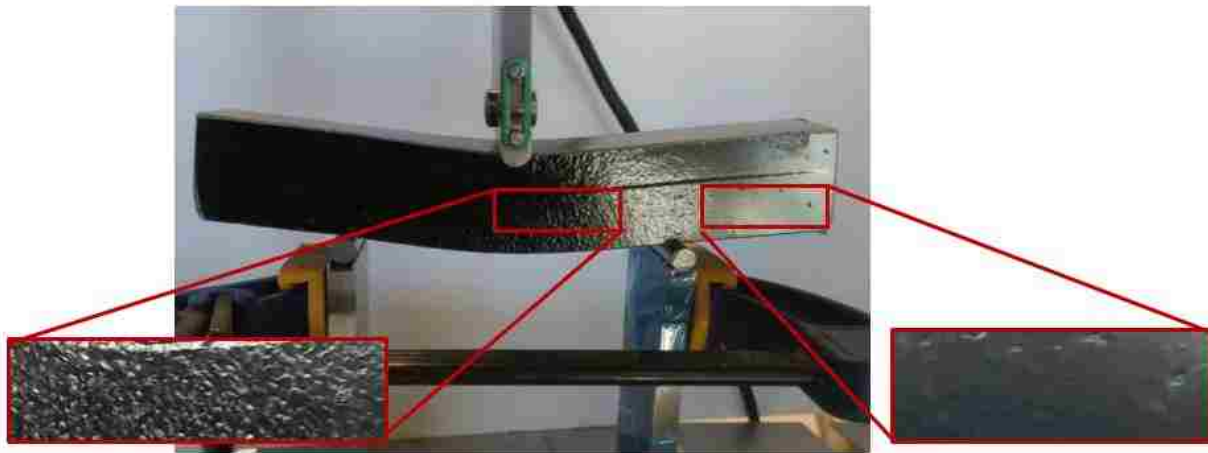


Figure 4.24: Flexural test of PC prisms using three-point bending showing stretched vs unstretched surface areas.

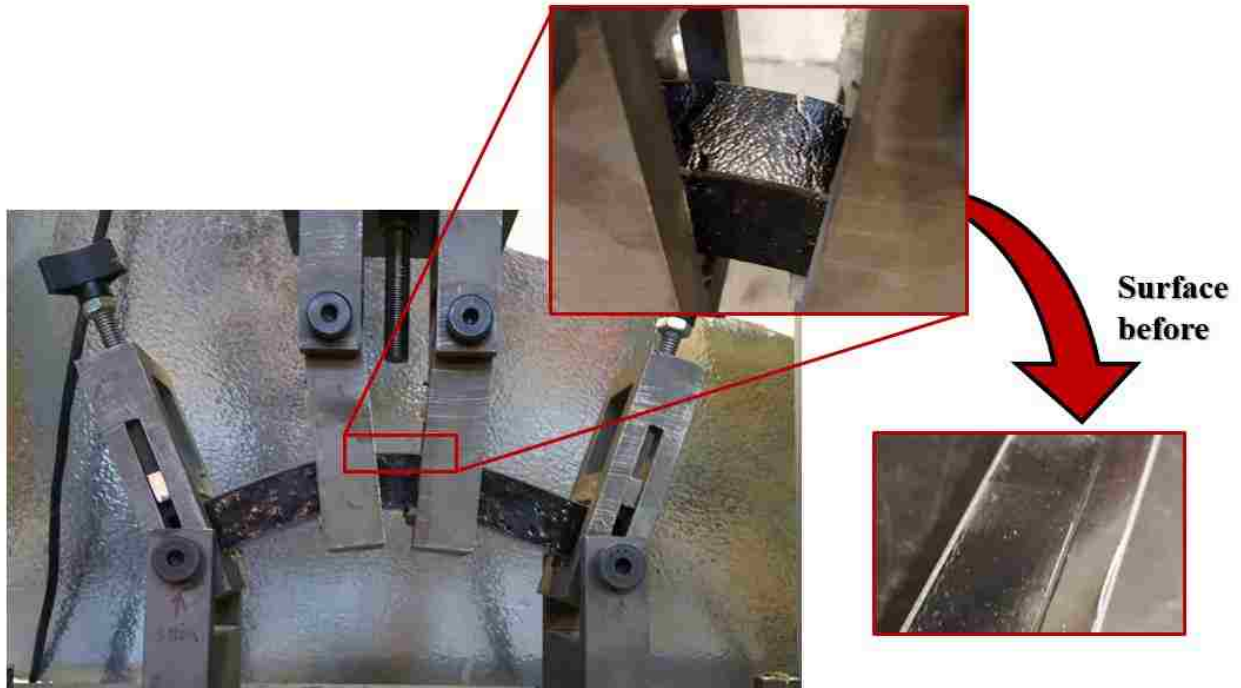


Figure 4.25: Flexural test of PC prisms using four-point bending showing excessive deformation (large ductility) and stretched vs unstretched surfaces.

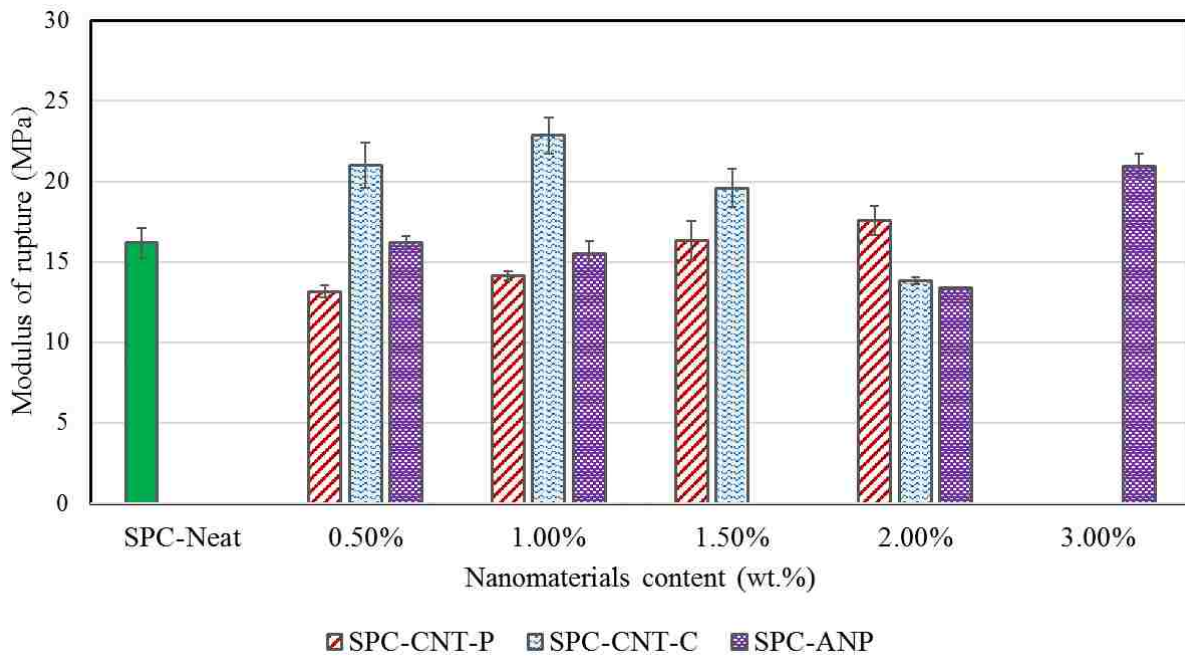


Figure 4.26: Modulus of rupture results of Siloxane PC (SPC).

In all tension tests (direct and flexural) the PC surface exhibited significant stretching of its surface. While the stretching in direct tension covered the entire length of the sample as shown

in Figure 4.10, only partial parts of the flexural specimen showed that stretching as shown in Figure 4.24. The previous emphasize why flexural strength patterns are different than that of direct tension test. In fact, mixes that exhibited increased failure strains in section 4.2.1.2 showed significantly large deformation, ductility, delayed failure, multiple cracking and surface stretching as shown in Figure 4.25. The previous effects and most critically excessive deformation produce significant limitations on the simplified modulus of rupture equations. Since the results of this test are only used partially for LEFM analysis and to aid in fracture toughness and fatigue, no further mechanics analysis was performed. The results of modulus of rupture obtained through three-point bending are shown in Figure 4.26. Previous results showed that different nanomaterials produce different effects on tensile strength and ductility at different contents. Since the stress in flexural test is affected by the specimen's arch and deformation, the modulus of rupture results show similar pattern to those depicted in toughness. Because of the analysis limitations, it's inaccurate to relate the effect of the different nanomaterials at various contents to the flexural strength. Nonetheless, the excessive deformation and multiple cracking suggest significant contribution to fracture process zone (FPZ) and emphasize a quasi-brittle behavior.

4.3 Fracture toughness test

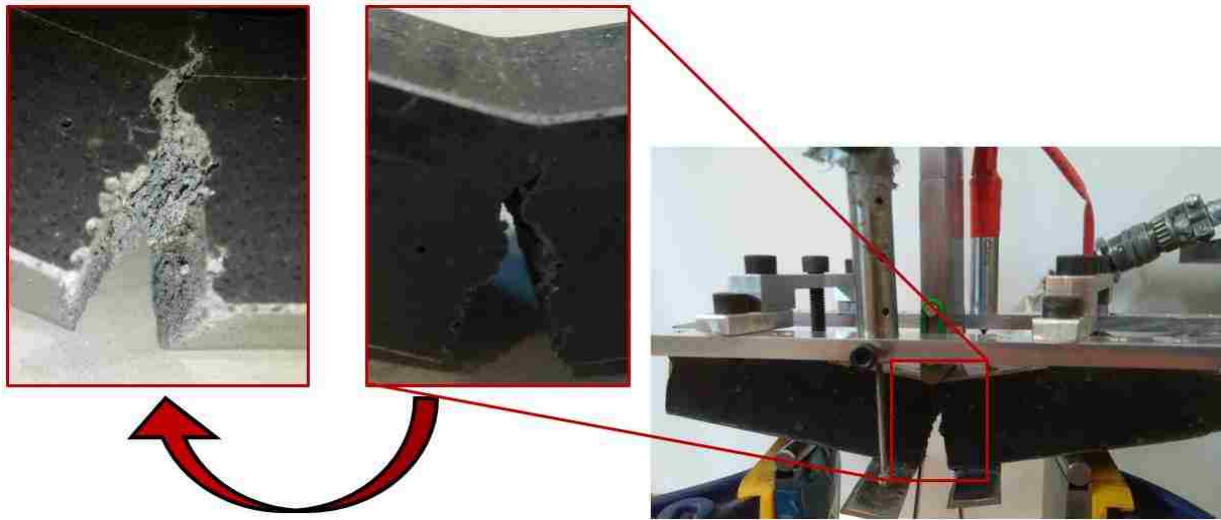


Figure 4.27: Fracture toughness test showing excessive crack mouth opening displacement (CMOD) and non-linear crack patterns.

The fracture toughness of the selected PC mixes was evaluated as described in section 3.5. During all tests, the samples exhibited slow crack propagation, excessive deformation, excessive crack mouth opening displacement (CMOD) and non-linear crack patterns as shown in Figure 4.27. Load, displacement, LVDT and CMOD were recorded for all specimens. As discussed in section 4.2.1, PC recovers deformation in slower rate than PCC. Since fracture toughness testing is dependent upon reaching the critical crack length that is strain rate sensitive, the load rates were adjusted to guarantee achieving the peak load within 3-5 minutes. The selected load rates are shown in Table 3-7 in section 3.5 describing the test setup. If the load rate was maintained constant, the high deformability of specific PC mixes can prolong initial loading up to 20 minutes allowing the formation of large FPZ. Thus, the fracture toughness of mixes with high ductility would report an overestimate of the actual values. The resulting load-CMOD curves of all specimens are shown in Figure 4.28: Crack mouth opening displacement (CMOD) – load curves for Siloxane PC (SPC) mixes containing P-MWCNTs. Figure 4.29, and Figure 4.30 for SPC mixes with P-MWCNTs,

COOH-MWCNTs and ANPs. It's important to emphasize however that the load-CMOD curves of all PC mixes show significant non-linear behavior that is uncommon to PCC. Furthermore, all SPC mixes show significantly large CMOD at failure and peak. In fact, the CMOD at peak load of all SPC mixes is in the range of 0.8 to 1.6 mm which is significantly higher than PCC's (Reda Taha et al. 2002). Mixes incorporating P-MWCNTs in general showed an increase in the CMOD at peak load with a decrease in peak load for all mixes as shown in Figure 4.28. On the other hand, PC mixes prepared with COOH-MWCNTs showed higher peak loads up to 1.5 wt.% content. A less significant increase in CMOD at peak load is also observed. Finally, PC mixes incorporating ANPs showed a decrease of peak load similar to that of P-MWCNTs except for SPC-ANP-3.0. More prominently, the CMOD value at failure significantly increased in all specimens than SPC-Neat. LEFM and QBFM using effective crack modulus and work of fracture were used in analyzing the results of this test in the below sections. However, the significant high CMOD at peak load and failure, non-linear stress-strain behavior in tension tests and the slow softening of load-CMOD curves questions the applicability of LEFM as well as K_{Ic} in describing fracture toughness of PC nanocomposites.

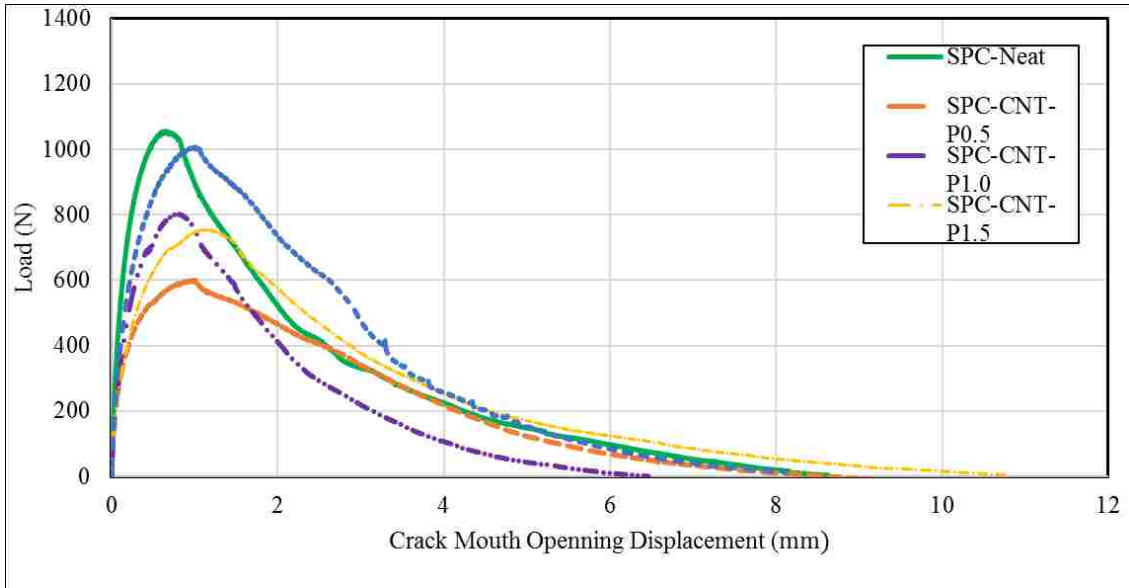


Figure 4.28: Crack mouth opening displacement (CMOD) – load curves for Siloxane PC (SPC) mixes containing P-MWCNTs.

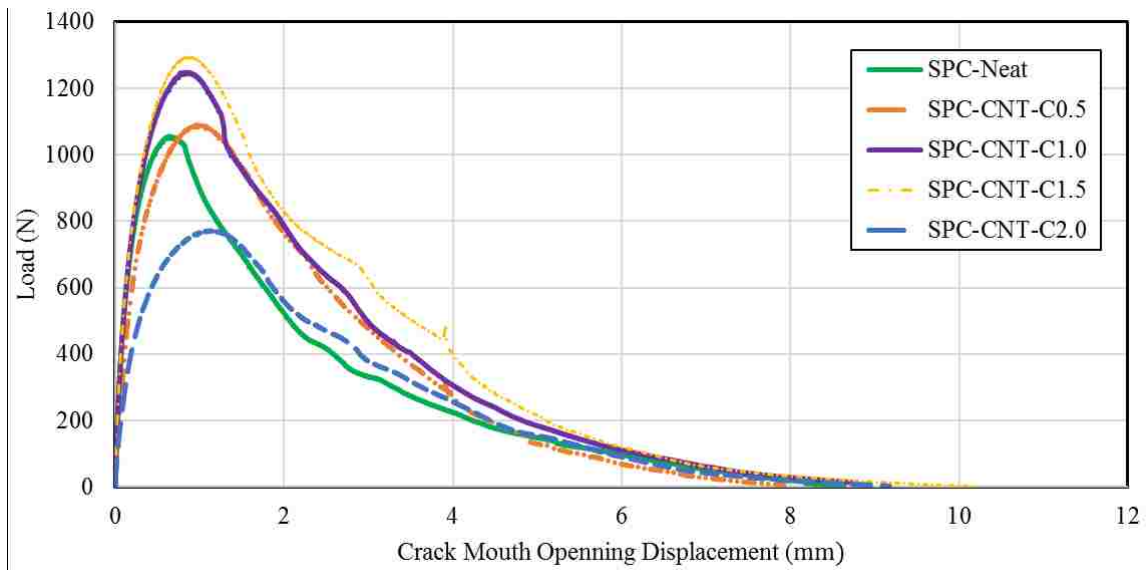


Figure 4.29: Crack mouth opening displacement (CMOD) – load curves for Siloxane PC (SPC) mixes containing COOH-MWCNTs.

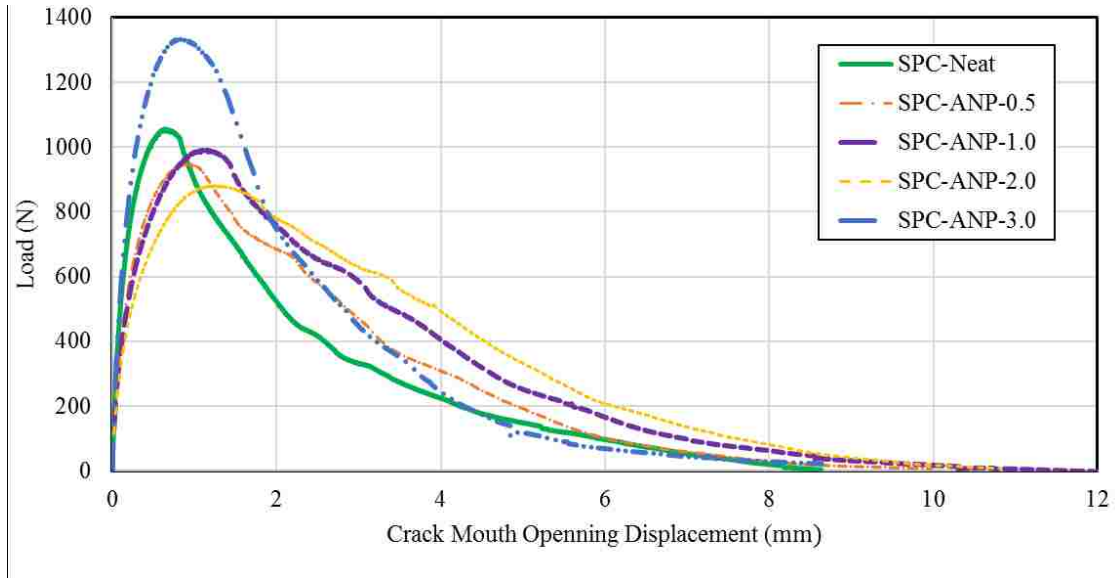


Figure 4.30: Crack mouth opening displacement (CMOD) – load curves for Siloxane PC (SPC) mixes containing ANPs.

4.3.1 Linear elastic fracture mechanics (LEFM) analysis

Using the methods of analysis described in 3.6.1 a Matlab code has been developed that appears in Appendix A.1. The resulting bilinear approximation curves generated are shown in Figure 4.31. Analysis of those curves allowed the calculation of the fracture toughness parameters and evaluate the effect of incorporating P-MWCNTs. Those results show a general increase in the fracture toughness of PC in the range of 24-73% measured by the fracture energy (G_F). To conduct the analysis, modulus of rupture values discussed in 4.2.2 and elastic modulus discussed in 4.1.4 were used. Analysis results along with the material properties extracted are shown in Table 4-1. Eq. (3.14) was then used to validate the applicability of LEFM analysis by measuring the minimum allowable dimension (l) and comparing it to the actual specimen dimensions. The measured value shown in Table 4-1 confirms that LEFM is not an applicable method of analysis as the specimen's actual minimum dimension is 8 mm (the crack length). These findings confirm to the previous discussed non-linear behavior depicted for all PC mixes depicted in load-CMOD curves as well as in tension tests.

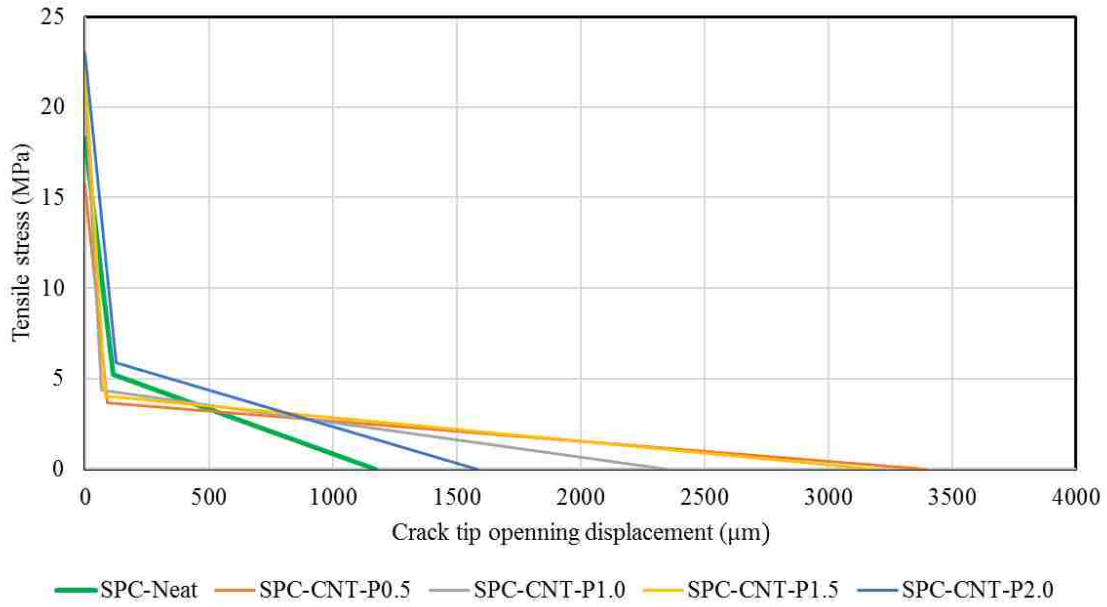


Figure 4.31: Bi-linear approximation of fracture toughness of Siloxane PC (SPC) containing P-MWCNTs.

Table 4-1: Linear elastic fracture mechanics (LEFM) analysis parameters and output.

<i>Value</i>	<i>SPC-Neat</i>	<i>SPC-CNT-P0.5</i>	<i>SPC-CNT-P1.0</i>	<i>SPC-CNT-P1.5</i>	<i>SPC-CNT-P2.0</i>
<i>E (GPa)</i>	14.2	6.07	11.2	9.37	5.53
<i>G_F (kN m/m²)</i>	4.09	6.77	5.06	7.08	5.80
<i>σ_y (MPa)</i>	16.1	8.9	10.7	10.6	10.2
<i>l (mm)</i>	560	1287	1231	1490	772

4.3.2 Quasi-brittle fracture mechanics analysis: Effective crack modulus method

As LEFM was shown to be inapplicable, a QBFM approach was chosen as described in section 3.5.2. Such method is also more suitable to quantify the non-linear behavior of PC described in section 4.2.1. Two approaches were taken to evaluate the fracture toughness of PC using QBFM namely the effective crack modulus method and work of fracture. In the effective crack modulus method, the elastic modulus of the initial specimen is equated to the elastic modulus at the critical crack length using secant compliance at maximum load. In general, quasi-brittle materials are characterized by their ability to incorporate other methods for energy consumption at the fracture process zone (FPZ). A general fracture toughness parameter, called T_{Ic} , incorporating both linear and non-linear energy release rates (G_{Ic} and J_{Ic}) is crucial to completely quantify the effect of nanomaterials. This is caused by the different effect of the various nanomaterials and contents that exhibit mechanical and chemical effects in PC. Furthermore, a linear elastic fracture toughness such as K_{Ic} is incapable of describing the change in the materials ability to resist crack propagation or crack arresting mechanisms induced by nanomaterials. Such parameter is rather more suitable to describe perfectly elastic materials. Nevertheless, Table 4-2 describes all four fracture toughness parameters of PC being K_{Ic} , G_{Ic} , J_{Ic} and T_{Ic} using the QBFM method of analysis described in section 3.5.2 and its Matlab code in Appendix A.3.

Table 4-2: QBFM analysis results using effective crack modulus

<i>Mix</i>	K_{Ic} (MPa \sqrt{m})	G_{Ic} (kN m/m ²)	J_{Ic} (kN m/m ²)	T_{Ic} (kN m/m ²)
<i>SPC-Neat</i>	2.77 ±0.56	1.63 ±0.65	3.04 ±0.55	4.67 ±1.20
<i>SPC-CNT-P0.5</i>	3.33 ±0.34	1.61 ±0.34	5.68 ±0.54	7.29 ±0.87
<i>SPC-CNT-P1.0</i>	2.69 ±0.36	0.58 ±0.15	2.63 ±0.80	3.21 ±0.95
<i>SPC-CNT-P1.5</i>	2.62 ±0.54	0.66 ±0.27	6.45 ±0.32	7.11 ±0.58
<i>SPC-CNT-P2.0</i>	3.12 ±0.56	1.57 ±0.56	5.28 ±1.34	6.85 ±1.90
<i>SPC-CNT-C0.5</i>	3.76 ±0.28	3.22 ±0.46	6.66 ±0.18	9.88 ±0.63
<i>SPC-CNT-C1.0</i>	3.85 ±0.15	2.81 ±0.23	6.67 ±0.47	9.48 ±0.69
<i>SPC-CNT-C1.5</i>	3.56 ±0.53	1.30 ±0.39	6.37 ±0.47	7.67 ±0.86
<i>SPC-CNT-C2.0</i>	3.34 ±0.64	1.07 ±0.41	7.39 ±1.46	8.46 ±1.88
<i>SPC-ANP-0.5</i>	3.12 ±0.32	2.09 ±0.45	4.69 ±1.01	6.78 ±1.46
<i>SPC-ANP-1.0</i>	2.95 ±0.17	1.50 ±0.17	6.36 ±0.77	7.86 ±0.94
<i>SPC-ANP-2.0</i>	3.12 ±0.70	1.40 ±0.65	8.25 ±1.99	9.65 ±2.64
<i>SPC-ANP-3.0</i>	4.21 ±0.42	4.14 ±0.80	6.50 ±0.56	10.64 ±1.36

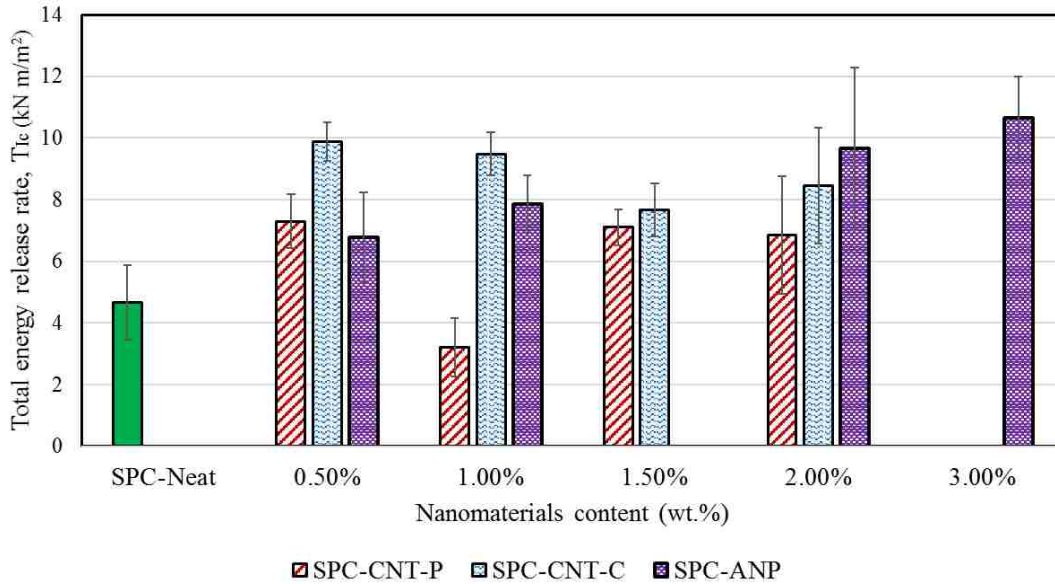


Figure 4.32: Total critical energy release rate (fracture toughness) results of quasi-brittle fracture mechanics analysis using effective crack modulus method of Siloxane PC (SPC).

Figure 4.32 shows the fracture toughness (T_{Ic}) of all selected PC mixes. It's evident that all mixes showed increase in fracture toughness in the range of 15% to 49%. An important feature evident in all mixes is that as the nanomaterials content increase the results' variation increase. This is attributed to the higher dispersion energy requirement at higher contents. Thus, causing a decrease in flowability as discussed in section 4.1 that relates to less uniformity between all samples. Nevertheless, statistical significance is present between the different contents of nanomaterials except for 0.5, 1.5 and 2.0 wt.% content of P-MWCNTs as will be discussed.

Of all mixes, the highest T_{Ic} value was that of SPC-ANP-3.0 while SPC-CNT-C0.5 showed very similar results. The energy release values obtained are significantly higher than fiber reinforced concrete and high performance concrete at 0.141 and 0.101 kN m/m² (Reda Taha et al. 2002). Furthermore, PC with nanomaterials approaches fracture toughness like that of mild steel at 12 kN m/m² (Roylance 1996). Furthermore, the recorded values are close to that reported for carbon epoxy laminates ranging from 1.0 to 4.0 kN m/m² (Davis et al. 1990, Wilkins et al. 1982,

Enchtermeyer et al. 1989 and Rusell 1985). To further depict the influence of varying the content of each of the nanomaterials investigated, the pattern against the content of PC prepared with P-MWCNTs, COOH-MWCNTs and ANPs are shown in Figure 4.33, Figure 4.34, and Figure 4.35 respectively.

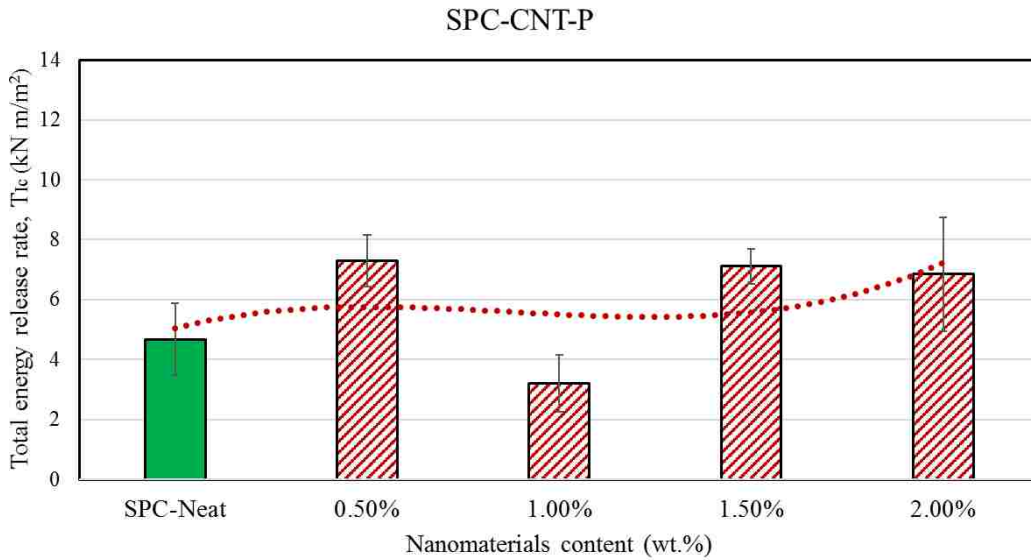


Figure 4.33: Total critical energy release rate (fracture toughness) results of quasi-brittle fracture mechanics analysis using effective crack modulus method of Siloxane PC (SPC) containing P-MWCNTs.

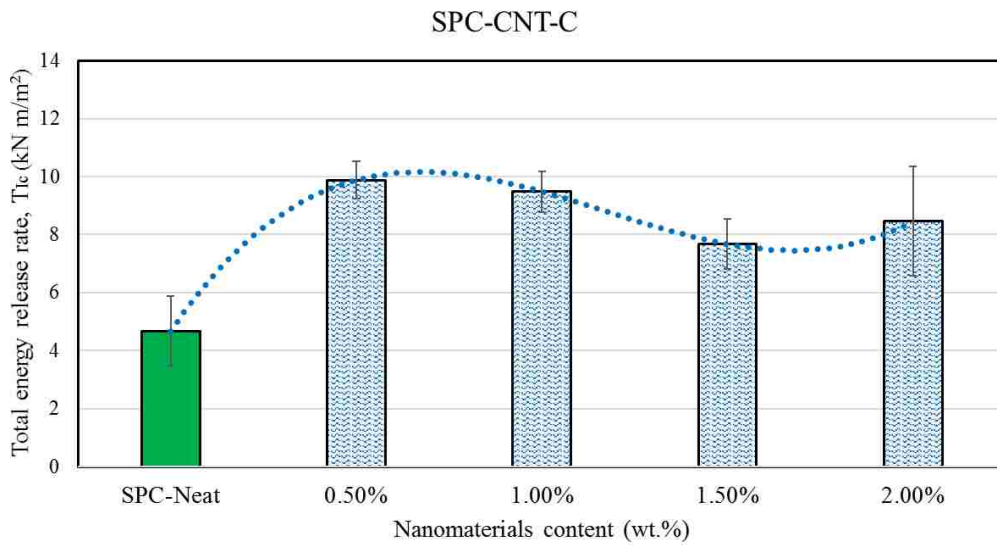


Figure 4.34: Total critical energy release rate (fracture toughness) results of quasi-brittle fracture mechanics analysis using effective crack modulus method of Siloxane PC (SPC) containing COOH-MWCNTs

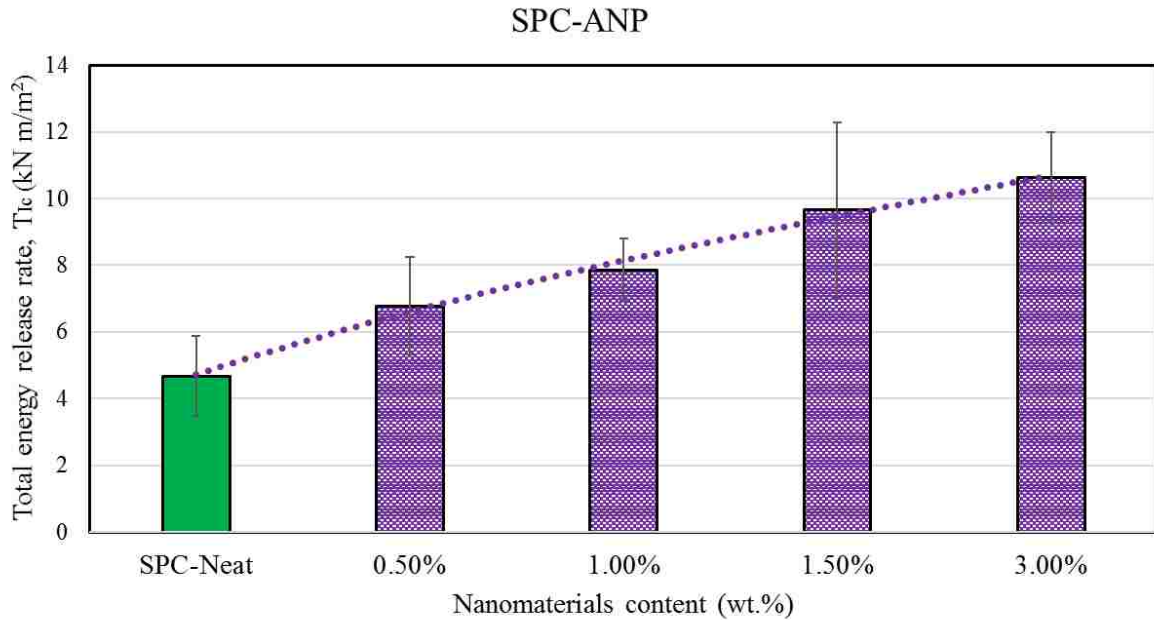


Figure 4.35: Total critical energy release rate (fracture toughness) results of quasi-brittle fracture mechanics analysis using effective crack modulus method of Siloxane PC (SPC) containing ANPS.

The trend observed for PC mixes with P-MWCNTs shown in Figure 4.33 is similar to that depicted in results of toughness in section 4.2.1.3. However, while different contents of P-MWCNTs showed varying effectiveness with toughness at different contents (varying from 0% to 75%), all contents showed an increase by $\approx 30\%$ except for SPC-CNT-P1.0 at 15% from PC-Neat. These results suggest that P-MWCNTs perform mechanical improvements in PC significantly more than chemically. This is attributed to the significantly high aspect ratio that lead to microfiber-like crack arresting mechanisms such as fiber pull-out or bridging (*Hseih et al. 2011*). Examining the elastic and plastic components of the fracture toughness of SPC-CNT-P mixes shown in Table 4-2: QBFM analysis results using effective crack modulus illustrates that at 0.5 and 2.0 wt.% contents, higher improvements are achieved in the elastic energy release rate (G_{1c}). At those contents, the values of the failure strains and toughness are also maximized as discussed previously. Therefore, the improvements in fracture toughness of SPC-CNT-P mixes is attributed to the improvements in ductility and energy absorption validating their fiber like characteristics.

Similarly, mixes incorporating COOH-MWCNTs showed similar trend to that depicted in toughness for all contents as shown in Figure 4.34. Overall, improvements in the T_{Ic} are recorded in the range of 35% to 45%. Lower contents of COOH-MWCNTs result in higher fracture toughness than higher contents. While the dominant effect of P-MWCNTs appeared in the elastic component of the energy release rate (G_{Ic}), mixes incorporating COOH-MWCNTs showed larger effect on the plastic component (J_{Ic}) as shown in Table 4-2: QBFM analysis results using effective crack modulus. The effect on this parameter was significantly present at low content and increased with increasing the content slowly. Thus, indicating that specific chemical processes affecting the FPZ is present for SPC-mixes. Furthermore, while the elastic component (G_{Ic}) increased at low contents indicating fiber like mechanisms, increasing the content resulted in rapidly decaying effect. Those findings agree with the results of toughness and ductility described in 4.2.1.2 and 4.2.1.3. Thus, the effect of COOH-MWCNTs on PC is chemically dominated rather than mechanically. Microstructural investigation examining the chemical processes that occur in PC incorporating COOH-MWCNTs discussed later can expand further on those chemical effects which is described in 4.6, 4.13 and 4.14.

Results of mixes incorporating ANPs also show similar patterns at different contents to those of toughness. In general, increasing the content of ANPs result in improving the fracture toughness (T_{Ic}). However, while in MWCNTs a dominant elastic or plastic energy release rate was present for P-MWCNTs and COOH-MWCNTs respectively, ANPs show different parameters' effect at different contents as shown in Table 4-2: QBFM analysis results using effective crack modulus. Up to 2.0 wt.% content, ANPs affect the plastic component (J_{Ic}) significantly more than the elastic component (G_{Ic}). In fact, increasing the content of ANPs shows an increase in the plastic energy release rate with small decrease in the elastic one. Thus, ANPs are expected to cause

chemical effects at those contents increasing the FPZ. At 3.0 wt.% content however, a decrease in the plastic energy release rate and an increase of the elastic one is observed compared to 2.0 wt.% content. While microstructural investigation is required to fully disclose the mechanisms occurring at each content, it's evident that fiber like behavior is achieved at 3.0 wt.% that does not present at lower contents. This can be explained by the difference of 0D vs 1D nanomaterials (ANPs vs MWCNTs) in which the high aspect ratio of MWCNTs allows fiber induced improvements that are only achieved at significantly high contents of ANPs.

4.3.3 Quasi-brittle fracture mechanics: Work of fracture

The values obtained in 4.3.2 agree with values of other scholars for carbon epoxy laminates (Davis et al. 1990, Wilkins et al. 1982, Enchtermeyer et al. 1989 and Rusell 1985). Nevertheless, a second approach using work of fracture has been used to verify QBFM behavior and the acquired results. This approach is discussed 3.6.3 and has been performed using Matlab with the code in Appendix A.2. While in 4.3.2 a total energy release rate (TIC) was required, this approach quantifies similar the quasi-brittle energy release rate using only the elastic component (G_f). Table 4 3 shows the results of this analysis for both K_{Ic} and G_f . As mentioned in 4.3.1 and 4.3.2 since the behavior of PC nanocomposites is non-linear and LEFM is not applicable, the results of the stress intensity factor K_{Ic} ca not represent the effect of nanomaterials. Therefore, the fracture toughness of all mixes is quantified through G_f alone as shown in Figure 4.36.

Table 4-3: QBFM analysis results using work of fracture.

<i>Mix</i>	K_{Ic} (MPa \sqrt{m})	G_f (kN m/m ²)
<i>SPC-Neat</i>	4.93 ±0.20	5.00 ±0.40
<i>SPC-CNT-P0.5</i>	5.86 ±0.31	4.97 ±0.53
<i>SPC-CNT-P1.0</i>	7.29 ±0.42	4.18 ±0.48
<i>SPC-CNT-P1.5</i>	8.00 ±0.48	6.02 ±0.70
<i>SPC-CNT-P2.0</i>	6.84 ±0.28	7.42 ±0.59
<i>SPC-CNT-C0.5</i>	6.16 ±0.30	8.10 ±0.44
<i>SPC-CNT-C1.0</i>	6.56 ±0.31	8.17 ±0.76
<i>SPC-CNT-C1.5</i>	8.73 ±0.47	7.71 ±0.84
<i>SPC-CNT-C2.0</i>	8.22 ±0.55	6.31 ±0.83
<i>SPC-ANP-0.5</i>	6.00 ±0.14	7.65 ±0.36
<i>SPC-ANP-1.0</i>	7.23 ±0.41	9.03 ±1.04
<i>SPC-ANP-2.0</i>	7.55 ±0.39	7.91 ±0.79
<i>SPC-ANP-3.0</i>	6.13 ±0.23	8.70 ±0.65

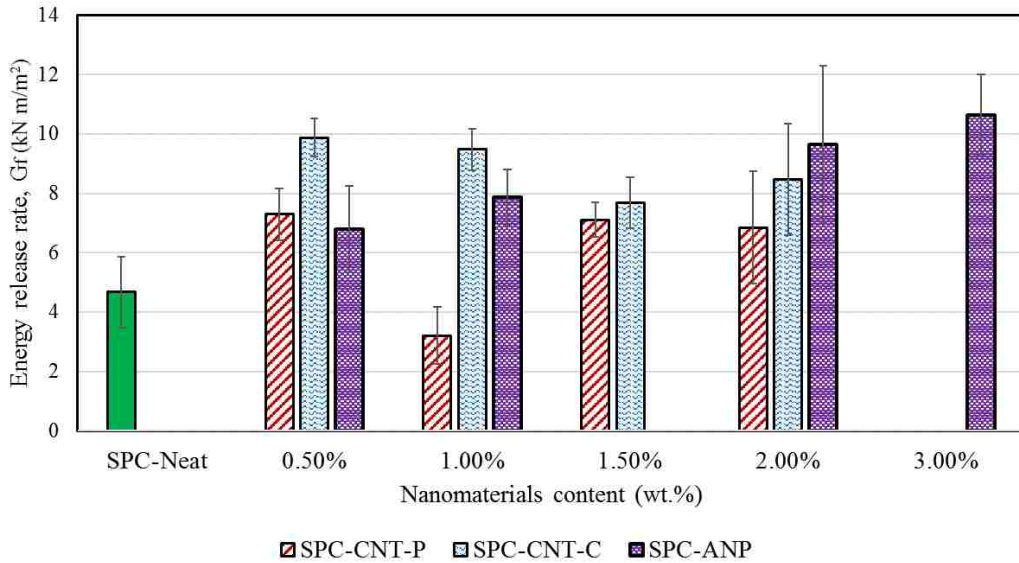


Figure 4.36: Energy release rate (fracture toughness) results of quasi-brittle fracture mechanics analysis using work of fracture method of Siloxane PC (SPC).

Similar results to those obtained in 4.3.2 are obtained using work of fracture approach as depicted in Figure 4.36. Furthermore, the variation of results obtained using this approach is like the values obtained in the previous sections in which the variance increase by increasing the nanomaterials content. Varying the content of each nanomaterial result in statistically different measurement except for PC mixes containing 0.5, 1.0 and 1.5 wt.% P-MWCNTs content as well as 0.5 and 1.0 wt.% ANPs. The values obtained through this method of analysis are in significant agreement with the result achieved in 4.3.2. The patterns of both QBFM approaches for P-MWCNTs, COOH-MWCNTs and ANPs are shown in Figure 4.37, Figure 4.38, and Figure 4.39.

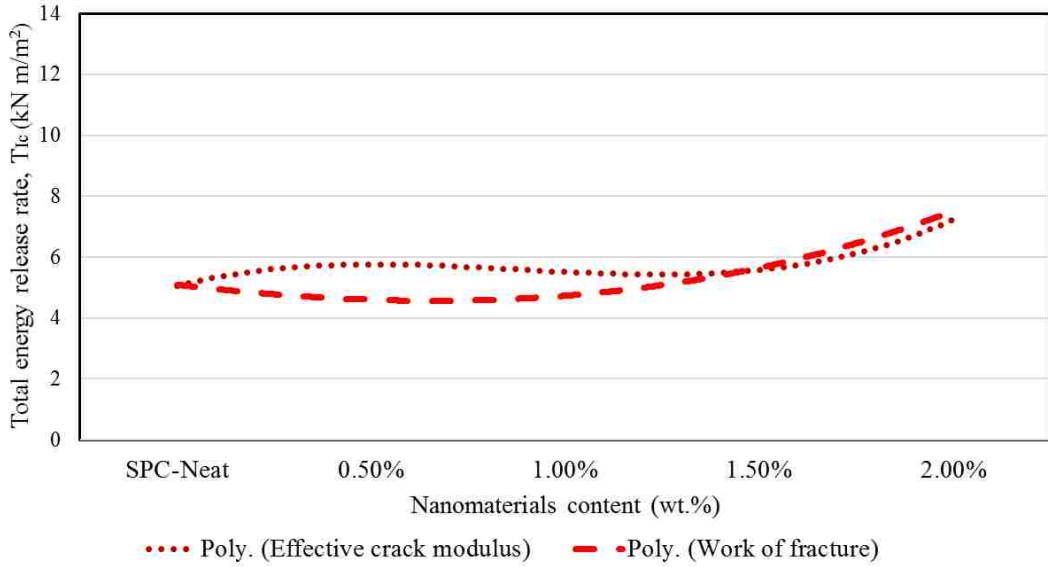


Figure 4.37: Comparison of quasi-brittle fracture mechanics models results of fracture toughness (measured with energy release rates) between effective crack modulus and work of fracture for Siloxane PC (SPC) containing P-MWCNTs.

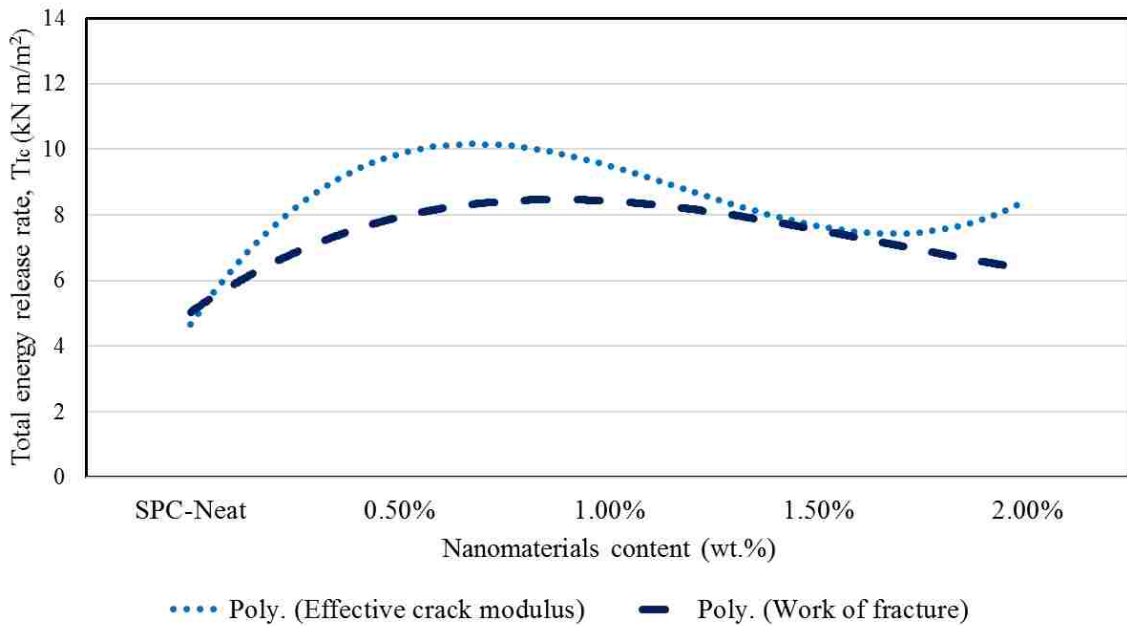


Figure 4.38: Comparison of quasi-brittle fracture mechanics models results of fracture toughness (measured with energy release rates) between effective crack modulus and work of fracture for Siloxane PC (SPC) containing COOH-MWCNTs.

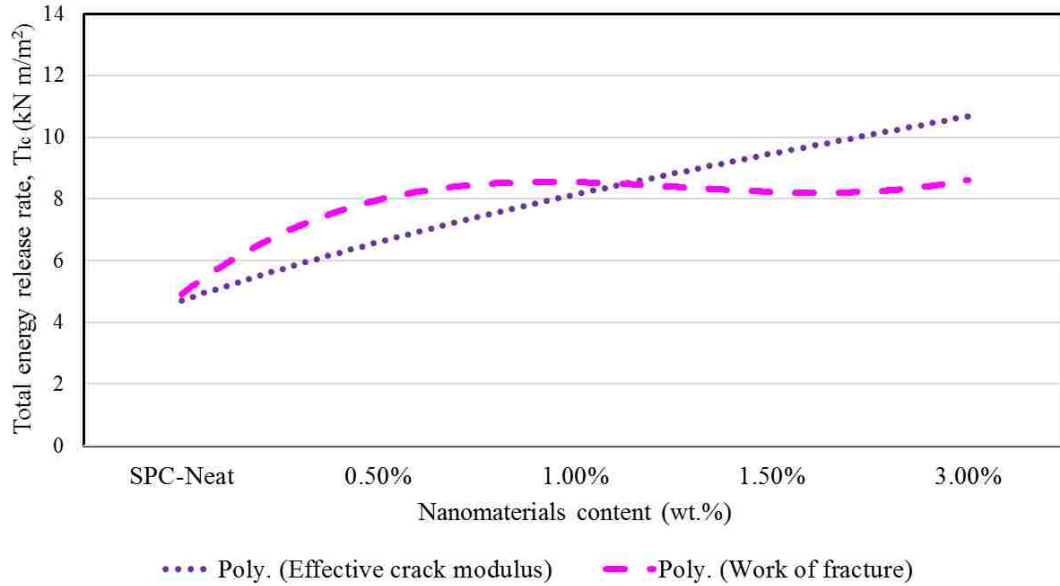


Figure 4.39: Comparison of quasi-brittle fracture mechanics models results of fracture toughness (measured with energy release rates) between effective crack modulus and work of fracture for Siloxane PC (SPC) containing ANPs.

In general, both QBFM methods predict similar results and are within 30% of each other. SPC-Neat in fact shows only 7% difference between both methods. It can be concluded therefore that the behavior of PC and PC nanocomposite can be well quantified using QBFM. Mixes incorporating P-MWCNTs showed the highest variation in results between both methods specifically at 0.5 wt.% content. That is, work of fracture method of analysis shows insignificant changes from that of SPC-Neat whereas the effective crack modulus shows significant improvement up to 50%. Higher P-MWCNTs content however show similar effect when compared to SPC-Neat for both analysis methods. Mixes incorporating COOH-MWCNTs also show similar pattern between both methods of analysis. However, at 2.0 wt.% content compared to their respective SPC-Neat results, work of fracture predicts significantly larger values than that of elastic crack modulus by 55%. Finally, specimens prepared with ANPs show strong agreement only at 0.5 and 2.0 wt.% contents. At 1.0 and 3.0 wt.% content work of fracture predicts an increase in fracture toughness compared to SPC-Neat by 49% and 54% respectively.

While both methods of analysis predict similar range of values and show similar variational patterns with respect to the nanomaterials content. The more detailed effective crack modulus approach predicts more conservative values for the fracture toughness of PCNC. In that method, the different mechanisms (mechanical and chemical) of the different nanomaterials in which the elastic and plastic energy release parameters are identified. In work of fracture however only the final fracture toughness is established regardless whether the elastic or FPZ energy requirements are altered. Nevertheless, both QBFM methods of analysis are more accurate than LEFM as they incorporate the non-linear behavior of PC and large CMOD values.

4.4 Fatigue test

Table 4-4: Mechanical properties of selected SPC mixes for fatigue test.

<i>PC mix</i>	<i>Tensile strength (MPa)</i>	<i>Strain at failure (%)</i>	<i>Elastic modulus, E (GPa)</i>	<i>Toughness (kJ/m³)</i>	<i>QBFM-effective crack, T_{Ic} (kN m/m²)</i>	<i>QBFM-work of fracture, G_{Ic} (kN m/m²)</i>
<i>SPC-Neat</i>	11.80	1.85	4.27	176	4.67	5.00
<i>SPC-CNT-P2.0</i>	10.20	2.90	5.53	221	6.85	7.42
<i>SPC-ANP-2.0</i>	11.40	3.60	6.33	365	9.65	7.91

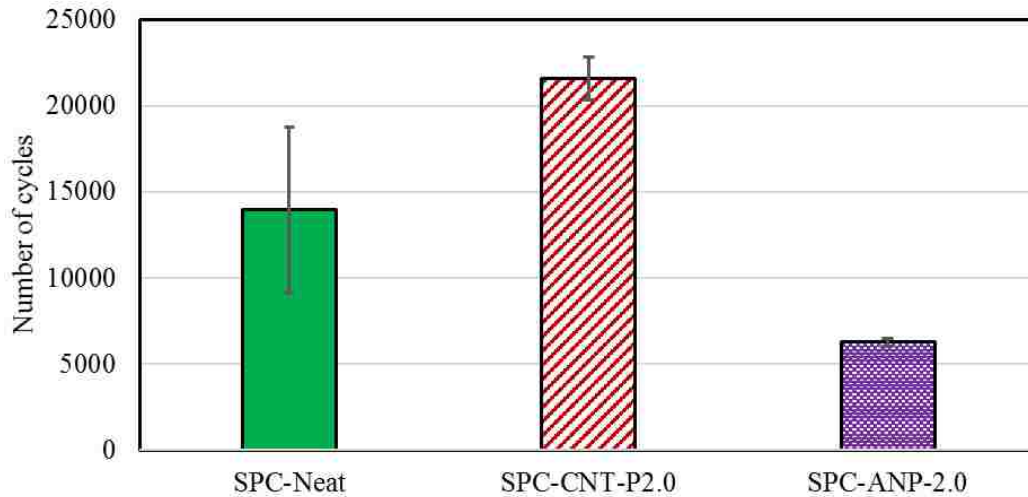


Figure 4.40: Fatigue test results of selected SPC mixes.

The previous sections showed that SPC mixes incorporating 2.0 wt.% P-MWCNTs, 3.0 wt.% ANPs and 0.5 wt.% COOH-MWCNTs provided the best performance for each of type of PCNC. Since COOH-MWCNTs and P-MWCNTs have the same geometrical features, provided similar fracture toughness and P-MWCNTs outperformed COOH-MWCNTs in ductility, only SPC-CNT-P2.0 was selected at this stage of all MWCNTs PCNC mixes. Further investigation on the functionalization effect on mechanical performance is discussed in section 4.6. To allow comparison between ANPs and MWCNTs and to accommodate the limitations discussed in section 3.6, the content of both nanomaterials must be similar. Since SPC-ANP-2.0 provided similar results to that of 3.0 wt.% content, it was also selected for this stage. Table 4-4 summarizes the mechanical performance of the selected mixes namely SPC-CNT-P2.0 and SPC-ANP-2.0 compared to SPC-Neat. The number of cycles required to produce 50% decrease in stiffness from the 50th cycle representing the fatigue life of PC are shown in Figure 4.40. Incorporating P-MWCNTs showed improvements in fatigue life by 55% while ANPs showed a decrease by 50%. Since both mixes showed similar mechanical performance in tension, elastic modulus, and fracture toughness and since both are non-functionalized nanomaterials, the effect in fatigue life can be

related to their geometrical properties. MWCNTs provide large aspect ratio (as 1D nanomaterials) while ANPs are completely in the nanoscale (as 0D nanomaterials). Therefore, MWCNTs can provide high crack arrest as well as crack branching resulting in more gradual loss of stiffness. While ANPs are also successful in improving the fracture toughness of PC, they do not provide any mechanical crack arresting mechanisms due to their short length. Therefore, it's evident that while two different types of nanomaterials can induce similar mechanical properties, the change in their physical and geometrical properties can significantly differ their effect in fatigue life and stiffness degradation.

4.5 Structural health monitoring (SHM)

The first step in this investigation was to evaluate the percolation limit of the selected SPC mixes. The percolation test aids in determining which of the examined PCNC mixes produce PC with sufficient conductivity that enables accurate monitoring of performance. No prior work was reported for conductive epoxy or polymers prepared with ANPs while some were reported for MWCNTs as discussed in section 2.3.8. Therefore, at this stage of SPC testing, only those mixes prepared with P-MWCNTs and COOH-MWCNTs were examined. The electrical and damage features were measured for SPC specimens at percolation limits during flexural test.

Structural health monitoring (SHM) was recorded for SPC as discussed in section 3.7. Monitoring was performed by defining an electrical damage feature $\lambda_e(t)$ representing the change in electrical resistivity/conductivity as defined in Eq. (4.1). The structural health was defined using mechanical damage feature (D_m) described in Eq. (4.3) based on the flexural rigidity (EI) defined in Eq. (4.2). In these equations, $EI(i)$ is the specimen flexural rigidity at any cycle i , E is the modulus of elasticity, I is the cross sectional second moment of inertia, $\Delta P(i)$ is the difference

between maximum and minimum loads at the same cycle, $\Delta\delta(i)$ is the corresponding difference between displacements, L is the span length of 175 mm, $D_m(i)$ is the fatigue damage in %, and $EI(0)$ is the initial flexural rigidity.

$$\lambda_e(t) = \frac{R(t) - R(t_0)}{R(t_0)} \quad (4.1)$$

$$EI(i) = \left(\frac{5}{288}\right) * \frac{\Delta P(i) * L^3}{\Delta \delta(i)} \quad (4.2)$$

$$D_m(i) = 1 - \frac{EI(i)}{EI(0)} \quad (4.3)$$

4.5.1 Percolation test

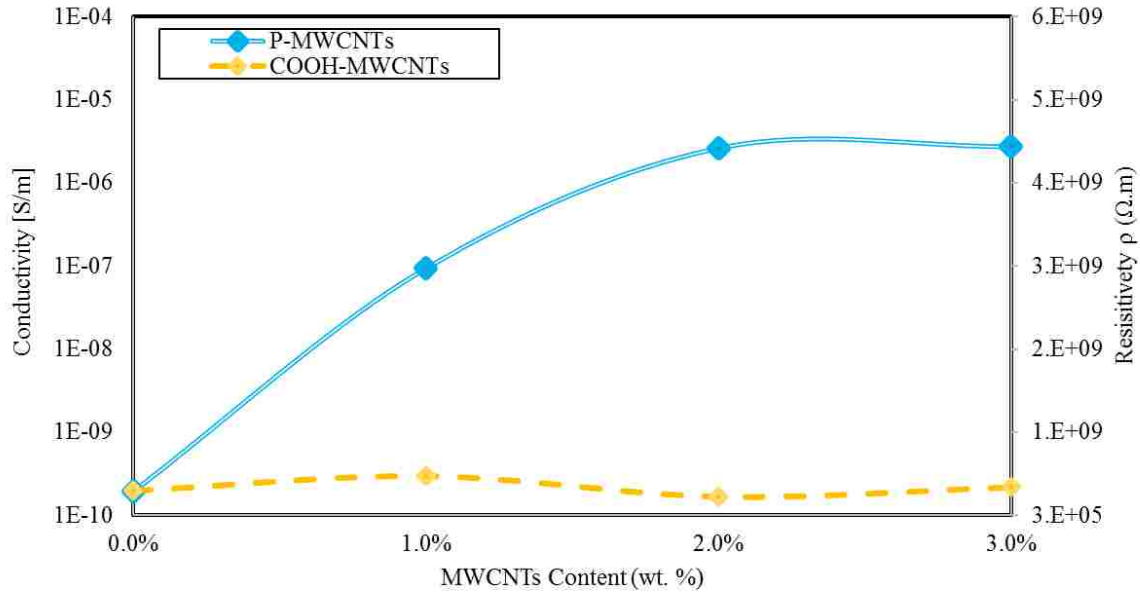


Figure 4.41: Percolation test for Siloxane epoxy containing P-MWCNTs and COOH-MWCNTs.

The percolation test was aimed to determine the optimum content of MWCNTs that enables sufficient and accurate electrical conductivity measurements. For this test, Siloxane epoxy coupons prepared with P-MWCNTs or COOH-MWCNTs at 1.0, 2.0 and 3.0 wt.% content were measured and results are shown in Figure 4.41. Incorporating COOH-MWCNTs show no change in electrical

conductivity while coupons prepared with P-MWCNTs show an increase in conductivity with content increase. At 2.0 wt.% content, the percolation limit is achieved at 3.0×10^{-6} S/m at three orders of magnitude higher than neat epoxy. Up to 2.0 wt.% P-MWCNTs content, an increase in content corresponds to an increase in electrical conductivity. Higher P-MWCNTs content however results in an insignificant increase in conductivity. Therefore, SPC-CNT-P2.0 was selected to be examined for SHM in the next stage. SPC-Neat was also tested to provide a reference sample expressing SHM of PC with low conductivity.

4.5.2 SHM in flexure

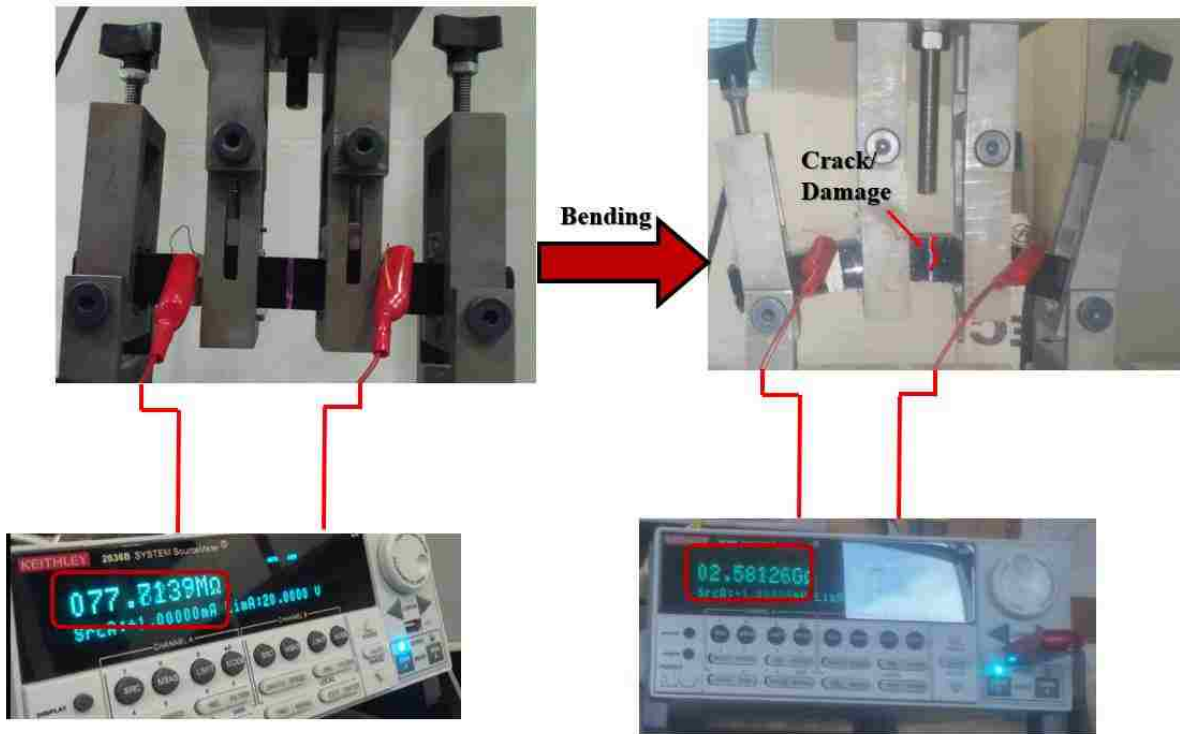


Figure 4.42: SHM of SPC-CNT-P2.0 in flexure

Flexural test using four-point bending where PC prisms were connected to electrical conductivity measuring device was performed for SPC-Neat and SPC-CNT-P2.0. Plastic plates were attached to the locations of contact between PC and the loading frame to eliminate any interference. The change in electrical conductivity, load and displacement were recorded for each

sample as shown in Figure 4.42. Eq. (4.1) – Eq. (4.3) were then used to quantify mechanical and electrical damage features of the collected data.

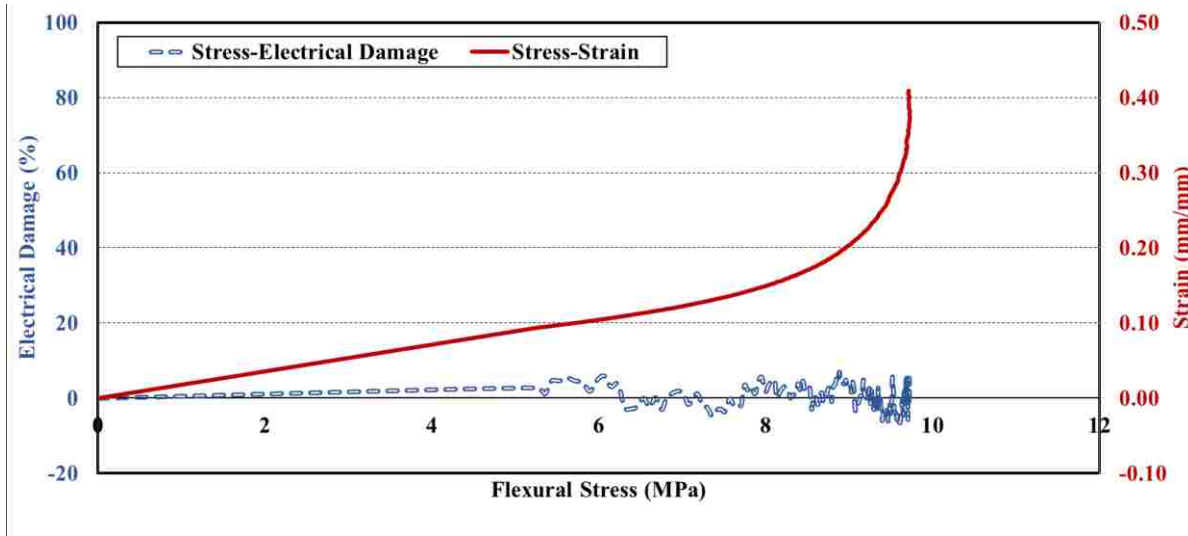


Figure 4.43: Electrical damage feature and strain in flexure test of SPC-Neat vs flexural stress.

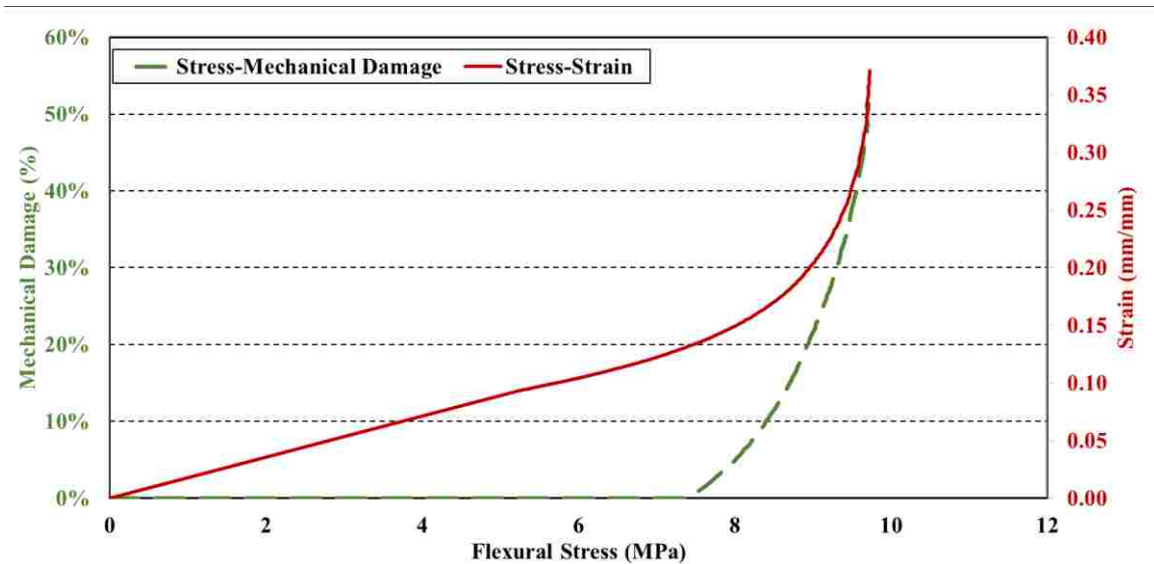


Figure 4.44: Mechanical damage feature and strain in flexure test of SPC-Neat vs flexural stress.

The flexural stress-strain of SPC-Neat was recorded along with the electrical and damage features. Results of this sample are used to validate the damage feature calculation and demonstrate the significance of MWCNTs in increasing PC's conductivity. The electrical conductivity in neat

samples is too low in which damage and cracking do not alter the electrical conductivity. Therefore, the electrical feature in Figure 4.43 shows no change with the increase in flexural stress or strain. The mechanical damage feature described in Eq. (4.2) and (4.3) shows good prediction of flexural strain as depicted in Figure 4.44. At stress values below yield, the displacement/strain observed in SPC-Neat is considered purely elastic and no mechanical damage is observed. Higher stresses however result in increasing the damage up to 50% at which failure occurs. The higher damage feature percentage indicate the high deformation of SPC-Neat reported in section 4.2.2. The results of SPC-Neat with mechanical damage by measuring the change in flexural rigidity therefore can be considered as an accurate measure.

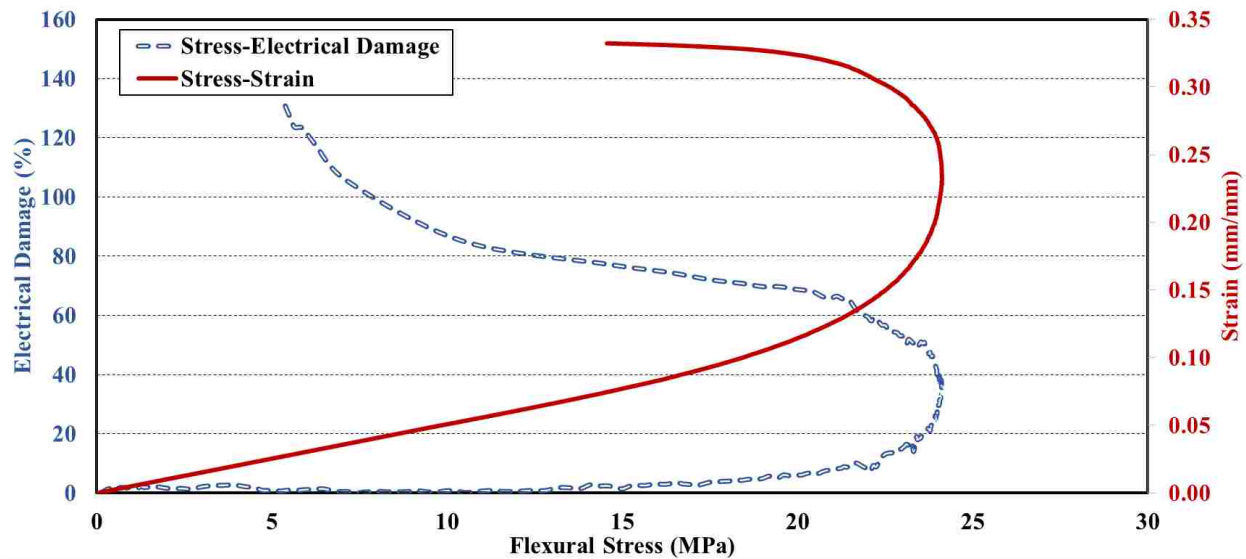


Figure 4.45: Electrical damage feature and strain in flexure test of SPC-CNT-P2.0 vs flexural stress.

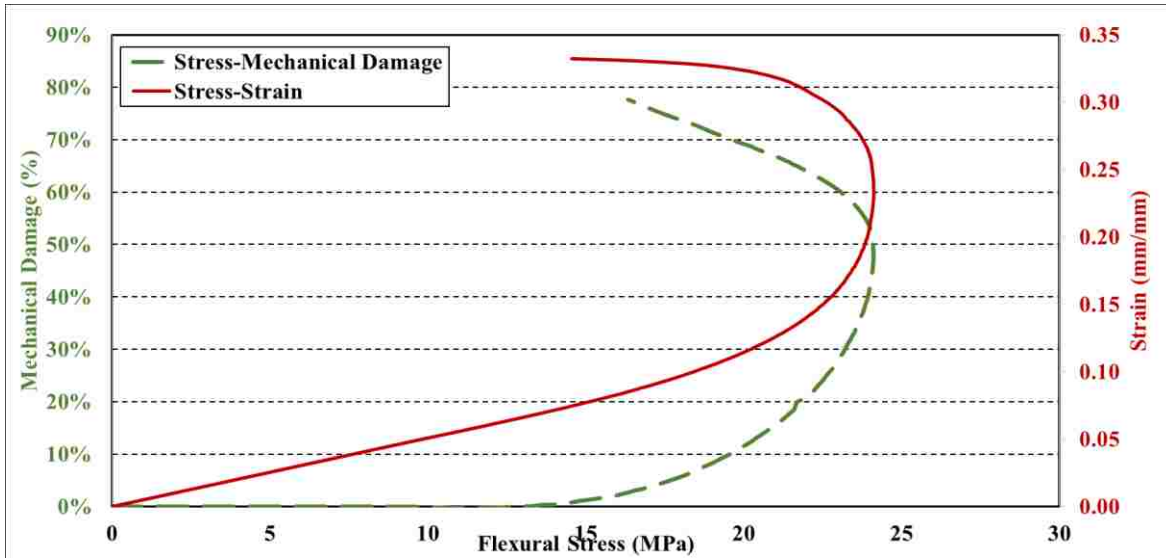


Figure 4.46: Mechanical damage feature and strain in flexure test of SPC-CNT-P2.0 vs flexural stress.

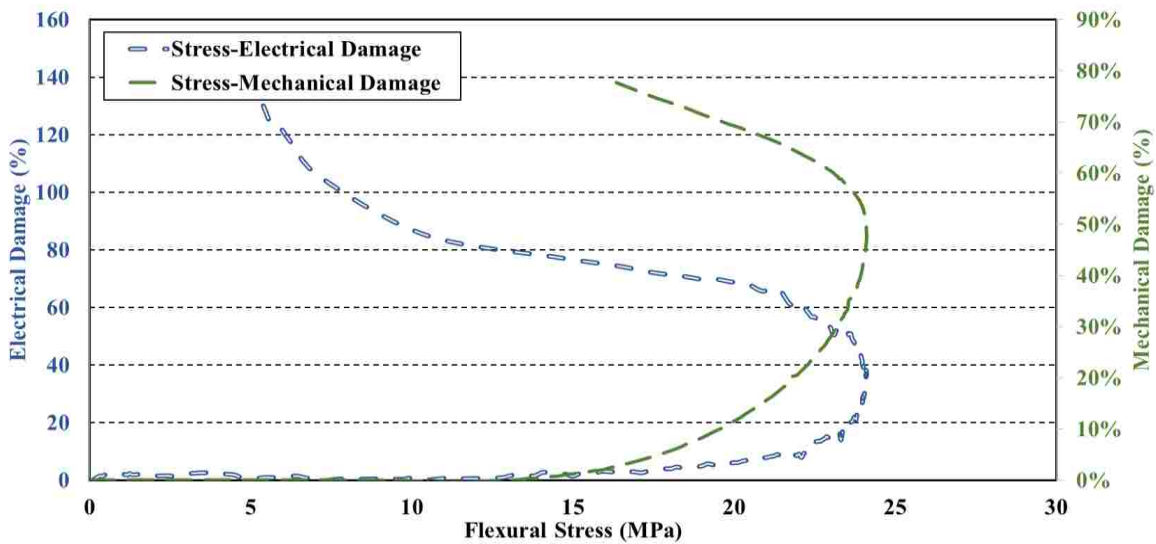


Figure 4.47: Electrical and Mechanical damage feature in flexure test of SPC-CNT-P2.0 vs flexural stress.

Stress-strain of SPC-CNT-P2.0 were plotted against the electrical and mechanical damage features as shown in Figure 4.45 and Figure 4.46. It's evident that PC incorporating 2.0 wt.% P-MWCNTs content produce sufficient conductivity that is sensitive to flexural strain as shown in Figure 4.45. The electrical damage feature shows that as PC strains, get damaged and cracks, the electrical conductivity decrease increasing the resistance $R(t)$. Therefore, it's evident that P-MWCNTs at 2.0 wt.% content (percolation limit) produce electrically conductive PC. The

mechanical damage feature verified with SPC-Neat shows strong agreement with the flexural strain. At flexural stress below yield the mechanical damage maintains 0%. Increasing the flexural stress however result in cracking of PC reducing flexural rigidity and corresponding to higher mechanical damage values. Since SPC-CNT-P2.0 has an increased failure strain and deformability, the mechanical damage feature extends to higher values than that of SPC-Neat reaching 80% compared to 50%. Finally, the electrical and mechanical damage features were plotted together against flexural stress as shown in Figure 4.47. It's evident that the electrical conductivity of PC prims change with respect to mechanical damage. However, since the electrical damage feature has not been calibrated to the mechanical damage, a shift between the two is observed. Hence, calibration was performed by shifting the electrical damage by a factor of 0.53 and the corresponding result is shown in Figure 4.48. When calibrated, the electrical damage feature accurately predicts mechanical damage. The increase of load during static flexural loading corresponds to an increase in microcrack development within the matrix. Such cracks result in decreasing P-MWCNTs network resulting in smaller conductivity measurement.

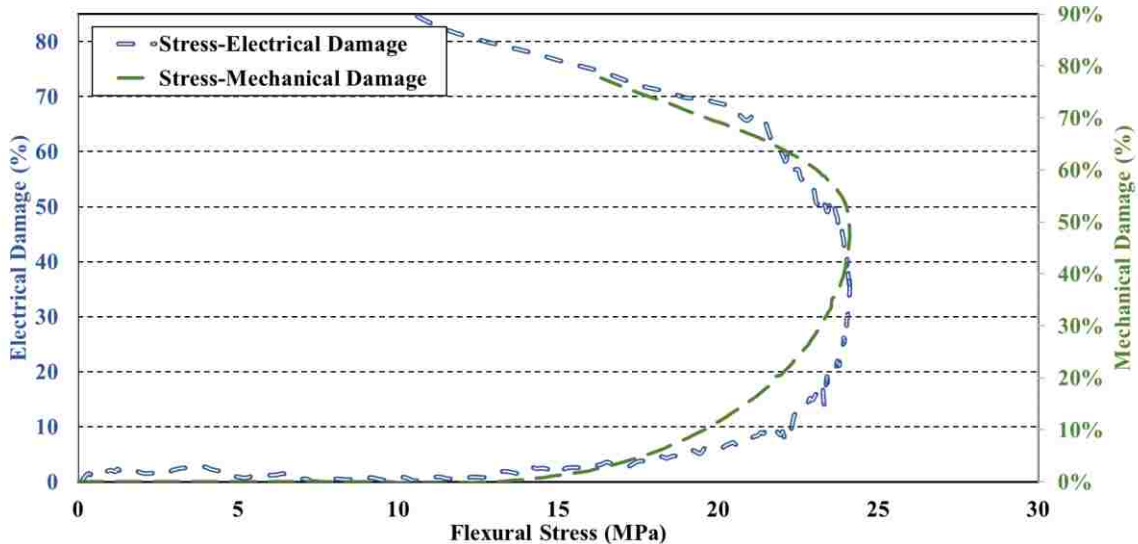


Figure 4.48: Calibrated electrical damage feature to the mechanical damage feature for SPC-CNT-P2.0

4.6 Functional group analysis

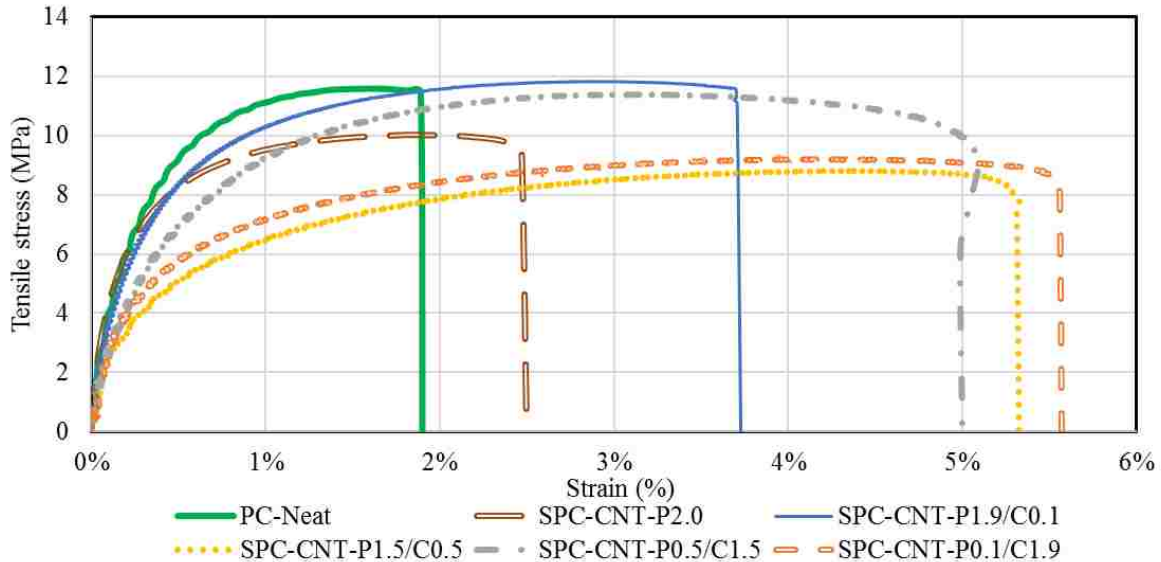


Figure 4.49: Tensile stress-strain curves of SPC mixes of hybrid P-MWCNTs and COOH-MWCNTs at 2.0 wt.% total content.

To facilitate dispersion, MWCNTs and nanomaterials are often surface functionalized with selected functional groups to generate repelling forces improving their dispersion and fluid suspension. Functionalization can also be utilized per the chemical reaction of the functional group with the host matrix in which polymerization either is improved or restricted. This section is designated to examine the effect of functionalization by measuring the tensile properties and the level of influence of the functional group content in PCNC. The content of MWCNTs was specified at 2.0 wt.% and the functional group content was varied by mixing P-MWCNTs and COOH-MWCNTs at different ratios of 0.1, 0.5, 1.5, 1.9 and 2.0 wt.%. Those ratios were selected based on the results of previous sections in which SPC-CNT-0.5, SPC-CNT-P2.0, SPC-CNT-C0.1 and SPC-CNT-C2.0 provided significant and key tensile properties. Furthermore, since MWCNTs are incorporated with respect to their weight, higher total content allows for more accurate measurement of the specific MWCNTs at 0.1 wt.% content. The tensile stress-strain curves of this investigation are shown in Figure 4.49.

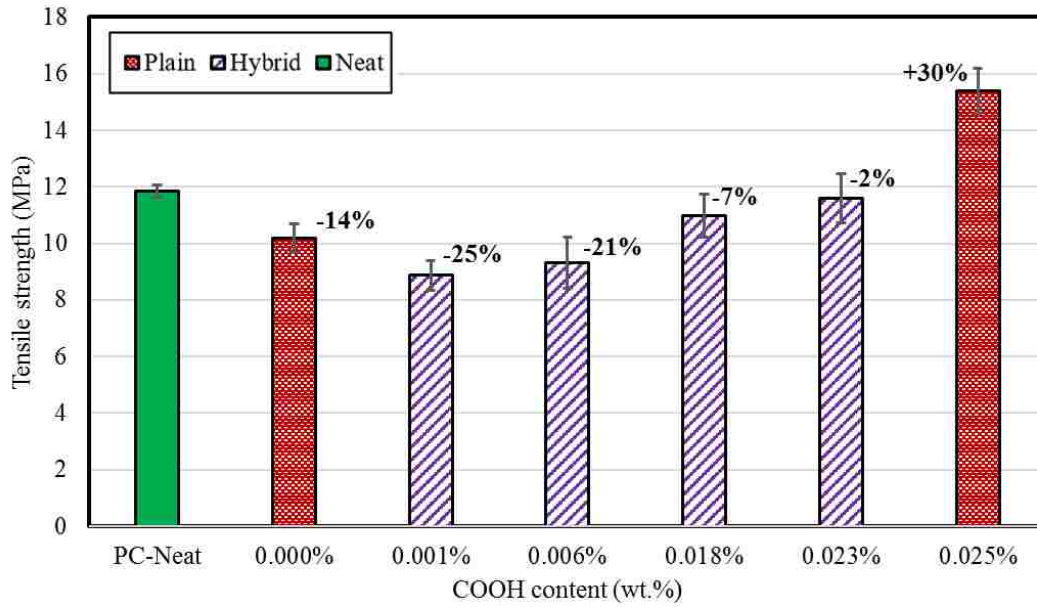


Figure 4.50: Tensile strength of SPC mixes at 2.0 wt.% MWCNTs content including P-MWCNTs, COOH-MWCNTs or mix of both.

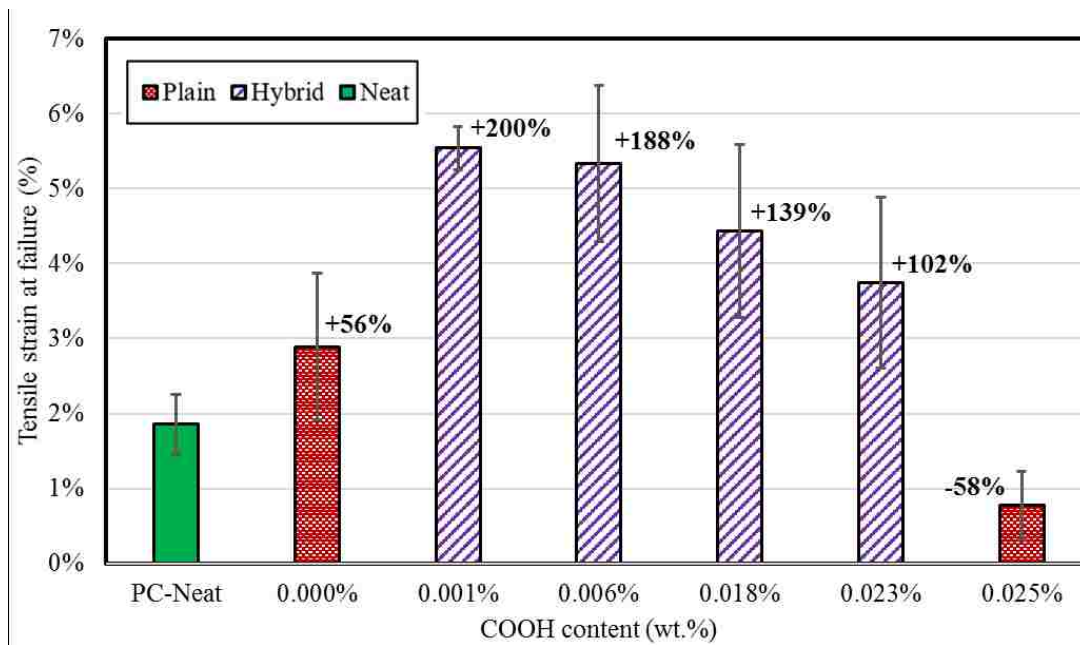


Figure 4.51: Tensile strain at failure of SPC mixes at 2.0 wt.% MWCNTs content including P-MWCNTs, COOH-MWCNTs or mix of both.

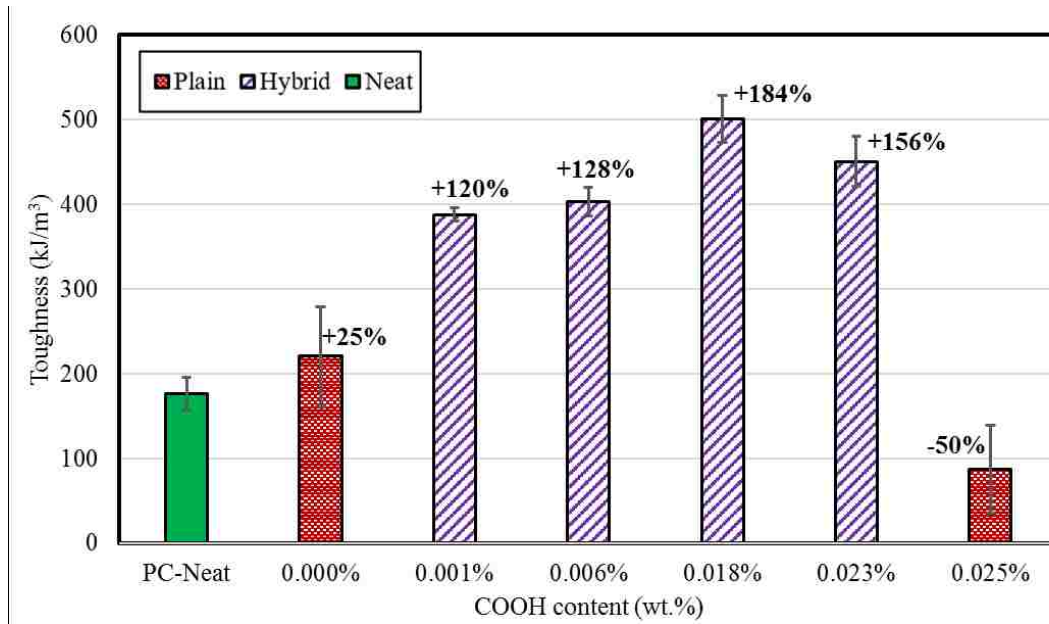


Figure 4.52: Toughness of SPC mixes at 2.0 wt.% MWCNTs content including P-MWCNTs, COOH-MWCNTs or mix of both.

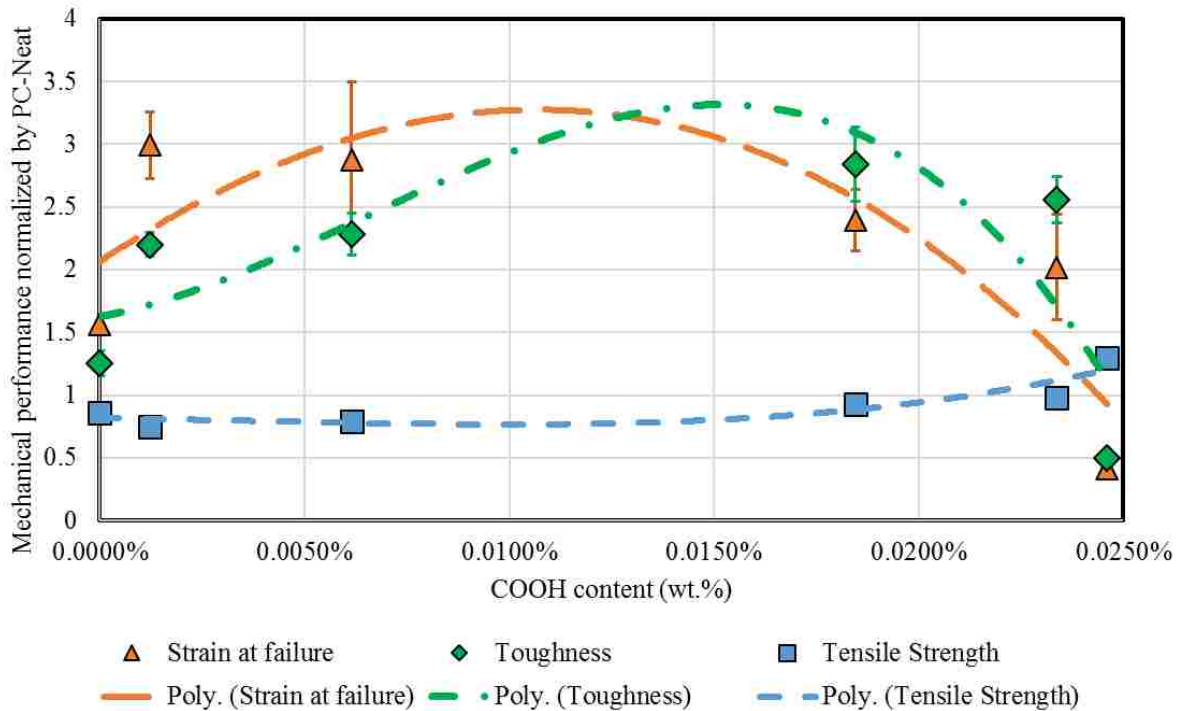


Figure 4.53: Mechanical performance of SPC mixes normalized by SPC-Neat (11.8 MPa, 1.85%, 176.3 kJ/m³) with respect to COOH weight content of epoxy resin at 2.0 wt.% total MWCNTs content.

Analysis of the stress-strain diagrams with respect to the COOH-content is shown in Figure 4.50, Figure 4.51 and Figure 4.52 for their tensile strength, strain at failure and toughness. Different

contents of P-MWCNTs and COOH-MWCNTs result in significantly different mechanical properties of PC. The best performing in tensile strength, strain at failure and toughness are mixes containing 2.0 wt.% COOH-MWCNTs, 1.9 wt.% P-MWCNTs with 0.1 wt.% COOH-MWCNTs, and 0.5 wt.% P-MWCNT with 1.5 wt.% COOH-MWCNTs respectively. At COOH contents under 0.018 wt.% (1.5 wt.% COOH-MWCNTs), a decrease in tensile strength in the range of 14% to 25% is observed. The lowest mean tensile strength was found to be of SPC-CNT-P1.9/C0.1 at 8.9 MPa. This is explained by previous results as SPC-CNT-C0.1 provided the lowest tensile strength of all SPC-CNT-C mixes. On the other hand, the highest tensile strength of PC was that of SPC-CNT-C2.0 of 15.4 MPa. Incorporating MWCNTs without functionalization result in reduced tensile strength. By introducing COOH onto MWCNTs, the tensile strength of PC with MWCNTs increase with increasing COOH content surpassing neat at concentrations greater than 0.023 wt.%.

Hybrid mixes showed significantly improved ductility than plain mixes of MWCNTs as well as previously discussed ANPs mixes as well as shown in Figure 4.51. By simultaneously incorporating 0.1 wt.% of P-MWCNTs and 1.9 wt.% of COOH-MWCNTs, PC attained extremely high and unprecedented strain at failure reaching a maximum of 5.5%; an order of magnitude higher than that of PCC (*Swaddiwudhipong et al. 2003*). The resulting value is 200% higher than that of PC-Neat as well. On the other hand, SPC-CNT-C2.0 which achieved the highest tensile strength showed the lowest tensile strain at failure of all PC mixes at 0.8%. This decrease represents 58% decrease in tensile strain from SPC-Neat and translates to a 50% decrease in toughness. All other PC mixes showed increase in toughness regardless of their tensile strength as shown in Figure 4.52. The highest toughness of SPC-CNT-P0.5/C1.5 represents 184% increase from SPC-Neat due to 139% increase in strain at failure with negligible 7% decrease in tensile strength. It's important to emphasize that all hybrid mixes incorporating both P-MWCNTs and

COOH-MWCNTs at 2.0 wt.% total content showed significantly improved performance than plain 2.0 wt.% mixes in tensile strain at failure and toughness. Further analysis of the mechanical performance of all hybrid mixes normalized by SPC-Neat is shown in Figure 4.53. In general, PC incorporating 2.0 wt.% MWCNTs shows minimal decrease of tensile strength maintain at least 9 MPa which is sufficient for all PC applications. The impact of functionalization however is critical on the ductility and toughness of PCNC mixes. The pattern results suggest that an optimal COOH content in the range of 0.006 to 0.018 wt.% can maximize PC's strains at failure and toughness. Further analysis on functionalization is discussed later examining the various chemical reactions present in sections 4.13 and 4.14.

4.7 Slant shear test

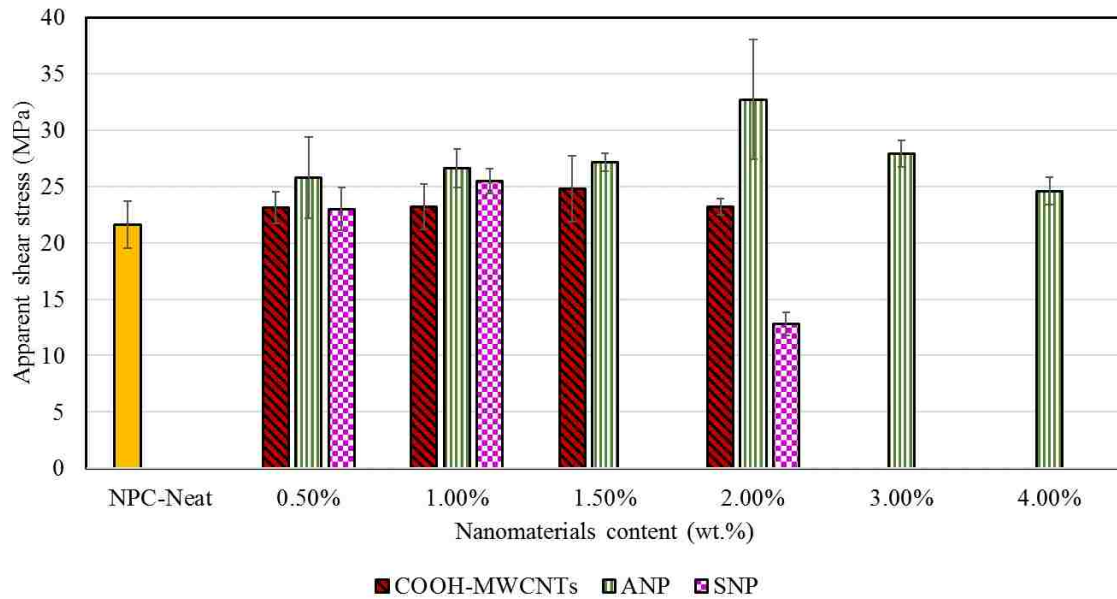


Figure 4.54: Apparent shear stress of Novolac PC (NPC) mixes using slant shear test.

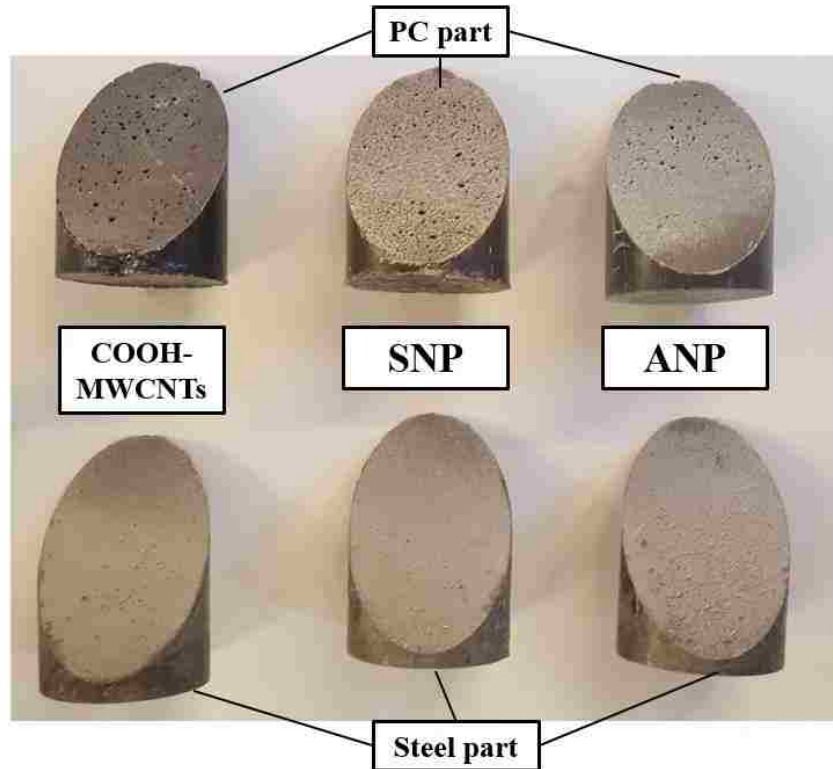


Figure 4.55: Slant shear fracture surface post-failure for Novolac PC (NPC) samples at 2.0 wt.% content of their respective nanomaterials content.

Apparent shear/bond strength results of slant shear tests of NPC and steel are shown in Figure 4.54. All test specimens failed at the adhesion interface and no cohesive failure (within each part) was observed as shown in Figure 4.55. For all NPC samples, failure was sudden and rapid in which the each of the slant shear test parts rapidly dissembled upon failure. The analysis described in section 4.10 will further discuss that at failure, all samples reached the energy criteria G_{II} . Nevertheless, incorporating nanomaterials to NPC proved to increase the apparent bond strength compared to NPC-Neat. Mixes incorporating COOH-MWCNTs at 0.5, 1.0 and 2.0 wt.% showed a constant increase of 7%. Thus, no advantage of incorporating higher content of COOH-MWCNTs is achieved beyond 0.5 wt.%. Mixes incorporating ANPs showed an increase in apparent bond strength up to 51% at 2.0 wt.% content with increasing the content. Higher ANPs content however resulted in a decrease from that of NPC-ANP-2.0. This can be attributed to the

possible chemical reaction of ANPs with -OH group formed on sand blasted steel surface (Zhai *et al.* 2006). Finally, mixes incorporating SNPs showed an increase with the apparent bond strength up to 18% at 1.0 wt.% content. Increasing SNPs content showed a rapid decrease in apparent bond strength with 41% decrease. The decrease at 2.0 wt.% content of SNPs that is also observed to a lessened level at 3.0 and 4.0 wt.% of ANPs can be attributed to their respective dimensions. SNPs have significantly smaller particle size (average of 7 nm) than ANPs (maximum of 50 nm). Thus, at similar contents, significantly higher number of SNPs particles are present than of ANPs. Higher particles numbers require greater dispersion energy. Since the dispersion was kept constant for all mixes, NPC-ANP-3.0, NPC-ANP-4.0 and NPC-SNP-2.0 showed worsened viscosity and flowability. Therefore, larger number of voids are present on the interface between PC and steel weakening their bond. Also, ANPs and COOH-MWCNTs both can chemically react with the steel surface where SNPs cannot. Therefore, larger number of SNPs particles at the PC-steel interface prevent chemical bonds formations between the polymer matrix and the steel.

4.8 Compression test

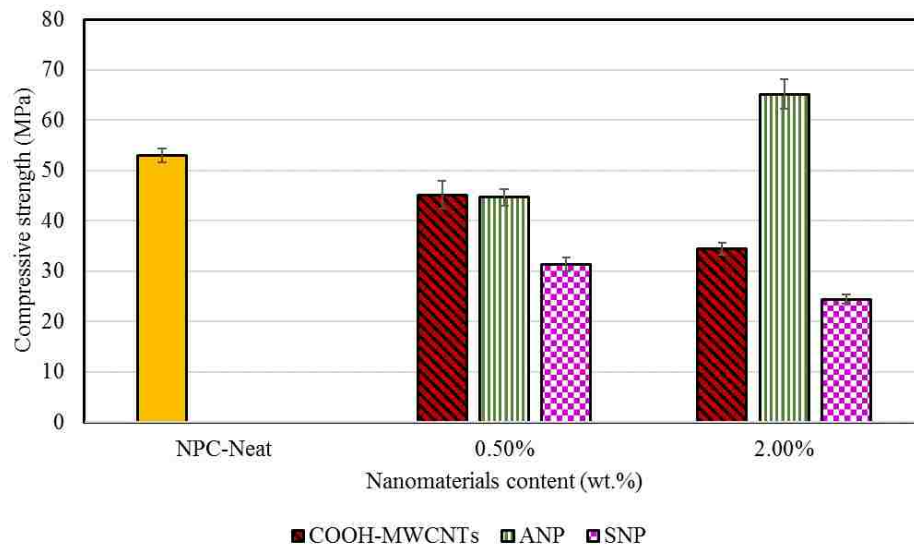


Figure 4.56: Compressive strength of selected Novolac PC (NPC) mixes based on best performance in slant shear test.



Figure 4.57: Before and after compression test showing extreme ductility of NPC-Neat

From the previous results, the best performance NPC prepared with ANPs and SNPs were at 2.0 and 0.5 wt.% respectively. All mixes with COOH-MWCNTs showed similar results regardless of their content. Therefore, mixes incorporating 0.5 and 2.0 wt.% of each nanomaterial were selected for the following testing stages. The compressive strength test was evaluated for the selected mixes and results are shown in Figure 4.56. NPC samples with and without nanomaterials exhibited significantly large ductility as shown in Figure 4.57. These findings are in parallel with previous SPC behavior described in section 4.2 for tension tests. Nevertheless, NPC-Neat shows high compressive strength that is comparable to PCC used in construction at 53 MPa. Incorporating COOH-MWCNTs and SNPs showed significant decrease in tensile strength by 15% - 35% and 41% - 54% respectively. On the other hand, mixes incorporating ANPs showed decrease of 16% at 0.5 wt.% and an increase at 2.0 wt.% by 23%. As all NPC mixes discussed in these sections are aimed for repairs, they provide sufficiently high compressive strength despite the decrease induced by nanomaterials.

4.9 Elastic properties

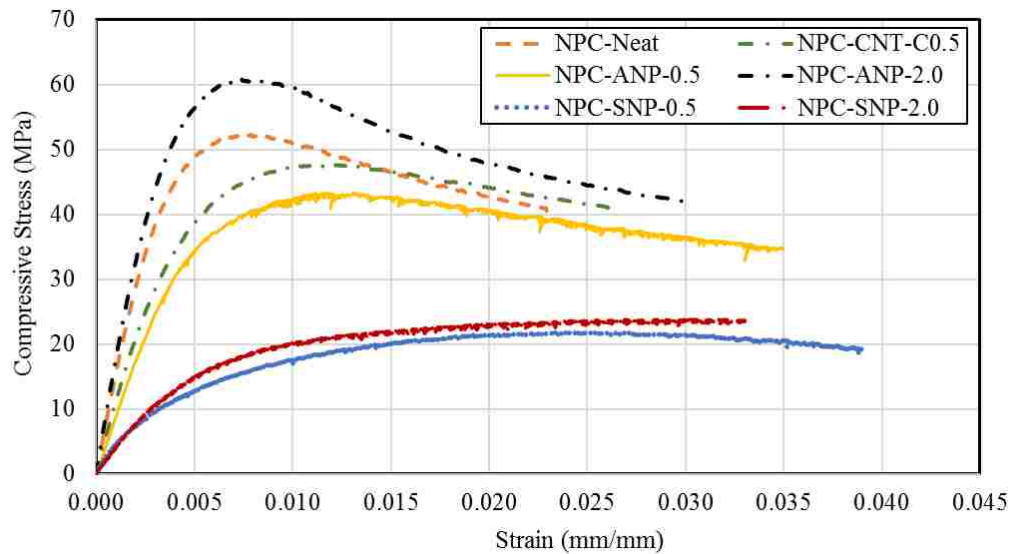


Figure 4.58: Stress-strain of Novolac PC (NPC) extracted from compression tests with strain gauges.

In all compression tests, strain gauges were attached to PC cylinders as discussed in section 3.9. The resulting stress-strain curves generated for all previous mixes are shown in Figure 4.58. The significant non-linearity observed in all mixes alongside previous discussed mechanical tests questions the accuracy of strain gauges. Concrete specimen exhibit smaller deformations and significantly lower strain values. As shown in Figure 4.57, PC in compression shows large deformations and low and slow elastic strain recovery. Hence, the elastic equations described in ASTM and presented in section 3.9 for Poisson's ratio calculations can result in overestimates. Also, there has been several models developed to describe the elastic properties of materials with micro inclusions such as rule of mixture. The sections below discuss the elastic properties of PC and PCNC measured using strain gauges as well as rule of mixture.

4.9.1 Experimental results

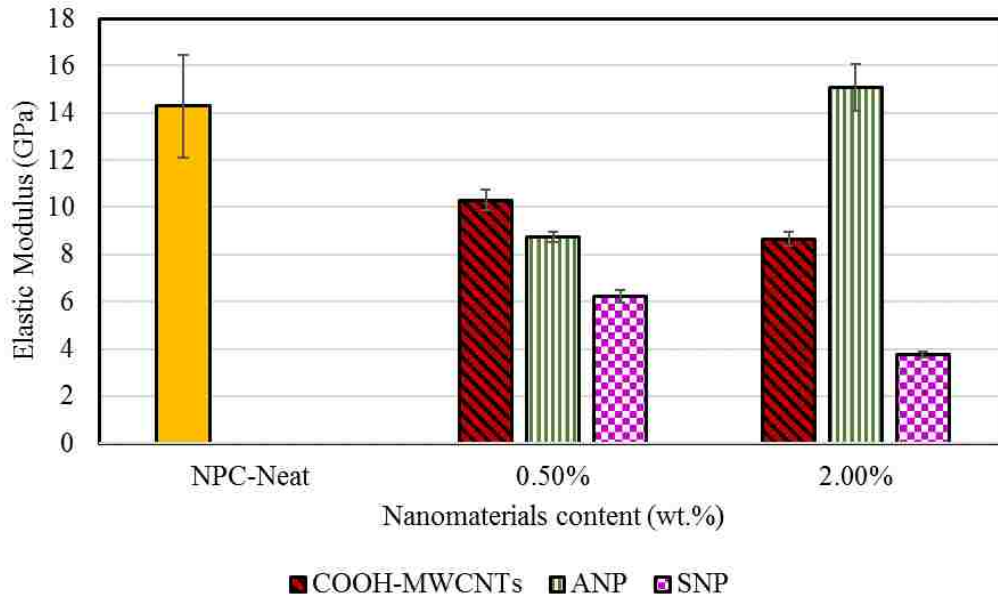


Figure 4.59: Elastic modulus measurements of Novolac PC (NPC) extracted from compression test with strain gauges.

The elastic modulus of the selected NPC mixes are shown in Figure 4.59. In general, all PCNC mixes showed a decrease in elastic modulus except for NPC-ANP-2.0. Those results are similar to those achieved in direct tension tests of SPC discussed in section 4.2.1.4. Thus, the use of strain gauges in evaluating the elastic modulus of PC are proven effective. The results show that low contents of ANPs result in decreasing the elastic modulus and the matrix stiffness. Increasing the content however reverse such effect only at sufficiently higher content. On the other hand, PC prepared with SNPs and COOH-MWCNTs show a decrease of elastic modulus and further decrease with higher contents.

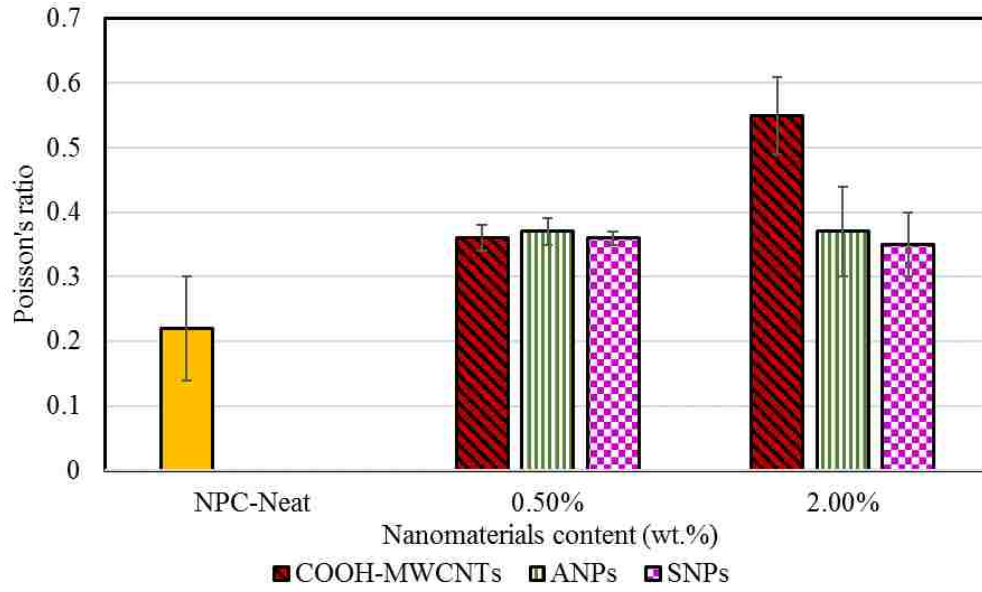


Figure 4.60: Poisson's ratio measurements of Novolac PC (NPC) extracted from compression test with strain gauges.

PC samples showed large lateral expansion under compression as shown in Figure 4.57. The measured Poisson's ratio for all mixes are shown Figure 4.60. Neat samples showed an expected Poisson's ratio values of 0.23 which is higher than PCC (0.20) and lower than polymers (0.40). Incorporating nanomaterials improves PC's ductility and toughness as discussed in section 4.2, this is evident also as Poisson's ratio of PCNC is higher than that of PC-Neat. NPC mixes incorporating ANPs and SNPs (0D nanomaterials) showed no relation between the nanomaterials content and Poisson's ratio. Those mixes maintained ~ 0.35 Poisson's ratio measured regardless of their type or content. Thus, it can be concluded that stress transfer mechanisms in nanocomposites utilizing 0D nanomaterials are independent of the type of nanomaterials or their dimensions. On the other hand, NPC-CNT-C mixes showed an increase in Poisson's ratio with the increase in content. In fact, the measured Poisson's ratio of NPC-CNT-C2.0 is 0.55 which is significantly higher than polymers. This disqualifies NPC-CNT-C2.0 as an isotropic linear elastic material as it results in a negative bulk modulus. All NPC mixes prepared with ANPs and SNPs showed values less than that of polymers. Therefore, further investigation to examine the significantly high

Poisson's ratio achieved of that mix. In order not to deviate from the scope of work of this thesis, NPC-CNT-C2.0 was discarded in the upcoming stages.

4.9.2 Rule of mixture

Nanomaterials can influence the mechanical properties of their host material including elastic modulus and Poisson's ratio as described in previous sections. While there are different models to predict the effect of incorporating micro structural reinforcement, this section aims to disclose the inapplicability of those models. This is due to the extreme dimensionality of nanomaterials as well as their significant chemical effect. Similar investigation has been carried by Zhang et al. investigating Halpin-Tsai dependent prediction models with SNP, rubber nanomaterials and CNTs (Zhang et al. 2015). Their results showed that numerical models based on micro systems cannot predict accurately the effect of nanomaterials on the mechanical properties of their host material. The sections below discuss a simpler version using the basic rule of mixture on predicting the elastic modulus. Several cases have been considered and are summarized in three models below. In these models, the elastic modulus of the PC nanocomposite is predicted and compared to the experimental value discussed in 5.4.1. The results of neat epoxy are a reference on the validity of the model and are used to determine the exact value of the aggregate modulus which lies within the material's range of 22-25 GPa. Since the modulus of elasticity of 2.0 wt.% content has been determined experimentally, a value similar to that is expected from the rule of mixture model if the model is applicable. None of the models listed below provide a close estimate or a positive elastic modulus for the epoxy samples. In all models, the change in volume is subject to the density of the specific nanomaterials used. However, since these values are difficult to obtain through mechanical testing. The values provided by the suppliers and through literature were used where ρ is density. The elastic modulus of the nanomaterials is also difficult to be determined

experimentally. Furthermore, many of the published research provide a wide range of experimental and numerical estimates of those values. Table 4-5 summarizes the values for density and elastic modulus with their respective symbols as used in the models.

Table 4-5: Elastic modulus and density values as used in rule of mixture analysis.

<i>Material</i>	<i>Density</i>	<i>Symbol</i>	<i>Elastic modulus</i>	<i>Symbol</i>
<i>ANPS</i>	3890 kg/m ³	ρ_{ANPS}	375 GPa	E_{ANPS}
<i>SNP</i>	2200 kg/m ³	ρ_{SNP}	73 GPa	E_{SNP}
<i>MWCNTs</i>	2100 kg/m ³	ρ_{MWCNTs}	900 GPa	E_{MWCNTs}

Model 1:

In this model, the effects of nanomaterials are considered to only affect the elastic modulus of the epoxy polymer binder. That is, there is no direct effect of the nanomaterials of the elastic modulus of PC and hence its volume is considered as part of the epoxy. Hence, the only changes that would occur would be that of the volume fractals. Table 4-6 describe the resultant volume of all materials. Eq. (4.4) below describes this model.

$$E_{PC} = \frac{V_E}{V_T} E_E + \frac{V_{ag}}{V_T} E_{ag} \quad (4.4)$$

The predicted elastic modulus values of the epoxy based on the measured PC elastic modulus values are shown in Table 4-7. While NPC-Neat and NPC-ANPS-2.0 both predict positive values that can be possible, all other mixes result in negative elastic modulus values. Therefore, this model shows that if the rule of mixture applies to nanoparticle inclusions, their

effect can not be absorbed into the epoxy completely and additional terms must be accounted for.

Table 4-6: Volume of nanomaterials and epoxy for model 1 of rule of mixture.

<i>Material</i>	<i>Nanomaterials content volume, V_N (m^3)</i>	<i>Volume of Epoxy (m^3)</i>	<i>Total volume, V_E (m^3)</i>
<i>NPC-Neat</i>	0		0
<i>NPC-ANPS-0.5</i>	0.000284	0.302	0.302284
<i>NPC-CNT-C0.5</i>	0.000526		0.302526
<i>NPC-SNP-0.5</i>	0.000502		0.302502
<i>NPC-SNP-2.0</i>	0.002009		0.304009
<i>NPC-ANPS-2.0</i>	0.001136		0.303136

Table 4-7: Elastic modulus predictions based on model 1.

<i>Material</i>	<i>Elastic modulus of PC measured experimentally, E_{PC} (GPa)</i>	<i>Predicted elastic modulus of epoxy, E_E (GPa)</i>
<i>NPC-Neat</i>	14.29	0.208
<i>NPC-ANPS-0.5</i>	8.74	-13.57
<i>NPC-CNT-C0.5</i>	10.3	-9.68
<i>NPC-SNP-0.5</i>	6.23	-19.83
<i>NPC-SNP-2.0</i>	3.76	-25.75
<i>NPC-ANPS-2.0</i>	15.09	2.368

Model 2:

In this model, the nanomaterials are examined to be identical to microparticles and micro fiber inclusions. That is, the effect on the elastic modulus is largely driven by mechanical mechanisms such as crack arrest, crack branching, stiffness, stress transfer and others. The effect of nanomaterials on the elastic properties of epoxy are considered negligible. Thus, the elastic

modulus of the epoxy polymer system is completely separated from that of the nanomaterials as shown in Eq. (4.5).

$$E_{PC} = \frac{V_E}{V_{T2}} E_E + \frac{V_{ag}}{V_{T2}} E_{ag} + \frac{V_N}{V_{T2}} E_N \quad (4.5)$$

Similar values for the volume of nanomaterials inclusions V_N are used in this model to the values provided in Table 4-6. The results of model 2 are then provided in Table 4-8. Similar results to that predicted by model 1 are achieved in this model. Both NPC-Neat and NPC-ANPS-2.0 predict positive and valid elastic modulus values for their respective epoxy. However, all other materials still predict negative values for their epoxies. Therefore, this model concludes that the effect of nanomaterials ca not be described to be purely mechanical and its chemical effect must be taken into effect by their influence on the epoxy properties.

Table 4-8: Elastic modulus predictions based on model 2.

<i>Material</i>	<i>Elastic modulus of PC measured experimentally, E_{PC} (GPa)</i>	<i>Predicted elastic modulus of epoxy, E_E (GPa)</i>
<i>NPC-Neat</i>	14.29	0.208
<i>NPC-ANPS-0.5</i>	8.74	-14.01
<i>NPC-CNT-C0.5</i>	10.3	-11.31
<i>NPC-SNP-0.5</i>	6.23	-20.05
<i>NPC-SNP-2.0</i>	3.76	-26.57
<i>NPC-ANPS-2.0</i>	15.09	0.853

Model 3:

In this model, the findings of the previous models are integrated together. This model therefore assumes that nanomaterials can have both mechanical and chemical effects.

However, the portion of nanomaterials than induce chemical changes to the epoxy polymer binder (designated as α) does not contribute mechanically. The model therefore separates the volume inclusions of nanomaterials that act mechanically ($(1-\alpha)V_N$) from that chemically (αV_N) as shown in Eq.(4.6).

$$E_{PC} = \frac{(V_E + \alpha V_N)}{V_{T2}} E_E + \frac{V_{ag}}{V_{T2}} E_{ag} + \frac{(1 - \alpha) V_N}{V_{T2}} E_N \quad (4.6)$$

Models 1 and 2 can be achieved in this model by using $\alpha=100$ and $\alpha=0$ respectively. Therefore, three different α values were examined: 0.25, 0.50 and 0.75 as shown in Table 4-9. The results however show similar results for all NPC mixes as discussed in previous models. Therefore, it can be concluded that either a more detailed rule of mixture must be used to predict the elastic modulus of epoxy nanocomposite or that such rule does not hold over the nanoscale. The rule of mixture was not further investigated however as it diverts from this work's goals. However, this section aim to highlight the significant work required to either adjust current prediction models or to develop new ones valid for nanocomposites.

Table 4-9: Elastic modulus predictions based on model 3 at different α values.

<i>Material</i>	<i>Predicted elastic modulus of epoxy with $\alpha=0.25$, E_E (GPa)</i>	<i>Predicted elastic modulus of epoxy with $\alpha=0.5$, E_E (GPa)</i>	<i>Predicted elastic modulus of epoxy with $\alpha=0.75$, E_E (GPa)</i>
<i>NPC-Neat</i>	0.208	0.208	0.208
<i>NPC-ANPS-0.5</i>	-13.922	-13.834	-13.746
<i>NPC-CNT-C0.5</i>	-10.923	-10.531	-10.139
<i>NPC-SNP-0.5</i>	-20.019	-19.989	-19.959
<i>NPC-SNP-2.0</i>	-26.439	-26.317	-26.196
<i>NPC-ANPS-2.0</i>	1.206	1.559	1.911

-Notation-

α : portion of nanomaterials inclusion volume altering the elastic modulus of epoxy

E_{PC} : the elastic modulus of PC

E_E : the elastic modulus of epoxy polymer binder

E_{ag} : the elastic modulus of the aggregate filler

E_{ANPS} : elastic modulus of alumina nanoparticles

E_{SNP} : elastic modulus of silica nanoparticles

E_{MWCNTs} : elastic modulus of multi-walled carbon nanotubes

V_E : volume of epoxy polymer binder with volume of nanomaterials

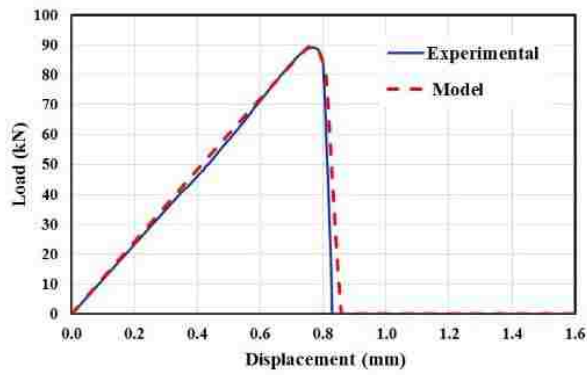
V_N : volume of the nanomaterials inclusions

V_{ag} : volume of the aggregate filler = 0.453 m³

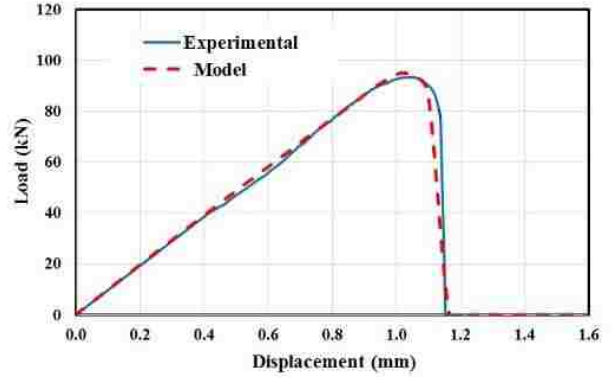
V_T : total volume = $V_E + V_{ag}$

V_{T2} : total volume = $V_E + V_{ag} + V_N$

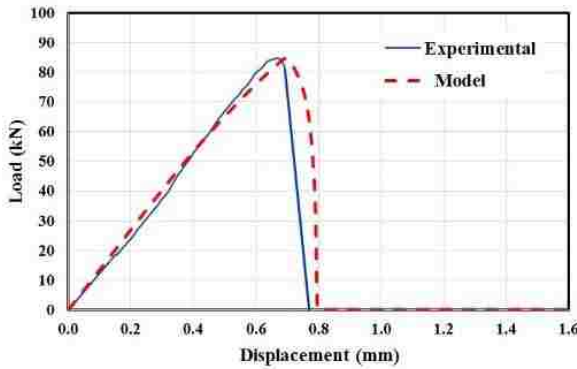
4.10 Finite element analysis using ABAQUS



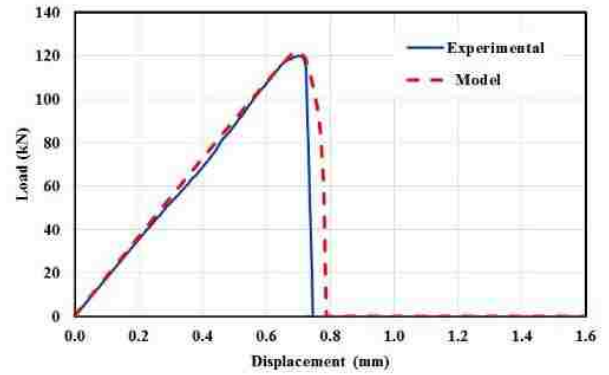
NPC-Neat



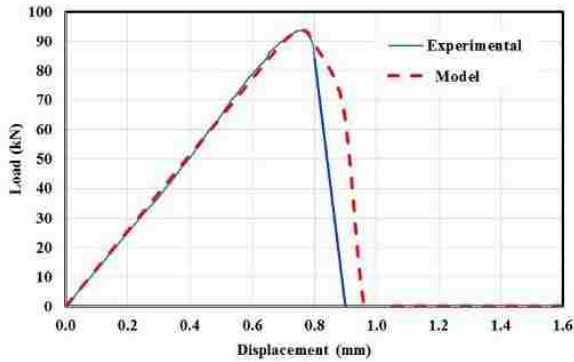
NPC-CNT-C0.5



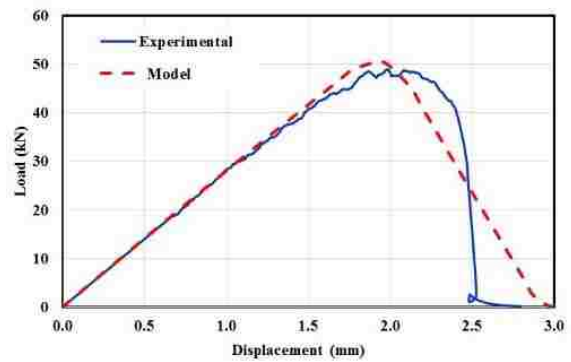
NPC-ANP-0.5



NPC-ANP-2.0



NPC-SNP-0.5



NPC-SNP-2.0

Figure 4.61: Load-displacement of Novolac PC (NPC) prepared with COOH-MWCNTs, ANPs and SNPs comparing experimental and FEA.

Table 4-10: Interface properties in slant shear test for damage and cohesive behavior definitions.

<i>Contact Property</i>	<i>Damage</i>			<i>Cohesive Behavior</i>
	<i>Initiation</i>	<i>Evolution</i>	<i>Stabilization</i>	
<i>Mix</i>	<i>Maximum shear stress (τ_u), MPa</i>	<i>Fracture energy (G_{II}), N/mm</i>	<i>Viscosity Coefficient (V)</i>	<i>Shear contact stiffness (K_t), MPa/mm</i>
<i>NPC-Neat</i>	43	19		56
<i>NPC-CNT-C0.5</i>	45	29		46
<i>NPC-ANP-0.5</i>	42	17	0.001	75
<i>NPC-ANP-2.0</i>	61	24		92
<i>NPC-SNP-0.5</i>	53	21		90
<i>NPC-SNP-2.0</i>	23	37		12

Finite element modeling (FEM) was performed using ABAQUS to determine the true shear stresses exerted in slant shear test of NPC specimen. Modeling was performed through back-solving method and matching load-displacement curves of all NPC specimen as described in section 3.13. To match the load-displacement curves, the interface properties utilizing damage and cohesive behavior were manipulated. The final contact properties resulting in the best match are shown in Table 4-10. The resulting load-displacement curves are shown in Figure 4.61 with respect to the experimental. All models were well matched to the experimental results. The FEM of NPC-SNP-2.0 shows larger deviation from all other models. This is attributed to the exceedingly small elastic modulus at 3.8 GPa compared to NPC-Neat’s 14.3 GPa resulting in more stable failure than experimentally observed. Nevertheless, all models match the true shear stress well.

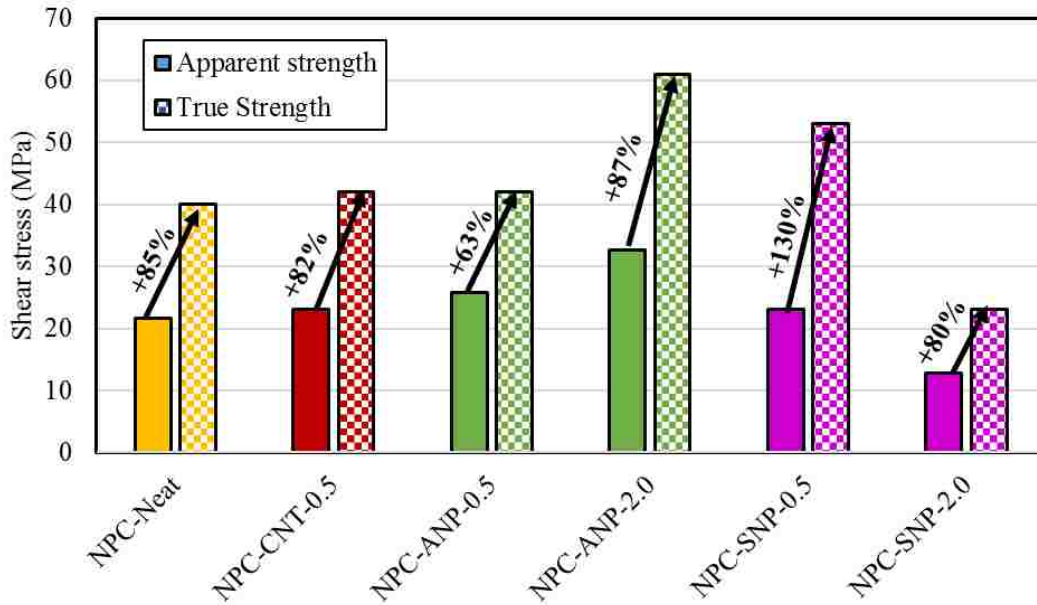


Figure 4.62: True shear strength compared to apparent shear strength of NPC mixes.

A comparison between apparent shear strength and true shear strength (from FEM) is shown Figure 4.62. Due to stiffness mismatch, significantly higher stress by 63% to 130% are exerted on the interface between PC and steel. Thus, the reported shear strength values of slant shear test using the method of dividing load over the slanted area is inaccurate. This is attributed to the large difference between the elastic modulus of the two slant shear test materials referred to in this thesis as stiffness mismatch. The mechanics that stiffness mismatch manipulates the stress state at the interface are discussed in section 4.11. Nevertheless, the trend of increasing the shear/bond strength by incorporating nanomaterials can still be observed. The results also show that the apparent shear stress is dependent on the test mechanics. Further analysis of the FE simulation results shows strong correlation between Poisson's ratio, the shear modulus G described as $G = \frac{E}{2(1+\nu)}$ and the maximum local shear stresses at the interface. Since all nanomaterials caused an increase in Poisson's ratio, the maximum local shear stress is decreased by the increase in Poisson's ratio. This analysis supports the results for NPC-CNT-C0.5 and NPC-ANP-0.5 in comparison with NPC-Neat. Furthermore, another important factor controlling the maximum local

shear stresses is the shear contact stiffness K_t . The shear contact stiffness controls the slippage occurring at the interface (see Figure 3.28 (b)) and may correspond to the friction between the contact surfaces. The effect of the shear contact stiffness on local shear stresses is apparent in the case of SNPs. FTIR analysis, discussed below, confirms that SNPs acted as an inert filler. This might explain its ability to increase interface friction compared with MWCNTs or ANPs, which apparently can chemically react with the epoxy matrix and/or the steel surface.

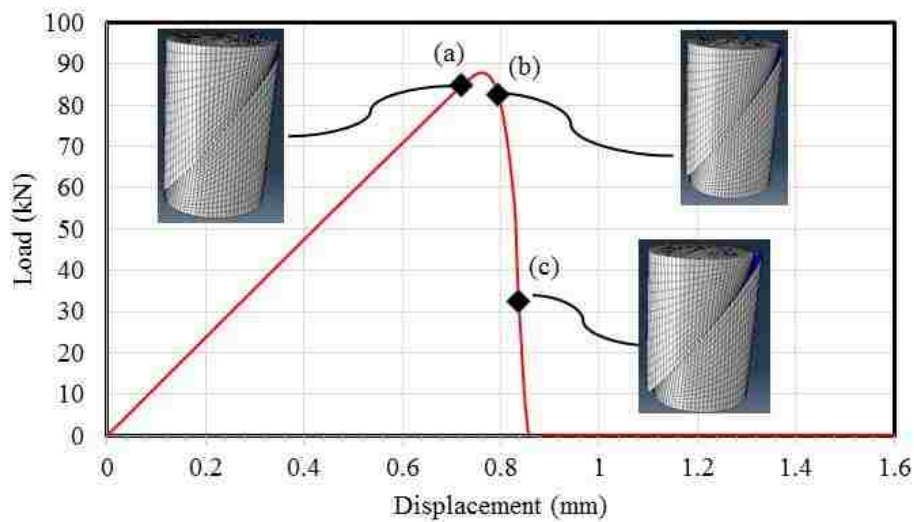


Figure 4.63: Load-displacement extract from finite element analysis of neat PC showing magnified slippage at 0.720mm, 0.802mm, and 0.837mm.

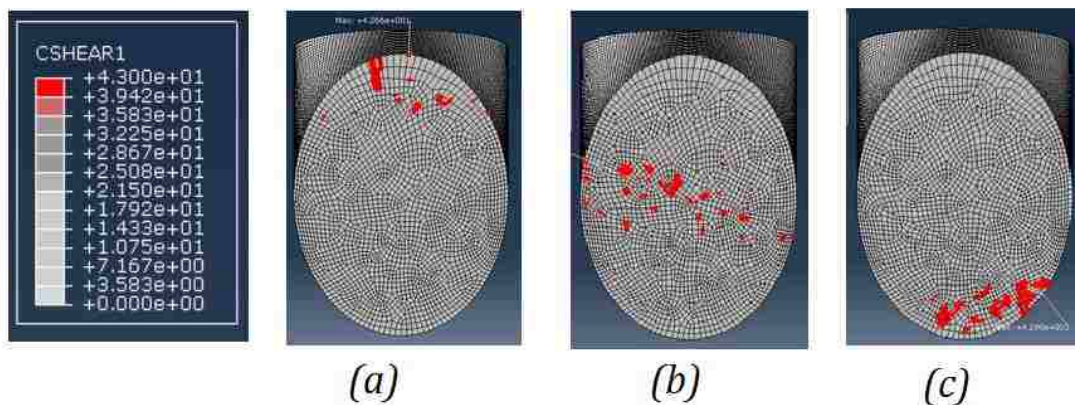


Figure 4.64: Shear contours showing locations of maximum local shear stress during slippage of SPC-CNT-0.5 of (a) 0.720 mm (b) 0.802 mm and (c) 0.837 mm.

Finally, FE analysis results were also used to examine the interfacial shear stress contours at the PC-steel interface. Figure 4.63 shows the load-displacement of NPC-CNT-C0.5 extracted from the FE model with magnified slippage in the assembly at vertical displacements of 0.720 mm, 0.802 mm, and 0.837 mm. At each of these points, shear contours on the interface were plotted showing the maximum local shear stress to reach 43 MPa. Locations of maximum local shear stress concentration on the interface are shown in Figure 4.64. Maximum local shear stress only develops at the location of minimum height of PC before reaching ultimate load as shown in Figure 4.63 and Figure 4.64 (a). As slippage occurs, the maximum local shear stress moves along the interface. The maximum local shear stress path follows the height of PC from minimum to maximum as shown in transition in Figure 4.64 from (a), (b) and (c). Slant shear tests show that complete slippage occurs after the ultimate load due to release of energy because of bond failure.

4.11 Stiffness mismatch analytical solution

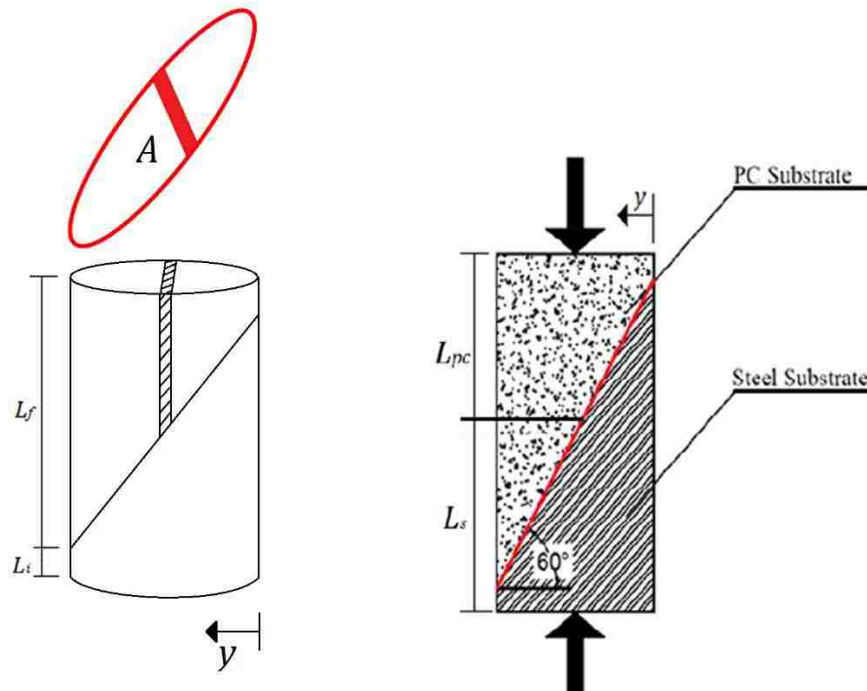


Figure 4.65: Schematics of slant shear stiffness mismatch variables

Test standards suggest obtaining the average bond strength through dividing the vertical load by the slanted area of contact leading to what is denoted in this thesis as the apparent bond/shear stress. This relation is shown in Eq. (4.7) where P is the vertical applied load, A is the cross-sectional area of the cylinder and τ_a is the apparent shear stress. As discussed previously, significant mismatch between apparent shear stress and true shear stress exist when comparing FEM with Eq. (4.7). This is attributed to the large mismatch between the modulus of elasticity of both PC and steel (E_{PC} and E_{steel} respectively) referred to as stiffness mismatch. The stiffness (K) at any point of uniaxial loaded member of length L is defined in Eq. (4.8) that defines the stiffness of the concrete (K_{PC}) and steel parts (K_{steel}) using Eq. (4.9) and (4.10) respectively. The stiffness mismatch can be described by the relative stiffness mismatch (κ) calculated by the difference in stiffness between both parts normalized by the part with minimum volume. Due to surface inclination, the stiffness of each part is strictly affected by the change in length of the respective part. The length of the concrete part (L_{PC}) and the steel part (L_{steel}) at a distance y are given in Eq. (4.11) and (4.12) based on the given initial minimum (L_i) and maximum lengths (L_f). Figure 4.65 shows the definition of all variables on slant shear test schematics. If the distance from the side with minimum PC volume is y , the relative stiffness mismatch (κ) is then calculated in Eq. (4.13) since the area in contact in between PC and steel are equivalent ($A_{PC}=A_{steel}$). By substituting the definitions of concrete and steel stiffness prescribed in Eq. (4.9) and (4.10) into Eq. (4.13), the relative stiffness mismatch can be rewritten and is function of the independent variable (y) as shown in Eq. (4.14). The elastic modulus ratio (λ) describing the elastic modulus of the top part normalized by the bottom part is described in Eq. (4.15) and used to simplify all figures.

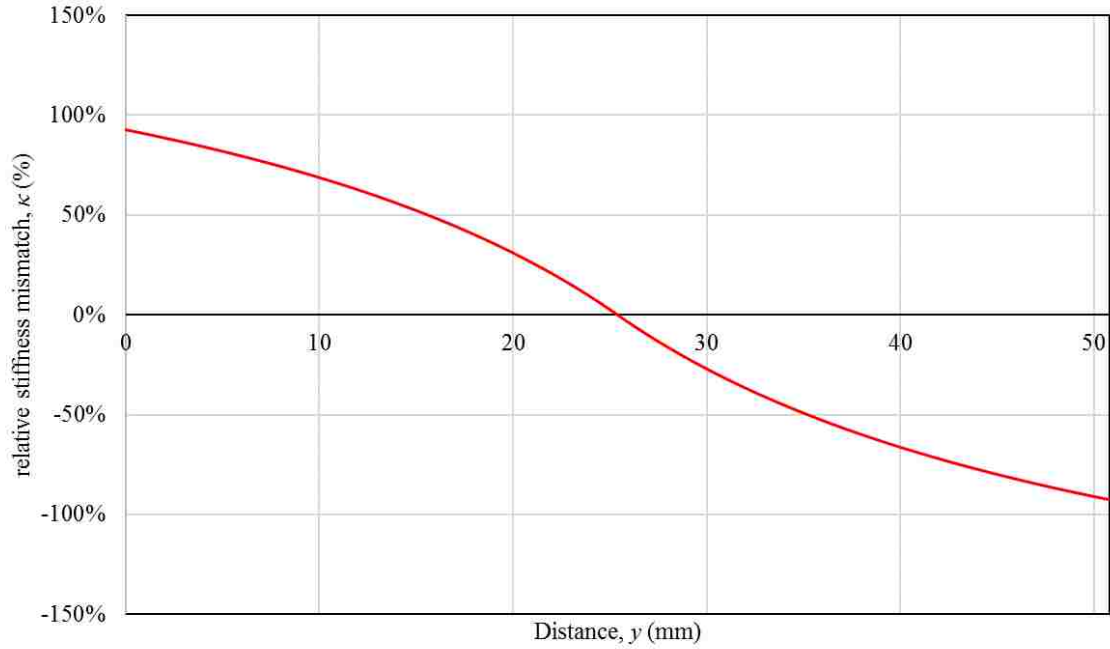


Figure 4.66: Relative stiffness mismatch calculated using Eq. (4.13) for two steel parts with respect to the distance across slant shear sample (y).

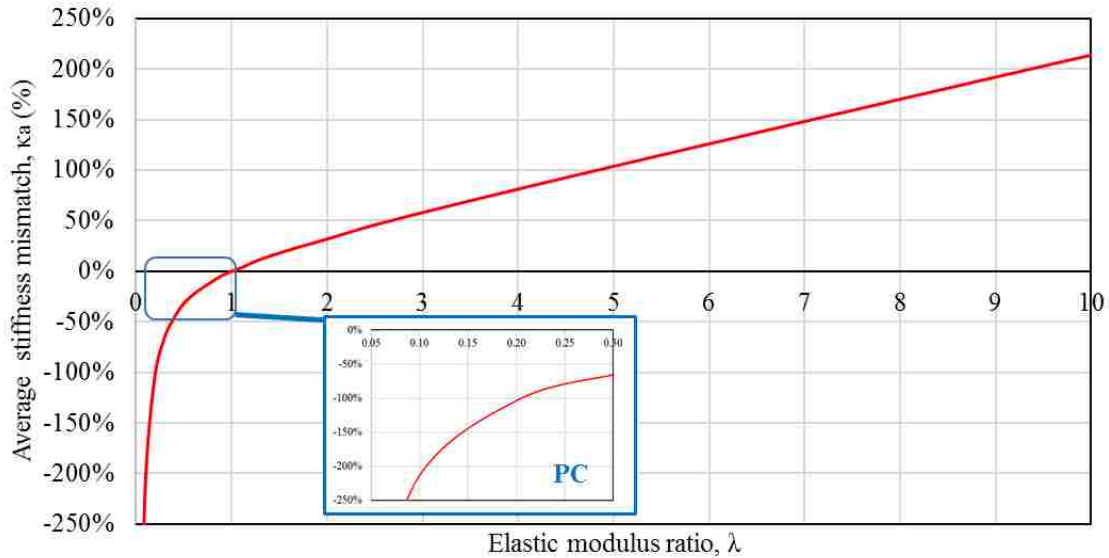


Figure 4.67: the variability of the average stiffness mismatch with the change of elastic modulus of the top part normalized by the bottom part (λ) described in Eq. (4.15).

The relative stiffness mismatch against the distance y is validated through evaluating Eq. (4.13) using two steel parts as shown in Figure 4.66. As expected, the stiffness mismatch is zero at the location where both parts are equal. The averaged stiffness mismatch (κ_a) over the length of

the sample described in Eq. (4.16) yields 0% when $\lambda = 1$. Hence, the apparent shear stress is a valid representation of the stress which averages the stress on the sample when the same material is used at both parts. By changing the stiffness of one part however, the stress distribution is greatly affected. Figure 4.67 shows the variability of the average stiffness mismatch with the change of elastic modulus of the top part normalized by the bottom part (λ). It's evident that when one part has a different modulus than the other part, the average relative stiffness mismatch no longer averages to zero. In fact, when the top part is at 10% of the stiffness of the bottom part, the average shear stress goes up to -214%. PC compared to steel provides λ values in the range of 0.02 up to 0.07 that corresponds to average stiffness mismatch between -1075% and -307%. As discussed previously, stiffness mismatch is not the sole factor that generates higher shear stresses. Other factors are the shear modulus impacted by Poisson's ratio, chemical interaction between PC and steel, interface stiffness and friction.

$$\tau_a = \frac{P \sin(60)}{A / \cos(60)} = \frac{P}{A} \sin(60) \cos(60) \quad (4.7)$$

$$K = \frac{E A}{L} \quad (4.8)$$

$$K_{PC} = \frac{E_{PC} A_{PC}}{L_{PC}} \quad (4.9)$$

$$K_{steel} = \frac{E_{steel} A_{steel}}{L_{steel}} \quad (4.10)$$

$$L_{PC}(y) = L_i + \left(\frac{L_f - L_i}{b} \right) y \quad (4.11)$$

$$L_{steel}(y) = L_f - \left(\frac{L_f - L_i}{b} \right) y \quad (4.12)$$

$$\kappa = f(x) = \begin{cases} \left(\frac{K_{steel} - K_{PC}}{K_{PC}} \right) \times 100, & y \leq \frac{b}{2} \\ \left(\frac{K_{steel} - K_{PC}}{K_{steel}} \right) \times 100, & y > \frac{b}{2} \end{cases} \quad (4.13)$$

$$\kappa(y) = \begin{cases} \left(\frac{E_{steel}L_{PC}(y) - E_{PC}L_{steel}(y)}{E_{PC}L_{steel}} \right) \times 100 & , y \leq \frac{b}{2} \\ \left(\frac{E_{steel}L_{PC}(y) - E_{PC}L_{steel}(y)}{E_{steel}L_{PC}(y)} \right) \times 100 & , y > \frac{b}{2} \end{cases} \quad (4.14)$$

$$\lambda = \frac{E_{Top\ part}}{E_{Bottom\ part}} \quad (4.15)$$

$$\kappa_a = \frac{1}{b} \int_{y=0}^{y=b} \kappa(y) dy \quad (4.16)$$

-Notation-

A : area of the interface

A_{PC} : interface area of the PC part

A_{steel} : interface area of the steel part

b : the diameter = 50.8 mm.

E : elastic modulus

E_{steel} : steel elastic modulus = 200 GPa.

E_{PC} : PC elastic modulus from section 4.9.1

K : stiffness

K_{PC} : PC stiffness

K_{steel} : steel stiffness

κ : relative stiffness mismatch

κ_a : average stiffness mismatch

L : length of slant shear sample

L_i : length of the short side of the slant shear part

L_f : length of the long side of the slant shear part

L_{PC} : length of PC at any distance y

L_{steel} : length of steel part at any distance y

λ : elastic modulus ratio

τ_a : apparent shear stress

P : applied force

4.12 Scanning Electron Microscope

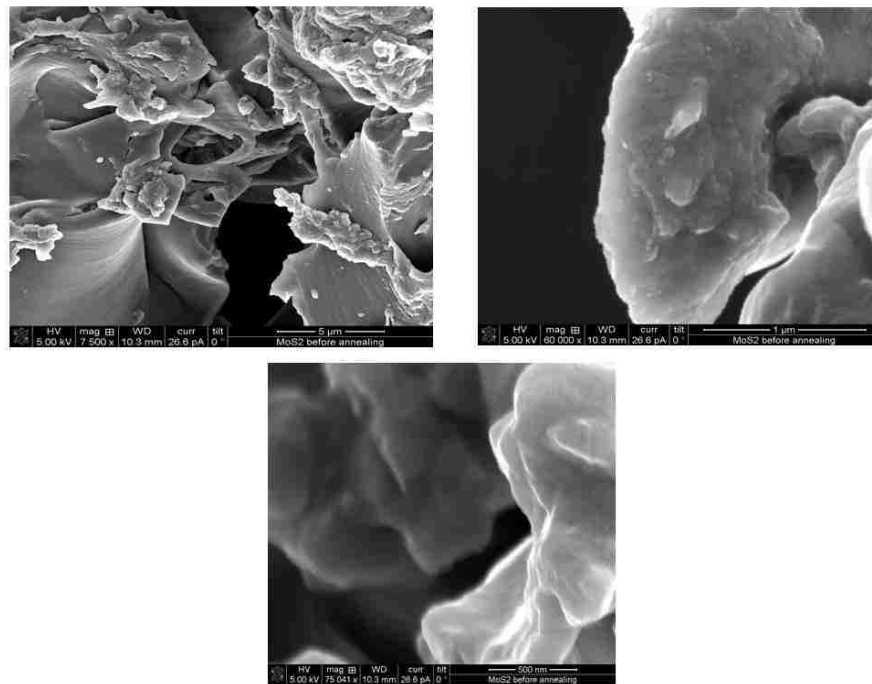


Figure 4.68: SEM scans of S-Neat used as reference for the topological feature.

To examine the effectiveness of the dispersion method used, scanning electron microscope images were collected of different mixes as discussed in section 3.10. As this work discusses large number of different nanomaterials and at different contents, this investigation was limited to

Siloxane epoxy samples with specific nanomaterials content. Siloxane PC as discussed in section 4.1 showed lower flowability than Novolac PC indicating higher polymer viscosity. As the same dispersion method was used for all mixes resulting in constant dispersion energy, ensuring that those mixes with higher shear energy requirements (that resulted in the least flowable PC) warrants sufficient dispersion for mixes with less demand. As changes are expected to appear within the epoxy topological surface and to well identify the presence of nanomaterials, scans of neat samples were collected as shown in Figure 4.68. Other scans collected of Siloxane epoxy samples are for those incorporating 0.5 and 3.0 wt.% ANPs, 2 wt.% P-MWCNTs, 2 wt.% COOH-MWCNTs, 1.9 wt.% P-MWCNTs with 0.1 wt.% COOH-MWCNTs, and 0.1 wt.% P-MWCNTs with 1.9 wt.% COOH-MWCNTs.

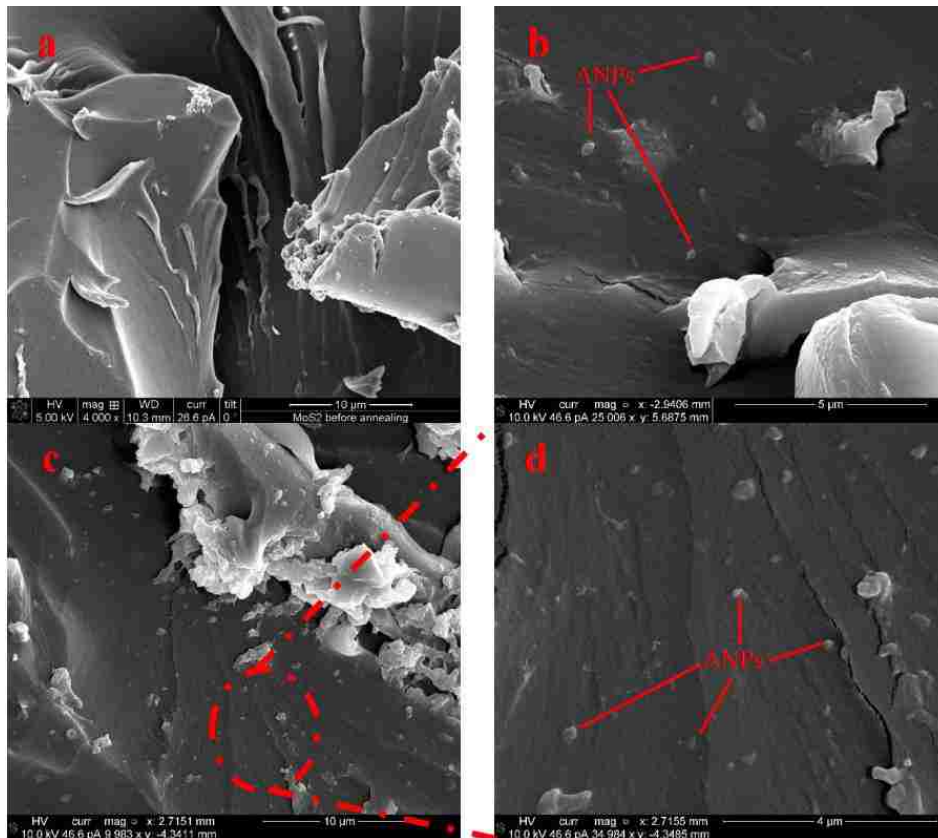


Figure 4.69: SEM scans for hardened epoxy containing (a) and (b) 0.5 wt.% ANP and (c) and (d) 3.0 wt.% ANP.

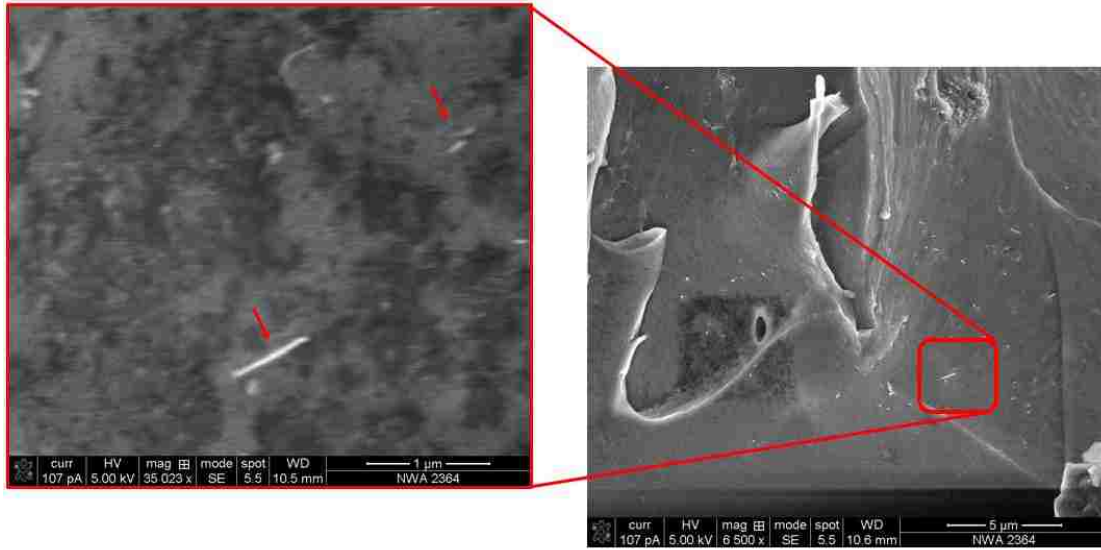


Figure 4.70: SEM images of epoxy samples containing P-MWCNTs showing no agglomeration at 2.0 wt.%.

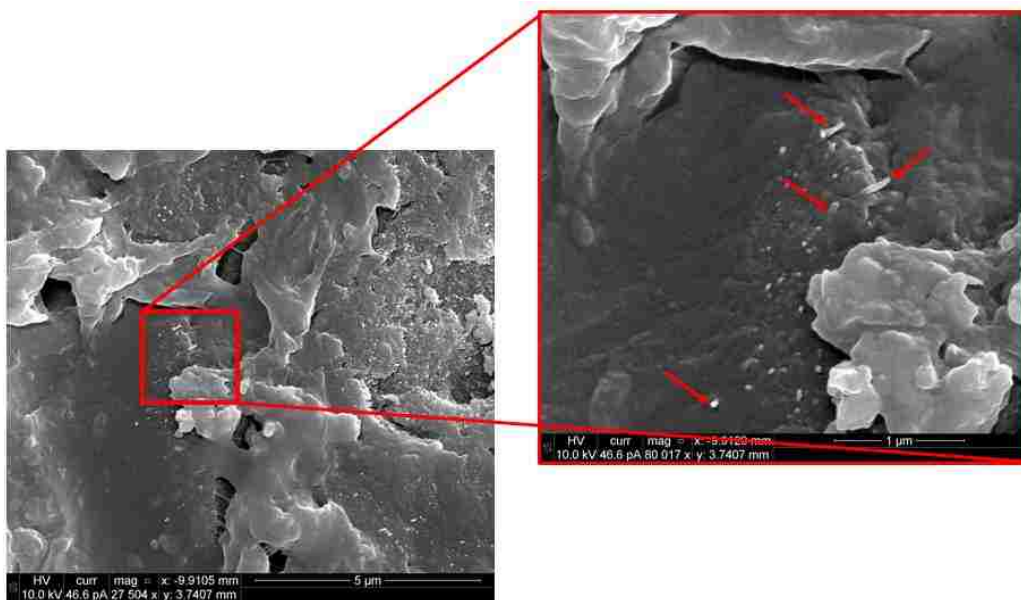


Figure 4.71: SEM images of epoxy samples containing COOH-MWCNTs showing uniform dispersion at 2.0 wt.%.

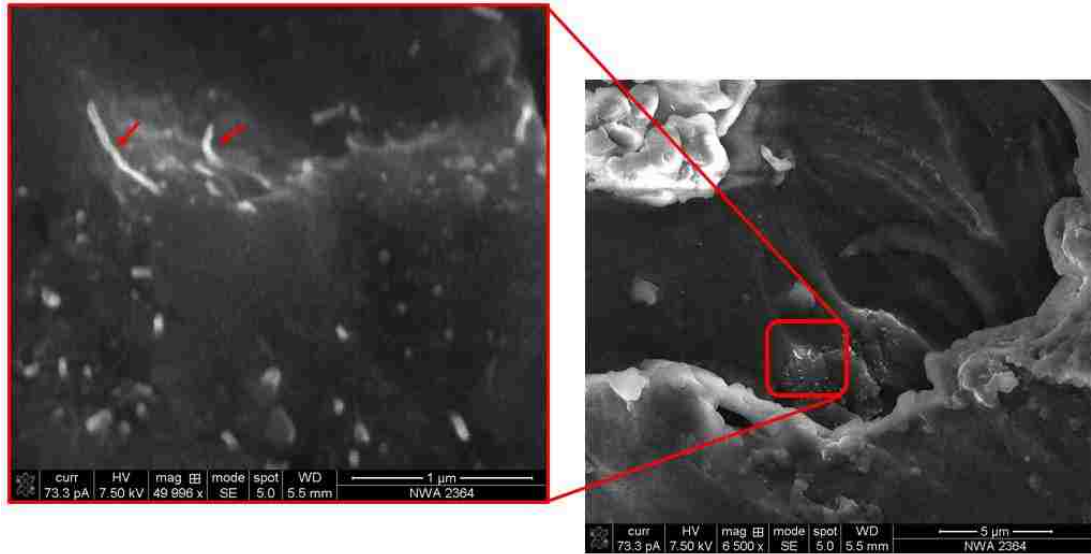


Figure 4.72: 1.9 wt.% P-MWCNTs with 0.1 wt.% COOH-MWCNTs

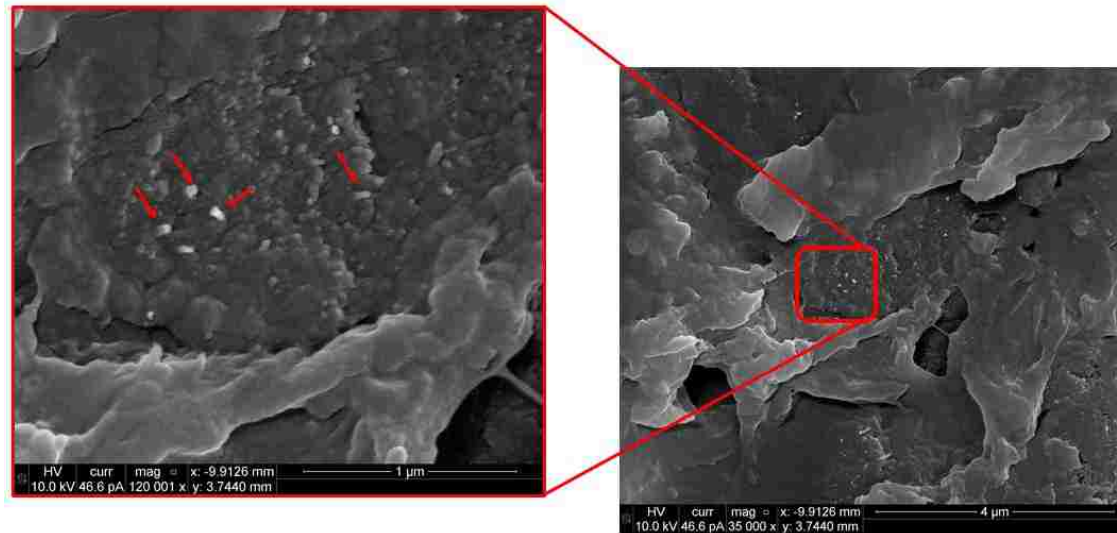


Figure 4.73: 0.1 wt.% P-MWCNTs with 1.9 wt.% COOH-MWCNTs

SEM scans of S-ANP-0.5, S-ANP-3.0, S-CNT-P2.0, S-CNT-C2.0, S-CNT-P1.9/C0.1 and S-CNT-P0.1/C1.9 are shown in Figure 4.69, Figure 4.70, Figure 4.71, Figure 4.72, and Figure 4.73 respectively. All scans collected show proper dispersion of nanomaterials at any given content. Poorly dispersed nanomaterials result in generating stress concentration points, high viscosity, low flowability, high friction and large voids within PC. Scans of specimen prepared with ANPs shows the best dispersion among all other nanomaterials in which all particles are separated with at least few micrometers in between. This is attributed to their small dimensions as ANPs are 0D

nanomaterials compared to MWCNTs 1D. Visual inspection of the scans shows no topological changes in the epoxy surface and complete embedment of all ANPs within the epoxy. Scans of MWCNTs also show good dispersion with minimal entanglement. However, the relative distance between MWCNTs is significantly less than that of ANPs. This is attributed to the large van der Waals and Coulomb attraction forces between individual nanotubes (*Zhu et al. 2004 and David et al. 2014*). Furthermore, the large length of MWCNTs result in partial embedment in which parts along MWCNTs' length or ends are not embedded within the epoxy. This supports the results of section 4.4 on fatigue tests in which MWCNTs can provide fiber like effects bridging cracks while ANPs cannot. It's also evident that different types of MWCNTs show different morphological features. Epoxy prepared with COOH-MWCNTs shows more rough topological features that are not apparent in samples prepared with ANPs, P-MWCNTs or neat. Thus, the change in topological feature can be attributed to the possible chemical reaction of the carboxyl group. This will be further discussed in FTIR and DMA sections. Further examination of P-MWCNTs scans against COOH-MWCNTs shows as if less number of MWCNTs are present in P-MWCNTs epoxy. This can be attributed to the possible shortening of MWCNTs due to functionalization resulting in higher number of MWCNTs at a fixed weight content (*Zheqiong et al. 2017, Chung et al. 2015, Samori et al.2010*). The possible shortening of COOH-MWCNTs can explain results of section 4.6 on the effect of functionalization of MWCNTs. Specifically, as the ratio of COOH-MWCNTs to P-MWCNTs increase; the relative number of MWCNTs within PC gets higher. This results in improved strain at failure and toughness due to improved stress transfer and crack arrest. Nevertheless, all SEM scans show evidently that the method of dispersion of ultrasonication and stirring is successful in producing well dispersed nanocomposites.

4.13 Fourier transform infrared spectroscopy (FTIR)

To discretize the various patterns observed in mechanical testing of PC and PCNC, several epoxy nanocomposite coupons were scans using FTIR. Scans included neat Siloxane epoxy and epoxy prepared with 0.5 and 2.0 wt.% P-MWCNTs, 0.5 and 2.0 wt.% COOH-MWCNTs, 0.5, 2.0 and 3.0 wt.% ANPs, and all hybrid mixes. Novolac epoxy scans were also collected for Neat, 1.0 wt.% of ANPs and COOH-MWCNTs, and 0.5, 1.0 and 2.0 wt.% SNPs.

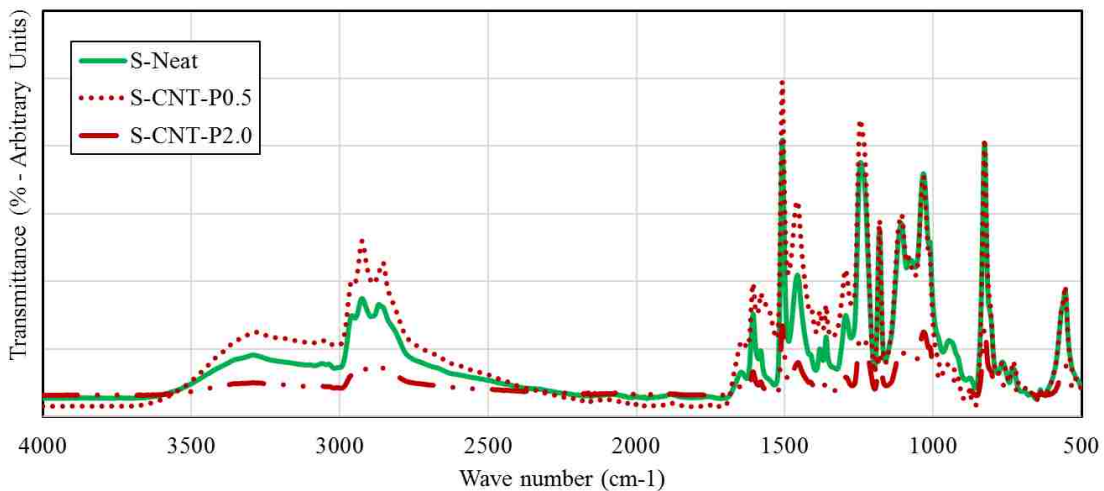


Figure 4.74: FTIR spectrograph for Siloxane epoxy with P-MWCNTs at 0.5 and 2.0 wt.% contents

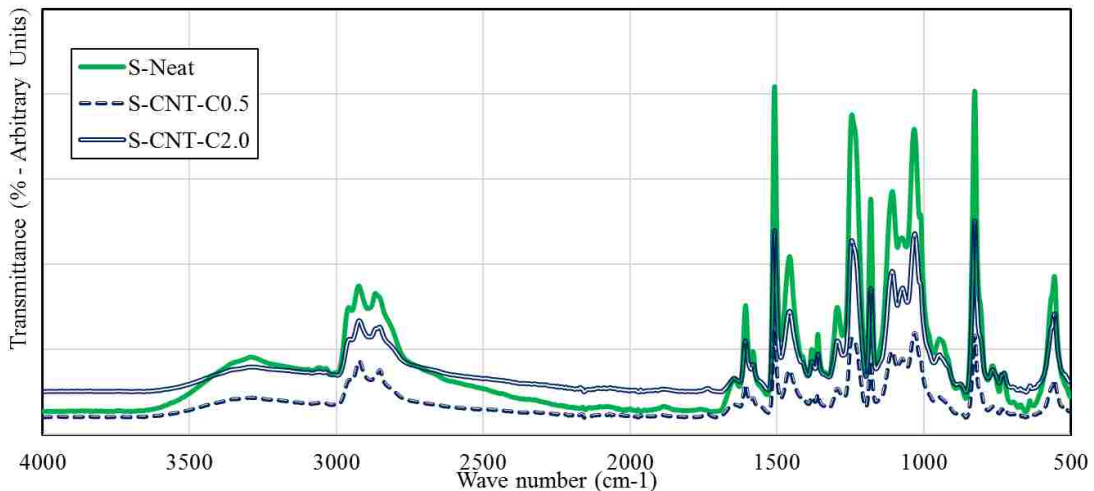


Figure 4.75: FTIR spectrograph of Siloxane epoxy with COOH-MWCNTs at 0.5 and 2.0 wt.% contents.

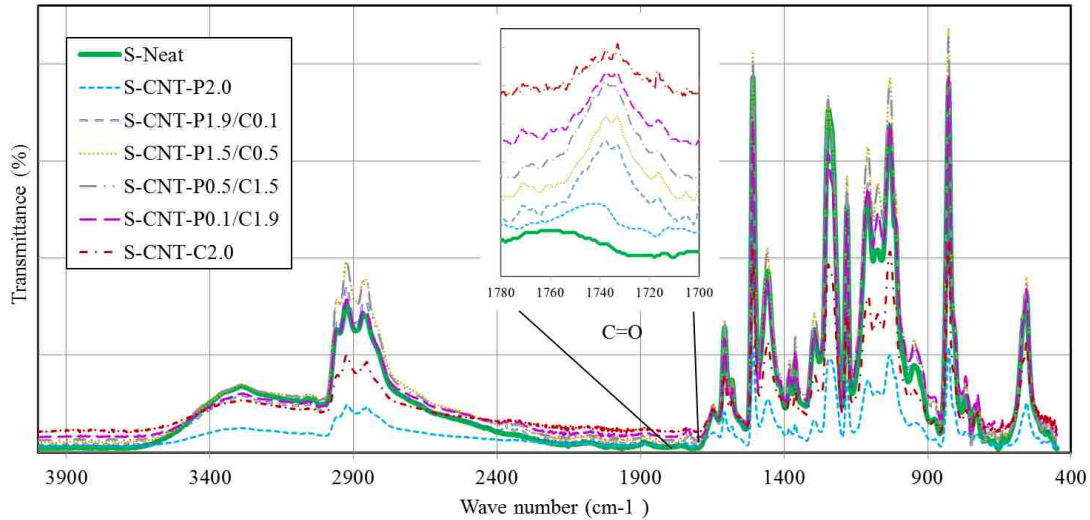
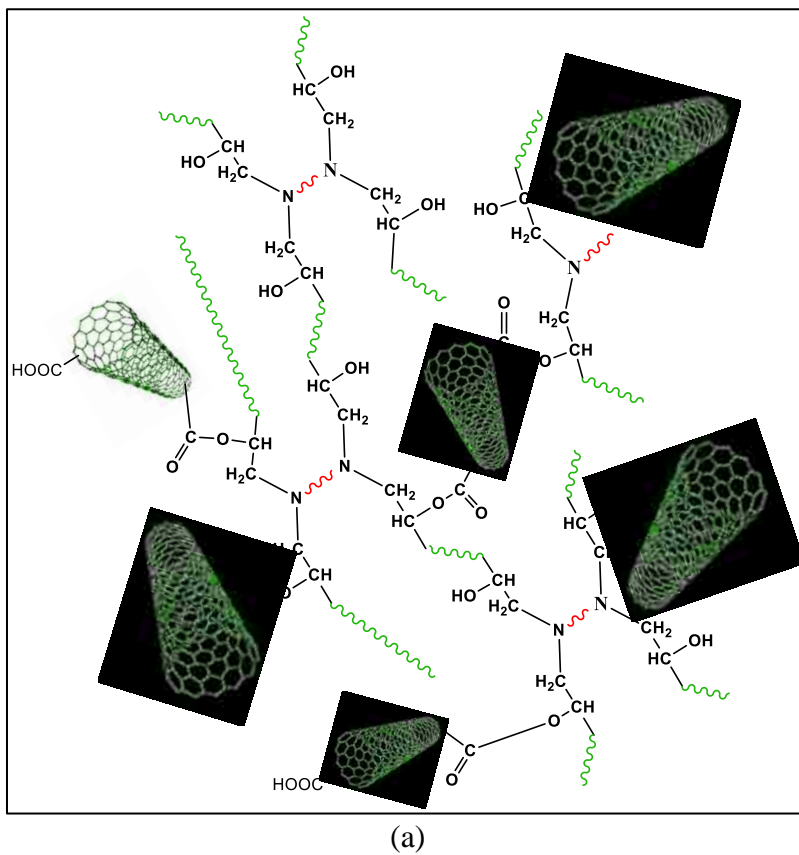
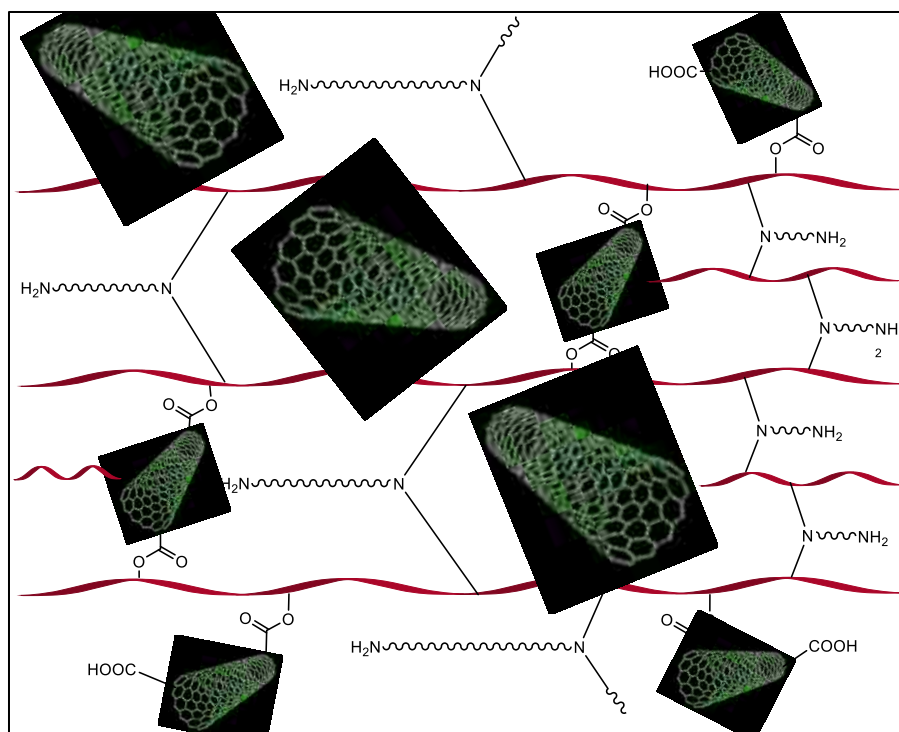


Figure 4.76: FTIR spectrograph of Siloxane epoxy for functional group analysis at 2.0 wt.% total content of both pristine and functionalized MWCNTs.

Scans of Siloxane epoxy samples are shown in Figure 4.74, Figure 4.75, and Figure 4.76 for P-MWCNTs, COOH-MWCNTs, and hybrid MWCNTs respectively. All scans with MWCNTs show the standard epoxy peaks; the absorption bands corresponding to C-H band (2860–2940 cm^{-1}), epoxide ring ($\sim 828 \text{ cm}^{-1}$), N-H band of primary amines (1592–1610 cm^{-1}), O-H groups ($\sim 3320 \text{ cm}^{-1}$), C-N band (1035–1117 cm^{-1}) and ether bands ($\sim 1250 \text{ cm}^{-1}$) are all apparent and have similar relative ratios to the base spectra. The carbonyl band (C=O) at 1738 cm^{-1} appears for all mixes containing COOH-MWCNTs and is absent in mixes containing P-MWCNTs or SPC-Neat. This absorption band is attributed to the carbonyl group of the ester formed via an esterification reaction between the epoxy resin and the COOH group of the COOH surface functionalized MWCNTs (*Borowski et al. 2015*). This is a good indication of a chemical reaction occurring between the carboxylic groups of the functionalized MWCNTs and the epoxy matrix. The increase in tensile strength with reduction in tensile strain is attributed to that reaction. A schematic for this reaction is suggested in Figure 4.77 (a) for hybrid mixes. Such chemical reaction will increase epoxy cross-linking improving the tensile strength and reducing the tensile strain of

PC. On the other hand, Figure 4.77 (b) is a schematic suggesting the way P-MWCNTs exists within the epoxy matrix without a chemical reaction when COOH-MWCNTs are also present. P-MWCNTs can disturb the epoxy matrix affecting its crosslinking and strength. The high aspect ratio of the free P-MWCNTs result also in improved strain at failure as they act as fibers preventing crack propagation. Hybrid mixes have another critical effect since functionalization enables better dispersion of MWCNTs. Higher contents of COOH-MWCNTs to P-MWCNTs result in better dispersion of MWCNTs increasing their crack arrest and in return improving stress transfer and tensile strength. Finally, and as mentioned in SEM, functionalization result in shortening of MWCNTs. Thus, as the ratio of COOH-MWCNTs to P-MWCNTs increased; the relative number of MWCNTs gets higher. This would result in improved strain at failure.





(b)

Figure 4.77: Schematic representing the chemical interaction of both types of MWCNTs with epoxy (a) COOH-MWCNTS reaction with epoxy (b) P-MWCNTs reaction with epoxy.

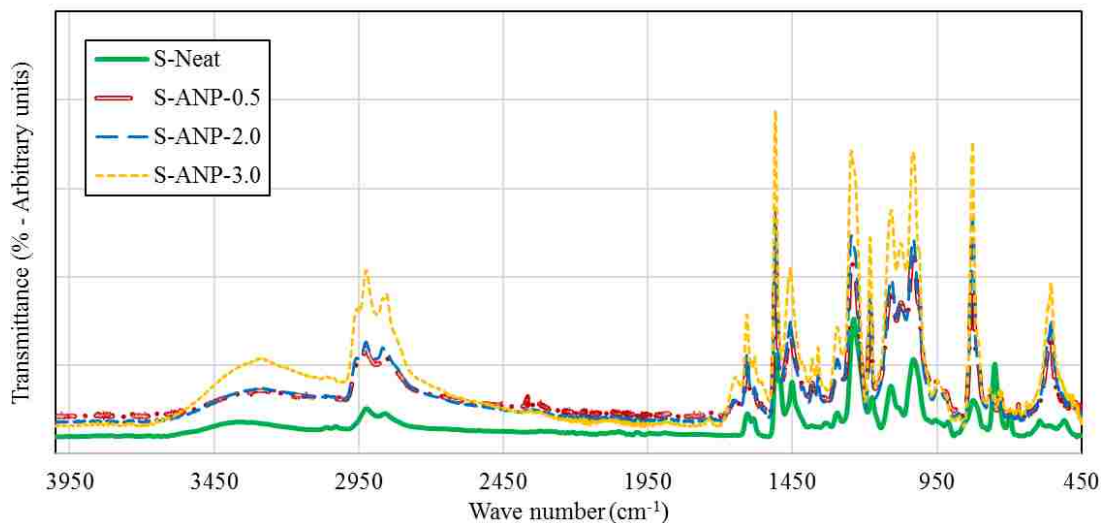


Figure 4.78: FTIR spectrograph of Siloxane epoxy with 0.5, 2.0 and 3.0 wt.% ANPs.

Scans of Siloxane with and without ANPs are shown in Figure 4.78. Based on the FTIR results; the characteristic peaks of the samples appeared at $3150\text{--}3550\text{ cm}^{-1}$ ($\nu_{\text{O-H}}$), $2780\text{--}2980\text{ cm}^{-1}$ (ν_{sym} and ν_{asym} of C-H), 1465 cm^{-1} ($\delta_{\text{C-H}}$, CH_2 and CH_3), $1035\text{--}1110\text{ cm}^{-1}$ ($\nu_{\text{Si-O-Si}}$ and $\nu_{\text{C-O}}$).

c), 1250 cm^{-1} ($\delta_{\text{C-H}}$ in Si-CH₃), 560 cm^{-1} ($\delta_{\text{Si-O-Si}}$) and epoxide ring at 830 cm^{-1} (Kwon *et al.* 2011; Wang *et al.* 2011; Byczyński *et al.* 2015). A peak appears near 1610 cm^{-1} due to Si-C₆H₅ vibrations (Hu *et al.* 2010). Comparing the O-H stretching bands of all epoxy-ANPs nanocomposite spectra with that in the neat specimen, it is noticed that O-H bands of epoxy-ANPs nanocomposites show lower absorption height with broader bands than that of the neat epoxy sample. This observation might be attributed to the effect of ANPs on the O-H association. It is well known that the broad complex band of the hydroxyl stretching vibration region at about $3200\text{--}3600\text{ cm}^{-1}$ is attributed to the combined effect of the differently associated hydroxyl groups, i.e. hydrogen bonding between hydroxyl and hydroxyl/carbonyl groups of different strength and hydrogen bonding of water molecules. In addition, a matrix having O-H groups could undergo two modes of hydrogen bonding: inter- and intramolecular hydrogen bonds between O-H groups (Mikhaylova *et al.* 2006). Overall, the O-H band broadening and intensity lowering can be attributed to redistribution in the arrangement of the hydroxyl group association due to the different geometry caused by the lowered cross-linked matrix. Consequently, it's hypothesized that incorporating ANPs in the epoxy matrix reduced epoxy crosslinking. Lowering the crosslinking bonds consequently changed the ratios of hydrogen bonding modes, which lead to different geometry with different force constants and consequently broadened O-H bands with lower absorption values as those observed in Figure 4.78.

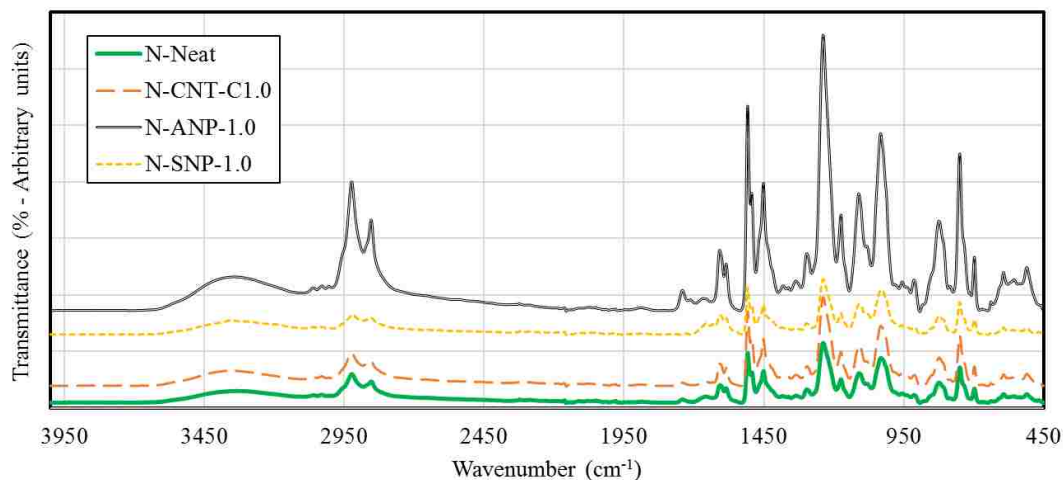


Figure 4.79: FTIR spectrograph for Novolac epoxy at 1.0 wt.% content for COOH-MWCNTs, ANPs and SNPs.

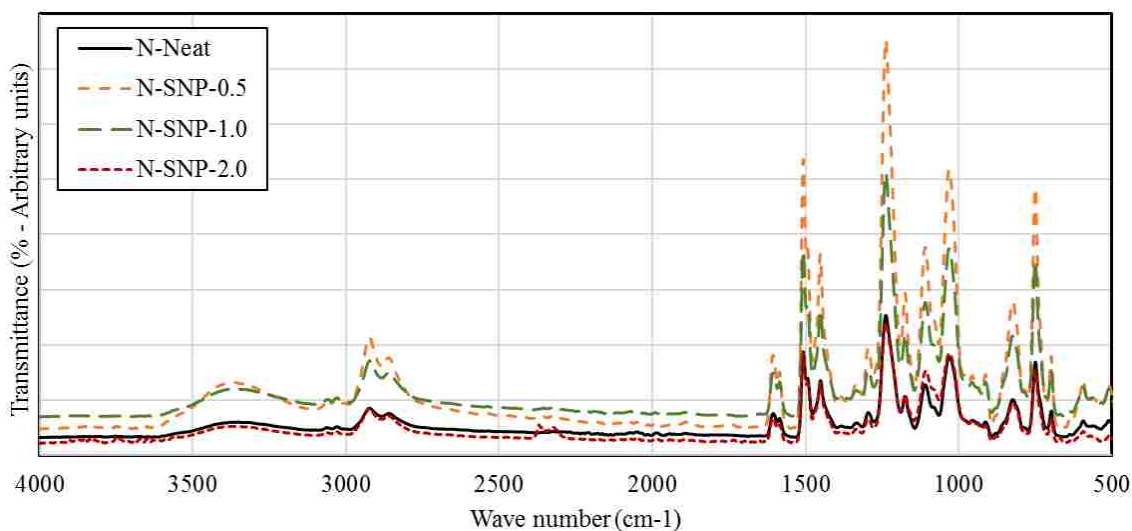


Figure 4.80: FTIR spectrograph of Novolac epoxy with SNPs at 0.5, 1.0 and 2.0 wt.% contents

Novolac epoxy samples show little difference to those of Siloxane showing the standard epoxy peaks. All FTIR scan results are shown in Figure 4.79 and Figure 4.80. The absorption bands corresponding to C-H band ($2850\text{--}2930\text{ cm}^{-1}$), epoxide ring ($\sim 830\text{ cm}^{-1}$), N-H band of primary amines ($1590\text{--}1615\text{ cm}^{-1}$), O-H groups ($\sim 3350\text{ cm}^{-1}$), C-N band ($1030\text{--}1115\text{ cm}^{-1}$) and ether bands ($\sim 1230\text{ cm}^{-1}$) are all apparent and have similar relative ratios to the base spectra. It's noted that there is very little difference between the spectra of neat epoxy and that of epoxy

incorporating SNPs and COOH-MWCNTs. The spectra of epoxy with ANPs look very different and the peaks have a relatively higher ratio to the base spectra. The difference in the epoxy-ANPs nanocomposite can be explained by the fact that alumina-particles are known as an amphoteric substance, meaning it can react with both acids and bases which allow it to act as an acid with a base and a base with an acid. ANPs thus reduce the epoxy curing reaction and consequently leave a relatively large amount of the epoxy resin groups (such as the epoxide ring, N-H band of primary amines, O-H groups) unreacted and available. Those results are like those discussed for Siloxane epoxy as well. The stretching of bands is represented by the significant increase in the epoxide ring, O-H and primary N-H band intensity in the FTIR spectra. This role of ANPs results in increasing the epoxy's chance to react with the sand blasted steel surface in slant shear test which improves the adhesion strength between PC and steel. Golru et al. and Kadar et al. show that ANPs can reduce epoxy curing (Golru et al. 2014, Kadar et al. 2008). The increase in ANPs content would be expected to further increase the amount of unreacted epoxy groups and consequently the adhesion strength. This explains the significant increase in bond strength (+51%) observed with 2.0 wt.% ANPs compared with neat epoxy. It might be important to note that in addition to the chemical effect, ANPs also worked as solid nanofiller and thus enabled increase of epoxy/PC stiffness at high content of 2.0% compared with neat PC. The final improved bond strength is apparently due to the combined effects of ANPs on the adhesion strength and the stiffness difference between PC and steel.

The FTIR spectra also show that MWCNTs with its COOH functionalization resulted in esterification reaction with epoxy and produced the ester and amide peaks appearing at 1740 cm^{-1} and 1665 cm^{-1} , respectively. However, the low content of COOH functionalizing in MWNCTs makes this reaction less effective in Novolac than in Siloxane epoxy. This explains why the

MWCNTs were not able to make significant improvement in adhesion strength between epoxy and steel. Finally, no special features can be detected due to the addition of SNPs to epoxy at any given content as shown in Figure 4.80. Therefore, SNPs seem to work as solid fillers with higher stiffness than epoxy and thus might only improve PC stiffness, but is unlikely to improve the bond strength with steel.

4.14 Dynamic modulus analyzer (DMA)

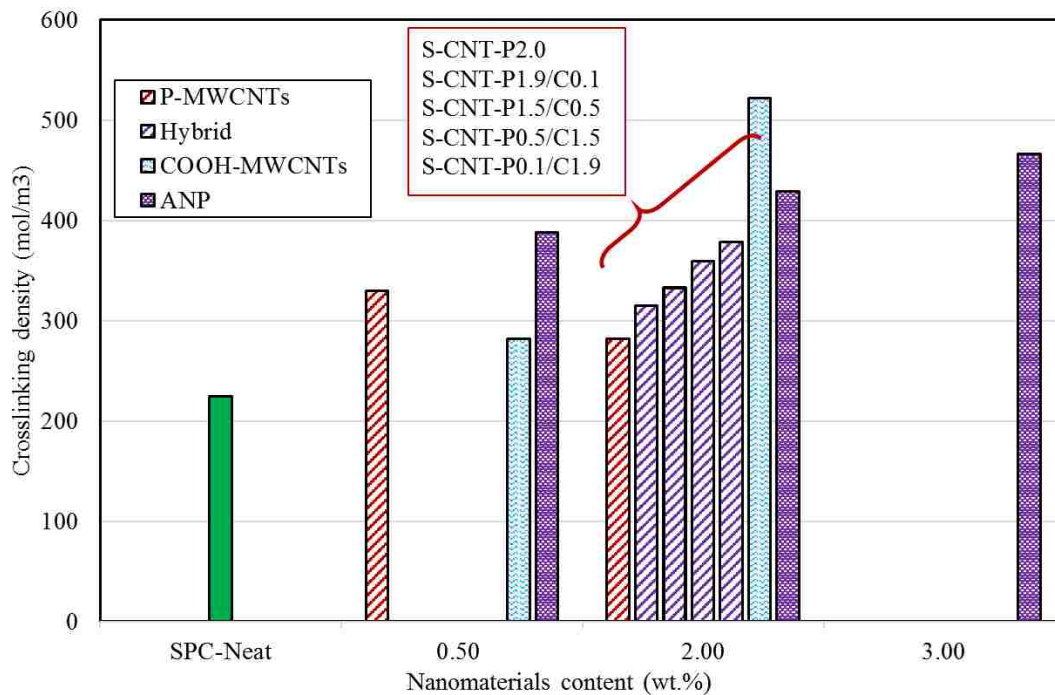


Figure 4.81: Crosslinking density of selected Siloxane epoxy samples using DMA.

The final stage of microstructural investigation utilized epoxy coupons in DMA tests to examine the crosslinking density of siloxane specimen with and without nanomaterials. Samples prepared with Novolac epoxy have not been investigated in this section. FTIR results showed no chemical changes associated with SNPs and because both Novolac and Siloxane utilize ANPs and COOH-MWCNTs while only Siloxane used P-MWCNTs, Novolac samples were not tested.

Results of crosslinking density calculated per section 3.12 are shown in Figure 4.81. It's evident that incorporating any type of nanomaterials at any content result in an increase in crosslinking density. Specimen incorporating ANPs and COOH-MWCNTs showed an increase of crosslinking density with an increase in nanomaterials content. On the other hand, while low contents of P-MWCNTs result in an increase in the measured crosslinking density, higher contents result in less crosslinking. This is supported by previous results discussed in FTIR section of hybrid MWCNTs mixes represented in Figure 4.77 (b). This is attributed to the ability of nonfunctionalized nanomaterials to block segmental motions of polymer chains which has been reported by others (*Zhu et al. 2010; Gu et al. 2012*). However, functionalization enables chemical interaction with the host matrix. The extent of this ability was examined using hybrid mixes of P-MWCNTs and COOH-MWCNTs to determine the relationship between COOH content and crosslinking density. While mixes incorporating P-MWCNTs result in improved crosslinking density by 26% from that of neat, by introducing COOH functional groups onto MWCNTs, the crosslinking density of the epoxy matrix increase. At 0.001 wt.% COOH and 2.0 wt.% MWCNTs content (0.1 COOH-MWCNTs with 1.9 P-MWCNTs namely S-CNT-P1.9/C0.1), a 12% increase in crosslinking density is observed. Higher contents of COOH result in higher crosslinking density values indicating increased carbonyl bands formations. In fact, at 0.025 wt.% COOH content an increase of 85% of crosslinking density is observed compared to 0 wt.% COOH content at the same MWCNTs content. The pattern of mechanical properties and microstructural investigation show that the presence of low contents of COOH result in improved strain at failure and toughness up to 0.018 wt.%. Higher COOH contents result in rapid decrease of ductility and increased strength.

CHAPTER 5: CONCLUSION

Polymer concrete (PC) is an established material used by the industry for bridge deck overlays, repairs, machine foundations, drainage systems, reservoirs and many others. The work discussed in this thesis examines the effects of incorporating different nanomaterials on the mechanical properties of PC. Two types of epoxies were used with 1D nanomaterials such as pristine and carboxyl multi-walled carbon nanotubes (P-MWCNTs and COOH-MWCNTs) and 0D nanomaterials such as alumina and silica nanoparticles (ANPs and SNPs). The content investigated ranged from 0.1 wt.% of epoxy resin up to 4.0 wt.%. Mechanical, analytical and microstructural investigations were carried for the various PC nanocomposites (PCNC) prepared. Mechanical characterization involved flowability, tension, three and four-point bending, fracture toughness, fatigue, structural health monitoring (SHM), compression and slant shear tests. Analytical investigation examined different fracture toughness analysis methods of linear elastic and quasi-brittle fracture mechanics (LEFM and QBFM), finite element modeling (FEM) using ABAQUS, rule of mixture and stiffness mismatch calculations. QBFM also involved two analysis methods namely the effective crack modulus and work of fracture. Microstructural investigation utilized scanning electron microscope (SEM), Fourier transform infrared spectroscopy (FTIR) and dynamic modulus analyzer (DMA). The investigation was designed to examine improving PC performance in bridge deck overlays and as repair material for wellbores. Several stages were utilized in which the best performing and critical contents of each type of nanomaterials were selected.

Mechanical and microstructural characterization show significant differences in PCNC properties between 0D and 1D, functionalized and non-functionalized, and different contents. All nanomaterials were dispersed using magnetic stirring followed by ultrasonication. SEM images

showed that such method produces sufficient shear energy for dispersion and particle suspension. The flowability of all PCNC decreased due to nanomaterials and the decrease was proportional to the content used. Smaller nanomaterials resulted in better flowability and functionalization proved effective in improving flowability.

Tension test results expressed unprecedented levels of ductility of PCNC reaching up to 5.5% strain, an order of magnitude higher than Portland cement concrete (PCC). All PCNC mixes also showed high tensile strength in the range of 9 – 15 MPa that is very appreciable for all PC applications. The best ductility and toughness were achieved for hybrid MWCNTs mixes, then ANPs and P-MWCNTs. Specimen incorporating COOH-MWCNTs showed the highest tensile strength at higher contents due to the chemical bonds between COOH and the polymer matrix. This was supported by FTIR scans and hybrid mixes exposed that higher COOH content result in higher crosslinking densities. Results also showed that content in the range of 0.006 to 0.018 wt.% can maximize PC's strains at failure and toughness at 2.0 wt.% total MWCNTs content.

Tensile and compressive stress-strain curves as well as load-crack mouth opening displacement (CMOD) curves exhibited significant non-linear behavior for all PC and PCNC specimen. This was supported by fracture toughness analysis showing inapplicability of LEFM. QBFM analysis in both methods confirm that all nanomaterial can improve the fracture toughness of PC. 1D nanomaterials showed significant improvements in the elastic fracture toughness energy release rates while 0D and functionalized 1D nanomaterials showed significant fracture process zone energy release rate contributions. Nevertheless, P-MWCNTs, COOH-MWCNTs and ANPs showed improvements in fracture toughness by maximum of 48%, 63% and 81% for work of fracture method and 61%, 80% and 49% for effective crack modulus method respectively.

The depicted patterns in which different nanomaterials improve fracture toughness were emphasized with findings of fatigue tests in which mixes of 2.0 wt.% P-MWCNTs showed 55% increase in fatigue life while ANPs at the same content showed a 50% decrease. 2.0 wt.% P-MWCNTs also improved the conductivity of PC by three orders of magnitude enabling SHM through electrical conductivity measurements. By quantifying the mechanical damage of PC prisms in flexural test using the change in flexural rigidity, PCNC damage can be depicted accurately using the change in electrical resistivity. Therefore, PC incorporating P-MWCNTs not only shows improved ductility, toughness, fracture toughness and fatigue life with appreciable tensile strength but also enables smart structural monitoring.

Slant shear test showed that nanomaterials are also able to improve the bond strength of PC to steel substrates. FTIR scans revealed that the nanomaterials effect in bond strength can be influenced significantly by chemical reactions. High contents of non-reactant nanomaterials such as SNPs result in worsening the bond strength by restricting the polymer-steel bonds. High contents of reactant nanomaterials however depend on the efficiency of chemical bonds. While COOH-MWCNTs can bond to steel substrates, they are also able to bond to the polymer matrix thus bond improvements are nonsignificant at different contents. On the other hand, ANPs only bond with steel substrates. Thus, higher contents of ANPs showed increased bond strengths until the viscosity of PC is significantly deteriorated in which significant air voids are generated.

Compression tests with strain gauges showed that nanomaterials decrease the elastic modulus of PC (as also have been shown by tension tests). More significantly, all nanomaterials showed significant improvements in Poisson's ratio reflected by reducing elastic strain rate recovery. The changes in elastic properties caused by nanomaterials, however, cannot be predicted using micro-filler models as have been shown in literature and by different applications of rule of

mixture. The significant changes in elastic properties resulted in stiffness mismatch in slant shear test which was examined through FEM in ABAQUS. Models utilized the shear slip model in which the interfacial damage and cohesive behavior properties were back-solved by matching load-displacement curves. Models showed that the method of measuring bond strength by dividing the load over the inclined area result in underestimating the true shear stresses. The true shear stresses occur where minimum PC volume is in contact with maximum steel volume reaching up to 130% increase in shear stresses.

An analytical solution measuring the relative stiffness mismatch was evaluated to examine such phenomenon. The suggested model shows that the average stiffness mismatch of PC and PCNC ranges between 307% and 1075%. While other parameters also influence the bond strength of PCNC to steel such as Poisson's ratio affecting the shear modulus and the chemical reactions at the interface, stiffness mismatch has been shown to significantly alter the apparent shear stress.

Future work on the elastic properties of PCNC are required to fully disclose the different mechanisms of different nanomaterials. This work showed that hybrid mixes of nanomaterials can outperform plain mixes by significant ranges. However, the only hybrid mixes utilized in this work involved the same physical and elastic properties (MWCNTs of same length) with only functional group content changes. Future work hybridizing 1D and 0D nanomaterials is therefore necessary. Further SHM utilizing electrical conductivity research is warranted for P-MWCNTs, graphene nanoplates or iron oxide nanomaterials. Hybridization involving any of these nanomaterials can result in improved performance as well. Field application of PCNC are necessary to expand the requirements of mechanical and chemical performance.

This work showed that PC utilizing nanomaterials can serve as an excellent tool to incorporate nanotechnology into civil engineering materials. It also showed that PCNC can provide

excellent and unprecedented mechanical properties lacking in the currently used materials. Many of the suggested PCNC mixes can be utilized for many applications other than what PC is currently limited to. The different contents and different nanomaterials can be further utilized to engineer PC to perform specific mechanical properties based on their application. The proposed PCNC not only serve as smart concrete materials but also are very promising for applications where extreme loading events occur such as earthquakes.

REFERENCES

- Aboubakr S.H., Kandil U.F., Reda Taha M.M. “Creep of epoxy-clay nanocomposite adhesive at the FRP interface: a multi-scale investigation”. *International journal of adhesion and adhesives*. 2014;54:1-12. doi:10.1016/j.ijadhadh.2014.04.003.
- ACI Committee 446, Report 5, “Fracture Toughness Testing of Concrete”, American Concrete Institute, 2009.
- ACI Committee 548. Guide for polymer concrete overlays, ACI 548.5R. Detroit, American Concrete Institute, pp. 1-26, 1998.
- ACI Committee 548. Polymer concrete-structural applications state of the art report, ACI 548.6R. Detroit, American Concrete Institute, pp. 1-23, 1996.
- Agavrioloaie, L., Oprea, S., Barbuta, M., & Luca, F. Characterization of polymer concrete with epoxy polyurethane acryl matrix. *Construction And Building Materials*, 37(1), 190-196. 2012. doi:10.1016/j.conbuildmat.2012.07.037
- Ahn, N., Park, D. K., Lee, J., & Lee, M. K. Structural test of precast polymer concrete. *Journal Of Applied Polymer Science*, 114(3), 1370-1376. 2009. doi:10.1002/app.30731
- Aïtcin, P. C. and Mehta, P. K. “Effect of coarse aggregate characteristics on mechanical properties of high-strength concrete,” *ACI Materials J.*, 87, 103-107, 1990.
- Aïtcin, P. C. and Neville, A., “High performance concrete demystified,” *Concrete Int.*, 15, 21-26 (1993).)
- Arboleda, L., Ares, A., Abad, M. J., Ferreira, A., Costa, P., & Lanceros-Mendez, S. Piezoresistive response of carbon nanotubes-polyamides composites processed by extrusion. *Journal Of Polymer Research*, 20(12), 1-11. 2013. doi:10.1007/s10965-013-0326-y
- ASTM C1421. Standard test methods for determination of fracture toughness of advanced ceramics at ambient temperature. ASTM International, West Conshohocken, PA. 2016
- ASTM C1437-13. Standard test method for flow of hydraulic cement mortar. ASTM International, West Conshohocken, PA. 2013
- ASTM C230/C230M. Standard Specification for Flow Table for Use in Tests of Hydraulic Cement. ASTM international, West Conshohocken, PA. 2014
- ASTM C39/C39M. Standard Test Method for Compressive Strength of Cylindrical Concrete Specimens. ASTM International, West Bonshohocken, PA. 2016
- ASTM C469/C469M. Standard test method for static modulus of elasticity and Poisson’s ratio of concrete in compression. ASTM International, West Conshohocken, PA. 2014.
- ASTM C882/C882M-13a. Standard test method for bond strength of epoxy-resin systems used with concrete by slant shear. ASTM International, West Conshohocken, PA. 2013.

ASTM D5054. Standard test methods for plain-strain fracture toughness and strain energy release rate of plastic materials. ASTM International, West Conshohocken, PA. 2014

ASTM D638-14. Standard test method for tensile properties of plastics. PA. 2014

ASTM E1820. Standard test method for measuring fracture toughness. ASTM International, West Conshohocken, PA. 2011

ASTM E2818. Standard practice for determination of quasistatic fracture toughness of welds. ASTM International, West Conshohocken, PA. 2016

Azhari, F., & Banthia, N. Cement-based sensors with carbon fibers and carbon nanotubes for piezoresistive sensing. *Cement And Concrete Composites*, 34(7), 866-873. 2012. doi:10.1016/j.cemconcomp.2012.04.007

Balakrishnan, A., & Saha, M. C. "Tensile fracture and thermal conductivity characterization of toughened epoxy/CNT nanocomposites". *Materials Science & Engineering A*, 528(3), 906-913, 2011. doi:10.1016/j.msea.2010.09.064

Barbuta, M., Harja, M., and Baran, I., "Comparison of mechanical properties for polymer concrete with different types of filler." *Journal of Materials in Civil Engineering*, Vol. 22, 2010, pp. 696-701.

Barnes, R. A., & Mays, G. C. The transfer of stress through a steel to concrete adhesive bond. *International Journal Of Adhesion And Adhesives*, 21(6), 495-502, 2001. doi:10.1016/S0143-7496(01)00031-8

Bazant, P. Z. "Analysis of work of fracture method for measuring fracture energy of concrete". *Journal of Engineering Mechanics*, 122(2), 138-144, 1996.

Bazant, P. Z. Concrete fracture models: testing and practice. *Engineering Fracture Mechanics*, 69, 165 – 205, 2002.

Bлага A, Beaudoin JJ. Polymer modified concrete. *Canadian building digest*, CBD-241. Institute for Research in Construction; 1985.

Borowski, Elisa, Eslam Soliman, Usama Kandil, and Mahmoud Taha. "Interlaminar Fracture Toughness of Cfrp Laminates Incorporating Multi-Walled Carbon Nanotubes." *Polymers* 7 (6): 1020–45, 2015. doi:10.3390/polym7061020.

Bridge deck overlay system [Brochure]. Unitex by Dayton Superior. Miamisburg, 2016 OH.

Byczyński, Ł., Dutkiewicz, M., and Maciejewski, H. "Synthesis and properties of high-solids hybrid materials obtained from epoxy functional urethanes and siloxanes." *Progress in Organic Coatings*, 84, 59–69, 2015.

Chakraborty, A. K., & Terrasi, G. P. "Carbon nanotube (CNT)-epoxy nanocomposites: a systematic investigation of CNT dispersion". *Journal of Nanoparticle Research*, 13(12), 6493-6506, 2011.

- Chen, X., Wang, J., Lin, M., Zhong, W., Feng, T., Chen, X., ... Xue, F. "Mechanical and thermal properties of epoxy nanocomposites reinforced with amino-functionalized multi-walled carbon nanotubes". *Materials Science & Engineering A*, 492(1-2), 236-242, 2008. doi:10.1016/j.msea.2008.04.044
- Chmielewska, B., Czarnecki, L., Sustersic, J., and Zajc, A., "The Influence of Silane Coupling Agents on the Polymer Mortar", *Cement & Concrete Composites*, Vol.28, No.9, 2006, pp.803-810.
- Chuah, S., Pan, Z., Sanjayan, J. G., Wang, C. M., & Duan, W. H. Nano reinforced cement and concrete composites and new perspective from graphene oxide. *Construction and Building Materials*, 73, 113-124, 2014. doi: 10.1016/j.conbuildmat.2014.09.040
- Chung, S., Kang, H., Ocon, J. D., Lee, J. K., & Lee, J. Enhanced electrical and mass transfer characteristics of acid-treated carbon nanotubes for capacitive deionization. *Current Applied Physics*, 15(11), 1539-1544, 2015. doi:10.1016/j.cap.2015.09.004
- Coppola L, Buoso A, Corazza F. The influence of AC and DC electrical resistance and piezoresistivity measurements of CNTs/Cement composites. In: *Résumé & Actes – abstracts & proceedings international congress on materials & structural stability-Congrès International Matériaux & Stabilité Structurale*; 2013
- Czarnecki, L., and Chmielewska, B., "The Influence of Coupling Agent on the Properties of Vinylester Mortar", *Proceedings of the Second International RILEM Symposium on Adhesion between Polymers and Concrete*, RILEM, Cachan, France, Sept. 1999, pp.57-65.
- Daghash, S., Soliman, E., Kandil, U., Reda Taha, M.M. "Improving impact resistance of polymer concrete using CNTs". *Journal of Concrete Structures and Materials*, 2016. DOI 10.1007/s40069-016-0165-4
- David, O. B., Banks-Sills, L., Aboudi, J., Fourman, V., Eliasi, R., Simhi, T., ... Raz, O. "Evaluation of the mechanical properties of pmma reinforced with carbon nanotubes - experiments and modeling". *Experimental Mechanics: An International Journal*, 54(2), 175-186, 2014. doi:10.1007/s11340-013-9792-8
- Davis, P. Cantwell, W.J., Kausch, H.H. "Delamination from thin starter films in carbon PEEK composites" *J Mater Sci Lett*, 9, 1990, pp. 1349–1350
- Douba A, Genedy M, Stormont J, Reda Taha M.M, Matteo E.N, and Kandil U.F. "The Significance of Nanoparticles on Bond Strength of Polymer Concrete to Steel." *International Journal of Adhesion and Adhesives* 74: 77–85, 2017. doi:10.1016/j.ijadhadh.2017.01.001.
- Dowling N. E., "Mechanical behavior of materials: Engineering methods for deformation, fracture, and fatigue", Third edition, 2007.
- Echtermeyer A.T., McGarry F.J., Mandell, J.F. "Effect of damage on the stress concentration ahead of a notch in crossplied composites". PPST Report 89-2, Massachusetts institute of technology; 1989.

- Elalaoui, Ghorbel, O., Mignot, E., & Ben Ouezdou, V. “Mechanical and physical properties of epoxy polymer concrete after exposure to temperatures up to 250 °C”. *Construction And Building Materials*, 27(1), 415-424, 2012. doi:10.1016/j.conbuildmat.2011.07.027
- Elices, M., Guinea, G. V., & Planas, J. On the Measurement of Concrete Fracture Energy Using Three-point Bend Tests. *Materials And Structures /*, 30(200), 375, 1997.
- Emiroglu, M. Douba A., Tarefder, R., Kandil, U., Reda Taha, M. M. “New polymer concrete with superior ductility and fracture toughness using alumina nanoparticles”, *Journal of Materials in Civil Engineering (ASCE)*. 84 (8–9). doi:10.1061/(ASCE)MT.1943-5533.0001894.
- Evaluation and Assignment of Nanoparticle Dispersion/Characterisation Methodologies, to be Developed under PROSPECT [Report]. *Ecotoxicology Test Protocols for Representative Nanomaterials in Support of the OECD Sponsorship Programme*, 2009.
- Fowler, D. W. “Polymers in concrete: a vision for the 21st century”. *Cement and Concrete Composites*, 21(5-6), 449-452, 1999. doi:10.1016/S0958-9465(99)00032-3
- Fowler, D. W. “Polymers in concrete—a vision for the 21st century,” *Cement and Concrete Composites*, 21, 449-452, 1999.
- Ganguli, S., Aglan, H., Dennig, P., & Irvin, G. “Effect of Loading and Surface Modification of MWCNTs on the Fracture Behavior of Epoxy Nanocomposites”. *Journal of Reinforced Plastics and Composites*, 25(2), 175-188, 2006.
- Garlof, S., Mecklenburg, M., Smazna, D., Mishra, Y. K., Adelung, R., Schulte, K., & Fiedler, B. “3D carbon networks and their polymer composites: Fabrication and electromechanical investigations of neat Aerographite and Aerographite-based PNCs under compressive load”. *Carbon*, 111, 2017.
- Gasda, S. E., Bachu, S., & Celia, M. A. “Spatial characterization of the location of potentially leaky wells penetrating a deep saline aquifer in a mature sedimentary basin”. *Environmental Geology : International Journal Of Geosciences*, 46(6-7), 707-720, 2004. doi:10.1007/s00254-004-1073-5
- Genedy, M., Kandil, U.F., Matteo, E.N., Stormont, J. and Reda Taha, M.M. “A new polymer nanocomposite repair material for restoring wellbore seal integrity”. *International Journal of Greenhouse Gas Control*, 58, 2017, pp.290–298.
- Ghosh, P. K., Kumar, K., & Chaudhary, N. “Influence of ultrasonic dual mixing on thermal and tensile properties of MWCNTs-epoxy composite”. *Composites Part B: Engineering*, 77, 139-144, 2015. doi:10.1016/j.compositesb.2015.03.028.
- Gojny, F. H., Wichmann, M. H. G., Köpcke, U., Fiedler, B., & Schulte, K. “Carbon nanotube-reinforced epoxy-composites: enhanced stiffness and fracture toughness at low nanotube content”. *Composites Science and Technology*, 64(15), 2363-2371, 2004.

Golru, S. S., Attar, M. M., Ramezanzadeh, B. "Studying the influence of nano-Al₂O₃ particles on the corrosion performance and hydrolytic degradation resistance of an epoxy/polyamide coating of AA-1050", *Progress in Organic Coatings*, 77, 2014, 1391-1399.

Gómez-del Río, T., Salazar, A., Pearson, R. A., & Rodríguez, J. "Fracture behaviour of epoxy nanocomposites modified with triblock copolymers and carbon nanotubes". *Composites Part B, Engineering*, 87, 343-349, 2016.

Gorninski, J. P., Dal Molin, D. C., and Kazmierczak, C.S., "Comparative assessment of isophthalic and orthophthalic polyester polymer concrete: Different costs, similar mechanical properties and durability." *Construction and Building Materials*, Vol. 21, 2007, pp. 546-555.

Grossiord, N., Loos J., Regev, O. Koning, C. E. Toolbox for dispersing carbon nanotubes into polymers to get conductive nanocomposites. *Chemistry of Materials*, 2006; 18: 1089-1099.

Gu, H., Tadakamalla, S., Huang, Y., Colorado, H. A., Luo, Z., Haldolaarachchige, N., Young, D. P., Wei, S., and Guo, Z. "Polyaniline Stabilized Magnetite Nanoparticle Reinforced Epoxy Nanocomposites." *ACS App. Mater. & Interfaces*, 4(10), 5613–5624, 2012.

Haidar, M., Ghorbel, E., Toutanji, H., "Optimization of the formulation of micro-polymer concretes." *Construction and Building Materials*, Vol. 25, 2011, pp. 1632-1644.

Haitao Liu, & Jianhua Mo. Study on Nanosilica Reinforced Stereolithography Resin. *Journal Of Reinforced Plastics And Composites*, 29(6), 909-920, 2010.

Haleem, Y. A., Liu, D., Chen, W., Wang, C., Hong, C., He, Z., ... Song, L. "Surface functionalization and structure characterizations of nanodiamond and its epoxy based nanocomposites". *Composites: Part B, Engineering*, 78, 2015.

Hameed, A., Islam, M., ahmad, I., Mahmood, N., Saeed, S., & Javed, H. "Thermal and mechanical properties of carbon nanotube/epoxy nanocomposites reinforced with pristine and functionalized multiwalled carbon nanotubes". *Polymer Composites*, 36(10), 1891-1898, 2015. doi:10.1002/pc.23097.

Hamidi, Y., Aktas, L., & Altan, M.. Effect of Nanoclay Content on Void Morphology in Resin Transfer Molded Composites. *Journal Of Thermoplastic Composite Materials*, 21(2), 141-163, 2008.

He, Z., Zhang, X., Chen, M., Li, M., Gu, Y., Zhang, Z., & Li, Q. Effect of the filler structure of carbon nanomaterials on the electrical, thermal, and rheological properties of epoxy composites. *Journal Of Applied Polymer Science*, 129(6), 2013, 3366-3372. doi:10.1002/app.39096

Hillerborg, A., Modéer, M., & Petersson, P. E. "Analysis of crack formation and crack growth in concrete by means of fracture mechanics and finite elements". *Cement And Concrete Research*, 6(6), 773-781, 1976. doi:10.1016/0008-8846(76)90007-7

Hsieh, T. H., Kinloch, A. J., Taylor, A. C., & Kinloch, I. A. "The effect of carbon nanotubes on the fracture toughness and fatigue performance of a thermosetting epoxy polymer". *Journal Of*

Materials Science: Full Set - Includes 'Journal Of Materials Science Letters', 46(23), 2011, 7525-7535. doi:10.1007/s10853-011-5724-0

Hu, C., Xu, G., Shen, X., Shao, C., and Yan, X. "The epoxy-siloxane/Al composite coatings with low infrared emissivity for high temperature applications." *App. Surface Sci.*, 256(11), 2010, 3459–3463.

Hwang, Y., Lee, J.-K., Lee, J.-K., Jeong, Y.-M., Cheong, S.-i., Ahn, Y.-C., & Kim, S. H. "Production and dispersion stability of nanomaterials in nanofluids". *Powder Technology*, 186(2), 2008, 145-153. doi:10.1016/j.powtec.2007.11.020

Hyun, S.-H., & Yeon, J. H. "Strength development characteristics of UP-MMA based polymer concrete with different curing temperature". *Construction And Building Materials*, 37(4), 2012, 387-397. doi:10.1016/j.conbuildmat.2012.07.094

Jeng Y. S., and S. P. Shah. "Nonlinear fracture parameters for cement based composites: theory and experiments". *NATO ASI Series, Series E: Applied Sciences*, 94 ed., pp. 319-359, 1985.

João Marciano Laredo dos Reis. "Mechanical characterization of fiber reinforced Polymer Concrete". *Materials Research*, 8(3), 2005, 357-360. doi:10.1590/S1516-14392005000300023

Julio, E., Branco, F., Silva, V. "Concrete-to-concrete bond strength. Influence of the roughness of the substrate surface". *Construction and Building Materials*. 2004; 18, 9, 675-681.

Kabir, M. E., Saha, M. C., & Jeelani, S. "Effect of ultrasound sonication in carbon nanofibers/polyurethane foam composite". *Materials Science & Engineering A*, 459(1-2), 111-116, 2007.

Kadar, P., Ebrahimi, M., Bastani, S., "Study the effect of nano-alumina particles on physical-mechanical properties of UV cured epoxy acrylate via nano-indentation". *Progress in Organic Coatings*, 62, 2008, 321-325.

Kaeding A.O. and Prusinki R., "Curtain Wall Panels", *ACI Special Publication*, Vol. 214, 2003, pp. 151-168.

Kardon, J. B. "Polymer-Modified Concrete: Review". *Journal of Materials In Civil Engineering*, 9(2), 1997, 85-92. doi:10.1061/(ASCE)0899-1561(1997)9:2(85)

Karihaloo, B. L., & Nallathambi, P. "Effective crack model for the determination of fracture toughness (K_{Ic}) of concrete. *Engineering Fracture Mechanics*, 35(4-5), 637-645, 1990. doi:10.1016/0013-7944(90)90146-8

Kwon, Y., Yim, B.-s., Kim, J.-m., and Kim, J. "Mechanical and wetting properties of epoxy resins: Amine-containing epoxy-terminated siloxane oligomer with or without reductant." *Microelectronics Reliability*, 51(4), 2011, 819–825.

Lakshmi Kanta Rao, V.V. and Krishnamoorthy, S. "Influence of resin and microfiller proportions on strength, density, and setting shrinkage of polyester polymer concrete". *ACI STRUCTURAL JOURNAL*, 95(2), 1998, pp.153–162.

- Liao, Y.-H., Marietta-Tondin, O., Liang, Z., Zhang, C., & Wang, B. "Investigation of the dispersion process of SWNTs/SC-15 epoxy resin nanocomposites". *Materials Science & Engineering: A*, 385(1/2), 2004.
- Liew, K. M., Kai, M. F., & Zhang, L. W. "Carbon nanotube reinforced cementitious composites: An overview". *Composites Part A: Part 1*, 91, 301-323, 2016. doi:10.1016/j.compositesa.2016.10.020
- Liu W, Hoa SV, Pugh M. "Organoclay-modified high performance epoxy nanocomposites". *J Compos Sci Technol* 2005;65:307–16
- Lu-Qi Liu, & Wagner, H. D. A comparison of the mechanical strength and stiffness of MWNT-PMMA and MWNT-epoxy nanocomposites. *Composite Interfaces*, 14(4), 2007.
- Ma, C., Liu, H.-Y., Du, X., Mach, L., Xu, F., & Mai, Y.-W. "Fracture resistance, thermal and electrical properties of epoxy composites containing aligned carbon nanotubes by low magnetic field". *Composites Science and Technology*, 114, 2015 126-135.
- Ma, P. C., Kim, J.-K., & Tang, B. Z. "Effects of silane functionalization on the properties of carbon nanotube/epoxy nanocomposites". *Composites Science and Technology*, 67(14), 2007, 2965-2972.
- Maggi, F. "Curing viscosity of htpb-based binder embedding micro- and nano-aluminum particles". *Propellants, Explosives, Pyrotechnics*, 39(5), 2014, 755-760. doi:10.1002/prop.201400010
- Maity P., Parameswaran V., Basu S., & Gupta N. "On the size and dielectric properties of the interphase in epoxy-alumina nanocomposite". *IEEE Transactions On Dielectrics And Electrical Insulation*, 17(6), 2010, 1665-1675. doi:10.1109/TDEI.2010.5658215
- Martínez-Barrera, G., Viguera-Santiago, E., Martínez-López, M., Ribeiro, M. C. S., Ferreira, A. J. M., & Brostow, W. "Luffa fibers and gamma radiation as improvement tools of polymer concrete". *Construction And Building Materials*, 47, 2013, 86-91. doi:10.1016/j.conbuildmat.2013.05.038
- Mikhaylova, Y., Adam, G., Häussler, L., Eichhorn, K. J., and Voit, B. "Temperature-dependent FTIR spectroscopic and thermoanalytic studies of hydrogen bonding of hydroxyl (phenolic group) terminated hyperbranched aromatic polyesters." *J. of Molecular Struct.*, 2006 788(1–3), 80–88.
- Momayez, A., Ehsani, M. R., Ramezani-pour, A. A. and Rajaie H. "Comparison of methods for evaluating bond strength between concrete substrate and repair materials. *Cem. & Conc. Res.* 2005; 35, 4, 748.
- Muszynski, L. C. "Polymer concrete", *Encyclopedia of polymer science and engineering*, New York: Wiley, 12, 462-470, 1988.
- Nair, P., Ku, D. H., Lee, C. W., Park, J. S., Park, H. Y., & Lee, W. M. "Mechanical properties and durability of PMMA impregnated mortar". *Korean Journal of Chemical Engineering*, 27(1), 2010, 334-339. doi:10.1007/s11814-009-0346-9

- Ohama, Y. "Recent progress in concrete polymer composites," *Cement and Concrete Composites*, 5, 31-40, 1997.
- Opelt, C. V., Becker, D., Lepienski, C. M., & Coelho, L. A. F. "Reinforcement and toughening mechanisms in polymer nanocomposites – Carbon nanotubes and aluminum oxide". *Composites: Part B, Engineering*, 75 (15), 2015, 119-126.
- Osorio, A.G.; Silveira, I.C.L.; Bueno, V.L.; Bergmann, C.P. "H₂SO₄/HNO₃/HCl—Functionalization and its effect on dispersion of carbon nanotubes in aqueous media". *Appl. Surf. Sci.* 2008, 255, 2485–2489.
- Oyawa W.O., "Steel encased polymer concrete under axial compressive loading: Analytical formulations", *Construction and Building Materials*, Vol. 21, 2007, pp. 57-65.
- Oyawa W.O., Sugiura K., and Eiichi Watanabe E., "Polymer concrete-filled steel tubes under axial compression", *Construction and Building Materials*, Vol. 15, 2001, pp. 187-197.
- Park S. K., Jo B. W., Park D. H., and Chun B. S.. "Flexural rigidity and ductility of high-strength reinforced polyester polymer concrete beams", *Advances in Cement Research*, Vol. 22, No. 2, 2010, pp. 91 –97.
- Park, S.-J., Heo, G.-Y., & Jin, F.-L. "Rheological properties and fracture toughness of epoxy resin/multi-walled carbon nanotube composites". *Polymer Engineering & Science*, 55(11), 2015, 2676-2682.
- Patankar S.N., Mohan R., Kelkar A.D., & Vaidyanathan R. "Processing and characterization of epoxy resin dispersed with multi walled carbon nanotube (MWNT) derived from camphor. *Materials Science And Engineering A*, 529(1), 2011, 253-256. doi:10.1016/j. msea.2011.09.025
- Paul D. K., John S. L., and Kimberly A. S. "Guidelines for selection of bridge deck overlays, sealers and treatments". *National Cooperative Highway Research Program (NCHRP) Transportation Research Board of The National Academies*. P.1-51, 2009.
- Pocius, A. V. "Adhesion and Adhesives Technology: An Introduction". 2nd ed. Hanser; 2011.
- Pratap, A. "Vinyl ester and acrylic based polymer concrete for electrical applications". *Progress In Crystal Growth And Characterization Of Materials*, 45(1), 117-125, 2002. doi:10.1016/S0960-8974(02)00036-0
- Prusinski R. C., "Study of Commercial Development in Precast Polymer Concrete", *ACI Special Publication*, Vol. 58, 1978, pp. 75-102.
- Qi, B., Zhang, Q.X., Bannister, M., Mai, Y.W. "Investigation of the mechanical properties of DGEBA-based epoxy resin with nanoclay additives". *J Compos Struct* 2006;75:514–9
- Rebeiz K.S., and Fowler D.W., "Flexure for reinforced polymer concrete using recycled PET", *Proceedings of the Materials Engineering Conference*, Vol. 2, 1996, pp. 1037-1044, *Materials for the New Millennium*.

Rebeiz, K. S., and Fowler, D. W., “Shear and Flexure Behavior of Reinforced Polymer Concrete Made with Recycled Plastic Wastes”, *ACI Materials Journal*, special publication, Vol. 166, 1996, pp. 61-78.

Rebeiz, K.S., Serhal, S.P., and Craft, A.P., “Properties of Polymer Concrete Using Fly Ash”, *ASCE-Journal of Materials in Civil Engineering*, Vol.16, No.1, 2004, pp.15-19.

Reda Taha, M. M., Xiao, X., Yi, J., & Shrive, N. G. (2002). Evaluation of flexural fracture toughness for quasi-brittle structural materials using a simple test method. *Canadian Journal of Civil Engineering*, 29(4), 567-575

Reis, J. M. L. Fracture and flexural characterization of natural fiber-reinforced polymer concrete. *Construction And Building Materials*, 20(9), 2006, 673-678. doi:10.1016/j.conbuildmat.2005.02.008

Reis, J. M. L., & Ferreira, A. J. M. “A contribution to the study of the fracture energy of polymer concrete and fibre reinforced polymer concrete”. *Polymer Testing*, 23(4), 2004, 437-440. doi:10.1016/j.polymertesting.2003.09.008

Reis, J. M. L., & Ferreira, A. J. M. “Assessment of fracture properties of epoxy polymer concrete reinforced with short carbon and glass fibers”. *Construction and Building Materials*, 18(7), 2004, 523-528. doi:10.1016/j.conbuildmat.2004.04.010

Ribeiro MCS, No´ voa PR, Ferreira AJM, Marques AT. Flexural performance of polyester and epoxy polymer mortars under severe thermal conditions. *Cem Concr Compos* 2004;26(7):803–9.

RILEM, TC50-FMC, Fracture mechanics of concrete, in: Determination of Fracture Energy of Mortar and Concrete by Means of Three Point Bend Tests on Notched Beams, Draft RILEM Recommendation, *Materials and Structures* vol. 18, 1985, pp. 283–296.

Roylance, D. *Mechanics of materials*. New York: Wiley, 1996.

Rusell, A.J. “Street Moisture and temperature effects on the mixed-mode delamination fracture of unidirectional graphite/epoxy Delamination Debond”. *Mater ASTM STP* 876, 1985, pp. 349–370

Russell, A.J. “Street Factors affecting the interlaminar fracture energy of graphite/epoxy laminates *Progress in science and engineering of composites*”, Tokyo (1982)

Saldanha, R., Julio, E., Dias-da-Costa, D., Santos, P. “A modified slant shear test designed to enforce adhesive failure”. *Construction and Building Materials*. 2013; 41, 673-680.

Samorì, C., Sainz, R., Ménard-Moyon, C., Toma, F. M., Venturelli, E., Singh, P., ... Bianco, A. “Potentiometric titration as a straightforward method to assess the number of functional groups on shortened carbon nanotubes”. *Carbon*, 48(9), 2010 2447-2454. doi:10.1016/j.carbon. 2010.03.015

Sarkar S, Das PK. Processing and properties of carbon nanotube/alumina nanocomposites: a review. *Rev Adv Mater Sci* 2014;37(1):53–82

- Seyhan, A. T., Tanođ lu, M., & Schulte, K. "Tensile mechanical behavior and fracture toughness of MWCNT and DWCNT modified vinyl-ester/polyester hybrid nanocomposites produced by 3-roll milling". *Materials Science & Engineering: A*, 523(1/2), 2009.
- Sha, J., Li, G., Chen, X., Xia, P., Luo, R., Yang, S., ... Xie, L. "Simultaneous ultrasonication-assisted internal mixing to prepare MWCNTs-filled epoxy composites with increased strength and thermal conductivity". *Polymer Composites*, 37(3), 2016, 870-880. doi:10.1002/pc.23245.
- Shah, S.P., Swartz, S.E., and Ouyang, C. "Fracture mechanics of concrete: applications of fracture mechanics to concrete, rock and other quasi-brittle materials". John Wiley & Sons, Inc., New York, N.Y, 1995.
- Shannon H. P., Richard D. L. "Overlays on existing bridge overlays". *Memos to Designers* 8-5, 1-3, 1996.
- Shimpi, N. G., Kakade, R. U., Sonawane, S. S., Mali, A. D., & Mishra, S. "Influence of nano-inorganic particles on properties of epoxy nanocomposites". *Polymer-Plastics Technology And Engineering*, 50(8), 2011, 758-761. doi:10.1080/03602559.2010.551437
- Shokrieh, M. M., Heidari-Rarani, M., Shakouri, M., & Kashizadeh, E. "Effects of thermal cycles on mechanical properties of an optimized polymer concrete". *Construction And Building Materials*, 25(8), 2011, 3540-3549. doi:10.1016/j.conbuildmat.2011.03.047
- Shokrieh, M. M., Kefayati, A. R., & Chitsazzadeh, M. "Fabrication and mechanical properties of clay/epoxy nanocomposite and its polymer concrete". *Materials And Design*, 40, 2012, 443-452. doi:10.1016/j.matdes.2012.03.008
- Shokrieh, M., Rezvani, S., & Mosalmani, R. "A novel polymer concrete made from fine silica sand and polyester". *Mechanics Of Composite Materials*, 51(5), 2015.
- Silfwerbrand, J. "Bonding between old and new concrete in structures loaded by static and time-dependent load." *Adhesion between polymers and concrete*, H. R. Sasse, ed., Chapman and Hall Ltd., New York, N.Y., 309-319, 1986.
- Soh, Y. S., Jo, Y. K., Park, H. S. "Effect of fillers on the mechanical properties of unsaturated polyester resin mortar," *Polymers in Concrete*, 67-74, 1997.
- Soliman E, Kandil UF, Reda Taha M. Limiting shear creep of epoxy adhesive at the FRP-concrete interface using multi-walled carbon nanotubes. *International Journal of Adhesion and Adhesives*. 2012;33:36-44.
- Soliman EM, Kandil UF, Reda Taha MM. Investigation of FRP lap splice using epoxy containing carbon nanotubes. *Journal of Composites for Construction*. 2015;19(2).
- Son, S.-W., & Yeon, J. H. Mechanical properties of acrylic polymer concrete containing methacrylic acid as an additive. *Construction And Building Materials*, 37(2), 2012, 669-679. doi:10.1016/j.conbuildmat.2012.07.093

- Sumfleth, J., Prehn, K., Wichmann, M. H. G., Wedekind, S., & Schulte, K. A comparative study of the electrical and mechanical properties of epoxy nanocomposites reinforced by CVD- and arc-grown multi-wall carbon nanotubes. *Composites Science and Technology*, 70(1), 2010, 173-180.
- Sun S, Yu X, Han B. “Sensing mechanism of self-monitoring CNT cementitious composite”. *J Test Eval* 2014;42(1):69–83
- Swaddiwudhipong, S., Lu, H.-R., & Wee, T.-H. “Direct tension test and tensile strain capacity of concrete at early age”. *Cement And Concrete Research*, 33(12), 2003, 2077-2084. doi:10.1016/S0008-8846(03)00231-X
- Tang, L.-C., Wan, Y.-J., Peng, K., Pei, Y.-B., Wu, L.-B., Chen, L.-M., ... Lai, G.-Q. “Fracture toughness and electrical conductivity of epoxy composites filled with carbon nanotubes and spherical particles”. *Composites Part A: Applied Science and Manufacturing*, 45(5453), 2013, 95-101.
- Tawfik, M., & Eskander, S. “Polymer concrete from marble wastes and recycled poly(ethylene terephthalate)”. *Journal Of Elastomers And Plastics*, 38(1), 65-79, 2006.
- Theodore, M., Hosur, M., Thomas, J., & Jeelani, S. “Influence of functionalization on properties of MWCNT–epoxy nanocomposites”. *Materials Science & Engineering: A*, 528(3), 2011.
- Thostenson, E. T., & Chou, T.-W. “Carbon nanotube-based health monitoring of mechanically fastened composite joints”. *Composites Science And Technology*, 68(12), 2008, 2557-2561. doi:10.1016/j.compscitech.2008.05.016
- Toufigh, V., Shirkorshidi, S. M., & Hosseinali, M. “Experimental investigation and constitutive modeling of polymer concrete and sand interface”. *International Journal Of Geomechanics*, 17(1), 2017, 04016043-04016043.
- Toufigh, V., Toufigh, V., Saadatmanesh, H., & Ahmari, S. “Strength evaluation and energy-dissipation behavior of fiber-reinforced polymer concrete”. *Advances In Civil Engineering Materials*, 2(1), 2013, 20130074. doi:10.1520/ACEM20130074
- Tyson, B. M., Abu Al-Rub, R. K., Yazdanbakhsh, A., & Grasley, Z. “A quantitative method for analyzing the dispersion and agglomeration of nano-particles in composite materials”. *Composites Part B*, 42(6), 2011, 1395-1403. doi:10.1016/j.compositesb.2011.05.020
- Vipulanandan, C. Mohammed, A. “Smart cement modified with iron oxide nanomaterials to enhance the piezoresistive behavior and compressive strength for oil well applications”. *Smart Materials and Structures*, 24(12), 2015. doi:10.1088/0964-1726/24/12/125020
- Vipulanandan, C., & Paul, E. “Characterization of polyester polymer and polymer concrete”. *Journal Of Materials In Civil Engineering*, 5(1), 1993, 62-82. doi:10.1061/(ASCE)0899-1561(1993)5:1(62)
- Wahby W. S. and Prusinki R., “Precast Polymer Concrete Building Panels: Case Studies with Longevity Experience”, *Collaboration and Harmonization in Creative Systems*, 2005, pp. 265-267.

- Wang, Q., Dai, J., Li, W., Wei, Z., & Jiang, J. "The effects of CNT alignment on electrical conductivity and mechanical properties of SWNT/epoxy nanocomposites". *Composites Science & Technology*, 68(7/8), 2008.
- Wang, S., Li, Y., Fei, X., Sun, M., Zhang, C., Li, Y., Yang, Q., and Hong, X. "Preparation of a durable superhydrophobic membrane by electrospinning poly (vinylidene fluoride) (PVDF) mixed with epoxy-siloxane modified SiO₂ nanomaterials: A possible route to superhydrophobic surfaces with low water sliding angle and high water contact angle." *J. of Colloid and Interface Sci.*, 359(2), 2011, 380-388.
- Wang, T., Zhang, J., & Zhang, Y. "Forming process and damping properties of carbon fiber-reinforced polymer concrete". *Journal Of Reinforced Plastics And Composites*, 33(1), 2013, 93-100. doi:10.1177/0731684413510753
- Wecharatana, M. and Shah, S. P. "Nonlinear fracture mechanics parameters". *Fracture Mechanics of concrete*, F. H. Wittmann, ed., Elsevier, Amsterdam, The Netherlands, 483-480, 1983.
- Wheat, D. L., Fowler, D. W., & Al-Negheimish A.I. "Thermal and fatigue behavior of polymer concrete overlaid beams". *Journal of Materials in Civil Engineering*, 5(4), 1993, 460-477.
- White, K. L., & Sue, H., -J. "Electrical conductivity and fracture behavior of epoxy/polyamide-12/multiwalled carbon nanotube composites". *Polymer Engineering & Science*, 51(11), 2011, 2245-2253.
- Wilkins, D.J., Eisenmann, J.R., Camin, R.A., Magrolis, W.S., Benson R.A. "Characterizing delamination growth in Graphite-Epoxy Damage". *Compos Mater ASTM STP*, 775, 1980, pp. 168-183
- Williams, J., Broughton, W., Koukoulas, T., & Rahatekar, S. S. "Plasma treatment as a method for functionalising and improving dispersion of carbon nanotubes in epoxy resins". *Journal Of Materials Science : Full Set - Includes `Journal Of Materials Science Letters'*, 48(3), 2013, 1005-1013. doi:10.1007/s10853-012-6830-3
- Xiao, H., Song, G., Li, H., & Sun, L. "Improved tensile properties of carbon nanotube modified epoxy and its continuous carbon fiber reinforced composites". *Polymer Composites*, 36(9), 2015, 1664-1668. doi:10.1002/pc.23076.
- Yamamoto, N., Guzman de Villoria, R., & Wardle, B. L. "Electrical and thermal property enhancement of fiber-reinforced polymer laminate composites through controlled implementation of multi-walled carbon nanotubes". *Composites Science And Technology*, 72(16), 2012, 2009-2015. doi:10.1016/j.compscitech.2012.09.006
- Yan, J., & Jeong, Y. G. "Roles of carbon nanotube and BaTiO₃ nanofiber in the electrical, dielectric and piezoelectric properties of flexible nanocomposite generators". *Composites Science And Technology*, 2017. doi:10.1016/j.compscitech.2017.03.015

Yeh, M.-K., Hsieh, T.-H., & Tai, N.-H. "Fabrication and mechanical properties of multi-walled carbon nanotubes/epoxy nanocomposites". *Materials Science & Engineering A*, 2008, 483-484, 289-292. doi:10.1016/j.msea.2006.09.138.

Yeon, K.-S., Cha, J.-Y., Yeon, J.H. and Seung, I.B. "Effects of Tmptma and Silane on the Compressive Strength of Low-Temperature Cured Acrylic Polymer Concrete". *Journal of Applied Polymer Science*, 131(20), 2014.

Yeon, K.-S., Yeon, J. H., Choi, Y.-S., & Min, S.-H. "Deformation behavior of acrylic polymer concrete: Effects of methacrylic acid and curing temperature". *Construction & Building Materials*, 63, 2014.

Yu, N., Zhang, Z. H., & He, S. Y. "Fracture toughness and fatigue life of MWCNT/epoxy composites". *Materials Science & Engineering A*, 494(1-2), 2008, 380-384.

Zhai, L., Ling, G., Li, J., and Wang, Y. "The effect of nanomaterials on the adhesion of epoxy adhesive". *Materials Letters*. 2006; 60, 3031-3033.

Zhang, Z., Tan, Y., Wang, X., Tan, H., & Li, J. "Mechanical behavior and fracture toughness of epoxy composites reinforced with combination of fibrous and spherical nanofillers". *Polymer Composites*, 36(12), 2015, 2147-2156.

Zheqiong Wu; Zhiqian Wang; Fang Yu; Megha Thakkar; Somenath Mitra. "Variation in chemical, colloidal and electrochemical properties of carbon nanotubes with the degree of carboxylation". *J Nanopart Res* 19:16, 2017.

Zhou, Y., Pervin, F., Lewis, L., & Jeelani, S. "Fabrication and characterization of carbon/epoxy composites mixed with multi-walled carbon nanotubes". *Materials Science & Engineering A*, 475(1-2), 2008, 157-165.

Zhu, J., Peng, H., Rodriguez-Macias, F., Margrave, J., Khabashesku, V., Imam, A. ... Barrera, E. "Reinforcing epoxy polymer composites through covalent integration of functionalized nanotubes". *Advanced Functional Materials*, 14(7), 2004, 643-648. doi:10.1002/adfm.200305162

Zhu, J., Wei, S., Ryu, J., Budhathoki, M., Liang, G., and Guo, Z. "In situ stabilized carbon nanofiber (CNF) reinforced epoxy nanocomposites." *J. of Mater. Chem.*, 20(23), 2010, 4937–4948.

Zhu, J.; Kim, J.; Peng, H.; Margrave, J.L.; Khabashesku, V.N.; Barrera, E.V. Improving the dispersion and integration of single-walled carbon nanotubes in epoxy composites through functionalization. *Nano Lett.* 2003, 3, 1107–1113.

APPENDIX A: MATLAB CODES

1. Linear elastic fracture mechanics codes:

These files were developed by Chapman (2011) and modified by the author (2016) to accommodate the sample's geometry and mechanical behavior of PC.

A.1.1 Reading text files

```
function [dim, P, LPD, CMOD] = get_data(FraMat1)
%Function "get_data" reads in the values from a text file and outputs the
%relevant data.
%Returns: P, the load (mm)
% LPD, the load point displacement (mm)
% CMOD, the crack mouth opening displacement (mm)
%Written by: Scott Chapman
%Modified: 8/2/2011
%Load dimension data
%from comma-separated or tab-delimited values
%Note: This section is very specific to a particular set of data.
%Change as needed, or comment out entirely and manually input specific
%data for your specimens
%Name of specimen dimensions file. Specimen dimensions should be in the
%following form:
%D, B, a0, preload

dim = [25.4 25.4 8.89 0];

%get pre-load
pre_load = dim(4);
%get specimen data
data2 = xlsread('FraMat1');
P = data2(1:end,1) + pre_load;
for i = 1:length(P)
LPD(i) = data2(i, 2);
CMOD(i) = data2(i, 3);
end
return
```

A.1.2 Curve fitting for evaluating "A" according to ACI 446 report

```
function [p] = get_A(x,y)
% This function fits a curve of P1 vs X (x and y inputs) and fits a curve
% of the order P1 = KX^2 + AX. The function outputs the coefficients of
% the quadratic fit as p = [K A 0]
% This method was taken from the following mathworks solution webpage:
```

```

% http://www.mathworks.com/support/solutions/en/data/1-12BBUC/?product=OP&s
% olution=1-12BBUC
%
%plot the original curve
plot(x,y);
x0 = 0;
y0 = 0;
%reshape the data into a column vector
x = x(:);
y = y(:);
% 'C' is the Vandermonde matrix for 'x'
n = 2; % Degree of polynomial to fit
V(:,n+1) = ones(length(x),1,class(x));
for j = n:-1:1
V(:,j) = x.*V(:,j+1);
end
C = V;
% 'd' is the vector of target values, 'y'.
d = y;
% There are no inequality constraints in this case, i.e.,
% We use linear equality constraints to force the curve to hit the required
point. In
% this case, 'Aeq' is the Vandermonde matrix for 'x0'
Aeq = x0.^(n:-1:0);
% and 'beq' is the value the curve should take at that point
beq = y0;
p = lsqlin( C, d, [], [], Aeq, beq );
% We can then use POLYVAL to evaluate the fitted curve
yhat = polyval( p, x );
% Plot original data
plot(x,y,'b-')
hold on
% Plot point to go through
plot(x0,y0,'gx','linewidth',4)
% Plot fitted data
plot(x,yhat,'r','linewidth',2)
hold off

```

A.1.3 Bi-linear approximation code

```

function bilinear_approximation
% This function determines key fracture parameters for the NBLII test.
% Written by: Scott Chapman
% Modified: 03/12/2016 by AlaEddin Douba
%pre_load = 730.00; %pre-load in Newtons
ft = 18.3; %splitting tensile strength in MPa, taken from Brazilian tests
specimen = 'spec64.txt';
S = 25.4*3; %Span length, mm
% D = 228.50; %Average Depth of specimen, mm;
% B = 151.48; %Average Width of specimen, mm;
% a0 = 80.40; %Average Notch Depth of specimen, mm;
[dim, Pc, LPDc, CMODc] = get_data(specimen);

```



```

D = dim(1);
B = dim(2);
a0 = dim(3);
b = D-a0;
h = 0.8; %Distance of the knife edges to specimen surface, mm
max_CMOD = 12; %Max crack mouth opening displacement allowed, mm
%Read in all relevant data
%Sensitivity analysis begins at 100% of the desired final CMOD range, and
%then does a number of iterations down to 20% of the final CMOD and finds
%key fracture parameters for each iteration. This tests the validity of
%the far tail constant, A, and its effect on the fracture parameters
num_iter = 100;%number of iterations for sensitivity analysis
%read in data for sensitivity analysis
percent_reduction = 0.6/num_iter;
CMOD_holder = max_CMOD;
for j = 1:num_iter
for i = 1:length(Pc)
if CMODc(i) < CMOD_holder
P(i,1) = Pc(i);
CMOD(i,1) = CMODc(i);
LPD(i,1) = LPDc(i);
end
end
[E(j,1), fp(j,1), l1(j,1), w1(j,1), GF(j,1), wg(j,1), wch(j,1),wc(j,1),
ok(j,1), wk(j,1), Gf(j,1)]= fracture_toughness(P,LPD,CMOD,B,D, a0,ft,S,
max_CMOD,b,h);
%prep CMOD_holder for next iteration
CMOD_holder = CMOD_holder * (1 - percent_reduction);
%free up memory
P = [];
CMOD = [];
LPD = [];
end
%Data to be used in excel files
props = [E, fp, l1, w1, GF, wg, wch, wc, ok, wk, w1, Gf];
sumE=0;
sumfp=0;
sumw1=0;
sumGF=0;
sumwg=0;
sumwc=0;
sumok=0;
sumwk=0;
sumGf=0;
for i = 1:100
sumE=0;
sumfp=sumfp+fp(i);
sumw1=sumw1+w1(i);
sumGF=sumGF+GF(i);
sumwg=sumwg+wg(i);
sumwc=sumwc+wc(i);
sumok=sumok+ok(i);
sumwk=sumwk+wk(i);
sumGf=sumGf+Gf(i);
end
avrfp=sumfp/100;
avrwl=sumw1/100;

```

```

avrGF=sumGF/100
avrwg=sumwg/100;
avrwc=sumwc/100
avrok=sumok/100
avrwk=sumwk/100
avrGf=sumGf/100;

```

```

return

```

A.1.4 Evaluating fracture toughness

```

function [E, fp, l1, w1, GF, wg, wch, wc, ok, wk, Gf] = ...
    fracture_toughness(P,LPD,CMOD, B, D, a0, ft, S, max_CMOD,b,h)
%This function determines key fracture parameters given load vs. LPD and
%load vs. CMOD data from a notched beam level II test.
%Inputs: arrays for the following:
% Load, P
% Crack Mouth Opening Displacement, CMOD
% Load Point Displacement, LPD
%Returns:
% Young's Modulus, E
% Plastic Flexural Strength, fp
% Brittleness Length, l1
% Horizontal intercept of initial portion of softening curve, w1
% Fracture Energy, GF
% Critical crack opening, wc
% Kink point stress, ok
% Kink point crack opening, wk
%Written by: Scott Chapman
%Modified: 2/28/2011
%Sensitivity analysis bug fix: Delete any 0 data points at end
while CMOD(end) == 0
    CMOD(end) = [];
    P(end) = [];
    LPD(end) = [];
end
Pm = max(P); %max recorded peak load
%Find location of max P
Pholder = 1;
for i = 1:length(P)
    if Pholder < P(i);
        Pholder = P(i);
        location = i;
    end
end
%9.2.2
%This section gets the values of CMOD and P and calculates the initial
%compliance, Ci
j = 1; %counter variable
for i = 1:location
    if P(i) > 0.15*Pm && P(i) < 0.55*Pm
        Ptemp(j) = P(i);
        Ctemp(j) = CMOD(i);
    end
end

```

```

        j = j+1;
    end
end
%Find Ci coefficient as CMOD / P
C = polyfit(Ptemp, Ctemp, 1);
Ci = C(1);
%9.2.3
alpha = (a0 + h)/(D + h);
%Calculation of Stress Intensity Factor
V1 = 0.8 - 1.7*alpha + 2.4*alpha^2 + 0.66/(1-alpha)^2 + ...
    4*D/S * (-0.04 - 0.58*alpha + 1.47*alpha^2 - 2.04*alpha^3);
%Calculation of Young's Modulus
E = 6*S*a0 / (Ci*B*D^2) * V1;
%Re-load matrices as necessary so that CMOD(end) <= max_CMOD
data_length = length(P);
for i = 1:data_length
    if CMOD(i) >= max_CMOD
        CMOD(i) = -1;
    end
end
%delete unnecessary data
while CMOD(end) == -1
    P(end) = [];
    LPD(end) = [];
    CMOD(end) = [];
end
%Get Residual Load
R = P(end);
%Get corrected peak load, P1
P1 = P - R;
%Find location of max P
Pholder = 1;
for i = 1:length(P1)
    if Pholder < P(i);
        Pholder = P(i);
        location = i;
    end
end
Plmax = max(P1);
%Determine far tail constant, A, using equation in section 9.3.4.
%Get all data correlated with P1 <= 5% of Plmax
counter = 1;
for i = location:length(P1)
    if P1(i) <= 0.05*Plmax;
        wm(counter) = CMOD(i);
        Plx(counter) = P1(i);
        counter = counter+1;
    end
end
%Get CMOD and LPD at end of test, wmr, and CMOD when P1 = 0, wma.
wmr = CMOD(end);
del_r = LPD(end);
%Special case, P1 does not cross x-axis on P vs. CMOD curve,
%so wma and del_a are 0;
counter = 1;
if P1(1) > 0
    wma = 0;

```

```

    del_a = 0;
else
    %Otherwise, find location where P1 crosses x-axis on P vs. CMOD curve
    while P1(counter) < 0;
        counter = counter+1;
    end
    wma = CMOD(counter);
    del_a = LPD(counter);
    %Adjust P1, CMOD, LPD so that there are no data correlated to P1 < 0
    j = 1;
    for i=counter:length(P1)
        P1(j) = P1(i);
        CMOD(j) = CMOD(i);
        LPD(j) = LPD(i);
        j = j+1;
    end
    %Delete left over data
    for i = length(P1) - counter:length(P1)
        P1(end) = [];
        CMOD(end) = [];
        LPD(end) = [];
    end
end
end
%Get X values, 9.3.4
for i = 1:length(P1x)

    X(i) = ((4*D)/S)^2 * (1/(wm(i) - wma)^2 - 1/(wmr - wma)^2);

end
%Perform least squares fit to get far tail constant, A
p = get_A(X,P1x);
A = p(2);
%Get effective Peak Load, Pmax
Pmax = P1max + A/(wmr - wma)^2;
%Get plastic flexural strength, fp, 9.4.2
fp = Pmax*S/(2*B*(D-a0)^2);
%Get brittleness length, l1, 9.5.1
%parameters
alpha_0 = a0/D;
k = 1 - alpha_0^1.7;
x = ft/fp;
l1 = k*D*(11.2/(x^2-1)^2 + 2.365/x^2);
%Get horizontal intercept, w1 in micrometers, 9.5.2
w1 = 1000*2*ft*l1/E;
%Get work of fracture from area under P1 vs. LPD curve
Wfm = trapz(LPD,P1);
%Get the total work of fracture
WF = Wfm + 2*A/(del_r - del_a);
%Get the fracture energy, GF, in N/m
GF = 1000*WF/(B*b);
%Get center of gravity of area under softening curve, wg, 9.7.1
wg = 4*A/(B*S*GF)*10^6;
%Get characteristic crack opening, wch, 9.8.2
wch = GF/ft;
%Get critical crack opening of bilinear approximation, wc, 9.8.3
wc = wch*(3*wg-w1)/(2*wch-w1) * (1 + sqrt(...

```

```

1 - 2*w1*(3*wg-2*wch)*(2*wch-w1)/(wch*(3*wg-w1)^2));
%Get stress at kink point, ok, 9.8.4
ok = ft*(2*wch - w1)/(wc - w1);
%Get crack opening at kink point, wk, 9.8.5
wk = w1*(wc - 2*wch)/(wc - w1);
%Get fracture energy Gf as area under initial part of softening curve
Gf = 0.5*w1*ft;
return

```

2. Work of fracture codes:

```

clear all
close all
clc

%This code evaluates the area under load-CMOD curves
%and evaluates the fracture energy Gf according to
%Hillerborg's model (1985)%

data = xlsread('Work');
P = data(1:end,1); % in N
CMOD=data(1:end,3); %in mm
L = length (P);
E= 3790; %Elastic modulus in MPa
nu=0.35; %Poisson's ratio of PC with nanomaterials
b=25.4; %width of the beam in mm
d=25.4; %depth of the beam in mm
a=8.4; %crack depth in mm
for i=1:L-1
    avgP=(P(i)+P(i+1))/2;
    if CMOD(i+1)>CMOD(i)
        delta_CMOD=CMOD(i+1)-CMOD(i);
    else
        delta_CMOD=0;
    end
    A(i)=avgP*delta_CMOD;
end
Gf=sum(A)/(b*(d-a)) %kN m/m2
K_Ic=sqrt(Gf*E/(1-nu^2))/sqrt(1000) %MPa sqrt(m)

```

3. Quasi brittle fracture mechanics codes:

A.3.1 Evaluating the critical crack depth and elastic fracture parameters (G & K)

```

close all;
clear all;
clc;

```

```

% The following program is used to determine the differnt fracture toghness
% parameters for concrete.The estimation of the effective crack length is
% based on the elastic crack model by Reda Taha and Shrive[2000].The
% following equations assume a simple beam notched at mid span and loaded
% in third point bending.

```

```

% Beam parameters :
% b = beam width in mm , d = beam depth in mm , L = beam length in mm ,
% S = beam loaded span in mm , a0 = initial notch depth in mm ,
% H0 = Initial un-cracked ligament in mm , W = Beam wt. in kgs

```

```

b = 25.4; %width in mm
d = 25.4; %depth in mm
l = 76.2; %Loading span length mm
Lt=2*l; % total length of the sample mm
a(1) = 8.4; %length of the initial crack mm
H0 = d - a(1);
alpha_e=a(1)/d;

```

```

%Analysis parameters
Elas_limit=0.9; %Elastic limit as function peak: P_peak/P_elastic
nu = 0.35; % nu = Poisson's ratio of concrete
E_uncracked=6070; %modulus of elasticity in MPa of uncracked specimen
K=100; %# of divisions to calculate a_critical
tol=0.01; %tolerance

```

```

%Self weight%
W = b*d*Lt*1E-9*2200; % this gives the weight in kgs
w = ( W * 9.81 ) / Lt; % N per mm

```

```

% Testing data :
% P(Load in kN) and delta(Deflection in mm) are any load and its
% corresponding deflection within the elastic range of loading.
% and
% to maximum load in mm.

```

```

data = xlsread('Fram');
P = data(1:end,1); % in N
delta=data(1:end,2); %in mm
L = length (P);
Pc=zeros(1);
for v=1:1:L
    if P(v)>Pc
        Pc=P(v);
        deltaC=delta(v);
        o=v; %o is the counter until peak
    end
end
Pe=Elas_limit*Pc;
for j=1:1:o
    if P(j)<Pe
        deltadum(j)=delta(j); %dummy variable
    else
        deltadum(j)=0;
    end
end

```

```

    end
end
deltaE=max(deltadum);
deltaAN(1)=0;
deltaAN(L+1)=0;
P(L+1)=-P(L);
%Area up to peak%
for z=2:1:L+1
    if delta(z-1)<=deltaC
        deltaAN(z)=delta(z-1);
        deltaAN(z+1)=delta(z);
    else
        deltaAN(z)=0;
        deltaAN(z+1)=0;
    end
    AN_col(z-1)=(deltaAN(z+1)-deltaAN(z))*(P(z-1)+P(z))/2;
end
AN=sum(AN_col)
% Evaluate g1, g and F

syms alpha
g1 = 1.122 - 1.4*alpha + 7.33*alpha^2 - 13.08*alpha^3 + 14*alpha^4;
g = pi^0.5 * g1;
F = int(alpha*(g^2));
% E for 3 point bending
syms PF deltaF F
E= 1/(b*d*deltaF) * ((13*w*1^4)/(32*d^2) + (3*PF*1^3)/(4*d^2) ...
    + (3*(1+nu)*PF*1)/4 + (9*PF*1^2*F)/(2*d));

delta_a=H0/K;
F_e=subs(F,alpha_e);
E_e=double(vpa(subs(E, [PF, deltaF, F], [Pe, deltaE, F_e])));
for i=1:1:K
    alpha(i)=a(i)/d;
    Fsub=subs(F,alpha(i));
    E_c(i)=double(vpa(subs(E, [PF, deltaF, F], [Pc, deltaC, Fsub])));
    Error(i)=double(vpa((abs(E_e-E_c(i)))/E_e));
    if Error(i)<tol
        a_ci(i)=a(i);
        a(i+1)=a(i)+delta_a;
    else
        a(i+1)=a(i)+delta_a;
        a_ci(i)=1000;
    end
end
end

a_c=min(a_ci); %Critical crack length%
sigma_c= 3*Pc*1/(2*d^3); %Critical stress applied
alpha_c=a_c/d;
g1_c=subs(g1,alpha_c); % Geometric function at a_c
K1c=vpa(g1_c*sigma_c*sqrt(pi*a_c)/sqrt(1000)) %K1C in Mpa*m ^1/2
G1c=10^3 *K1c^2*(1-nu^2)/E_uncracked %Fracture toughness in kN*m/m^2
Hc=d-a_c
Pc

```

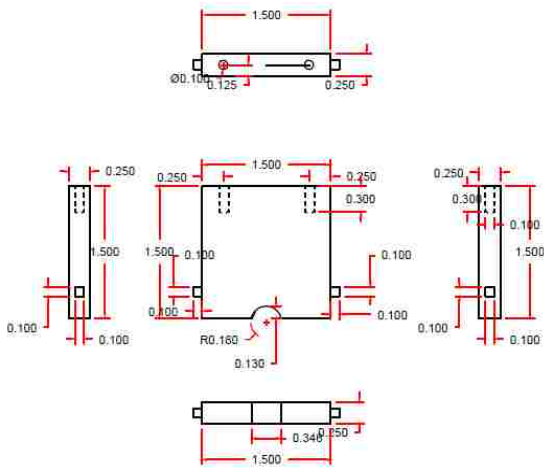
A.3.2 Evaluating the J-integral

```
clear all
close all
clc

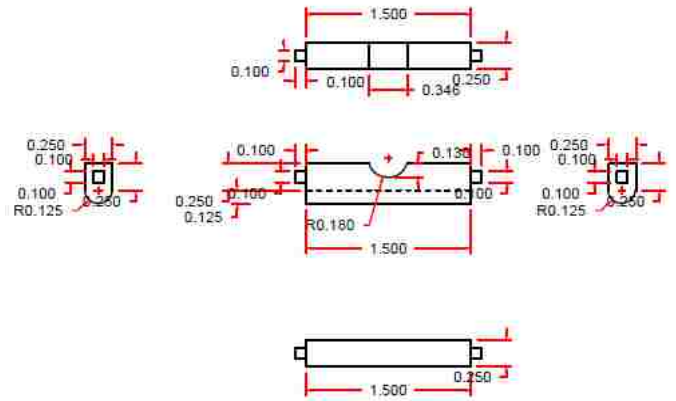
% measures the uncracked area up to peak load%

data = xlsread('Bend');
P = data(1:end,1); % in N
delta=data(1:end,2); %in mm
L = length (P);
Pc_dum=zeros(1);
Pc=998.5;
b=25.4; %sample's width in mm
h=25.4; %sample's height in mm
Lt=25.4*3; %span length in mm
deltaAUN(1)=0;
deltaAUN(L+1)=0;
P(L+1)=-P(L);
for v=1:1:L
    if P(v)>Pc_dum
        Pc_dum=P(v);
        deltaC_dum=delta(v);
        o=v; %o is the counter until peak
    end
end
for u=1:1:L
    if delta(u)<deltaC_dum
        if P(u)<Pc
            deltaC=delta(u);
        end
    end
end
%Area up to peak%
for z=2:1:L+1
    if delta(z-1)<=deltaC
        deltaAUN(z)=delta(z-1);
        deltaAUN(z+1)=delta(z);
    else
        deltaAUN(z)=0;
        deltaAUN(z+1)=0;
    end
    AUN_col(z)=(deltaAUN(z+1)-deltaAUN(z))*(P(z-1)+P(z))/2;
end
AUN=sum(AUN_col) % in N*mm
MOR=3*Pc_dum * Lt/(2*b*h^2)
```

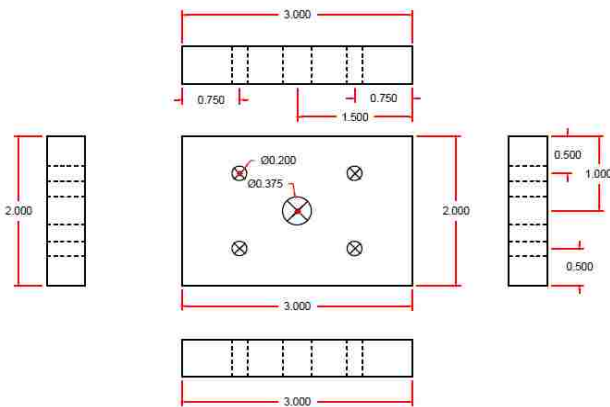

APPENDIX B: FRACUTRE TEST SETUP SHOP-DRAWINGS



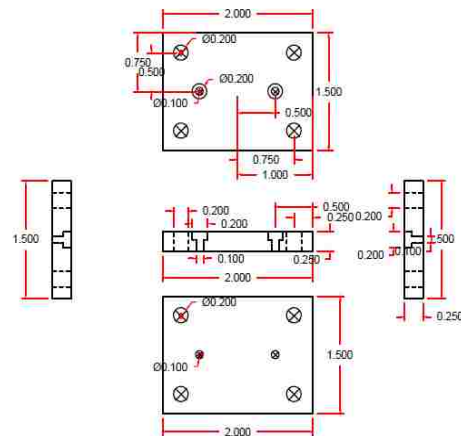
(a) Loading head: Top part



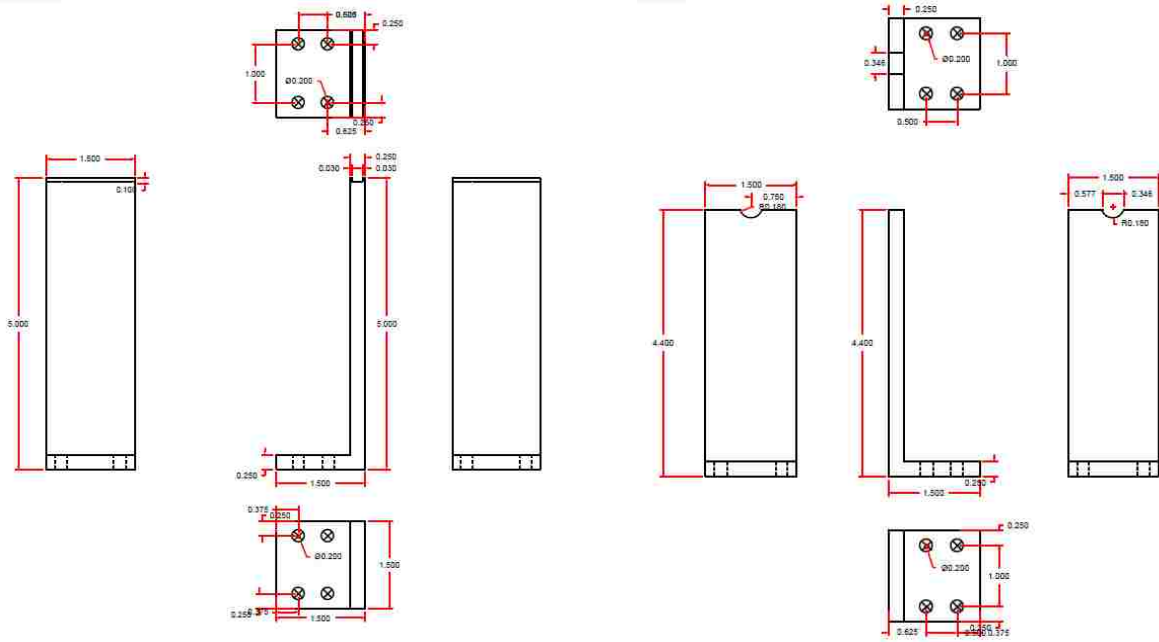
(b) Loading head: Bottom part



(c) Loading head: Loading plate

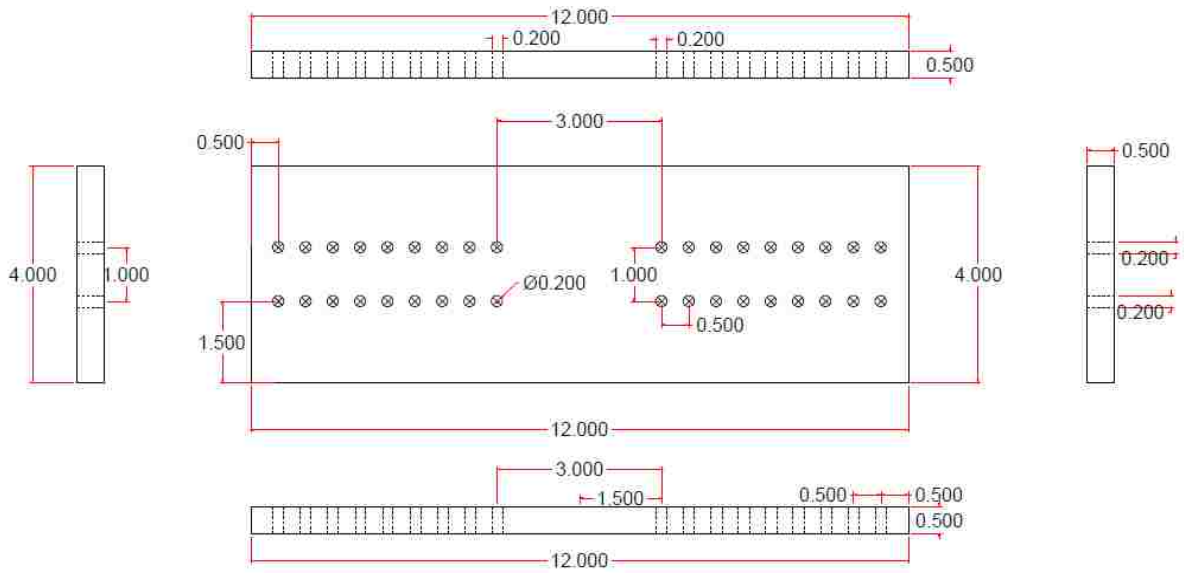


(d) Loading head: Intermediate plate

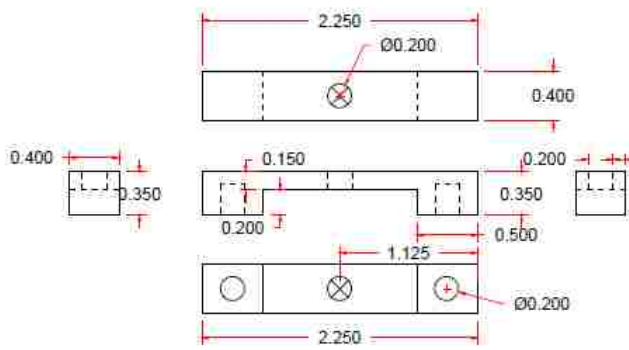


(e) Loading frame: Left support

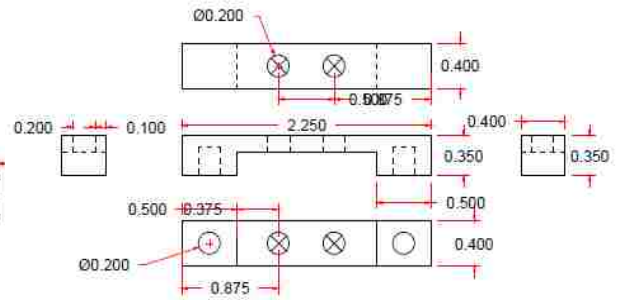
(f) Loading frame: Right support



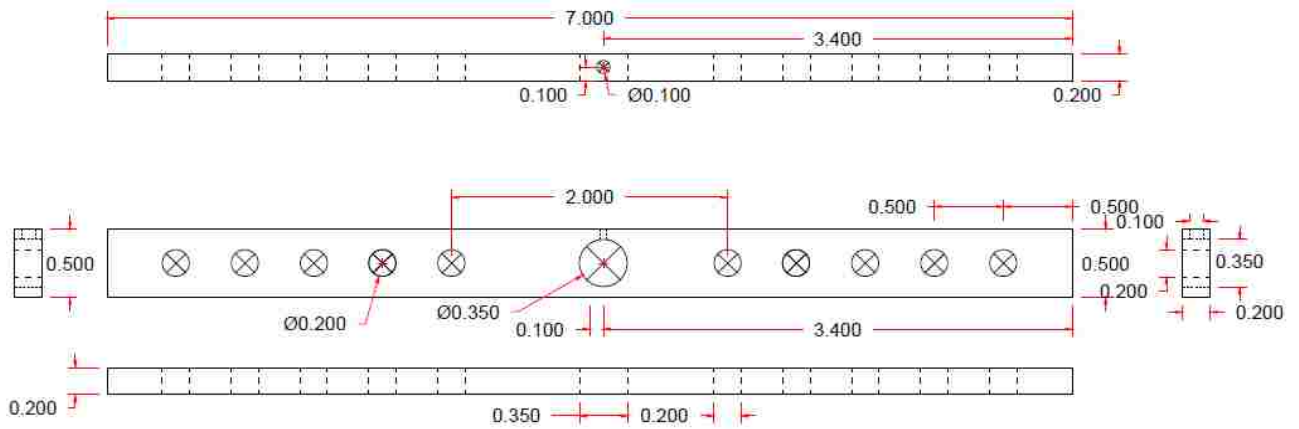
(g) Loading frame: Loading plate



(h) Reference frame: Top part – First support



(i) Reference frame: Top part – Second support



(j) Reference frame: Bottom part